

# Improved Micro-oil Droplet Coalescence for Oil-water Separation by Spider Silk-like Structures

## Verbesserte Koaleszenz von Mikro-Öltropfen für die Öl-Wasser-Trennung durch spinnenseidenartige Strukturen

Von der Fakultät Energie-, Verfahrens- und Biotechnik der Universität Stuttgart zur Erlangung der Würde eines Doktor-Ingenieurs (Dr.-Ing.) genehmigte Abhandlung

vorgelegt von

**Maryam Aliabadi**

aus Khomein, Iran

Hauptberichter: Prof. Dr.-Ing. Götz Theodor Gresser

Mitberichter: PD Dr. Dr. Wilfried Konrad

Tag der mündlichen Prüfung: 14.07.2023

Deutsche Institute für Textil- und Faserforschung Denkendorf (DITF)  
in Zusammenarbeit mit dem Institut für Textil- und Fasertechnologien (ITFT)  
der Universität Stuttgart

**2023**



*This work is dedicated to all 172 beautiful souls who tragically lost their lives in the  
crashed Flight PS752 near Tehran, Iran.*





# Preface and Acknowledgments

This dissertation is part of my work as a research associate at the German Institutes of Textile and Fiber Research (DITF) in Denkendorf. At this point, I would like to thank DFG for providing me with the funding and all the people who made this thesis possible, and an unforgettable experience.

First and foremost, I would like to express my deepest appreciation to my main supervisor Prof. Dr. Götz T. Gresser for his continuous support and guidance during my work. His encouragement throughout the work was the key to conduct rewarding and memorable research. I appreciate all his contributions of time and ideas and for making my experience productive and stimulating. My sincere thanks go to my co-supervisor PD Dr. Thomas Stegmaier for his systematic guidance during our invaluable meetings and the great effort he put into training me in both scientific and business fields.

I owe my deepest gratitude to my external co-supervisor PD Dr. Dr. Wilfried Konrad for his support and help during this work. It is a real privilege and an honor for me to have his support and brilliant knowledge and ideas for my work.

I thank my colleagues Dr. Andreas Scherrieble, Matthias Schweins, my ex-colleague Dr. Volkmar von Arnim, and all colleagues in the Competence Center Textile Chemistry, Environment & Energy as well as the mechanical workshop for the fruitful discussions and their support in the laboratory. I would like to extend my thanks to my colleague Ulrike Burger and also my friend Omid Taheri, who supported me in expanding my EDP skills and knowledge.

I express my sincere thanks to my external project partners especially to Prof. Yan Liu, Prof. Guoyong Wang, and Dr. Bin Zhan for the very pleasant and intelligent working atmosphere during my stay at Key Laboratory of Bionic Engineering of Jilin University.

I sincerely thank my family, especially my parents and my brother Vahid for their loving support and best wishes in my plans to study abroad.

Last but not least, I would like to express my very profound gratitude to my husband, Mohsen, for his endless support, love, patience, and continued encouragement throughout my life and years of study. Finally, I would like to thank my little Jana (Djana) who, with her incredible companionship, paved the way for me to compile this dissertation. Love you.

Stuttgart, January 2023

Maryam Aliabadi



## Kurzfassung

Ölhaltige Abwässer mit fein verteilten Tröpfchen (Durchmesser  $< 10 \mu\text{m}$ ) sind weltweit zu einer weit verbreiteten Umweltverschmutzung und angesichts der zunehmenden Wasserknappheit zu einer ernsthaften Bedrohung der Wasserressourcen geworden. Daher muss ein zuverlässiges Verfahren für die Trennung von Öl und Wasser gefunden werden, um das Wasser in das öffentliche Abwassersystem einleiten oder in den Kreislauf zurückführen zu können. Unter den konventionellen Abscheidetechniken haben Vliesstoff-Koaleszenz-Filtermedien mit gleichmäßigen Fasern enorme Fortschritte bei verschiedenen Filtrationsproblemen ermöglicht. Es wurde jedoch festgestellt, dass es zu Leistungsgipfeln kommt, wenn sie aufgrund einer verzögerten Koaleszenz und Ablösung der Tröpfchen verstopfen. Hinsichtlich dieses Problems war die Beobachtung biologischer Strukturen in der Natur und das Herausfinden der faszinierenden Struktur-Funktions-Beziehungen, die zur Realisierung der gerichteten Sammlung von Wassertröpfchen beitragen, eine wichtige Inspiration für diese Arbeit. Ziel dieser Studie war es, ein hochwertiges Vliesstoff-Koaleszenz-Filtermedium zu entwickeln, das spindelförmige, strukturierte Fasern enthält, die eine schnelle Koaleszenz der feinen Öltröpfchen sowie einen akzeptablen zeitlichen Kompromiss zwischen dem Auffangen und Freisetzen der koaleszierten Öltröpfchen ermöglichen.

Im Rahmen dieser Arbeit wurde aufgezeigt, dass die Mechanismen des Wassersammelverhaltens in der Fangseide der cribellaten Spinnen auf der dynamischen Wechselwirkung der stark aufgeblähten elastischen Nanofasern und der periodischen Spindelknoten mit Wassertropfen beruhen. Mit den gewonnenen Erkenntnissen wurde die Dynamik der gerichteten Bewegung von Tröpfchen auf Oberflächen mit geometrischen Gradienten (bioinspirierte nanobeschichtete 3D-gedruckte konische Modelle) in einem anderen flüssigen Medium eingehend untersucht und numerisch modelliert. Das erarbeitete theoretische Modell erlaubt die Berechnung der zeitabhängigen Bewegung von Tröpfchen in Abhängigkeit von systemrelevanten Parametern wie den geometrischen Eigenschaften (Länge und halber Apex-Winkel des Filaments, Kontaktwinkel zwischen Filament und Tröpfchen) und den benetzungs- und viskoelastischen Eigenschaften der beiden Fluide. Darüber hinaus wurde eine neue Mess- und Auswertemethode zur Bewertung des dynamischen Kontaktwinkels zwischen Fasern und Spindelknoten entwickelt. Dieser ist einer der ursächlichen Parameter für die gerichtete Bewegung der Tropfen von den Verbindungsstellen zum Zentrum der Spindelknoten.

Ausgehend von den theoretischen Erkenntnissen wurde der Fokus bei der Materialentwicklung auf eine vielversprechende Herstellungsmethode, das Elektrospleißenverfahren, gelegt. Mit diesem konnten Netzwerke aus spindelgeknüpften Fasern in laufenden Metern hergestellt werden, die als Filtermedium oder Membran dienen.

Um die Abscheideleistung der Filtermembranen bei der Öl-Wasser-Trennung zu quantifizieren, wurde ein Prüfstand mit entsprechendem Filtergehäuse konzipiert, gebaut und eingesetzt. Die elektrogewebte Membran aus Polyvinylidenfluorid 7,5 Gew. % aus strukturierten Fasern analog zum betrachteten biologischen Vorbild beschleunigte das Erreichen des Schwellenvolumens bei dem Öltröpfchen sich ablösen und aufsteigen. Durch eine anschließende mechanische Trennung können diese leicht von der Flüssigkeitsoberfläche abgeschöpft werden. Die Anwendung der Ergebnisse der vorliegenden Arbeit kann die Öl/Wasser-Trennung sehr erleichtern.

## Abstract

Oily wastewater with finely dispersed droplets (size  $< 10 \mu\text{m}$ ) has become a widespread pollutant around the world for the environment and, in view of the increasing scarcity of fresh water, a serious threat to freshwater resources. Therefore, finding a promising solution for the separation of oil-in-water emulsions prior to their discharge or return back to the processing circle is urgent. Among the conventional separation techniques, nonwoven coalescer filter media containing uniform fibers offer tremendous advances to various filtration problems. Nevertheless, it has been found that performance bottlenecks occur when they are blocked or plugged due to delayed droplet coalescence and detachment. In this regard, a key inspiration for this work were biological structures in nature and the structure-function relationships they use to realize the directional collection of water droplets. Applying these findings, this study aimed to develop value-added nonwoven coalescing filter media containing spindle-knotted structured fibers that endow a rapid coalescence of the fine oil droplets as well as a timely compromise and a good trade-off between the capture and release of coalesced oil droplets.

In this thesis, a thorough analysis of the directional water collection mechanism in the capture silk of cribellate spiders revealed the dynamic interaction between the highly puffed elastic nanofibers and the periodic spindle-knots with water droplets. By the knowledge gained, the dynamics of the directed motion of droplets on a surface with geometric gradients (bio-inspired nano-coated 3D-printed conical models) in another fluid medium were thoroughly investigated and modeled numerically. The developed theoretical model allowed the calculation of the time-dependent motion of droplets as a function of system-relevant parameters such as the geometric properties (length and half-apex angle of the filament, contact angle between fiber and droplets) and the wetting and viscoelastic properties of the two fluids. Furthermore, a new measurement and evaluation method were developed to evaluate the dynamic contact angle between droplets and fibers with spindle-knots, which is known to be one of the responsible causative parameters for the directional movement of droplets from joints toward the center of spindle-knots.

Based on the theoretical findings, the development of materials focused on one of the most promising fabrication methods, the electrospinning method, by which the network of spindle-knotted fibers could be fabricated in running meters, in the frame of the filter medium/membrane. To quantify the separation efficiency of the filter membranes in oil/water separation, a test stand with corresponding filter housing was designed, built, and used. The electrospun membranes made of Polyvinylidenfluorid (PVDF) 7.5 wt% with the structured fibers analogous to the considered biological model accelerate the growth process of the oil droplets. Indeed, the oil droplets attain the threshold volume for detachment from the fiber more rapidly and rise earlier to the liquid surface from where

they can subsequently be mechanically separated. Application of the results of the present work may facilitate oil/water separation profoundly.

# Table of contents

Preface and Acknowledgments .....	I
Kurzfassung .....	III
Abstract.....	V
Table of contents .....	VII
List of abbreviations .....	XI
List of symbols.....	XIII
<b>1. Introduction.....</b>	<b>1</b>
1.1 Background.....	1
1.2 Motivation.....	4
<b>2. State-of-the-art of science and technology.....</b>	<b>7</b>
2.1 Nonwoven coalescing filter for liquid-liquid filtration (state-of-the-art).....	7
2.2 Fundamental models.....	10
2.2.1 Wettability.....	10
2.2.2 Drop shape on a cylindrical fiber (fiber wetting).....	13
2.2.3 Young–Laplace equation (Laplace pressure).....	14
2.2.4 Drag Theory .....	16
2.2.5 Plateau-Rayleigh Instability (PRI) .....	18
2.3 Surface modification on fibers and textiles .....	19
2.4 Bionic study of directional movement of droplets in nature .....	20
2.4.1 Capture silk (thread) of cribellate spiders .....	21
2.5 Analysis of the mechanism of directional movement of droplets.....	25
2.6 Bio-inspired material causing directional movement of droplets .....	28
2.6.1 Liquid-gas separation.....	29
2.6.2 Liquid-liquid separation.....	40
2.7 Electrospun spindle-knotted fibers.....	46
2.8 Summary of the state-of-the-art .....	53
<b>3. Objective, hypothesis and approach.....</b>	<b>57</b>
3.1 Objectives of the thesis.....	58
3.2 Research hypothesis .....	58
3.3 Methodological approach .....	59
<b>4. Materials and methods.....</b>	<b>61</b>
4.1 Used materials.....	61
4.1.1 Liquids (Oil/water).....	61

4.1.2	Polymeric and coating materials .....	62
4.2	Test methods .....	63
4.2.1	Particle size distribution .....	63
4.2.2	UV-Vis Spectroscopy .....	64
4.2.3	Surface and interfacial tension measurement .....	65
4.2.4	Static and dynamic contact angle measurement on flat solid surfaces.....	68
4.2.5	Dynamic contact angle measurement for a single fiber with a uniform circular cross-section (Axisymmetric fiber of constant cross-section) .....	68
4.2.6	Morphology and geometry analysis .....	69
4.2.7	Numerical computations .....	70
<b>5.</b>	<b>Material development .....</b>	<b>71</b>
5.1	Single fiber with spindle-knot structure .....	71
5.1.1	Functionality in collection/separation of emulsified oil droplets.....	74
5.2	Spunbond/meltblown nonwoven textile with spindle-knotted fibers .....	76
5.3	Electrospun nonwoven textile with spindle-knotted fibers .....	80
5.3.1	Wettability of the prepared electrospun membranes .....	83
5.4	Additive manufacturing (3D-printing) process.....	84
5.4.1	Wettability of the fabricated conical models .....	86
<b>6.</b>	<b>Mathematical modeling of self-driven directional movement of underwater oil droplets .....</b>	<b>89</b>
6.1	Simplification for solid model geometry and oil droplet shape regime .....	89
6.2	Forces acting on the droplet.....	90
6.2.1	Laplace force.....	90
6.2.2	Hysteresis force.....	91
6.2.3	Friction force (internal dissipation) .....	92
6.2.4	Drag force .....	92
6.2.5	Gravity force .....	94
6.3	Theoretical model: equation of motion .....	95
6.4	Validation of the theoretical model.....	98
6.5	Conclusion of modeling of self-driven directional movement of underwater oil droplets .....	104
<b>7.</b>	<b>A novel method for measuring dynamic contact angles of fibers with spindle-knots .....</b>	<b>105</b>
7.1	Basic idea.....	105
7.2	Axisymmetric fiber of constant cross-section .....	105
7.3	Axisymmetric fiber of varying cross-section .....	107



---

7.4	Validation of the model .....	113
7.5	Conclusion of a novel method for measuring dynamic contact angles of fibers with spindle-knots.....	115
<b>8.</b>	<b>Evaluation of the electrospun PVDF membrane with regard to oil-in-water collection/separation.....</b>	<b>117</b>
8.1	Development of a filtration setup.....	117
8.2	Predicting the functionality of the electrospun spindle-knotted fibers with the theoretical model .....	118
8.3	Evaluation of electrospun PVDF membrane with regard to oil-in-water separation efficiency.....	121
<b>9.</b>	<b>Summary and future scope .....</b>	<b>129</b>
9.1	Summary.....	129
9.2	Future scope.....	131
	References.....	XV
	List of formulas .....	XXIX
	List of figures .....	XXXIII
	List of tables.....	XXXVII
	Appendix.....	XXXIX



## List of abbreviations

CA .....	Contact angle
DMF .....	Dimethylformamide
FESEM .....	Field Emission Scanning Electron Microscopy
GO .....	Graphene oxide
LBM .....	Lattice Boltzmann method
N/A .....	Not applicable
PAN .....	Polyacrylonitrile
PCL.....	Polycaprolactone
PDMS .....	Polydimethylsiloxane
PET.....	Polyethylenterephthalat
PLA .....	Poly lactide
PMMA .....	Poly (methyl methacrylate)
PRI.....	Plateau-Rayleigh instability
PS .....	Polystyrene
PVAc .....	Polyvinyl acetate
PVDF.....	Polyvinylidene fluoride
PVOH .....	Polyvinyl alcohol
rpm .....	Round per minute
SEM.....	Scanning electronic microscopy
TCL .....	Three contact line
THF .....	Tetrahydrofuran
UV-VIS.....	Ultraviolet-visible spectroscopy
wt%.....	Mass fraction (g/g)
3D .....	Three dimensional



## List of symbols

Symbol	Unit	Description
$A$	$\text{mm}^2$	Area
$c_o$	-	Oil concentration in water (wt%)
$d$	mm	Average thickness of the droplet
$E$	J	Released surface energy during the coalescence process
$C_D$	-	Drag coefficient
$D$	$\mu\text{m}$ , mm	Droplet diameter
$D_{50}$	$\mu\text{m}$	50% quantile of the size of the dispersed oil droplets
$F$	N	Wetting force
$F_b$	N	Buoyancy force
$F_c$	N	Chemical force (due to surface energy gradient)
$F_d$	N	Driving force (due to Laplace pressure gradient)
$F_D$	N	Drag force
$F_E$	N	Electro-capillary pressure force
$F_f$	N	Friction force (due to drag)
$F_G$	N	Unbalanced force generated by the porous surface
$F_h$	N	Hysteresis force
$F_H$	N	Hysteresis force
$F_L$	N	Laplace force
$F_t$	N	Force resulting from the surface tension of the liquid
$F_v$	N	Viscous force
$F_w$	N	Gravity force (due to weight of the fiber)
$g$	$\text{m s}^{-2}$	Gravitational acceleration
$G$	J	Gibbs free energy
$h$	mm	Maximum thickness of the droplet
$j$	-	Denotes joint position
$k$	-	Fitting parameter in theoretical model or denotes spindle-knot
$l$	-	Constant factor in friction force equation
$l_{TCL}$	mm	Length of the region enclosed by the TCL
$\ell$	mm	Length of the fiber
$L$	mm	Length of the droplet parallel to the cone surface
$M$	g	Mass

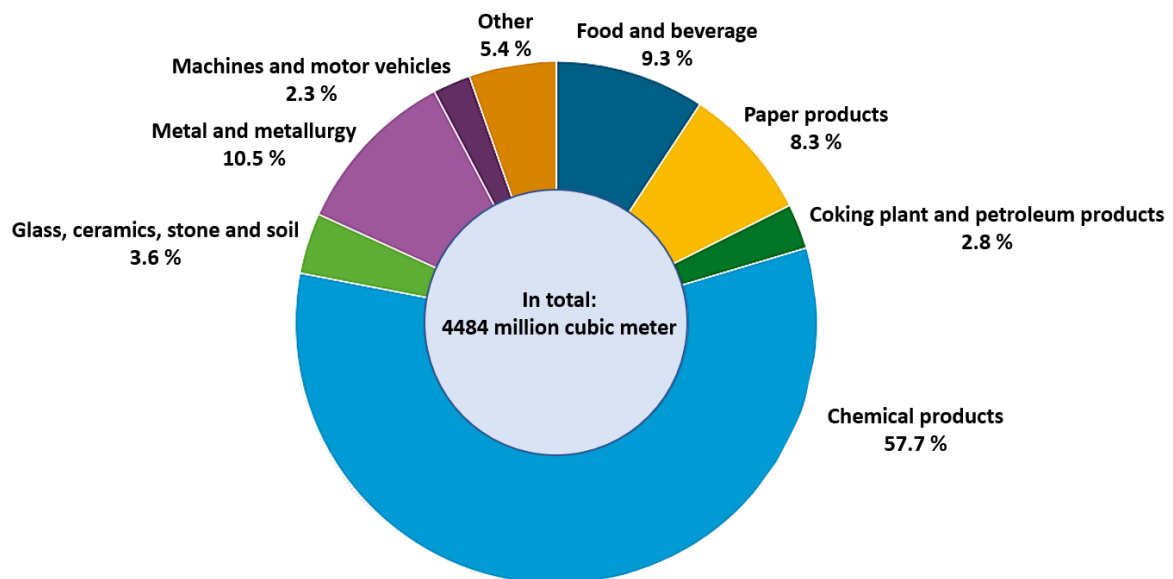
$o$	-	Oil
$P$	$\text{N m}^{-2}$	Laplace pressure
$Q_{flux}$	$\text{mL s}^{-1} \text{cm}^{-2}$	Volumetric flux
$r$	$\mu\text{m}, \text{mm}$	The local radius of the fiber/cone
$R$	$\mu\text{m}, \text{mm}$	Oil droplet Radius
$R_0$	$\mu\text{m}, \text{mm}$	Water droplet radius
$R_1$	$\text{mm}$	The local radius of the cone at the rear-side of the droplet
$R_2$	$\text{mm}$	The local radius of the cone at the front-side of the droplet
$S_{TCL}$	$\text{mm}^2$	Area of the region enclosed by the TCL
$t$	$\text{s}, \text{min}, \text{h}$	Time
$u$	$\text{mm}$	Immersion depth in liquid
$v$	$\text{mm s}^{-1}$	Velocity
$v_0$	$\text{mm s}^{-1}$	Initial velocity of the droplet
$V$	$\text{kV}$	Voltage
$V$	$\text{mm}^{-3}$	Volume
$w$	-	Water
$W$	-	Separation efficiency
$z$	$\mu\text{m}, \text{mm}$	Symmetry axis of the cone
$z_h$	$\mu\text{m}, \text{mm}$	The position, where the hysteresis force vanishes
$z_f$	$\mu\text{m}, \text{mm}$	Final position of the droplet on the cone
$z_0$	$\mu\text{m}, \text{mm}$	Initial position of droplet on the cone
$\alpha$	$^\circ$	Half-apex angle
$\beta$	$^\circ$	Tilt angle
$\gamma$	$\text{mN m}^{-1}$	Surface/Interfacial tension
$\theta$	$^\circ$	Contact angle or liquid wedge angle
$\theta_a$	$^\circ$	Advancing contact angle
$\theta_r$	$^\circ$	Receding contact angle
$\lambda_c$	$\text{mm}$	Capillary length
$\mu$	$\text{mPa s}$	Dynamic viscosity
$\rho$	$\text{kg m}^{-3}$	Density
$\chi$	$^\circ$	Hysteresis (half) angle
$\Omega$	$\mu\text{L}, \text{mm}^{-3}$	Droplet volume

# 1. Introduction

## 1.1 Background

Oily wastewater of various origins has become an extremely common pollutant around the world for the environment and, in view of the increasing scarcity of water, a serious threat to freshwater resources. The oily wastewater stems from oil extraction, refining, and petrochemical activities. Many oil-related industries such as metal/steel, mining, tannery, food and beverage, textile, cosmetic, paint, machinery and daily life activities, or car washes produce high amount of oily wastewater as well. The frequent oil-leakages and spills during oil exploration and transportation also contaminate water. [1–10]

The German Federal Environmental Agency (Umweltbundesamt) reports that the direct and virtual (shares for energy supply, industry, agriculture, etc) water footprint for each person is about 4000 liters per capita and day. It is estimated that around 16 % of the water consumption – almost 4.5 billion cubic meters – can be attributed to manufacturing companies. [11]



**Fig. 1.1** Water consumption in manufacturing industries in Germany in 2016 [11].

As shown in Fig. 1.1, the chemical industry consumed almost 58 % of the total water used in the manufacturing industry. The food and beverage, paper, and metal industries each use about 10 % of the water (448 billion liters per year). Around 78 % of the water used is provided from nature (mainly ground, spring, and surface water). Due to resource scarcity, there has been a keen interest for decades in reducing the need for water from natural resources by resorting to recycling and returning it directly to the processing circle. In some industries, for instance the metal industry, lubricating greases and oils are used extensively within the process chains, therefore the water cannot be recycled or even disposed to the

environment before the oily contaminants have been removed by appropriate treatment. Due to the significant initial costs of related treatment systems plus the costs of energy consumption and annual maintenance, it is cheaper in most cases to use freshwater than treated water in the industry. Nevertheless, due to strict regulations on costly water treatment before discharge, as well as the issue of sustainability (which is becoming an increasingly important image and economic factor within the industry), the focus should be on the treatment and recycling of water in all sectors that produce oily wastewater. [11]

Contaminations caused by oil, which consist mainly of insoluble hydrocarbons or fatty glycerides, come as free-floating oil droplets ( $D > 150 \mu\text{m}$ ), dispersed oil droplets ( $20 \mu\text{m} < D < 150 \mu\text{m}$ ), or stable emulsified oil droplets ( $D < 20 \mu\text{m}$ ) [4,8]. Among these, in particular, the separation of the stable emulsified oil droplets from the surrounding water remains an unsolved challenge for phase separation. The difficulty is due to (i) the very small size of the oil droplets, and (ii) the small density gradient between the oil droplets and the surrounding water phase. [8]

Based on the type of oily wastewater with regard to its droplet size distribution, a variety of oil/water separation techniques and materials have already been developed. Commonly used oil-water separation techniques include physical, chemical and biological methods or a combination of these. Skimming, adsorption, air flotation, centrifugation, ignition, and chemical coagulation are some examples of the methods mentioned [2,4,6,8,12]. Some of these have offered great promise, however, due to existing disadvantages they are still under development or even gradual extinction. Shortcomings are high energy consumption, secondary pollution, low separation efficiency, need for chemical input, time consumption, and complex operational processes. Most importantly, they are seldom capable of separating stable emulsified oily wastewater [4,6,8]. Alternatively, filtration known as a physical process plays an important role and is the keystone in the purification and decontamination of oil-polluted water [12,13]. Accordingly, developed membrane separation technologies based on microfiltration (MF), ultrafiltration (UF), and nanofiltration (NF) have been explored to separate the emulsified oil droplets [4,12]. Aside from the mentioned filtration technologies, separation by nonwoven textile materials, especially fiber-based coalescing filter media, has received great attention. Highlighted features are high efficiency, operational simplicity, environmentally friendliness, energy-saving processes, flexibility during design, and the absence of secondary pollution [3,4,8,12,14]. Nevertheless, bottlenecks remain in conventional nonwoven coalescing filter media due to low porosity, small pores, a low permeation flow, and the required high drive pressure of several bars. Therefore, further efforts are highly desired to develop a feasible, rational, and specialized filter medium for the effective separation of different oil-in-water emulsions [4,8].



Generally speaking, filtration is a mechanical separation process, in which the dispersed phase (liquid, solid) can be filtered out from a continuous phase (gas, liquid) based on the density difference between the phases [15]. The filtration process falls into two types; surface and depth filtration [12]. The surface filtration occurs when the droplet size of the dispersed phase is bigger than the pore size of the filter medium. In this case, the dispersed phase is separated from the continuous phase on the upstream side of the filter medium. Conversely, if the droplet size of the dispersed phase is smaller than the pore size of the filter medium, the droplets can pass through the filter medium while being captured by the fibers to coalesce with other droplets into a larger droplet which is then more easily to be separated on the downstream side. The focus of this work is on liquid-liquid filtration when both dispersed and continuous phases are present in the liquid phase and micro-oil droplets are separated from the water via nonwoven coalescing filter media governed by depth filtration mechanisms. [16]

The filter medium is evaluated by its quality factor, which is related to the separation efficiency of the filtration process as well as the pressure drop [17]. The selection of the appropriate filter medium/membrane, which is known to be the heart of any filtration process, is very important and its performance should ideally be improved [12]. The nonwoven textile filter media with uniform cylindrical fibers and manufactured from natural or synthetic raw material by technologies such as wetlaid, drylaid (carding, airlaying), and meltspinning (spunbonding, meltblowing, electrospinning) have been state-of-the-art for decades and have drawn significant attention due to excellent mechanical strength and improved filtration properties [18,19]. The exclusive global market of nonwovens used for filter media is approximately \$2 billion [18]. As the capabilities of the nonwoven textile materials improve through integration into the nanofibers production, they have been known to be a potential alternative to conventional membrane processes such as microfiltration, ultrafiltration, and nanofiltration [20]. In this regard, research on electrospun fibrous separation membranes has recently received more attention due to their intriguing advantages including diverse structure, high porosity, high surface area, tunable wettability, ease of scalable production, and offering high permeation fluxes at lower drive pressures. [4,8] Despite the advantages mentioned, using the conventional nonwoven coalescing filter media, which mainly contain the uniform cylindrical fibers, much time is required for oil droplets to be enlarged to reach the threshold volume required for the detachment from the fibers. The time-consuming stationary collection and coalescence of oil droplets would severely block the surface pores, decrease the wetting selectivity, and delay the rebirth of the oil collection cycle on the fibers, all of which contribute to reduced separation efficiency [4]. Because of the mentioned defect, the concept of droplet-on-fiber motion is being strongly considered for industrial applications dealing with droplet coalescence and drainage, and therefore inspires a novel idea to improve and control the

performance of coalescing filter media through the purposeful directional movement of droplets along the fibers [21].

With the progress of science and technology, scientists and engineers are no longer content with single-function materials offering fixed properties and limited functionality in the corresponding applications. Various surface treatment processes that allow modifying the physical and/or chemical nature of textiles and fibers contribute to the revolution in advanced fibrous materials. Specifically, nature has suggested novel ideas for developing surface modification techniques on artificial models, in this case, for developing biomimetic fibers with superior surface functions. Therefore, past decades have witnessed the explosive growth of interest in the field of bioinspired materials, of which the structures and properties can be well utilized for industrial and bioengineering applications [22]. Functional structures of living systems, for example, beetle back, cactus spine, and spider silk with highly tuned wettability have drawn increasing attention during the past decades. Among the most commonly developed biomimetic fibers exhibiting wettability functionality, spindle-knotted structured fibers, bioinspired by cribellate spider's capture silk, have been devised in a wide spectrum. Most importantly, its directional water collection function inspires the idea that a coalescing filter media with such structured fibers could impart directional movement onto droplets, ensuring rapid regeneration of deposit sites and hence continuous and efficient oil collection [23].

## 1.2 Motivation

The further we can reduce contaminants and pollutants from water, the greater the benefit for our environment. In this regard, as well understood, the motion of drops and control of the rate and direction of liquid droplet migration on fibers is of scientific and economic interest for applications in filters and membranes to remove or neutralize chemically harmful droplets [21]. In this study, an innovative research approach for improved oil coalescence efficiency will be derived from the mechanisms of directional droplet collection and coalescence on structured natural surfaces like spider web fibers. Their 'spindle-knots', a so-called 'beads-on-a-string' structure, promotes the coalescence of dew water droplets on the fibers [24]. In a unique methodology, the known structure-property relationships of droplet coalescence in the three-phase-system fiber-air-water will be transferred into the fiber-water-oil system and investigated by theoretical modeling and special fiber spinning. Therefore, the motivation is to conduct fundamental studies and bridge the findings to the new material development, particularly value-added nonwoven coalescing filter media containing spindle-knotted structured fibers that contribute to better performance in liquid-liquid filtration. It is believed that the outcome of this work can accelerate the treatment of oily wastewater, and also have prospective applications in catalytic reactions, energy-efficient water collection, droplet transportation and

manipulation, selective separation, and micro/nanofluidic devices [23,25]. Chapter 2 below provides a detailed overview of the research works that have been developed and published to date on this topic.



## 2. State-of-the-art of science and technology

This chapter provides an overview of nonwoven coalescing filter media for liquid-liquid separation/filtration and their functionality in terms of droplet capture mechanism by the fibers and the present lack of adequate performance. It also reports the corresponding fundamental models and concepts that form the basis of this work. Furthermore, the behavior of directional movement of droplets in biological models in nature and the parameters and forces that contribute to this movement are reviewed. Also the underlying mechanism between structural features and the enabled functionality, that lead to directional water collection behavior are discussed [26]. Finally, it summarizes the-state-of-the-art of science and technology of bioinspired solid models developed so far in terms of functionality and of the theoretical models on which the directional movement behavior of droplets along solid structures are based.

### 2.1 Nonwoven coalescing filter for liquid-liquid filtration (state-of-the-art)

Separation of liquid/liquid dispersions can be carried out in various processes depending on the fluid's properties, droplets size, concentration, etc [15]. This work focuses on oil/water emulsion separation via mechanical separation i.e. filtration, which utilizes the difference between the mass densities of oil and water. The density contrast generates a buoyancy force that drives the oil droplets to the surface of the liquid, from where they can be skimmed mechanically. According to equation (2.1), if the oil phase of the emulsion consists of very small droplets, the buoyancy force ( $F_b$ ) proportional to the droplet volume is very small and the separation proceeds very slowly, especially when the two phases possess similar densities.

$$F_b = (\rho_w - \rho_o)g \Omega \quad (2.1)$$

$\rho_w$  and  $\rho_o$  are the densities of oil and water, respectively,  $g$  is the gravitational acceleration and  $\Omega$  is the volume occupied by the oil droplet. Therefore, to destabilize the emulsion and enlarge the droplets by merging smaller into larger ones, an efficient process must be used before separation can occur [15]. From this perspective, many advances have been made based on the filtration and absorption methods using various materials as shown in Fig. 2.1. So far, with regard to the principle of separating oil/water mixtures, the used materials can be divided into two types: filtration and the absorption materials. Filtration materials only let oil or water through and repel the other phase, resulting in selective separation. The absorbent materials can selectively absorb water or oil on the surface, preventing the other phase from penetrating the absorbent [7].

Amongst the materials introduced in Fig. 2.1, filter materials comprising nonwoven (fiber-based) coalescers have shown unique and enhanced capabilities when used for oil/water emulsion separation due to low cost, lightweight, mechanical stability, and corrosion-resistant properties [1,7,14]. Because fiber-based textile materials are very flexible, they are capable of separating the oil/water mixture very efficiently once the advantageous interactions between the surface chemistry and the surface architecture are exploited.

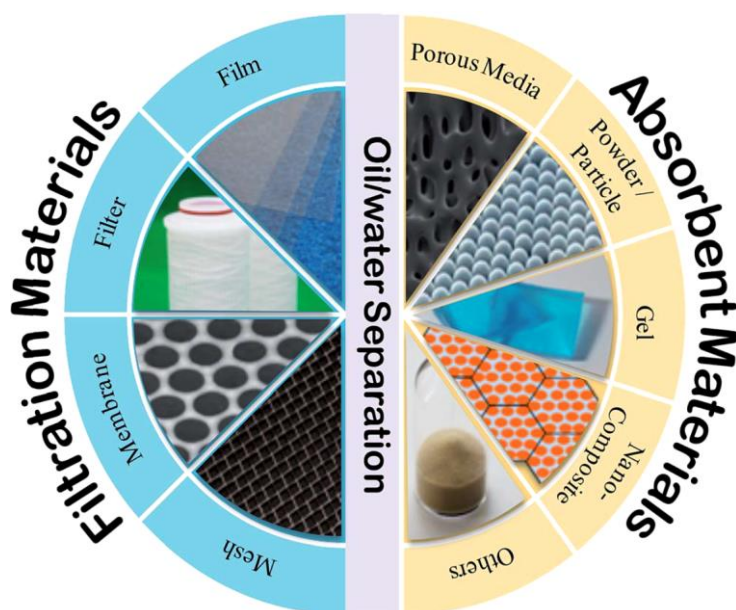


Fig. 2.1 Typical materials used for oil/water separation [1].

Nonwovens made from cotton, wool, or synthetic materials can generally be described as a random fibrous web in which the fibers are air-laid, wet-laid, entangled, or bonded by mechanical or heat fusing into the web and are capable of removing a percentage of particles/liquid droplets from liquid or gaseous fluid streams [12,18]. Another possible method of fabrication of the nonwovens is the application of a direct polymer melt process in which fibers are created in a spinning process and immediately cast onto a moving belt forming a continuous web [18].

The separation process that occurs in the nonwoven coalescing filter materials is a type of depth filtration, which traps dispersed droplets throughout the media itself, rather than just on its surface. Here, the main performance of the coalescer medium is to physically intercept particles to create as large droplets as possible on the downstream side of coalescer medium to prevent them from ending up in the final filtered liquid. [14,27]

Droplet capture, coalescence, and drainage from filter media are three key factors affecting the coalescing filter performance and they all are controlled by the behavior of individual drops on the fibers [21].

The dispersed droplets are captured by the fibers of the coalescing medium through different mechanisms: sieving, interception, inertial impaction, diffusion, and electrostatic attraction [13,17]. If it is assumed that all fibers are identical, the capture mechanism in a single fiber represents the entire filter medium. This assumption, the single fiber mechanism, has been widely accepted by the filtration industry as it leads to comparable results with experiments [28].

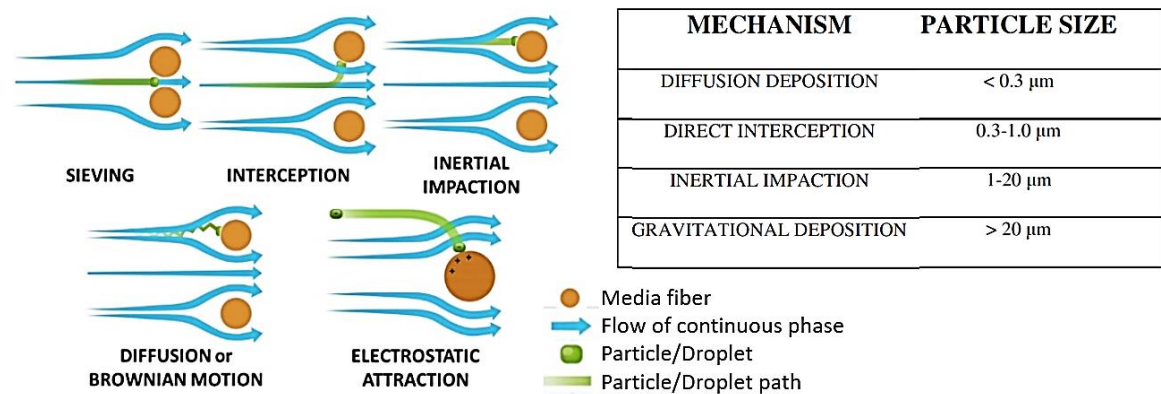
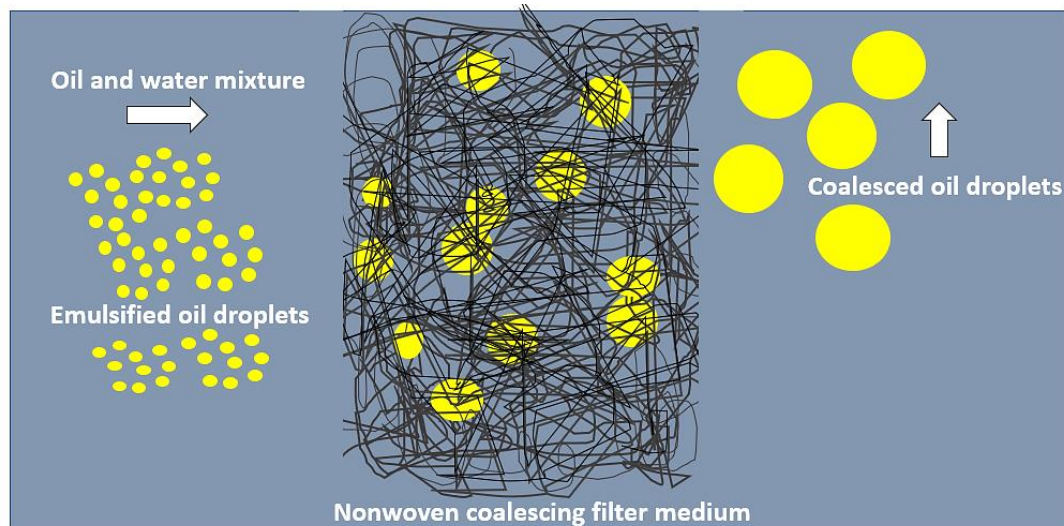


Fig. 2.2 Droplet capturing mechanism [13,19].

In a realistic scenario, due to a wide distribution of droplet sizes, all capture mechanisms have to be considered. However, depending on the size of droplets, fiber, and pores, it can be assumed that the capturing process is dominated by only one or several mechanisms. In this work and generally in typical liquid-liquid separation processes, where the size of the considered oil droplets is usually in the range of 0.5-50  $\mu\text{m}$ , the interceptions and inertial impaction can be assumed to be the dominant capture processes (Fig. 2.2 (b)) [15]. After the droplets are caught on the fibers, the coalescence process occurs, in which the adjacent droplets are merged during contact to form a bigger droplet and drained out from the downstream side of the coalescing filter medium [17].



**Fig. 2.3 Functional schematic of nonwoven coalescing filter medium in oil-in-water separation.**

Several factors affect the coalescence process of the liquid droplets trapped on the fibers. The performance of filter media depends on the properties of the emulsion, such as droplet size, concentration, density, and viscosity, as well as the filter properties, including fiber surface wettability, size, structure, orientation, and porosity [17,29]. On the one hand, maximizing the collection process and accelerating the integration of small droplets on the coalescer structure to generate larger droplets, on the other hand, rapid detachment and the on-time release of the coalesced droplets from the fibers are the key points to achieve high separation efficiency.

It is known that if sufficiently large droplets cannot be generated via a timely coalescence process, the droplets smaller than the pore size will enter the pores and contribute to intrapore fouling. In addition, the slow detachment of the coalesced droplets leads to fouling of the coalescing filter medium, which drastically reduces the efficiency. Therefore, it is not only important to trap the dispersed droplets on the fibers efficiently, but the coalescence and detachment from the fibers, i. e the surface refreshment should also occur rapidly. In addition to the influence of pore size, surface energy, and the size ratio between fibers and droplets, this also requires a well-thought-out design of the coalescing filter media with regard to the structure and morphology of its single fibers. [5]

## 2.2 Fundamental models

In this section, the key fundamental models applied in this study are introduced.

### 2.2.1 Wettability

The wettability of a solid surface is a significant physical property and depends on the chemical composition and microstructure of the surface [7,17]. This property is



characterized by the contact angle (either static or dynamic), which is specific for any given system and is determined by the interactions across the three interfaces between gas, liquid and solid. If the water wets the surface with contact angle value of  $\theta < 90^\circ$ , it refers to as a hydrophilic surface. If the water does not wet the surface and the value of the contact angle is  $\theta > 90^\circ$ , it refers to as a hydrophobic surface. The term hydrophobic/-philic, that was originally only applied to water, is often used to describe the contact of a solid surface with any liquid (e.g. the term oleophobic/-philic is used in reference to wetting by oil and organic liquids). A completely wetting solid surface is characterized by  $\theta = 0^\circ$ . A surface is considered superhydrophobic/superoleophobic when  $\theta$  is greater than  $150^\circ$  and the contact angle hysteresis, defined as the difference between advancing and receding contact angle, is low [7,30]. Advancing contact angle ( $\theta_a$ ) and receding contact angle ( $\theta_r$ ) are the maximum and minimum observed angles at the front and rear sides of the droplet, respectively [7,26,31,32]. Contact angle hysteresis is directly attributed to adhesion since differences in contact angles around the drop perimeter can result in a surface tension force resisting droplet motion [33].

Three main wetting theories have been proposed to determine the contact angle: Young's model, Wenzel's model, and Cassie's model. [7,8,32]

If a liquid droplet is placed on a physically smooth and chemically homogenous solid surface in air, the solid-air and liquid-air interfaces meet with a static contact angle  $\theta$  and the wetting condition is determined by Young's equation. The value of  $\theta$  can be determined from the condition of the total energy of the system being minimized as [7,17,22,26,31,33–35]

$$\gamma_{sg} - \gamma_{sl} = \gamma_{lg} \cos \theta \quad (2.2)$$

where  $\gamma_{sg}$ ,  $\gamma_{sl}$  and  $\gamma_{lg}$  are the surface tensions between the phases solid-gas, solid-liquid, and liquid-gas, respectively ( $\gamma_{ij}$ , which  $i$  and  $j$  denote two phases). It is a measure of how much energy is required to make a unit area of interface between two immiscible liquids, thus  $\text{mN m}^{-1}$  or  $\text{dyn cm}^{-1}$ , which have dimensions force/length, are the two common units for the surface tension [36]. In other words, the surface tension represents the cohesion between adjacent surfaces and generally is a property of the interface between two immiscible phases [26]. When one of the phases is air, it is termed surface tension and is caused by the unbalanced intermolecular forces applied on the surface molecules, which are pulled to join the liquid but not the other medium [34]. When the phases are both liquids, it is called interfacial tension.

For a droplet on a rough solid surface whose typical roughness size is smaller than the size of the drop, Wenzel's law applies. In this case the liquid completely penetrates the roughness grooves of the surface. Therefore, the adhesion between a Wenzel-state droplet

and the substrate is usually high, which produces large hysteresis. Wenzel's law is described as [7,22,26,30,31,33,34]

$$\cos \theta^* = r \cos \theta \quad (2.3)$$

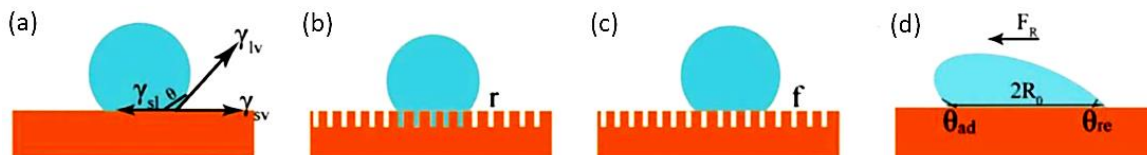
where  $r$  is surface roughness and denotes the ratio between the actual and the apparent surface area of the rough surface.  $\theta^*$  and  $\theta$  are the apparent and intrinsic contact angles on rough and smooth surfaces, respectively. Wenzel's law states that the surface roughness amplifies the intrinsic wettability property, i.e. a hydrophilic surface becomes more hydrophilic and the hydrophobicity of the hydrophobic surface is enhanced with increasing roughness. [26,37]

Based on the Wenzel model, Cassie and Baxter further expanded and modified the Young's equation [32]. Cassie's model describes the case that liquid droplets rest on the rough grooves of the surface with air packets trapped underneath and the apparent contact angle is given by

$$\cos \theta^* = f_s (\cos \theta + 1) - 1 \quad (2.4)$$

where  $f_s$  is the ratio of the liquid-solid contact area to the entire contact area. [7,22,30,31,33,34,38]

Generally speaking, both the Wenzel and the Cassie model illustrate the mechanism of wettability on the rough surface, and it is confirmed that under special circumstances, one state can swap to the other [7].



**Fig. 2.4 Wetting models of a droplet on solid surface [22];**  
**(a) Young's model, (b) Wenzel's model, (c) Cassie's model, (d) contact angle hysteresis.**

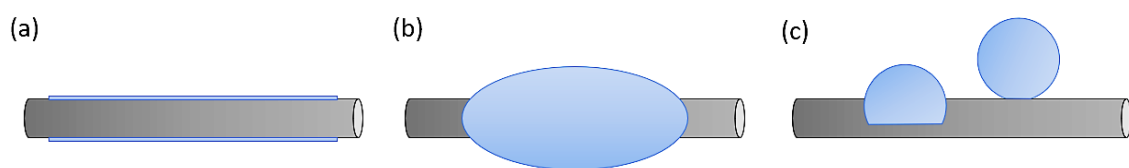
Apart from using the static contact angle, reported as the most common approach for wettability analysis of the surfaces in many studies [39–42], the dynamic contact angle is also used to quantify the wetting behavior of solid materials [41,43–45]. Direct optical contact angle measuring and force tensiometry (section 4.2.4 and 4.2.5) are the most popular and most often applied approaches to estimate the wettability of textiles and fibers through dynamic contact angle measurement [41,44]. The direct optical method, known as a general characterization method, is used when a sufficiently large flat surface of a moderate hydrophilic or hydrophobic material is accessible [46–48]. In the case of fibers, force tensiometry has been proposed for determining the dynamic contact angle for single

fibers with a uniform cross-sectional shape as well as for fiber bundles (e.g. carbon fibers) [45,48–50]. [51]

### 2.2.2 Drop shape on a cylindrical fiber (fiber wetting)

The essential difference between the wetting of flat plates or surfaces and the wetting of fibers is that for a small droplet placed on the wetted surfaces there is only one droplet shape regime; a spherical cap shape with an equilibrium contact angle,  $\theta$ , given by Young's model (equation (2.2)) [52,53]. On the fiber, referred to as a one-dimensional surface, this shape regime can be divided into several different shapes depending on the wettability of the surface and the relative sizes of the liquid droplet and the fiber. The various configurations, their stability, as well as the ability to retain the previous configuration or swap from one to another have been studied in reasonable depth in the literature. [15,53,54]

*McHale et al.* [52,55] studied the two distinctly different equilibrium shapes of liquid drops on fibers: a barrel and a clamshell. Their results revealed that when the droplet volume is large or the contact angle is small, an axisymmetric barrel shape is the preferred shape. In contrast, by reducing the volume or increasing the contact angle the clamshell shape is preferred. *Chou et al.* [56] found also that barrel shapes occur for large droplets and fibers with good wetting properties, while clamshell shapes are more likely to occur for small droplets or high contact angles. *Mullins et al.* [53] predicted three distinct shapes for a drop on a fiber: (a) film flow, (b) axisymmetric barrel-shaped drops, and (c) axially asymmetric clamshell-shaped drops. For a barrel-shaped droplet, *Lorenceanu et al.* [57] proposed two axisymmetric regimes based on the relative size of the droplet and the fiber: (a) an axisymmetric cylindrical thin droplet, and (b) an axisymmetric spherical droplet.



**Fig. 2.5 The different configurations of a droplet on a fiber;**

**(a)** Film flow, **(b)** barrel shape (drop positioned symmetrically around the fiber), **(c)** clamshell shape (the droplet does not share the axis of symmetry with the fiber [17,21,53].

To summarize, barrel-shaped droplets are axially symmetrical with respect to the model's central axis, while the clamshell type has a more complicated asymmetric profile [58]. A transition from barrel to clamshell shape, the so-called 'roll-up' process, is reported to occur under the following circumstances: (i) by increasing the contact angle, (ii) by increasing the surface tension of the liquid, (iii) by increasing the diameter of the fiber, (iv) by decreasing the volume of the droplet. It has further been reported that for large drops with

contact angles  $< 90^\circ$ , the axisymmetric barrel shape will be stable for any fibre radius. [34,52]

### 2.2.3 Young–Laplace equation (Laplace pressure)

Assuming that the surface of a drop is in mechanical equilibrium, the Laplace pressure is introduced by Young and Laplace as the pressure between the inside of the drop and the outside of the curved surface caused by the surface tension [34,59]. Based on the principle that the work done by surface tension is equal to the work done by Laplace pressure, the Laplace pressure equation can be derived by taking an infinitesimal section of a surface of an arbitrarily curved surface, as shown in Fig. 2.6 [34].

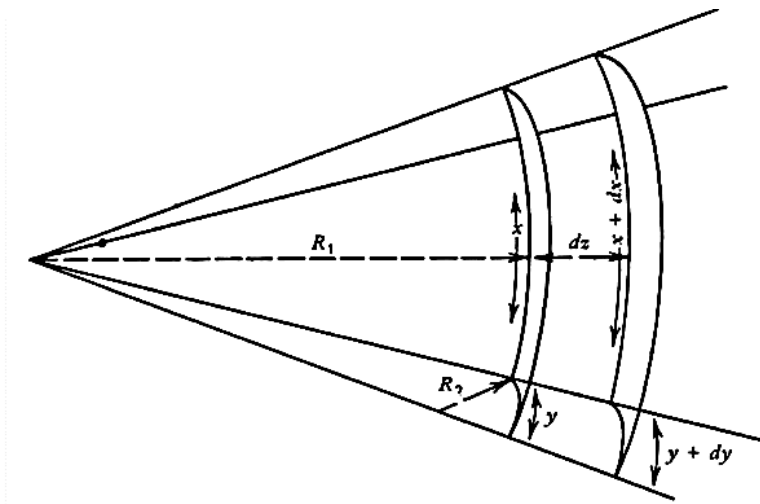


Fig. 2.6 The condition for mechanical equilibrium for an arbitrarily curved surface [34].

In Fig. 2.6, the two main radii of curvature are marked with  $R_1$  and  $R_2$ , which are assumed to be constant and perpendicular to each other. If the surface is shifted outward a small distance, the change in area is given by (the sentence  $(dx dy)$  is very small and can therefore be ignored compared to other sentences)

$$\Delta A = (x + dx)(y + dy) - xy = x dy + y dx \quad (2.5)$$

The work done by surface tension in creating this extra surface area is

$$W = \gamma(x dy + y dx) \quad (2.6)$$

Since the expansion was caused by an increase in pressure, therefore the pressure difference  $\Delta P$  across the surface can balance the work done by surface tension, that is

$$W = \Delta P xy dz \quad (2.7)$$

Considering the geometric relationship for similarity of triangles gives  $dx = \frac{x dz}{R_1}$  and  $dy = \frac{y dz}{R_2}$ . Inserting them into equation (2.6), we obtain

$$\Delta P = \gamma \left( \frac{1}{R_1} + \frac{1}{R_2} \right) \quad (2.8)$$

for Laplace pressure.

*Lorencean et al.* [57] found in a fundamental study that on conical fibers the variation of the fiber radius causes a spatial variation of the capillary pressure, which drives adhering droplets towards the wider end of the cone. They investigated the behavior of the drop on a conical copper wire prepared with a chemical etching process (the diameter increased from 300 to 700  $\mu\text{m}$  over a length of 3 cm, giving an average half-apex angle of  $\alpha \approx 0.38$ ) [57]. The base of their study resorts to the work of *Carroll* [60,61] describing the equilibrium shape of small droplet deposited on thin fibers.

The capillary length  $\lambda_c$  is expressed as [34,62,63]

$$\lambda_c = \sqrt{\frac{\gamma}{\Delta \rho g}} \quad (2.9)$$

where  $\gamma$  is the surface tension of the fluid interface,  $g$  is the gravitational acceleration, and  $\Delta \rho$  is the mass density difference of the fluids. According to Laplace's Law, *Carroll* [60,61] expressed that for a droplet, which is smaller than its capillary length (gravitational effects are negligible) the curvature is constant and approximately proportional to its overpressure  $\Delta P$ . *Carroll* [60] then showed that for a droplet sitting on a constant curvature surface (e.g. a cylindrical fiber), this law can be expressed analytically as [22,34,52,57]

$$\Delta P = \frac{2\gamma}{r+h} \quad (2.10)$$

where  $r$  is the radius of the curvature (fiber) and  $h$  is the maximal thickness of the droplet from the centerline. [57,64]

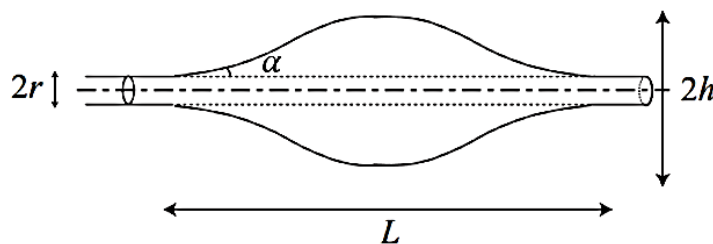


Fig. 2.7 Shape of a wetting drop on a cylindrical fiber [65].

*Lorenceanu et al.* [22,34,52,57] used Carroll's analytical results and expanded the relation in equation (2.10) to conical fibers assuming that the effect of curvature on the shape of the drop is neglected, since its gradient was smaller than  $10^{-2}$ . [57,63] In contrast to a cylindrical fiber, where the pressure inside a drop is constant, the radius gradient along a conical fiber sets a pressure gradient along the drop. This pressure gradient along the fiber axis can be expressed as

$$\left. \frac{dP}{dz} \right|_{\Omega} = \frac{2\gamma}{(r+h)^2} \left( \frac{dr}{dz} + \frac{dh}{dz} \right)_{\Omega} \quad (2.11)$$

where the pressure inside the droplet is evaluated as a function of its position along the fiber  $z$ , its maximum thickness  $h$ , the liquid surface tension  $\gamma$ , and the local fiber radius  $r$ . The subscript of  $\Omega$  reminds us that the derivatives are computed by keeping the volume ( $\Omega$ ) constant. To evaluate the pressure gradient along the drop on the cone, the changes in height ( $h$ ) of a drop of a given volume as a function of the radius ( $r$ ) should be known. Defining the corresponding boundary conditions [57], *Lorenceanu et al.* simplified the equation in (2.11) for the case of quasi-spherical drops, where the local mean radius of the fiber is smaller than the radius of the droplet ( $r < R_0$ ) and  $h$  is close to being constant and equal to  $R_0$ . Thereby, an expression for the force driving a drop on a conical fiber was derived as

$$\left. \frac{dP}{dz} \right|_{\Omega} = \frac{2\gamma}{(r+h)^2} \alpha \quad (2.12)$$

where  $\alpha$  is the half-apex angle of the cone.

## 2.2.4 Drag Theory

One of the essential parameters governing the motion of dispersed particles (or droplets) in a flow is the drag force arising from the interaction between the particle's surface and the surrounding fluid [66]. In fluid dynamics, drag forces hinder the motion of droplets and normally act opposite to the relative motion of any object moving with respect to a surrounding fluid. They can arise between two fluid layers, or between a solid and a fluid. Unlike other resistive forces, which are independent of velocity, drag forces depend on droplet velocity. [17,46]

The Reynolds number is defined as the ratio of inertial forces to viscous forces and consequently quantifies the relative importance of these two types of forces for given flow conditions. This non-dimensional number is defined as

$$Re = \frac{\rho v L}{\mu} \quad (2.13)$$

where  $\rho$  is the fluid density,  $v$  is the mean relative velocity,  $L$  is a characteristic linear dimension of the solid, and  $\mu$  is the dynamic viscosity of the fluid.

For small Reynolds numbers ( $Re \lesssim 10^{-1}$ ) the drag force is proportional to  $|v|$  and Stokes' law applies as [67]

$$F_D = (3\pi\mu d) |v| \quad (2.14)$$

where  $\mu$  denotes the fluid dynamic viscosity,  $v$  is the velocity of the object relative to the fluid, and  $d$  is the diameter of the object. For high Reynolds numbers ( $Re \gtrsim 10^3$ ), in contrast, the drag force is proportional to  $|v|^2$  (Newton's Law) as follows, and turbulent flow can occur [17,67]

$$F_D = \left(C_D \frac{\pi}{8} \rho d^2\right) |v|^2 \quad (2.15)$$

where  $\rho$  denotes the density of the fluid and  $C_D$  is the drag coefficient. In the intermediate (transition) region between these endmembers more complicated dependencies on the velocity are observed and modeled (Fig. 2.8). [68]

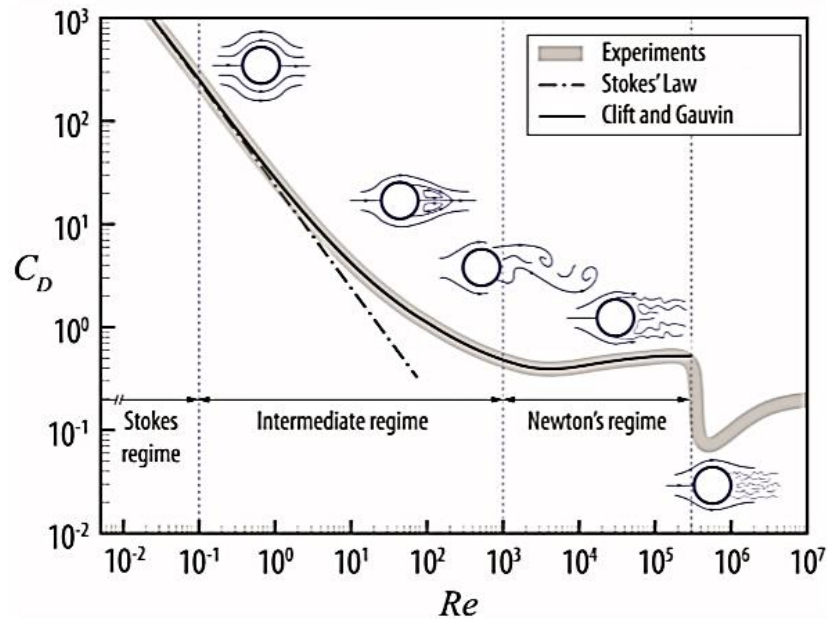


Fig. 2.8 Relation between drag coefficient ( $C_D$ ) and Reynolds number ( $Re$ ) [69].

One way to express the drag force is by means of the drag equation attributed to Lord Rayleigh [70]

$$F_D = \frac{1}{2} \rho v^2 C_D A \quad (2.16)$$

where  $A$  is the cross-sectional area. In fluid dynamics, the drag coefficient is defined as a dimensionless quantity used to quantify the drag of an object in a fluid environment and *Kelbaliyev* [17] obtained the expression

$$C_D = C v^n d^m \mu_c^k, \quad n = m = -k \quad (2.17)$$

assuming that the drag coefficient in isothermal flow depends on the flow velocity ( $v$ ), viscosity ( $\mu$ ), and the particle shape via introducing some equivalent diameter  $d$ . Given the arbitrariness of the coefficient  $C$ , the expression for the drag coefficient appears as

$$C_D = C Re^{-k} = \frac{C}{Re} f(Re) \quad (2.18)$$

As shown by theoretical calculations and experimental investigations, the drag coefficient for spherical particles (solid particles, liquid drops, gas bubbles) at  $Re \ll 1$  (Stokes flow) obeys the following equation [71,72]

$$C_D = \frac{24}{Re} \quad (2.19)$$

For somewhat larger  $Re$  values, the equation can be rewritten as

$$C_D = \frac{24}{Re} (1 + \zeta(Re)) \quad (2.20)$$

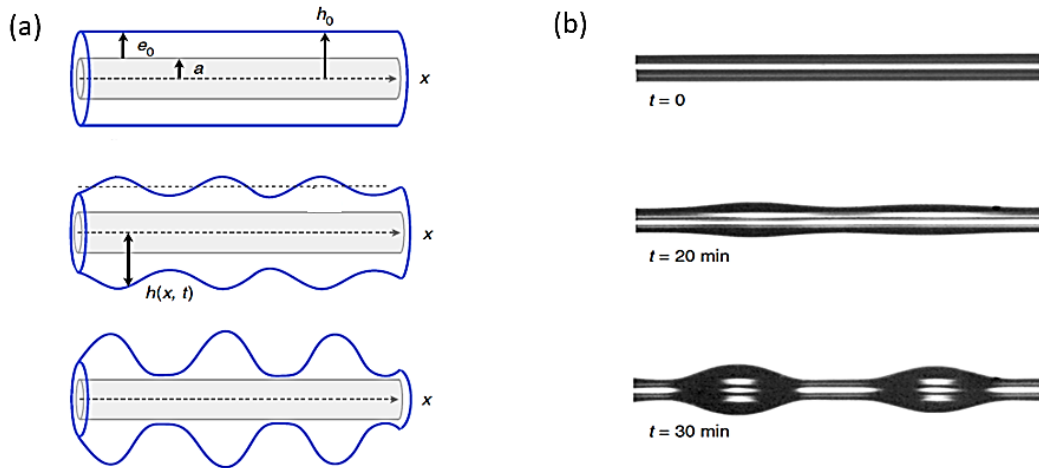
Where, in most cases,  $\zeta(Re)$  is an empirical function of  $Re$  derived from experimental data. [17]

### 2.2.5 Plateau-Rayleigh Instability (PRI)

Plateau-Rayleigh instability (PRI) explains why and how a falling stream of liquid ruptures into smaller periodic droplets of the same volume but less surface area. [24,34] Because of the Plateau-Rayleigh instability, fine liquid films on cylindrical elements are also unstable and break up into an array of small droplets. In the case of a fiber, the convex surface indicates that there will be a positive curvature on any coating film that develops, resulting in a positive Laplace overpressure acting on the film-air interface [73]. The Laplace pressure generally attempts to spread a liquid over a surface, and where the film radius at the solid-liquid interface differs from that at the liquid-vapor interface, this pressure acts to push the liquid out of the film and thereby bring it into an instability. Eventually, the surface tension of the liquid comes into play to minimize the free surface area and therefore the liquid film ripples and breaks up into a series of droplets. [74,75]



There are a number of applications where this phenomenon can be beneficial; fibers manufacturing, wire coating, electrospinning, fuel cells, optical fibers, surgical textiles, and mist/droplet filtration. [75] In the context of this work, the fabrication of spindle-knotted fibers by dip-coating the fibers in a polymeric solution as well as by the electrospinning process under specific circumstances are known manifestations of the PRI phenomenon. Fig. 2.9 (a-b) shows schematically and experimentally the break up of a liquid polystyrene (PS) film on glass fiber into droplets due to PRI [74].



**Fig. 2.9 Plateau-Rayleigh instability on a fiber [74];**

**(a)** Schematic and **(b)** optical micrographs illustrating the PRI for a liquid PS film on a glass fiber. The thickness of the glass fiber ( $a$ ) and the PS film ( $e_0$ ) (at  $t=0$ ) are about  $13.2 \mu\text{m}$  and  $9.6 \mu\text{m}$ , respectively. The width of optical images is  $560 \mu\text{m}$ .

## 2.3 Surface modification on fibers and textiles

Various surface treatment methods that permit modifying the physical and/or chemical nature of textiles and fibers contribute to the revolution in advanced materials. [30,34,51]. These methods contain surface coating by application of polymers [34], thin film metallic glasses [76,77], hydrogels, and sol-gels [78,79], or surface modifications by treatments with gas plasma, corona discharge, roughening, hydrosilylation, and the technology of direct laser writing. [7,26,31,34,38–40,47,51,79]

Apart from these methodologies, biological constructs may supply a significant source of inspiration for the design of next-generation structural materials because millions of years of evolution allowed plants and animals to develop structures and functions that are well adapted to changing environmental conditions [23,26]. The study and simulation of biological structures found in nature with respect to their technological potential are referred to as "bionics". Bionics tries to infer technical solutions from nature to transfer and implementate them creatively into engineering systems and modern technology applications, especially in textile science. [31,32,80] In this sense, new ideas for the development of surface modification techniques are proposed by nature, in this case, the


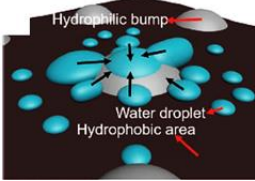

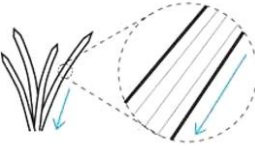
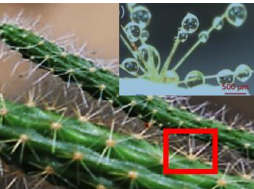
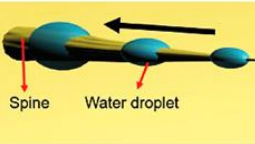

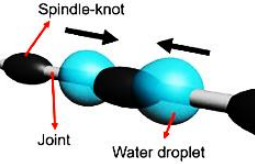
development of biomimetic fibers with superior surface functions. Functional structures of living systems, such as beetle backs, cactus spines, and spider silk with highly tuned wettability, have attracted increasing attention in recent decades. [51]

## 2.4 Bionic study of directional movement of droplets in nature

Atmospheric water and fog make up about 10% of all fresh water on Earth [40]. Fog is a visible aerosol made up of tiny water droplets suspended in the air on or near the surface of the earth and is a dominant water resource in deserts where water and rainfalls are scarce. [81–85] Fog consists of water droplets on the order of 10-50  $\mu\text{m}$  in diameter with a concentration of about 10-100 droplets per cubic centimeter [81,86].

The limited water access in relatively hostile environments such as deserts and arid regions drives both plants and animals that live there to evolve sophisticated organs or structures in order to adapt and survive. [23,32,37,82,83] Therefore, animals and plants living there developed efficient solutions to harvest water from fog and show an excellent ability to manipulate the water transportation in the desired directions towards the demanding organs. These solutions rely on unique chemistry, structural arrangement, and special micro-structures on or within their surfaces. [25,26,32,33,64,83]

**Tab. 2.1 Biological models and selected dimensions describing the water collecting species;**

Species	Image	Water collection behavior	Dimensions	Reference
Beetle ( <i>Stenocara gracilipes</i> )			Hydrophilic spot diameter: 0.2-0.5 mm Pitch: 0.5-1.5 mm	[26,34,87]
Grass ( <i>Stipagrostis sabulicola</i> )			Cross section: C-shaped Width: ~ 2 mm Length: <2000 mm Groove width: ~ 0.3 mm Groove pitch: ~ 0.4 mm	[88,89]
Cactus spine			Spine length: ~ 1.5 mm Base diameter: ~ 50 $\mu\text{m}$ Tip (apex) angle: $10^\circ$ Barbed length: top 1/4 <sup>th</sup> of the spine length Groove length: bottom 3/4 <sup>th</sup> of the spine length Groove width: ~ 2 $\mu\text{m}$ Groove pitch: ~ 20 $\mu\text{m}$	[23,90]
Spider web (Cribellate capture silk)			Wetted spindle length: Wetted spindle diameter: 21 $\pm$ 2.7 $\mu\text{m}$ Wetted joint diameter: 5.9 $\pm$ 1.2 $\mu\text{m}$ Apex angle: $19^\circ$ Periodicity: 89.3 $\pm$ 13.5 $\mu\text{m}$	[22,37,91]

Every species shown in Tab. 2.1 efficiently collects water from fog and uses a different mechanism to transport the collected water directionally to a location where it is consumed or stored. Mechanisms include heterogeneous wettability, grooves, and the Laplace pressure gradient due to the conical geometry. [23,64]

For instance, the carapace of the beetle *Stenocara gracilipes* from the Namib desert consists of a series of smooth, hydrophilic bumps surrounded by an area covered with microstructured hydrophobic wax [64,82,83]. Such intertwined hydrophilic/hydrophobic patterns facilitate the capture, nucleation, and directional transportation of tiny water droplets. Indeed, the fog droplets that encounter the beetle back will be primarily immobilized and accumulated on the hydrophilic spots. Once a coalesced droplet reaches a critical size, it will detach and then roll/slide down toward the mouth. [24,26,37,40,63,82,85,92–96]

The Namib Desert grass (*Stipagrostis sabulicola*) uses longitudinally running grooves to collect tiny water droplets from fog and to conduct them to the roots. [88,97]

It was discovered that many members of the Cactaceae family feature clusters of well-distributed conical spines, which assist the continuous and efficient collection of droplets from a humid atmosphere and therefore can survive [22,23,82]. The micron-sized water droplets are condensed and collected on the barbs. Once they grow to a critical size, they can be transported directionally from the tip to the base and finally towards the roots of the cacti. Hereby, their conical morphology of the spines leads to a Laplace pressure gradient and a wettability gradient. [25,32,64,84,93,98–100]

The picture of a spider web adorned with dew drops also demonstrates its ability to collect water droplets from fog [37,83]. Capture silk comprises alternating spindle-knots and joints, which exhibit different levels of surface micro/nanoscale roughness [26]. Exploiting the integration of both wettability and the curvature gradient between spindle-knots and joints, the water droplets are collected and spontaneously transported from joints to spindle-knots. [22,24,25,32–34,37,63,82,84,85,91,94–96,100]

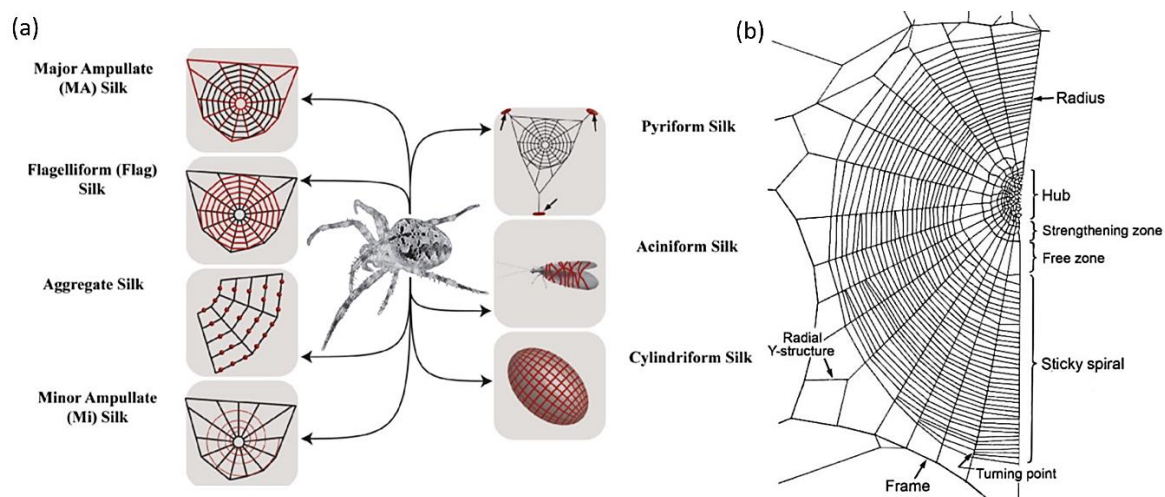
#### 2.4.1 Capture silk (thread) of cribellate spiders

In addition to the extraordinary properties of spider silks, such as strength [34,83], toughness [93], elasticity [34], robustness [101], and biomedical properties [102], another intriguing but less studied feature is its anisotropic wetting [32,34,37,83,84,86,91,93]. Anisotropic wetting results from roughness heterogeneity or chemical heterogeneity of a solid substrate or from the unique structural features, which spider webs utilize in their amazing ability for water collection [26]. *Venkatesan et al.* [83] found that spider webs exploit the last-mentioned trait to restore the distorted shape resulting from rearrangement of the hydrogen bonding of protein chains when subjected to prey impact, harsh weather,

and falling debris. Spider silk's ability to absorb moisture in a humid atmosphere facilitates super contraction in the fiber, resulting in a reorientation of the protein chains in the fiber to lower high-entropy energy levels. This is a typical shape memory effect induced by moisture, whereby the web changes its shape to recover from deterioration and deformation. [83]

Among the different types of biological models showing extraordinary characteristics with regard to the collection and directional transportation of water droplets (some introduced in Tab. 2.1), the capture silk of cribellate spiders is taken as a biological model in this study.

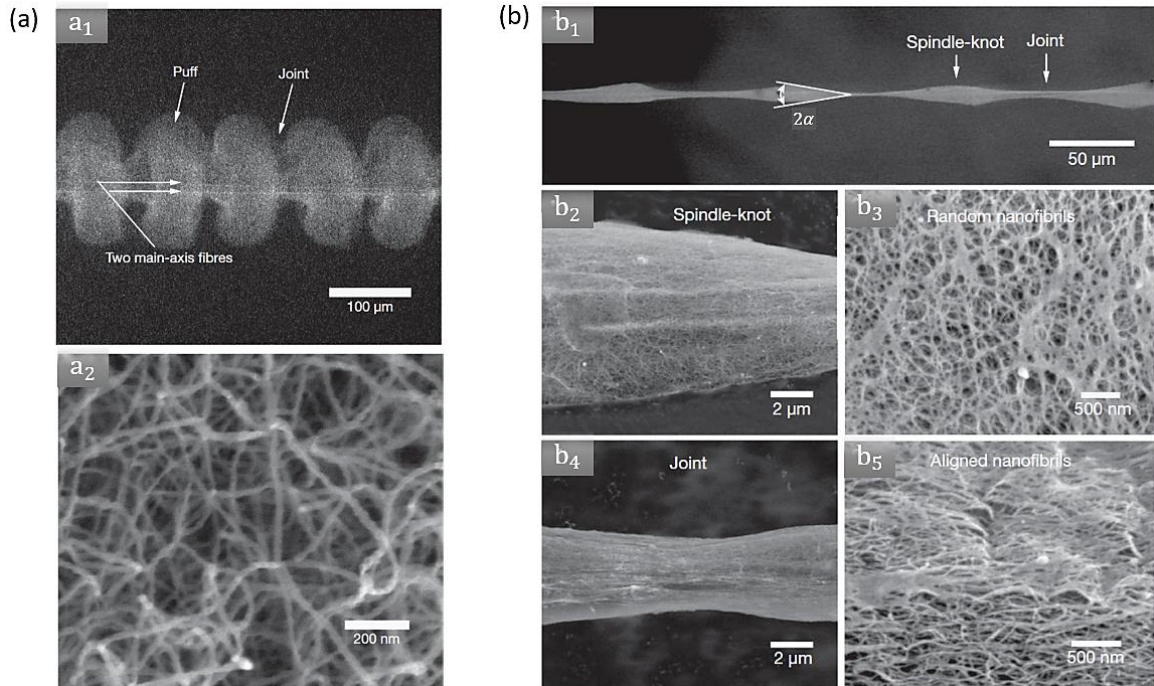
Of the about 40,000 described spider species approximately 9% are attributed to the Uloboridae family, known as cribellate orb weaver spiders [103–105]. As shown in Fig. 2.10 (a), the orb-weaving spiders have evolved the ability to secrete seven different silk proteins with diverse characteristics and biological functions such as predation, reproduction, nesting, and other life activities that are important tools for spiders to survive. [83,101,102,106–108] Fig. 2.10 (b) shows the organization of an orb web of Uloboridae. They have evolved a way to extrude nanofibrils from their silk-spinning organ (the cribellum), which consists of one or more plates covered in thousands of tiny spigots. [104] These nanofibrils are then separated into many exceedingly fine fibers by the calamistrum, a comb-like organ, as they are drawn-out from the cribellum. [37,106,108] The web construction starts with producing the frame and the radius. During web construction, the radial threads are connected in the center to form the hub, the resting place for the spider once the web is finished. Between the radial threads, first, an auxiliary spiral is spun, which is replaced later by sticky threads for entangling prey. [103]



**Fig. 2.10 Different spider silk and their specific purpose;**

**(a)** Schematic overview of different silk types produced by female orb weaving spiders (Araneae). Each silk type (highlighted in red) is tailored for a specific purpose [101], **(b)** left half of a typical orb web including the terms of the structures found [103].

Engineering spider webs from the aspect of moisture collection was initially reported by Jiang and his coworkers (2010), who studied the capture silk in the web of a cribellate spider in detail. Fig. 2.11 (a) and (b) shows the SEM images of capture silk of *Uloborus walckenaerius* (a cribellate orb weaver spider) in a dry and wet environment, respectively [37,84].



**Fig. 2.11 Structure of dry and wet-rebuilt spider silk [37];**

**(a)** SEM images of dry capture silk of the cribellate spider *Uloborus walckenaerius*, **(b)** SEM images of wet-rebuilt capture silk of *Uloborus walckenaerius*.

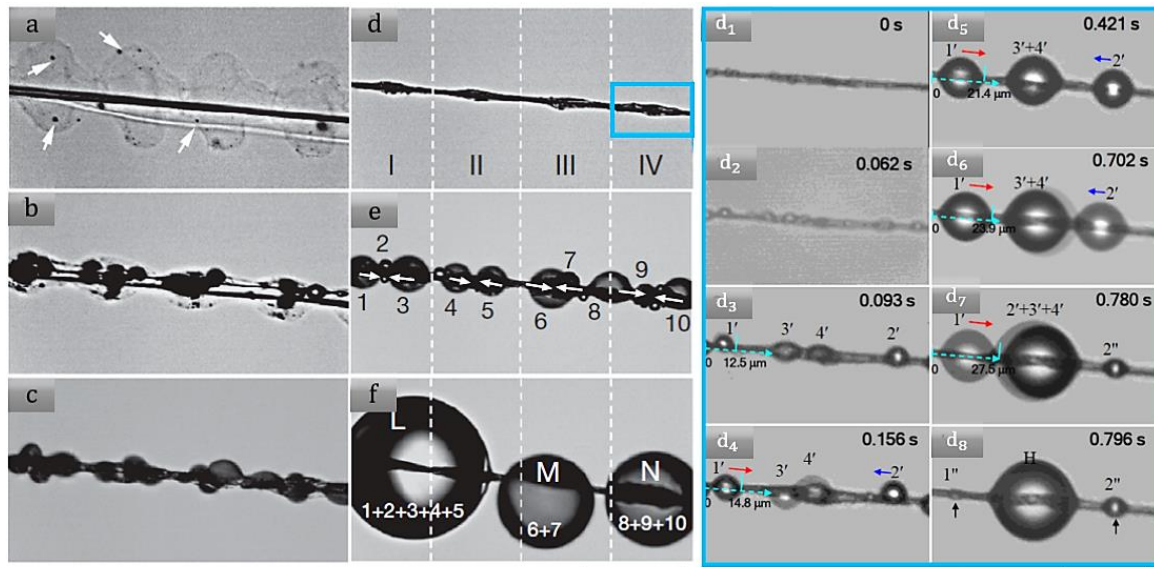
The sticky capture threads consist of two core fibers (Fig. 2.11 (a<sub>1</sub>)) that are made of flagelliform silk (structural proteins) and additionally contain either glue droplets (glycoprotein coating from aggregate gland) or capture wool consisting of randomly arranged nanofibers with a diameter of 10 to 30 nm (Fig. 2.11 (a<sub>2</sub>)). [83,86,103] The nanofibers are arranged in a sequence of puffs and joints (Fig. 2.11) [37,106]. Puffs are elastic nanofibers that are spaced along two main-axis fibers with a periodicity of  $85.6 \pm 5.1 \mu\text{m}$  and a diameter of  $130.8 \pm 11.1 \mu\text{m}$  (Fig. 2.11 (a<sub>1</sub>)) [37,91]. The puffs are separated by the joints with a diameter of  $41.6 \pm 8.3 \mu\text{m}$ , which are simply there because of the fabrication process used by the spider, namely cyclic brushing.

In the presence of fog, tiny water droplets accumulate on the structure due to the presence of moisture-sensitive hydrophilic so-called highly hygroscopic nanofibrils [37,83]. The fluid interfaces of the water droplets produce surface tension (capillary) forces that tend to maximize the wetted area. Since the elastic nanofibers are very flexible and delicate, the capillary forces can influence and easily manipulate the morphology of nanofibrils



structure. As a consequence of this manipulation, a series of nanofibril puffs transform into wet bundles via the kind of elastocapillary self-assembly process which ultimately results in the formation of a periodic spindle-knotted structure (Fig. 2.11 (b<sub>1</sub>)). [109] In Fig. 2.11 (b<sub>2</sub>-b<sub>3</sub>) and (b<sub>4</sub>-b<sub>5</sub>) the zoomed SEM images of the spindle-knot and the joint of the wet-rebuilt capture silk are shown, respectively.

*Jiang et al.* (2010) stated that the directional water collection behavior of the cribellate capture silk starts after this structural wet-rebuilding, that is, after transformation from the puffy structure to the periodic spindle-knotted structure [37,84]. In order to clearly observe this behavior, they exposed dry capture silk in mist with a relative humidity of 90~99% and observed that the tiny water droplets (black dots shown by arrows) were accumulated on the semitransparent puffs (Fig. 2.12 (a)). As the water accumulation continued the puffs shrank into opaque spindles and the nanofibrils are then stretched and the knots are separated from one another, creating the joints. (Fig. 2.12 (b)). In Fig. 2.12 (d) the examined capture silk is divided into four regions, each including a single spindle-knot. After that the periodic spindle-knotted structure was built, the droplets (indicated by number 1 to 10) formed randomly on the silk. As the accumulation continued, the droplets grew in size and the adjacent droplets were coalesced and directed towards the nearest spindle-knots (shown by white arrows in Fig. 2.12 (e)). Fig. 2.12 (f) shows that the droplets 1-5 were coalesced into a large droplet (L) covering the spindle-knots in region I and II, while the coalesced medium-sized droplets (M and N) covered the single spindle-knot in region III and IV, respectively. The zoomed-in images in Fig. 2.12 (d<sub>1</sub>- d<sub>8</sub>) display the detailed process that takes place in region IV. The initial time was set when wetted spider silk was exposed to the relative humidity of ~95% (Fig. 2.12 (d<sub>1</sub>)). Fig. 2.12 (d<sub>2</sub>) shows the tiny water drops that gradually and randomly were accumulated on the spider silk. The four accumulated droplets denoted by 1', 2', 3', and 4' are highlighted in Fig. 2.12 (d<sub>3</sub>). In Fig. 2.12 (d<sub>4</sub>) it can be seen that the adjacent droplets 3' and 4', which were already accumulated at the site of spindle-knot, began to merge at the center of spindle-knot. The droplets 1' and 2' that were accumulated at the site of the joints moved spontaneously toward the nearest spindle-knot when reaching the critical size and coalesce into larger water droplets (Fig. 2.12 (d<sub>5</sub>-d<sub>7</sub>)). After the joints were refreshed, the two regenerated accumulated droplets 1" and 2" became larger and a new water collection cycle began (Fig. 2.12 (d<sub>8</sub>)). In-situ observation of directional water collection on the capture silk of cribellate spider indicated that the forming drops move quickly from the joint to the spindle-knot (denoted with blue and red arrows). [22,37]



**Fig. 2.12 Detailed directional water collection behavior along spindle-knotted capture silk [37];**  
scale bar: (a-f): 100  $\mu\text{m}$ , (d<sub>1</sub>-d<sub>8</sub>): 30  $\mu\text{m}$ .

The observations of *Jiang et al.* [22,37] demonstrated that the spindle-knotted structure of capture silk plays an key role in the directional water collection behavior. They proved this hypothesis when they in particular carried out the control experiments with silkworm silk as well as partially damaged spider silk without periodic spindle-knotted structure.

In summary, it was found that the spindle-knots initially serve as sites of water accumulation and, after some time, as collecting sites for the coalescence of smaller droplets originating from the joints. The joints serve primarily as accumulation sites where water droplets after accumulation and merging with other neighboring droplets are transported towards the spindle-knots. That was also observed after the water droplets leave the joints and collect on the spindle-knots, a new cycle of water accumulation in joints and directional droplet movement towards the spindle-knots begins. [32]

## 2.5 Analysis of the mechanism of directional movement of droplets

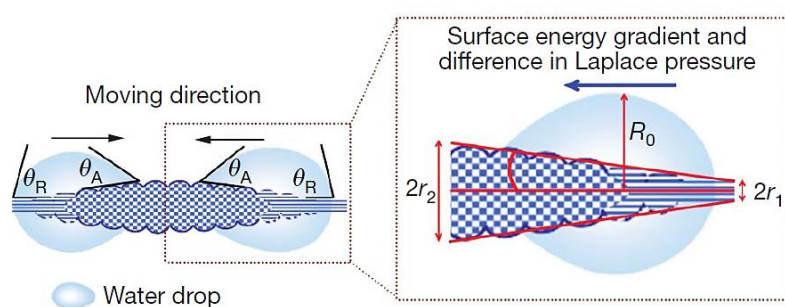
In principle, a static droplet on a solid surface is subjected to counterbalanced forces. Once the equilibrium of forces is disturbed, the droplet moves toward a certain direction, performing the directional movement. In all of the biological models described in section 2.4, the directional movements of droplets on surfaces are caused by unbalanced capillary forces. In general, these movements can be divided into two types: movements caused by non-uniform surface wettability and movements caused by asymmetrically shaped surfaces. It is known that the capillary forces are the product of a characteristic length ( $d$ ) and the surface tension ( $\gamma$ ), therefore a directional motion can occur as soon as a droplet experiences a gradient concerned with the mentioned parameters. The Marangoni effect

denotes mass transport due to a gradient in surface tension forces, which results, in turn, from gradients in temperature, electric field, or chemical composition. The effect of the variable characteristic length is best revealed in the work of *Lorenceanu* (2004), described in section 2.2.3, causing the self-driven motion of a droplet deposited on a conical fiber. [63,84]

In this section, the directional water collection in the capture silk of cribellate spiders will be analyzed in detail. The prevailing conclusion from the literature is that this behavior relies on the cooperative effects of special structural features and the wettability of capture silk. [22,25,37,82–84,91,94,98] In what follows, these synergetic effects are described in detail.

As shown in Fig. 2.10 (a), the capture silk is composed of flagelliform proteins, which is humidity-sensitive and hydrophilic. Therefore, the nanofibrils of both spindle-knots and joints are hydrophilic. This wettability contributes to the impressive capturing of tiny water droplets in a humid environment and is favorable for accumulating water drops. [37,83] The wettability properties that lead to the directional movement of water droplets are rooted in surface energy gradients which can arise from differences either in surface chemistry or surface roughness. Such gradients propel water droplets towards the more wettable area with a higher surface energy region. [35,37,110–113]

In the case of capture silk, the chemical composition of the silk is the same at spindle-knot and joint positions, but there is a roughness gradient. As shown in Fig. 2.13, this gradient introduces a smaller contact angle to the water at its end near the spindle-knot position (higher roughness, that is, more hydrophilic) compared to its end near to joint (less roughness, that is, less hydrophilic). [32,37,84]



**Fig. 2.13 Mechanism scheme showing the directional water collection on spindle-knot [37].**

The spindle-knot thus has a higher surface energy compared to joints and drives water toward itself due to the surface energy gradient. As liquid contact angle is usually applied to assess the wettability of a solid surface, the force generated by a surface energy gradient resulting from a difference in surface roughness is given by [22,32,37,84,91,94,99,110,111]



$$F_C = \int_{L_j}^{L_k} \gamma_{lg} (\cos \theta_A - \cos \theta_R) dl \quad (2.21)$$

where  $\gamma_{lg}$  is the surface tension of water,  $\theta_A$  and  $\theta_R$  are the advancing (front side) and receding (rear side) contact angles of a water drop on the spider silk, respectively.  $dl$  is the integration variable along the length from the joint ( $L_j$ ) to the spindle-knot ( $L_k$ ). As already explained,  $\theta_A < \theta_R$ , therefore the sign of the force in equation (2.21) is positive, which results in a directional movement of water droplets from joints towards the spindle-knots.

Once again, the two regions of spindle-knot and joint have the same chemical composition (made of flagelliform silk) but different surface topographies. This topography gradient leads to hysteresis force arising from the difference in advancing and receding contact angles at the two ends of a water droplet and affect the spreading and the movement of droplets. The zoomed-in images in Fig. 2.11 (b<sub>3</sub>) and (b<sub>5</sub>) show the topography of the nanofibrils at spindle-knot and joint positions, respectively. It reveals that nanofibrils at spindle-knots are randomly distributed and therefore offer high roughness, the nanofibrils at the joint position, in contrast, are mostly smoothly aligned fibers parallel to the silk fiber axis. The aligned fibers at the joint offer a continuous three-phase (vapor-liquid-solid) contact line (TCL) to the positioned water droplet, while the random nanofibrils at the spindle-knot lead to a discontinuous TCL. Therefore, the water droplets positioned at the site of the joint face a smaller hysteresis force and can move more easily, while the more pronounced hysteresis forces on the droplets positioned at the spindle-knots oppose the movement of these droplets due to the discontinuous TCL. [37,84]

It turned out that the directional water collection is caused also by structural features, in addition to the gradient in wettability property. Indeed, one of the sources of asymmetry in materials science arises from asymmetries in geometry and structure [33]. Therefore, the other possible force exerting a directional movement on water droplets arises from the shape of the knots, which generates a difference in Laplace pressure. [37] The spindle-knots and joints in Fig. 2.11 (b) show a periodicity of  $89.3 \pm 13.5 \mu\text{m}$  and diameters of  $21.0 \pm 2.7 \mu\text{m}$  and  $5.9 \pm 1.2 \mu\text{m}$ , respectively. The apex angle  $2\alpha$  of the spindle-knots amount to about  $2\alpha \approx 19^\circ$ . [37,91,114]

As shown in the magnified inset in Fig. 2.13, a spindle-knot can be assumed to be composed of two oppositely joined conical objects. According to equation (2.12), each conical object with a curvature gradient will give rise to a difference in Laplace pressure ( $\Delta P$ ) acting on the droplet by the following formula [22,32,37,57,84,86,91,94,99,115]

$$\Delta P = - \int_{r_1}^{r_2} \frac{2\gamma}{(r + R_0)^2} \sin \alpha dz \quad (2.22)$$

where  $r$  is the local radius,  $R_0$  is the radius of the water droplet,  $\alpha$  is the half-apex angle of the spindle-knot and  $z$  is the integrating variable along the diameter of the spindle-knot. As can be seen in Fig. 2.13, the joint with a local radius of  $r_1$  has a higher curvature (larger Laplace pressure) compared to the spindle-knot with a local radius of  $r_2$  (smaller Laplace pressure). Therefore, this gradient in the Laplace pressure leads to a directional movement of water droplets from the position of greater Laplace pressure (joints) towards the positions of less Laplace pressure (spindle-knot). [37]

In summary, the wettability (surface energy) and the structure of the capture silk play a crucial role in the impressive water management of capture silk. Indeed, it turned out that the gradients in surface free energy and in Laplace pressure are the primary driving forces behind the phenomenon of directional movement of water droplets from joints towards the spindle-knots. Accordingly, the hydrophilic nanofibrils initially allow the capture and accumulation of micron-sized water droplets on the nanofibrils from the atmosphere. Once the micron-sized water drops grow to a critical size, the gradients in surface energy gradient and Laplace pressure act cooperatively to overcome the hysteresis forces and therefore allow the droplets to accumulate directionally and coalesce at spindle-knot positions to form larger droplets. [32,37,82,83,86,98]

## 2.6 Bio-inspired material causing directional movement of droplets

Observations from nature (e.g. the spiders and their silk fibers) have undoubtedly encouraged many scientists to develop bioinspired materials with surfaces that allow to manipulate the behavior of liquid droplets, such as the directional transport of tiny liquid droplets. Inspired by the special surfaces of creatures described in section 2.4, multi-functional surfaces with chemical composition or physical structure gradients have been designed to realize the controllable transport of liquid droplets. In addition, hysteresis forces could create major barriers to the rapid and continuous movement of liquid droplets on the surfaces exploiting only the asymmetric geometry and wettability gradient. [84,100] To mitigate hysteresis, besides exploiting geometry and wettability gradient, many external-field-sensitive surfaces responding to diverse external stimuli such as magnetic fields, electric fields, chemical potential, temperature, light, humidity, and pH have been fabricated to achieve surface wettability gradients for the efficient transport of liquid droplets. [22,25,26,37,62,94,116]

All in all, a large number of researches have shown that bio-inspired structures exerting drop motion are of significant and economic interest for a wide spectrum of applications. Applications are in the field of printing, surface coating, drying, drug delivery and release, single-cell gene sequencing, colloidal synthesis, micro/nanofluidic devices, catalytic reactions, interface catalysis, energy transfer, and selective separation. [21,22,24,26,33,35,46,62,63,78,83,84,94,98,114,116–118] Among these interesting fields, droplet manipulation (capture, transfer, and release) in terms of control of the rate and direction of droplet migration in filters and membranes with application in gas-liquid and liquid-liquid separation, has aroused extensive interest in the recent decade [21,23,64,78]. The next two sections list the most highlighted works and achievements for bio-inspired structures developed so far, corresponding fundamental models and mechanisms for droplet motion, and their application in two categories of liquid-gas and liquid-liquid separation.

### 2.6.1 Liquid-gas separation

Collecting water from a humid environment by fog collectors has attracted a lot of attention due to its large water capacity and the origin of the world water crisis [32,64,98,100]. Some of the fog collectors rely on gravity or other external forces to transport or remove the collected water. Nevertheless, the large size required for water droplets to move by gravity on the solid surface prevents the rebirth of the fog collection cycle [98]. Furthermore, existing fog collectors are still being modified to eliminate pore-clogging from collected droplets and the re-entrainment of the water collected from ribbons by the wind [86,119]. In this regard, the incorporation of bio-inspired surfaces that exploit wettability and structural gradients for purposeful droplet transport from position to position can accelerate this phenomenon and could therefore be addressed as one of the dominant applications in liquid-gas separation [32]. Various attempts have been made to study the water collection from the fog and to develop the diverse kinds of fog collectors inspired by spindle-knotted spider silk as well as conical spines of cacti, which have functionally analogous structures such as wet-rebuilt capture silk [22]. As these two biological models follow similar mechanisms for their water collection behavior [32], this work reviews the materials developed so far inspired by each of them.

Following the pioneering studies of *Lorenceanu et al.* [57] and *Jiang et al.* [37], *Zheng et al.* [120] studied the self-motion of nanoscale water droplets and tendencies of motion of a water molecule on curved surfaces by molecule dynamics (MD) simulations and analytical methods. Interestingly, their simulation results revealed that a released nanoscale water droplet on the outer surface of a cone (made of graphene) always spontaneously moves to the larger end of the cone and on the inner surface to the smaller end, and this behavior is independent of the wetting properties.

In another study, *Michielsen et al.* [116] also implied that droplets can move spontaneously on conical fibers. They used minimum Gibbs free energy analysis to predict the possible final positions of a droplet. They expressed the Gibbs free energy ( $G$ ) as

$$G = \gamma_{lv}A_{lv} + \gamma_{sl}A_{sl} + \gamma_{sv}A_{sv} \quad (2.23)$$

where,  $\gamma$  is the surface energy and  $A$  is the interfacial area between the different phases of solid, liquid, gas denoted by s, l, v, respectively. By extending the expression in (2.23) as well as the Carroll's equations [60] to a drop on a cylindrical fiber, they have found the dependency of  $G$  on four factors; the half-apex angle of the conical fiber ( $\alpha$ ), the contact angle ( $\theta$ ), the liquid volume ( $\Omega$ ), and the initial place where the drop is located ( $x_1$ ). According to their predictions, there is only one minimum in  $G$  along the length of the cone, and in absence of gravitational effects a drop will stop at this point. For a fixed  $\alpha$  the point of minimum  $G$  moves towards the tip of the cone as  $\theta$  increases. Similarly, for a fixed  $\theta$ , as  $\alpha$  increases, the minimum  $G$ -point moves towards the tip. They then verified these hypotheses by carrying out the corresponding experiments using water and dodecane droplets on glass cones.

The key for artificial cactus bio-inspired designs as one of the surfaces with curvature gradients is to obtain multiscale needle-like conical structures that are capable to collect water and to transport water from the tip to the base of the cones. Accordingly, individual and arrays of artificial cactus spines were fabricated via electrochemical and electroetching methods using pristine metallic needles [54,57,78,84], or molding [78] and additive manufacturing [98] methods using polymeric materials. [32]

In one pioneering study and inspired by the efficient fog collection on cactus spines, *Ju et al.* [54] fabricated conical copper wires with different wettability by electrochemical corrosion followed by chemical modification (Fig. 2.14 (a-c)). As shown in Fig. 2.14 (a) and (b), they concluded that the droplets on the hydrophilic and hydrophobic surfaces prevail in barrel-shaped and clamshell configurations, respectively (section 2.2.2). On the cones with unique wettability, either hydrophilic or hydrophobic, the single Laplace driving force, which governs the directional movement of droplets was considered according to equation (2.8).

$$F_{L_{hydrophilic}} \approx \gamma \left( \frac{1}{R_1} + \frac{1}{R_2} \right) S_{TCL_{barrel}} \quad (2.24)$$

$$F_{L_{hydrophobic}} \approx \gamma \left( \frac{1}{R_1} + \frac{1}{R_2} \right) S_{TCL_{clamshell}} \quad (2.25)$$

where  $R_1$  and  $R_2$  are the local radii of the cone at two opposite sides of the droplet and  $\gamma$  is the surface tension.  $S_{TCL}$  is the area of the region enclosed by the TCL. They concluded that the Laplace force generated on the hydrophilic surface is larger than that on the hydrophobic surface ( $S_{TCL_{barrel}} > S_{TCL_{clamshell}}$ ). They believed that the ratio between droplet motion speed and droplet growth rate is critical for efficient fog collection. In view of this, compared to conical copper wires with purely hydrophobic or hydrophilic surfaces, they have shown that the conical models with gradient wettability show higher fog-collection capacity in terms of both large water transport speed ( $l/t$ ) and large water collecting velocity ( $\Omega/t$ ) (Fig. 2.14 (d)). The reason for this is that for the conical models with gradient wettability, besides the Laplace force, the chemical force arising from the wettability gradient acts as another driving force. According to equation (2.21), they modeled this force as

$$F_C \approx \gamma(\cos \theta_a - \cos \theta_r)l_{TCL} \quad (2.26)$$

where the parameters are defined as in equation (2.21).

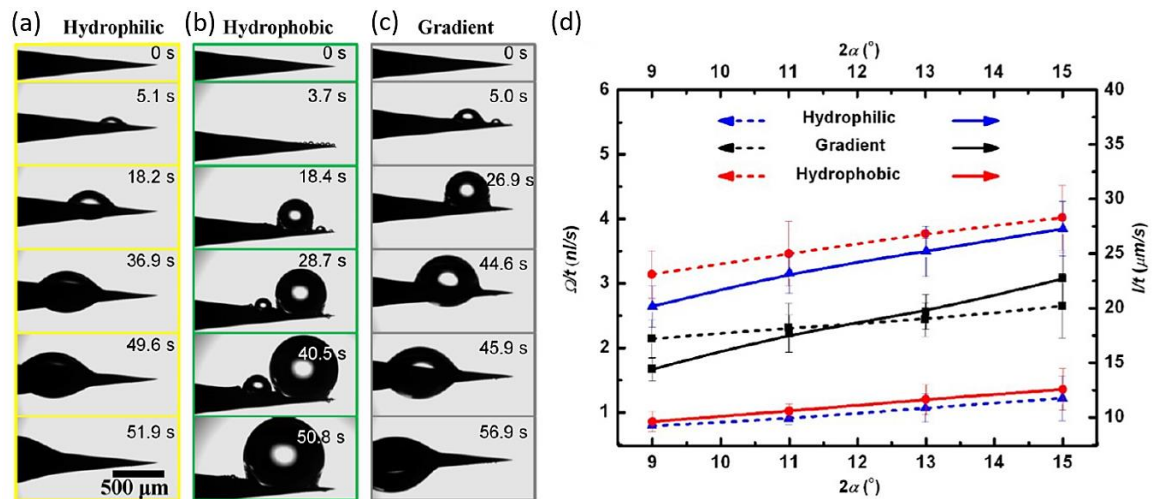
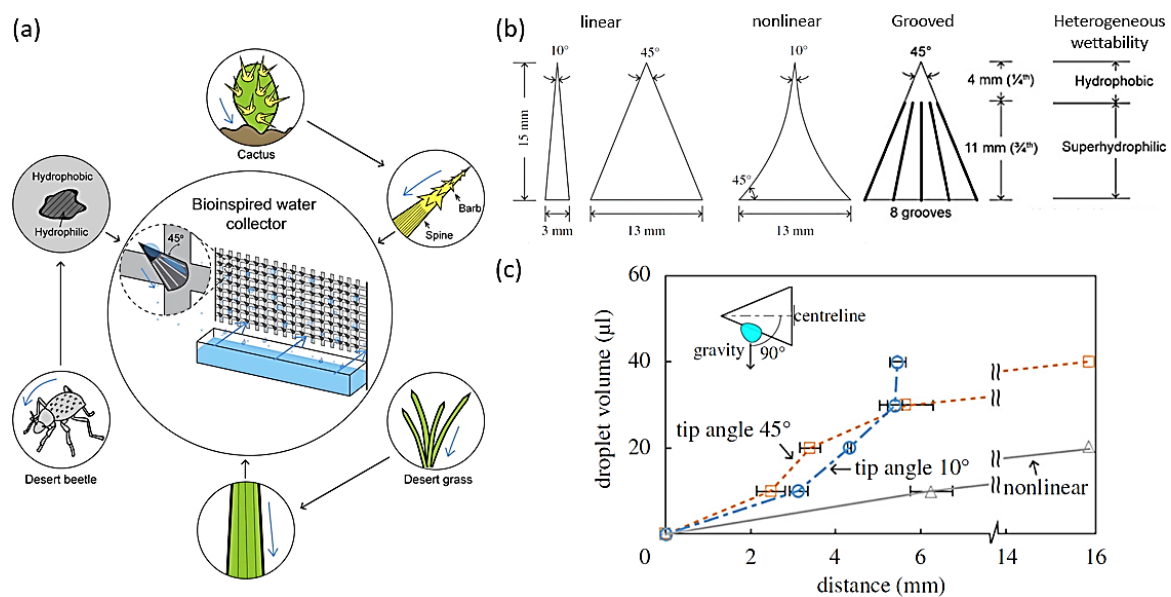


Fig. 2.14 Microscopic observation of fog collection on cones [54];

(a-c) Directional water movement on the conical models with different wettability, (d) a diagram showing droplet motion velocity and droplet growth rate for cones of different wettability.

Some years later, in a series of systematic studies by *Bhushan* and coworkers [64,121–123], a design guideline for a water collection tower that was bio-inspired by the back of a beetle, desert grass, and cactus spines featuring heterogeneous wettability, grooves, and conical geometry, respectively, was developed (Fig. 2.15 (a)). Here, the effect of each mechanism on the movement and collection of water droplets in the fog was examined. Fig. 2.15 (b) shows the diverse conical models made of an acrylic polymer (water contact angle of  $\sim 61^\circ$ ) and fabricated by the 3D-printing method. The considered forces attributing to the

movement of droplets from top to bottom were gravity and the force due to the Laplace pressure gradient. Based on their experimental observations, at  $0^\circ$  inclination (representing that the cone is parallel to the fog flow), the Laplace pressure gradient dominates, and a shorter cone length delivers a higher rate of water collection at the base, while at  $45^\circ$  inclination gravity dominates and a larger surface area provides a higher rate of water collection at the base. Therefore, a higher inclination angle provides a higher water collection rate compared to a lower one due to the contributions of gravity. It was found that a cone with a smaller tip angle ( $10^\circ$ ) transports a water droplet farther along the cone compared to a larger one ( $45^\circ$ ). Grooves help in channeling the water and heterogeneous wettability i.e. a hydrophobic tip and a superhydrophilic base also increased the water collection rate. A single droplet of known volume is transported farther on a horizontal nonlinear cone (shown in Fig. 2.15 (b)) due to a high Laplace pressure gradient in the beginning and increasing the gravitational effect later. Fig. 2.15 (c) sketches the effect of tip angle and nonlinear structure of the cone on the droplet movement and confirms that a smaller tip angle and broader base diameter with a higher surface slope are beneficial for a high water collection rate.



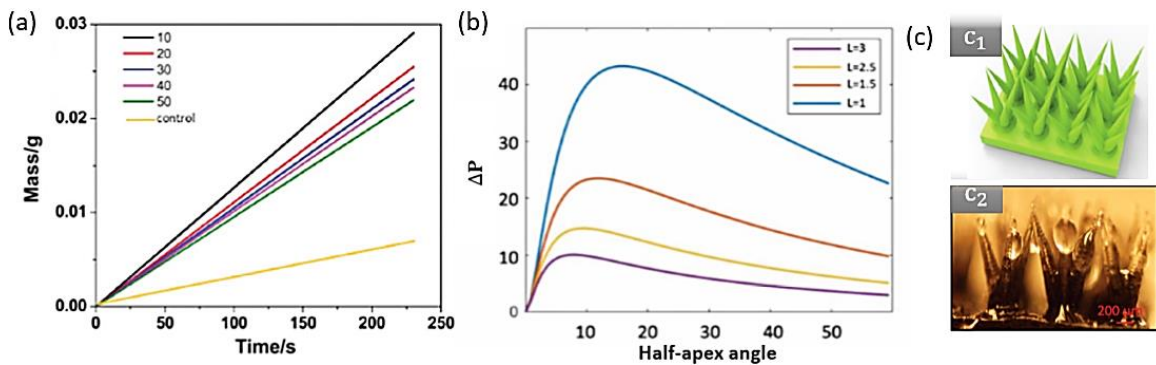
**Fig. 2.15 Fog collection tower inspired by beetle back, desert grass, and cactus spine;** (a) Schematic of the water collection tower [64], (b) diverse design of 3D-printed conical models [121,122], (c) a diagram showing the distance traveled by the single droplet on different conical models: a fixed volume droplet moves further when the non-linear cone model is used [121,122].

Li *et al.* [98] have developed a cactus-inspired surface decorated with multiple artificial spines for highly efficient water collection and transportation. Similar to the work reported so far, the underlying mechanism was found to be that the water drops on a spine-structured object feel different Laplace pressures on the two opposite sides and this triggers a

directional movement. Starting from equation (2.22), they expanded the Laplace pressure gradient as

$$\begin{aligned} \Delta P_{curvature} &= - \int_0^{L \tan \frac{\alpha}{2}} \frac{2\gamma_w}{(R + R_0)^2} \sin \frac{\alpha}{2} dz \\ &= \frac{2\gamma_w \sin \frac{\alpha}{2}}{\left[ (L - 2R_0) \tan \frac{\alpha}{2} + R_0 \right]^2} - \frac{2\gamma_w \sin \frac{\alpha}{2}}{\left( L \tan \frac{\alpha}{2} + R_0 \right)^2} \end{aligned} \quad (2.27)$$

where  $\Delta P_{curvature}$  is the gradient of Laplace pressure,  $L$  is the height of the cone,  $R$  and  $R_0$  are the radii of the cone and the collected water droplet, respectively.  $\alpha$  is the apex angle of the cone and  $dz$  is the integral variable of the cone. Applying the 3D-printing method, they have fabricated conical spines with apex angle of  $10^\circ$ ,  $20^\circ$ ,  $30^\circ$ ,  $40^\circ$ , and  $50^\circ$ . By carrying out the fog collection experiment they observed that the collected water masses are greater for spines with smaller apex angle (see Fig. 2.16 (a)).



**Fig. 2.16 Water collection on 3D-printed cactus-mimetic spine structure [98];**

(a) The collected water masses as a function of time for the surface decorated with and without (control line) spines of different apex angles, (b) the Laplace pressure difference ( $\Delta P$  in  $\text{Pa mm}^{-1}$ ) for the spines designed with different apex angles (in degree) and heights ( $L$  in mm), (c)  $c_1$ : Hexagonally arranged branched spines using Solidworks,  $c_2$ : Coated 3D-printed Hexagonally arranged branched spines with water collection functionality.

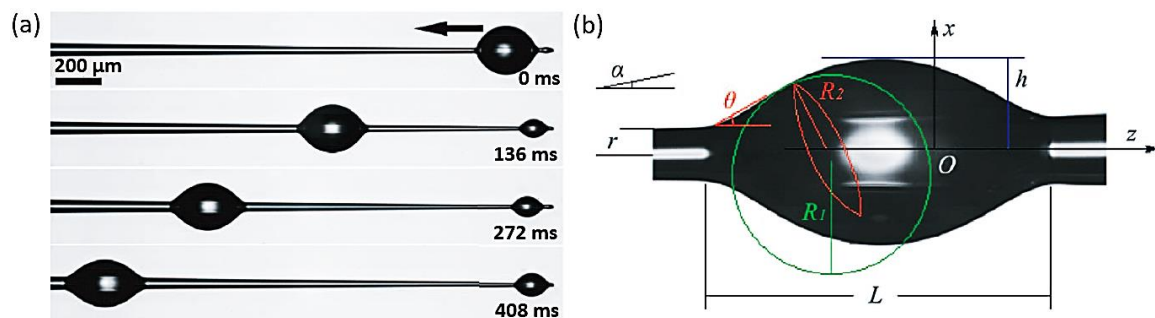
They optimized the apex angle of the cactus-inspired spine based on its length for fast water transportation along the spines. As shown in Fig. 2.16 (b), for fixed height, the pressure increased at first dramatically to its peak value and then decreased with increasing apex angle. The optimal apex angle of 3D-printed cactus-mimetic spines for fast water transportation becomes smaller if its length is increased. The 3D-printed cactus-mimetic spines achieved fast water transportation with optimal apex angle of  $15^\circ$  for  $L = 1$  mm and  $10^\circ$  for  $L = 1.5$  mm, respectively. Based on Kelvin's equation [124], they found that the condensation of water droplets is easier to occur on the hydrophobic surface than on hydrophilic surface under the same conditions. Therefore, the surface wettability of the cones was modified with a nanoscale superhydrophobic layer leading to a lower surface

tension (increase in water contact angle from  $65^\circ$  to  $137^\circ$ ). In their study, 3D-printed cones with  $10^\circ$  apex angle in hexagonally arranged branched spines and coated with hydrophobic nano-coating offered promising results in terms of water collection and transportation (Fig. 2.16 (c)). [98]

*Li et al.* [63] studied the capillary-driven movement of a microdroplet along a pre-wetted conical fibers that were produced by heating and pulling glass capillaries. Different liquids (water and oil) with varying surface tension and viscosity were fed to the tip of the conical glass fiber and their movement along the cones towards their thicker part was observed (Fig. 2.17 (a)). Compared to *Lorenceanu et al.* [57], the thinner conical model was applied, for which the diameter at the tip was about  $16 \mu\text{m}$  and increased over  $4 \text{ mm}$  to about  $140 \mu\text{m}$ , giving an average half-apex angle of  $\alpha \approx 0.89$ . They determined the absolute strength of the driving capillary pressure (the Laplace force) for a quasi-spherical droplet as in the study of *Lorenceanu et al.* (2004) (see section 2.2.3). What further distinguishes their work from other previous works is taking the viscous friction into consideration, which counteracts the capillary driving force. In contrast to a thin drop, where the viscous friction occurs essentially within the drop, they believed that in a quasi-spherical drop, the viscous friction acts mainly within the liquid wedge angle  $\theta$  as shown in Fig. 2.17 (b). For a quasi-spherical droplet,  $\theta$  is given by Hoffman-Tanner's Law [57,125,126] as

$$\theta \sim (l\mu v/\gamma)^{1/3} \quad (2.28)$$

which states a local balance between surface tension  $\gamma$  and viscosity  $\mu$ .  $v$  is the velocity and  $l$  is defined below.



**Fig. 2.17 A silicon oil on a conical glass fiber [63];**

**(a)** The motion of a 10 centistokes (cSt) silicone oil droplet with a radius ( $R_0$ ) of  $220 \mu\text{m}$  on a glass fiber with an initial radius ( $r_0$ ) of  $8 \mu\text{m}$ , **(b)** a wetting barrel-shaped droplet on a conical fiber.

The no-slip boundary condition causes the stress to increase with the velocity gradient when the layer becomes thinner close to the end of the wedge, i.e.,  $\sim \mu(dv/dx)$ , where  $x$  is in the radial direction as shown in Fig. 2.17 (b). The thickness of the wedge varies as  $\theta z$ , where  $z$  is measured from the tip of the wedge. This gives a local magnitude of the friction



$$df \sim \mu v / (\theta z) \quad (2.29)$$

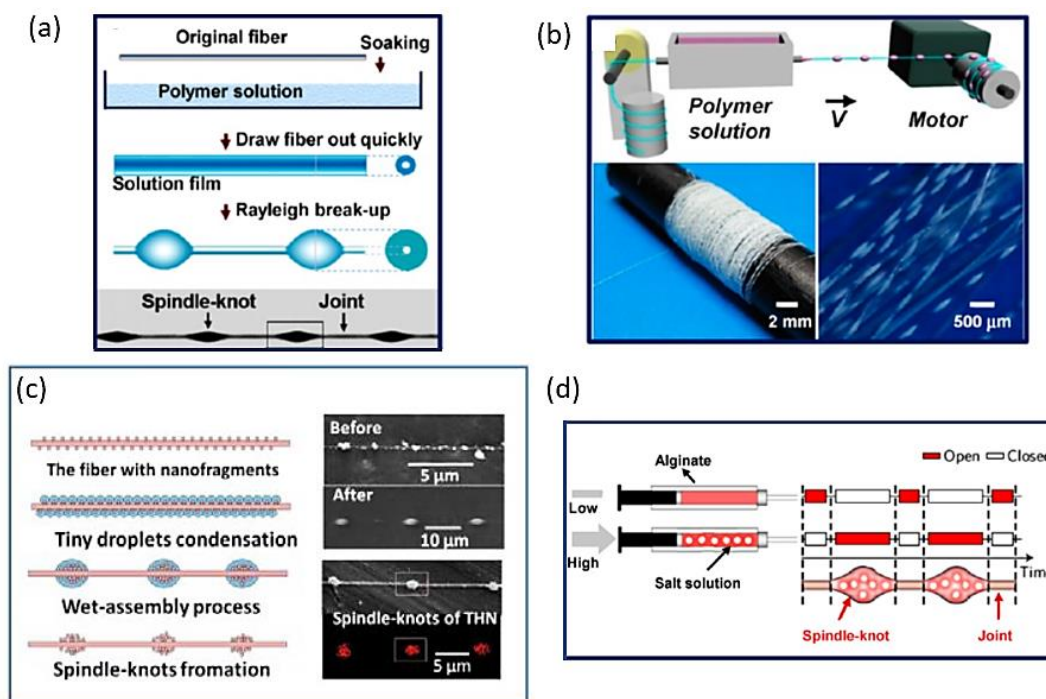
To find the total friction, the integration of equation (2.29) must be calculated. For drop moving on a dry solid, this integration gives a logarithmic singularity near the tip of the wedge, which must be modeled by a molecular cut-off length [125]. This integration yields  $\mu v r l / \theta$  ( $r$  is the fiber radius) and the factor  $l$  arises from the logarithmic cut-off [57]. For a liquid spreading on a dry surface, it amounts to about  $l \approx 15$  [57,125] and for a liquid spreading on a prewetted surface, it is about  $l \approx 5$  [127]. The reduction of the viscous friction in the latter case results from the wedge slipping on the pre-wetted film. They finally obtained expression (2.30) for the viscous friction in terms of the quasi-spherical droplet.

$$f_{\text{viscous friction}} \sim r \gamma^{1/3} (\mu l v)^{2/3} \quad (2.30)$$

In addition to advances in developing conical models for water collection, various studies have dealt with the development of artificial spindle-knotted models. Here, the key point in creating artificial spider silk is to generate a wettability gradient, either by gradients of chemical composition or roughness or by a geometry gradient (i.e. the curvature of the solid surface).

To this end, many fabrication methods have been developed, including dip-coating [37,114,128] fluid-coating [85], wet-assembly [129], and microfluidic technology [32]. Applying dip- and fluid-coating, synthetic fibers with periodic spindle-knots have been developed, mainly based on nylon filaments coated with petroleum-derived synthetic polymer solutions. In a dip-coating method (Fig. 2.18 (a)), the fiber is immersed in a polymeric solution and drawn out. Due to the Plateau-Rayleigh instability (section 2.2.5), the coating film eventually breaks up into periodic droplets, which become spindle-knots after evaporation of the solvent. [84] As mentioned before, the driving force behind the Plateau-Rayleigh instability is that liquids tend to minimize their surface area due to their surface tension. [34] Using the dip-coating method, only a short length of fibers can be treated in a single immersing-in/drawing-out operation [85]. Therefore, a fluid-coating process suitable for large-scale production has been developed as an alternative [85]. In the fluid-coating method (Fig. 2.18 (b)), a fiber is conveyed through two capillary tubes to pass through a reservoir that contains a polymeric coating solution. The fiber is steadily pulled out of the reservoir by a motor from the other side. The subsequent processes of breaking the polymer solution film and forming the periodic spindle-knots are the same as in the dip-coating method. [84,85,91] The methods of obtaining spindle-knotted structured fibers are not limited to the Rayleigh instability phenomenon. For instance, wet-assembly is also a technique to design spindle-knotted fibers [129]. Fig. 2.18 (c) shows the fiber covered with

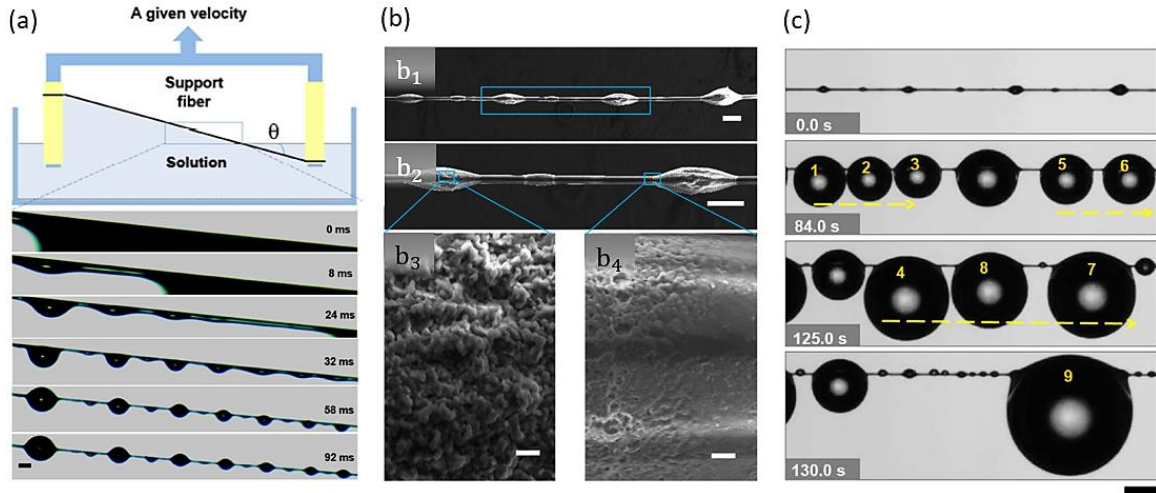
nanoparticles that is placed in a humid environment. Tiny droplets start to condense on the nanoparticles and will coalesce with each other. Using the energy of droplet coalescence, the nano-particles can self-assemble to form ordered spindle-knots. Beyond these techniques, microfluidic technology inspired by the real silk-spinning process of natural spiders, has been developed as another continuous fabrication technique. [84,91] In Fig. 2.18 (d), an alginate/salt solution is fed into a channel at a high feeding rate for forming a spindle-knot, while an alginate solution is fed into another channel at a low feeding rate to form the main fiber. By modulating and alternately opening/closing the valve operation of two channels, a porous spindle-knot/joint structure is obtained after removing the salt component by dissolution. [84,91]



**Fig. 2.18 Fabrication techniques for creating the spindle-knotted fibers [84,85,91];**  
**(a)** Dip-coating, **(b)** fluid-coating, **(c)** wet-assembly, and **(d)** microfluidic technique.

Application of the above methods and of various polymeric solutions, such as polyvinyl acetate (PVAc), polymethyl methacrylate (PMMA), polystyrene (PS), polyvinylidene fluoride (PVDF), polyvinyl alcohol (PVOH), and polydimethylsiloxane (PDMS), led to a variety of spindle-knotted fibers. [32,93,130–136] Compared with fibers without spindle-knots, all these spindle-knotted fibers with bionic origins could significantly increase the efficiency of water collection. Additionally, they were improved by regulating micro/nanostructures, surface energies, spindle size, etc. It turned out that fibers with the same spindle-knot size were limited in long-distance and large-scale transport of collected droplets to generate sufficiently large droplets, resulting in a delay in droplet detachment from the fiber surface. To combat this deficiency, *Chen et al.* (2013) improved the classic

dip-coating process and used tilt-coating to produce bionic fibers incorporating the multi-sized spindle-knots. Fig. 2.19 (b<sub>1</sub>- b<sub>2</sub>) shows the SEM images of spindle-knotted fibers with multi-gradient sizes and the zoomed images show the roughness gradient that forms from the center region (b<sub>3</sub>) to the side region (b<sub>4</sub>) of the spindle-knot. Fig. 2.19 (c) demonstrates the water collection functionality by exploiting the long-distance and large-scale transport behavior, realizing the generation of large droplets and an improved collection efficiency due to the different capillary forces produced by different-sized spindle-knots. [32,93]

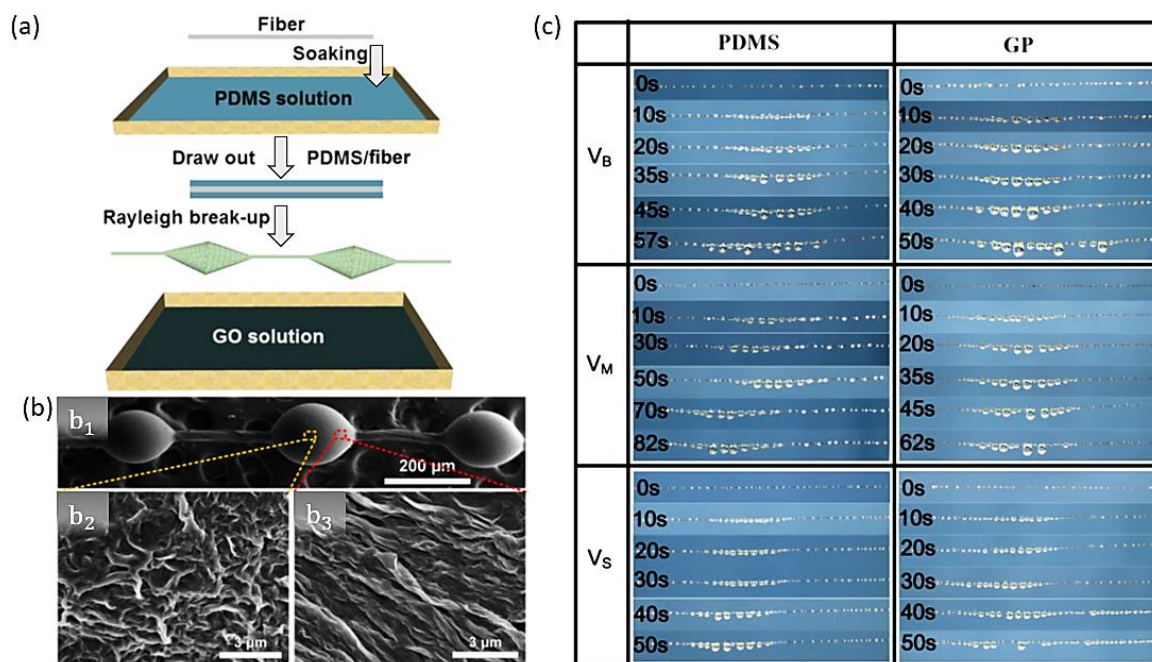


**Fig. 2.19 Bioinspired fibers with gradient spindle-knots, tilt-angle dip-coating method [93];** (a) Scheme showing the production of bio-inspired spindle-knotted models by the tilt-angle dip-coating method. A nylon fiber (18  $\mu\text{m}$ ) is fixed on a support and inserted into a polymer solution (PVDF in Dimethylformamide (DMF)) at a specific speed, (b) SEM images of spindle-knotted fiber with multi-gradient size, (c) water collection with long-distance transport behavior. Scale bars: 200  $\mu\text{m}$  (a), 100  $\mu\text{m}$  (b<sub>1</sub> and b<sub>2</sub>), 1  $\mu\text{m}$  (b<sub>3</sub> and b<sub>4</sub>), 500  $\mu\text{m}$  (c).

In another study *Song et al.* [94] applied the twice dip-coating process to fabricate another series of multi-level bio-inspired GO/PDMS (GP) fibers combining polydimethylsiloxane (PDMS) and graphene oxide (GO) (Fig. 2.20 (a)). The SEM images in Fig. 2.20 (b) show the structural feature of GP spindle-knots. By controlling the drawing velocity, they could fabricate spindle-knotted fibers with different spindle-knot sizes: big, medium, and small, labeled  $V_B$ ,  $V_M$ , and  $V_S$  in Fig. 2.20 (c), respectively. They showed that, compared to pristine PDMS spindle-knotted fibers, the movement of water droplets and eventually a much stronger hanging-drop ability (longer TCL) could be achieved effectively for GP spindle-knots (Fig. 2.20 (c)). In addition to the wettability and Laplace force gradients defined in (2.21) and (2.22), they considered the released surface energy ( $\Delta E$ ) during the coalescence process of the droplets merging along the spindle-knots as another driving force.

$$\Delta E = \gamma_{lv}\Delta A_{lv} + \gamma_{sl}\Delta A_{sl} + \gamma_{sv}\Delta A_{sv} \quad (2.31)$$

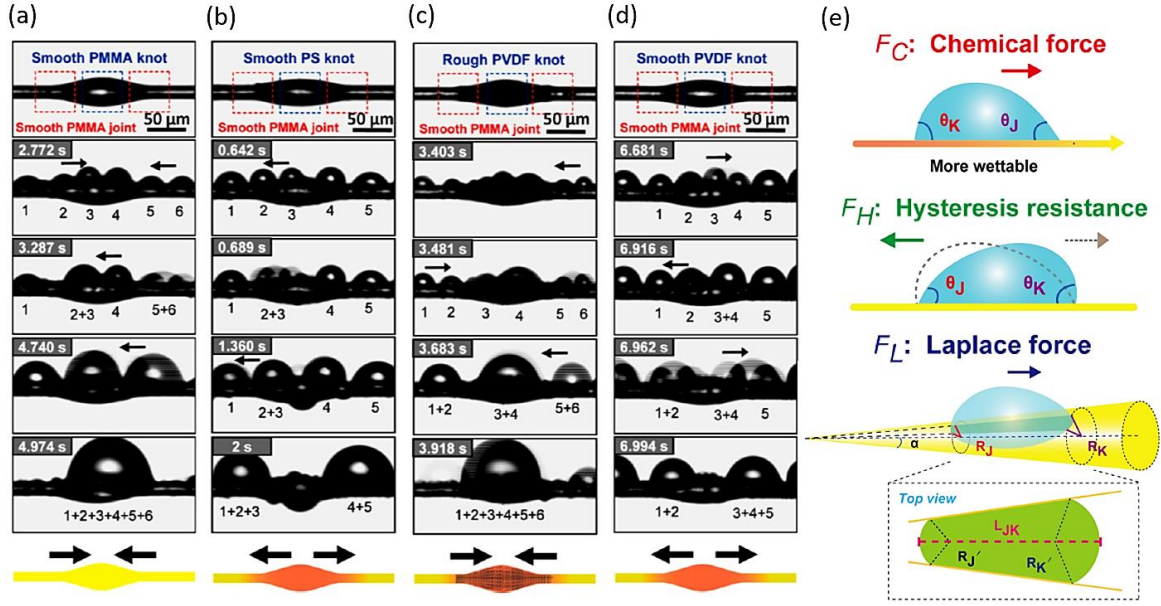
where,  $\gamma$  is the surface tension and  $\Delta A$  refers to the variations of the area of the liquid-vapor ( $lv$ ), the solid-liquid ( $sl$ ), and the solid-vapor ( $sv$ ) interfaces.



**Fig. 2.20 Bioinspired fibers with multi-level spindle-knots, twice dip-coating method [94];** (a) The schematic showing the bio-inspired spindle-knotted models fabricated by twice dip-coating method, in which a carbon fiber was inserted at a specific rate into PDMS and GO solutions, respectively, (b) SEM images of the GP spindle-knots with roughness gradient from center to side region of spindle-knot, (c) water collection behavior on PDMS and GP spindle-knots of different spindle-knot sizes.

Generally speaking, water droplets on natural and ordinary bio-inspired synthetic spindle-knotted fibers have been found to move directionally from joints to spindle-knots. In a unique study by *Bai et al.* [114], the special spindle-knotted fiber models were fabricated by changing the chemical composition and optimizing the cooperation of curvature, chemical, and roughness gradients on the fiber surfaces. In these models, the directional movement of droplets from joints to spindle-knots as well as the inversive motion of water droplets, i.e. movements from spindle-knots to joints, were realized. Fig. 2.21 (a-d) show the fabricated spindle-knot models with all joints covered with smooth PMMA, but with spindle-knots of different compositions: (a) smooth PMMA, (b) smooth PS, (c) rough PVDF, and (d) smooth PVDF. When these models were placed in the same fog stream, spindle-knots made of smooth PMMA and rough PVDF directed the droplets from joints toward the center of spindle-knots (Fig. 2.21 (a) and (c)). In contrast, droplets on models made of smooth PS and PVDF were propelled in the reverse direction, that is, from spindle-knots towards the joints (Fig. 2.21 (b) and (d)).





**Fig. 2.21** In situ observation of moving tiny water droplets with controllable direction on synthetic spider silk [114];

(a-d) The bio-inspired spindle-knotted models with various characteristic exerting a directional movement on droplets from joints to spindle-knots ((a) and (c)) or vice versa ((b) and (d)), (e) the different forces acting on the moving droplet on the spindle-knot model.

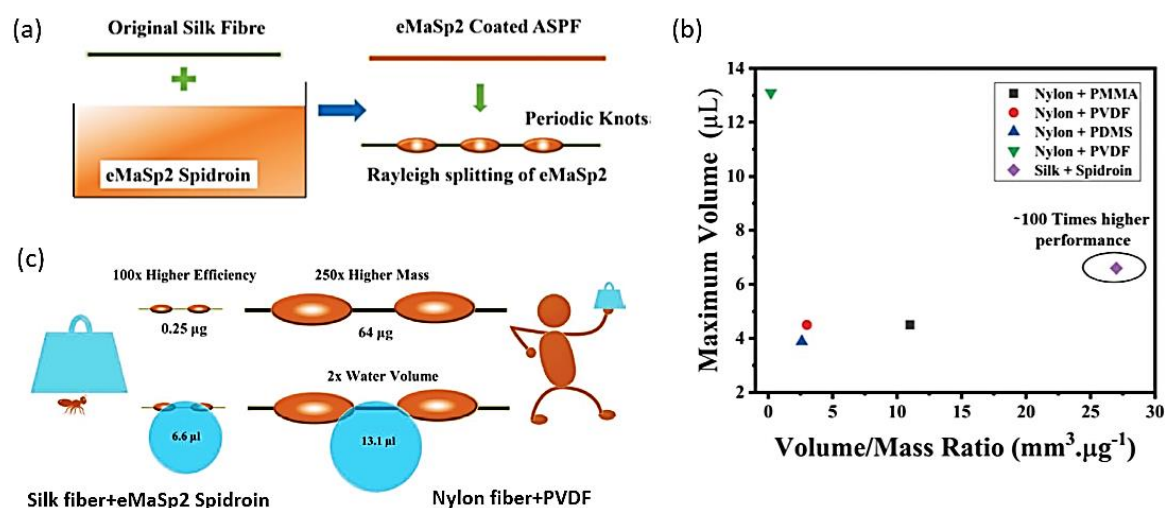
Bai *et al.* (2010) have then determined a model (2.32) incorporating the comprehensive forces arising from the chemical gradient ( $F_C$ ), contact angle hysteresis ( $F_h$ ), and Laplace pressure gradient ( $F_L$ ), to predict the direction of water droplets on a prepared spindle-knotted fiber (Fig. 2.21 (e)).

$$\begin{aligned}
 F_{total} &= F_C - F_h - F_L \\
 &\approx \pi R_0 \gamma_w (\cos \theta_j - \cos \theta_k) \\
 &\quad - \pi R_0 \gamma_w [(\cos \theta_{rj} - \cos \theta_{aj}) - (\cos \theta_{rk} - \cos \theta_{ak})] \quad (2.32) \\
 &\quad - \gamma_w \left( \frac{1}{R'_k} - \frac{1}{R'_j} \right) \frac{\sin \alpha}{R_k - R_j} \frac{4}{3} \pi \left( \frac{R_0}{2} \right)^3
 \end{aligned}$$

where  $R_0$ ,  $\gamma_w$ , and  $\alpha$  are the droplet radius, the surface tension of water, and the half-apex angle of the spindle-knot model, respectively.  $\theta_i$ ,  $\theta_{ri}$ , and  $\theta_{ai}$  are the local static, receding, and advancing contact angles, respectively.  $R_i$  and  $R'_i$  are the local radius and local curvature of the contact lines of the drop. Substitution of the index  $i$  with  $j$  and  $k$  refers to the joint and spindle-knots positions, respectively. They interpreted that when  $F_{total} < 0$ , drops are driven toward the spindle-knot, and when  $F_{total} > 0$ , drops are driven away from the spindle-knot. [84,114]

Distinct from developing spindle-knotted fibers from synthetic polymers, Venkatesan *et al.* [83] were inspired to develop a novel spindle-knotted fiber made of natural sources, that is, an all silk-protein fiber (ASPF). Fig. 2.22 (a) demonstrates schematically the dip-coating

procedure, in which a main body consisting of *B. mori* degummed silk was coated with recombinant engineered major ampullate spidroin 2 of spider dragline silk. As Fig. 2.22 (b) shows, such spindle-knotted fibers collect a maximum water volume of 6.6  $\mu\text{L}$  and has 100 times higher water collection efficiency compared to the best performing spindle-knotted nylon fiber. Fig. 2.22 (c) sketches the comparison of water collection functionality between them. Such an extremely high water collection efficiency was attributed to the synergistic effect of the geometric structure and hydrophilicity of silk protein materials.



**Fig. 2.22 An all silk-protein fiber (ASPF), dip-coating method [83];**

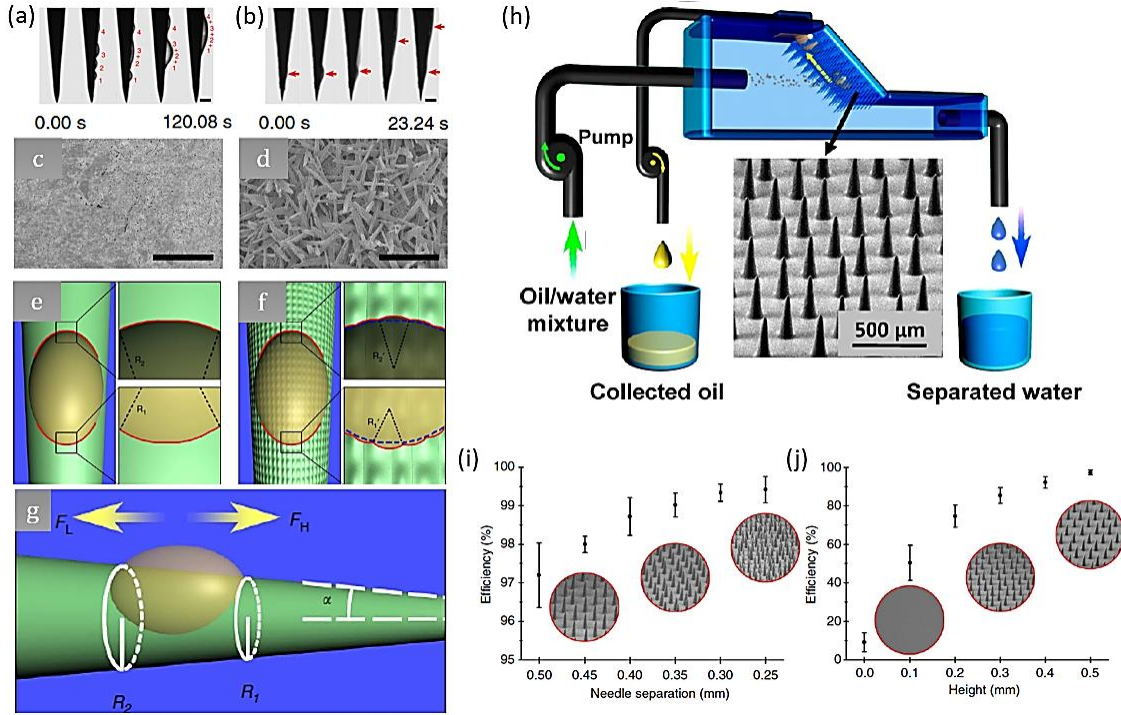
(a) Schematic drawing showing the preparation procedure of spindle-knotted fibers made of natural sources (ASPF), (b) the maximum volume as a function of the volume-to-mass ratio for the ASPF and various artificial spindle-knotted fibers, (c) schematic representation of a comparison of water collection performance between ASPF and the best performing nylon fiber.

## 2.6.2 Liquid-liquid separation

The previous section reported studies focusing on the fabricated structured surface, either conical or spindle-knotted, with wide application in the air-water-solid three-phase system. This section considers the directionally-controlled transport of liquids in a second liquid phase, specifically the water-oil-solid three-phase system, and summarizes the structures, the theoretical models, and the experimental and visual efforts developed so far.

*Li et al.* [78], one of the pioneering research groups in this field, showed that, inspired by the collection of tiny water droplets on conical cactus spines in nature, the oleophilic conical needle structures could collect similar-sized oil droplets ( $< 10 \mu\text{m}$ ) from the emulsion. Accordingly, the whole process of oil collection can be described in three phases; deposition, growth, and self-driven motion from the tip to the base of the needle for convergence at the upper edge of the conical needle. They utilized electroetching and the template method to fabricate single cones made of copper (Cu) and conical needle arrays made of PDMS, respectively. Fig. 2.23 (a) and (b) show the functionality and Fig. 2.23 (c)

and (d) show the SEM images of smooth and rough single copper cones, respectively. Micrometer-sized oil droplets on individual needles slowly moved towards the base on the smooth Cu cone, on the rough Cu-based needles, however, they moved to the base very quickly. The difference between these two phenomena arises from the increased oleophilicity caused by the surface roughness when the droplets are in the Wenzel state (described in 2.2.1). Therefore, apart from oleophilicity and a conical structure, they found roughness as a key factor for continuous oil collection.



**Fig. 2.23 Structured conical models for continuous and effective collection of micron-sized oil droplets from water [78,84];**

(a) In situ observation of the oil collection process on the smooth Cu cone, (b) in situ observation of the oil collection process on the rough Cu cone, (c) SEM image of the smooth Cu cone, (d) SEM image of the rough Cu cone, (e) TCL indication on the smooth Cu cone, (f) TCL indication on the rough Cu cone, (g) acting forces on the oil droplet moving along a cone, (h) schematic of the oil collection set-up, (i) and (j) oil collection efficiency of PDMS needle arrays as a function of the cone's density on the surface and cone's height, respectively.

Here, gravity and buoyancy forces were neglected and it was conjectured that the droplets were subjected only to the Laplace force  $F_L$  and the hysteresis resistance force  $F_H$  as [78,84]

$$F_L \approx (\gamma_w - \gamma_o) \left( \frac{1}{R_1} - \frac{1}{R_2} \right) \frac{\sin 2\alpha}{R_2 - R_1} \Omega \quad (2.33)$$

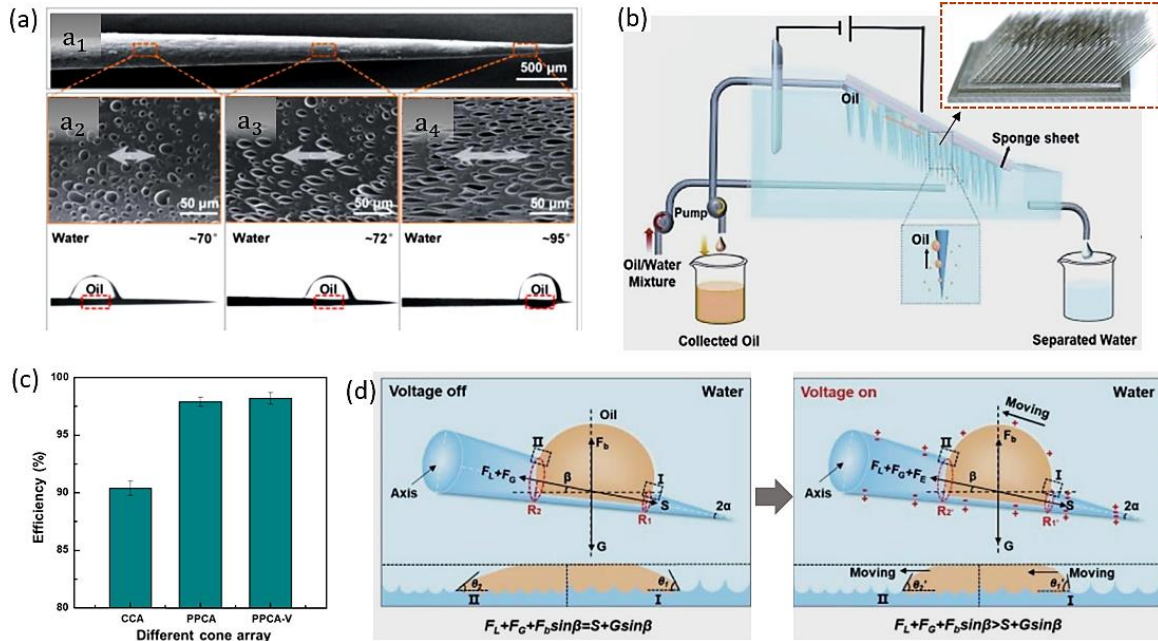
$$F_H \approx \pi R_0 (\gamma_w - \gamma_o) (\cos \theta_r - \cos \theta_a) \quad (2.34)$$

where,  $\gamma_w$  and  $\gamma_o$  are the surface tension of water and oil, respectively, and  $(\gamma_w - \gamma_o)$  is the interfacial tension between them.  $\alpha$  is the half-apex angle of the cone.  $\theta_r$  and  $\theta_a$  are the contact angles at the rear and front side of the oil droplet, respectively.  $R_0$  and  $\Omega$  are the radius and the volume of the oil droplet, respectively.  $R_1, R_2$  are the local radii of the oil-water-solid three-phase contact line at two opposite sides of the oil droplet, respectively. As shown in Fig. 2.23 (e) and (f), the rough needle leads to smaller initial radii for the driven droplets ( $R'_1 < R_1$  and  $R'_2 < R_2$ ). This results in the Laplace pressure on the rough surface ( $\Delta P'$ ) being larger than the Laplace pressure on the smooth surface ( $\Delta P$ ). Fig. 2.23 (g) shows the forces acting on the oil droplets. To see the functionality of the cone assembly, they fabricated a PDMS cones array and then evaluated it in terms of oil-in-water separation efficiency in the designed set-up, as depicted in Fig. 2.23 (h). They considered the various design factors such as the density of the cones (Fig. 2.23 (i)) on the surface and the height of the cones (Fig. 2.23 (j)) and observed that an increase in both factors brings an advantage to the increase of the efficiency.

According to the results of *Li et al.* [78], *Yan et al.* [25] demonstrated a new strategy for highly efficient directional collection of underwater oil droplets on conical models. They believed that hysteresis forces impede the efficient collection and directional movement of oil droplets under water and it could be mitigated by using an external stimulus, here an electric field. They first electro-etched the copper wires and prepared the copper cone array (CCP). Next, they vertically coated the prepared conical models in a 6 wt% PS in Tetrahydrofuran (THF) solution at a speed of  $30 \text{ mm min}^{-1}$  with a relative humidity of 65%. Thereby, the hydrophobic/oleophilic porous gradient PS-coated cone array (PPCA) was produced, a single cone of which is shown in Fig. 2.24 (a). SEM images in Fig. 2.24 (a2-a4) depict the porous gradient and its elongation direction from base to tip of the conical model with an apex angle of  $2^\circ$ . It can be seen that the underwater oil contact angle (wettability) is also different at positions with different porous gradient.

It turned out that the cone apex angle is crucial for the transport process of oil droplets under water. For this, the conical models were prepared with three different apex angles of  $2^\circ, 4^\circ,$  and  $6^\circ$  and it was seen that an oil droplet ( $3 \mu\text{L}$ ) moved on them at speeds of about  $3.82, 2.14,$  and  $1.17 \text{ mm s}^{-1}$ , respectively. Based on these results, they concluded that small tip angles are beneficial for fast movements.





**Fig. 2.24** Electric field-assisted collection of micron-sized oil droplets from water using the structured porous cone array [25];

(a) SEM images of a hydrophobic/oleophilic porous gradient PS coated cone array (PPCA), (b) schematic of the oil collection set-up supplied with electric-field, (c) the oil collection efficiency for each cone array, (d) a schematic diagram of the mechanism of electric field-assisted directional transport of oil droplets on the porous cone.

Additionally, they considered the effect of water buoyancy on the movement of an oil droplet by positioning the cones at various tilt angles ( $\beta$ ) of  $0^\circ$ ,  $-45^\circ$ ,  $-90^\circ$ ,  $45^\circ$ , and  $90^\circ$ . It was found that the droplets positioned at  $45^\circ$  and  $90^\circ$  did not move towards the base. In contrast, the oil droplets moved at speeds of 2.14, 2.91, and  $5.58 \text{ mm s}^{-1}$  when the tilt angles were  $0^\circ$ ,  $-45^\circ$ , and  $-90^\circ$ , respectively.

They carried out oil-in-water separation experiments using the set-up shown in Fig. 2.24 (b), which was similar to the set-up in Fig. 2.23 but supplied with an electric field. As Fig. 2.24 (c) demonstrates, the collection efficiency results were about 90.4%, 97.9%, and 98.2 % for CCP, PPCA, and PPCA-V (porous gradient PS-coated cone array with an applied voltage), respectively. They modeled the mechanism of the underwater oil droplet directional movement on the porous PS within the following formula

$$F_L + F_G + F_b \sin \beta = S + G \sin \beta \quad (2.35)$$

where  $F_b$  is the buoyant force defined in equation (2.1).  $S$  and  $G = Mg$  are stiction (friction force) on the porous PS surface and gravity force, respectively.  $F_L$ ,  $F_G$  are Laplace force and unbalanced force generated by the porous surface, respectively. Approximate expression for  $F_L$  and  $F_G$  are given as equations (2.33) and (2.36), respectively.

$$F_G = \int_S^L \gamma_{ow} (\cos \theta_L - \cos \theta_S) dl \quad (2.36)$$

where  $\gamma_{ow}$  is the interfacial tension between oil and water and  $\theta_L, \theta_S$  are the contact angles of the oil droplet on the large pore and small pore areas, respectively, and  $dl$  is the corresponding length of the oil droplet on the gradient surface. if an electric field is used, the electro-capillary pressure force ( $F_E$ ) should also be considered:

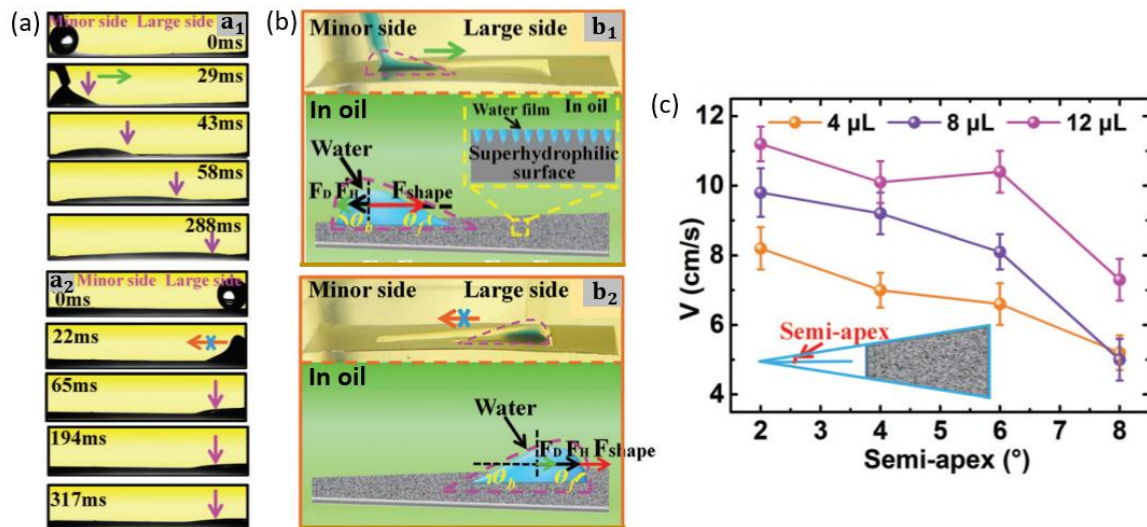
$$F_E = \frac{l}{A} \frac{1}{2} \frac{\epsilon_0 \epsilon_1}{d} (V - V_T)^2 \quad (2.37)$$

where  $l$  is the pore circumference and  $A$  is the cross-sectional area of the pore.  $\epsilon_0$  and  $\epsilon_1$  are the permittivity of vacuum and the dielectric layer.  $d$  is the thickness of the dielectric layer.  $V$  and  $V_T$  are the applied and threshold voltage ( $\sim 120$  V), respectively. They showed that experiments where PPCA-V was used (that is, when exploiting an electric field), apart from the cooperative effects of a Laplace pressure gradient, a porous microstructure gradient, and a buoyant force, underwater oil droplets moved towards the base of the cone more efficiently. Fig. 2.24 (d) shows schematically the mechanism of the oil droplet directional transport without/with electric field, respectively.

As another structured solid model for directionally-controlled transport of liquid in the second liquid phase, *Wu et al.* [46] have developed a superhydrophilic shape-gradient stainless-steel platform with nanoparticle coating using femtosecond laser direct writing technology. In contrast to the research works that depend on external energy supplies and impart directional movement to droplets, they believed that the priority must be given to the development of structural surfaces, which do not rely on external energy input. As Fig. 2.25 (a<sub>1</sub>) shows, the trapezoidal platform can spontaneously and directionally transport the under-oil water droplet from the minor to the large side of the surface. While Fig. 2.25 (a<sub>2</sub>) shows that the positioned droplet on the large side could not move directionally toward the minor side of the surface. Fig. 2.25 (b) shows the forces acting on the under-oil water droplet when positioned at minor (b<sub>1</sub>) or large side (b<sub>2</sub>). Here, the geometry-gradient driving force ( $F_{shape}$ ), the hysteresis resistance force ( $F_H$ ), and the drag resistance force of oil ( $F_D$ ) are the three governing forces for the movement of the water droplet. The resulting total force amounts then to

$$\begin{aligned} F &= F_{shape} + F_H + F_D \\ &= \gamma_o l_{TCL} (\cos \theta_f - \cos \theta_b) + \gamma_o l_{TCL} (\cos \theta_r - \cos \theta_a) \\ &\quad + \frac{1}{2} C_D \rho v^2 A \end{aligned} \quad (2.38)$$

where,  $\gamma_o$  is the surface tension of oil,  $l_{TCL}$  is the length of the three-phase line of contact.  $\theta_f$  and  $\theta_b$  are the front- and rear-side under-oil water contact angle, and  $\theta_r$  and  $\theta_a$  are receding and advancing under-oil water contact angle.  $C_D$  and  $\rho$  are the drag coefficient and density of oil, respectively, and  $v$  and  $A$  are the transport velocity and cross-sectional area of water, respectively. They assumed that due to the superwettability characteristic of the prepared material the  $\theta_r$  and  $\theta_a$  can be taken as  $0^\circ$ , therefore the hysteresis force can be considered to be close to zero ( $F_H \approx 0$ ). They have studied the effect of the trapezoid half-apex angle, the tilt angle of the platform, and the volume of the water droplet on the droplet transportation velocity from the minor to the large side. Fig. 2.25 (c) shows the dependency of the transportation velocity on the half-apex angle and the droplet volume. It was observed that the velocity of transportation decreased with increasing the half-apex angle and the increase in the water droplet volume led to the increase in transportation velocity. Experimental results also showed that the increase in the tilt angle of the platform led to a significant decrease in the velocity. Applying the same procedure of femtosecond laser scanning on the different materials showed that the capacity of trapezoidal geometry-gradient platform for self-driven and directional transport of water in oil is independent of substrate materials.



**Fig. 2.25** Directional transport of under-oil water droplet on the trapezoidal platform surface [46];

(a) Directional movement of a water droplet from the minor to the large side (a<sub>1</sub>) and the water droplet released on the large side with no directional movement towards the minor side (a<sub>2</sub>), (b) a schematic representation of the movement mechanism for water droplets released on the minor (b<sub>1</sub>) and large side (b<sub>2</sub>), (c) a diagram showing the water transport velocity released on the minor side as a function of the half-apex angle of the trapezoidal platform and the droplet volume.

## 2.7 Electrospun spindle-knotted fibers

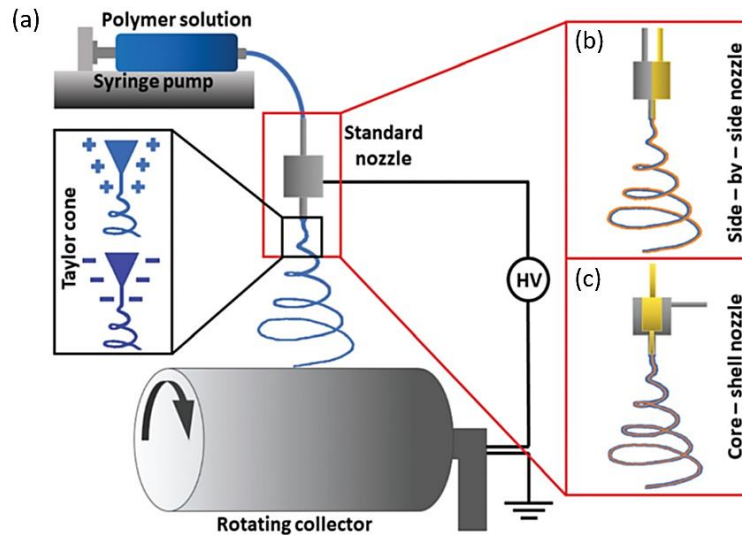
In the previous two sections, several fabrication techniques were presented that have been successfully devised to engineer structured solid models with unprecedented capability to separate liquid droplets from gases and liquids by exploiting the directional collection of droplets. It is known that fiber networks achieve a larger scale of droplet collection compared to individual fibers under the same conditions. The fabrication methods described so far for the production of spindle-knotted fibers such as dip-coating, fluid-coating, microfluidic, etc. are very limited for a large-scale (mass) production [22,26,91,96]. Therefore, the focus should be given to one of the most promising fabrication methods by which the network of spindle-knotted fibers can be fabricated in running meters, in the frame of the filter medium/membrane.

In competition with existing nonwoven fabrication methods such as melt-blowing, spunbond, etc., electrospinning is an effective avenue and is generally considered to be a versatile and effective method of manufacturing nanofibers with controllable morphologies and compositions. [1,12,13,137–139] Specifically, the electrospun nanofibers have become a promising versatile platform for the separation of oil/water mixtures and emulsions owing to low basis weight, high porosity, interconnected nanoscale pore structures, high permeability, high surface-to-volume ratio as well as their diameter of up to 10-100 times smaller than conventional meltblown microfibers. [1,4,13,140,141]

Electrospun fibers used in filtration have been mass-produced for at least three decades. The production of fibers by electrospinning is relatively economical and efficient. Only the purchase of an electrospinning pilot plant based on either a multi-nozzle system or a nozzle-free system is relatively expensive. Moreover, the cost of mass production depends on the type and price of selected polymers and solvents used. Therefore, the cost of manufacturing filter media for filtration applications could be reasonable if the usual electrospinning system and commonly used polymers are selected. [86]

In electrospinning, electrostatic forces are used to draw charged threads from a polymer solution to create fibers with diameters ranging from several microns down to tens of nanometers [8,13]. The electrospinning system includes three main components: a high-voltage power supply, a nozzle, and a grounded collector [8]. As shown in Fig. 2.26 (a-c), based on the nozzle type including the standard, side-by-side, and core-shell (coaxial), the electrospinning process can be carried out in a wide variety of modes [86]. The basic principle of electrospinning is that the polymer solution forms a liquid drop at the end of the needle under high electrostatic voltage. As the voltage increases, the shape of the droplet gradually changes to form a tiny conical droplet (Taylor cone). In parallel, there is competition between the viscous resistance, the surface tension, and the electrical field strength that the polymer solution suffers. When the electric field force reaches a certain

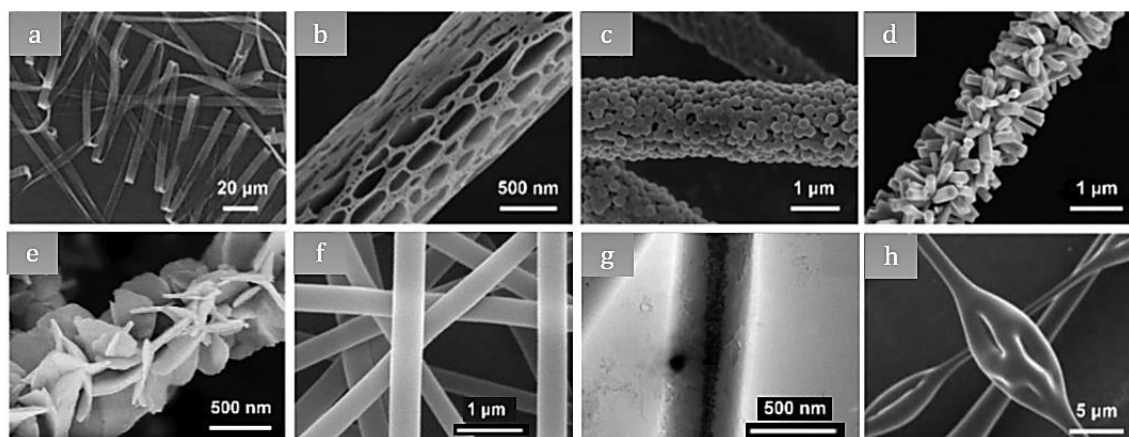
critical value, the liquid drops overcome the surface tension and the viscous resistance. Then the droplets of the polymer solution are ejected from the needle tip, and after evaporation of the solvent, fibers are solidified and deposited on a grounded collector. [8,86,137]



**Fig. 2.26 Schematic of an electrospinning system with different nozzle systems [86];**  
**(a)** Standard nozzle, **(b)** side-by-side nozzle, **(c)** core-shell nozzle system.

The processing flexibility of electrospinning allows fibers to be produced from a wide variety of materials including polymers, ceramics, carbons, and even hybrid compounds. Among different materials, various polymer membranes comprising the interweaved nanofibers have been fabricated by electrospinning the polymeric solution such as PVDF, PS, PMMA, polyacrylonitrile (PAN), etc. This facile technique also yields nanofiber membranes with different structures including nanotextures on individual nanofibers and spatial arrays of nanofibers. [8]

Due to the chaotic nature of electrical instability, electrospinning is classified as a technique for fabricating surfaces with random roughness, meaning the average roughness can be tuned but the detailed structures are not exquisitely controlled [26]. Nevertheless, as shown in Fig. 2.27, the various structures (morphology) of individual nanofibers can be obtained such as ribbon, porous, nanosphere protrusion, nanorod protrusion, nanosheet protrusion, cylindrical with smooth surface, core-shell structure, and bead-on-string (spindle-knot) [8,142].



**Fig. 2.27** Fibers with different morphological structures, obtained by electrospinning [8,142]; (a) ribbon, (b) porous, (c) nanosphere protrusion, (d) nanorod protrusion, (e) nanosheet protrusion, (f) cylindrical with smooth surface, (g) core-shell structure, (h) bead-on-string (spindle-knot).

Among the various structures presented in Fig. 2.27, the electrospun spindle-knotted fibers with the beads-on-string structure were thought to be an unwanted by-product having adverse properties and were generally discarded and to be avoided as far as possible [96]. Nevertheless, recently they have attracted attention as they are viewed as having the structure of periodic knots, which resembles the shape of natural spider silk to some extent and therefore can offer promising applications in many areas including tissue engineering, drug delivery, and air/water filtration.

Factors influencing bead-on-string fiber formation can be discussed from three main aspects: surface tension, viscosity, and charge density of the spinning solution. Results of *Zuo et al.* [143] and *Fong et al.* [144] showed that greater surface tension of the polymer solution was more likely to result in spindle-knotted structured fibers. This is because the surface tension of the polymer solution tries to achieve a smaller surface-to-mass ratio by shrinking the jet into a sphere. Therefore, when the jets break, this increases the Rayleigh instability and the formation of spindle-knotted structured fibers. Overall, the viscosity of the polymer solution had also an important influence on the formation of spindle-knotted fibers, which can be inhibited by increasing the viscosity of the polymer solution. Therefore, increasing the viscosity of the solution makes the beading less likely. A higher charge density reduces the possibility of beading, as well. [137]

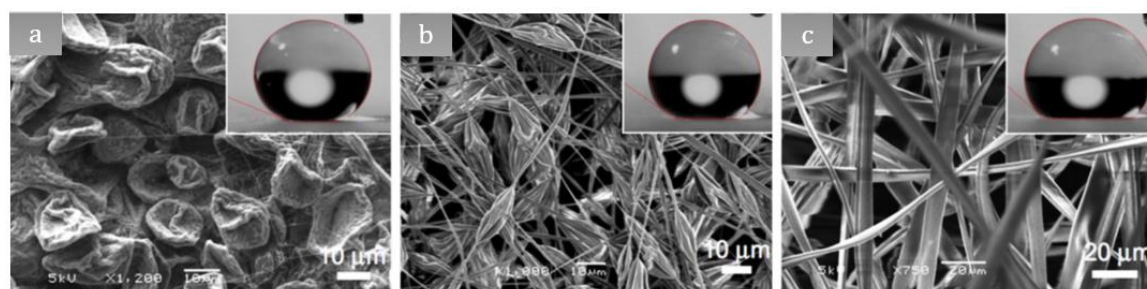
In addition, it is known that the collecting distance, spinning rate, and solvent evaporation rate can also affect the formation of beads. The collecting distance is characterized by the distance from the nozzle to the collecting plate. When the motion and movement time of the jet and the time for solvent evaporation become longer in the electric field, the number of beads decreases and the diameter of beads becomes smaller. Meanwhile, the increase of collecting distance reduces electric field force to weaken stretch jet suffered, which is favorable to decreasing number of beads. [137,145] The faster the jet moves, the shorter



the jet's residence time in the air. On the one hand, molecular chains of the polymer solution cannot draw enough under electric field strength, on the other hand, there is no time to fully evaporate the solvent, thereby forming the bead-on-string fibers. Environmental parameters including temperature, humidity, and air velocity can also affect the formation of bead-on-string fibers, however, the effect of environmental factors on spinning is not easy to control and adjust. Therefore, keeping the external environmental factors stable and not interfering with the movement of the jet process is also important. [137,146]

Despite knowledge of the foregoing factors, to the best of our knowledge, no systematic modeling and fundamental research have been developed so far to theoretically study, predict, and describe the mechanism of bead-on-string fiber formation. Therefore, as applications of bead-on-string fibers increase, it is hoped that the morphology and number of bead-on-string fibers can be precisely controlled to achieve specific applications.

*Tuteja et al.* [30] found that one approach to modifying the surface texture of the electrospun membrane fibers could be achieved by varying the concentration of the polymer solution. To do this, using a custom-built electrospinning device, they fabricated electrospun mats applying varying concentrations of PMMA plus fluorodecyl POSS in a common solvent, Asahiklin AK-225. The key operational parameters were as  $0.04 \text{ ml min}^{-1}$ , 25 cm, and 20 kV for the flow rate, plate-to-plate distance, and voltage, respectively. Using the concentrations of 2, 5, and 7.5 wt% results in different morphologies of the beads-only (Fig. 2.28 (a)), the beads-on-strings (b), and the fibers-only structure (c), respectively.

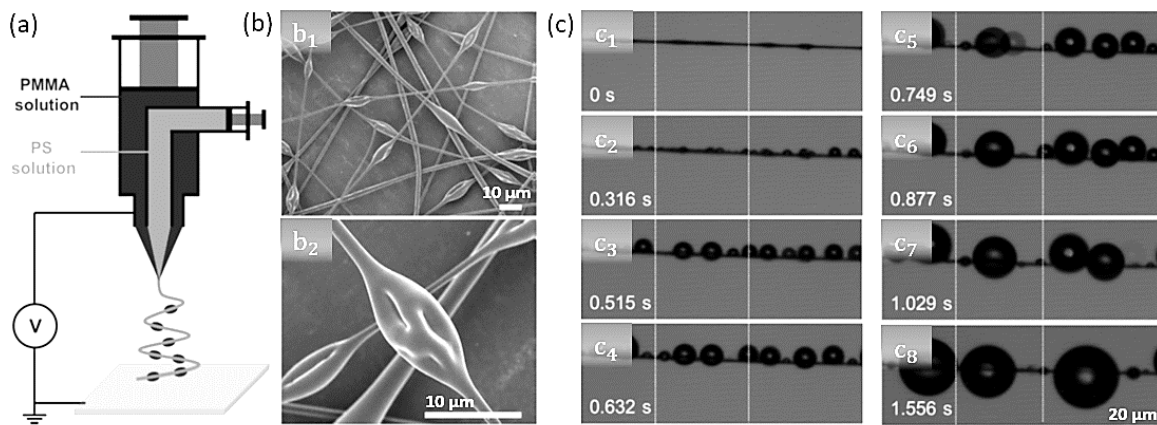


**Fig. 2.28 Controlling the morphology of electrospun surfaces by varying the polymer concentration [30];**

**(a-c)** SEM images of the electrospun mat prepared by 2, 5, and 7.5 wt% PMMA+ fluorodecyl POSS in Asahiklin AK-225, respectively.

In another pioneering study, *Jiang et al.* (2012) employed the Rayleigh instability effect to generate spindle-knots on fibers using a coaxial electrospinning method, in which the electrospinning jet consisted of inside and outside channels as shown in Fig. 2.29 (a). They applied a dilute solution of PMMA as outer fluid, which could be electro-sprayed into micro-particles owing to Rayleigh instability. Meanwhile, a viscous solution of concentrated PS was chosen as the inner solution, which could be electrospun into

micro/nano-fibers. When a high-voltage electric field was applied, the viscous PS solution stretched and formed fiber and the PMMA solution flowed out with the inner solution and adhered to the PS thread. Due to low concentration and low viscosity, the PMMA solution film then broke into discontinuous liquid droplets and solidified into periodic spindle-knots on the PS fiber. After the complete volatilization, the PMMA-knotted PS fibers were obtained (Fig. 2.29 (b)). They found that the flow rates of the two solutions and the concentration of the dilute external solution markedly affected the morphology of the fibers, producing the fibers with random or spindle-shaped droplets to just uniform ones. Fig. 2.29 (c) shows the water collection functionality of a single electrospun spindle-knotted fiber. When fiber was placed in foggy air, tiny water droplets were collected on it and moved toward the spindle-knot. They were then coalesced and increased in size at the spindle-knot positions and as a result, the fiber could achieve an efficient water-collecting function. [84,91,96]



**Fig. 2.29 Coaxial electrospinning method [84,91,96];**

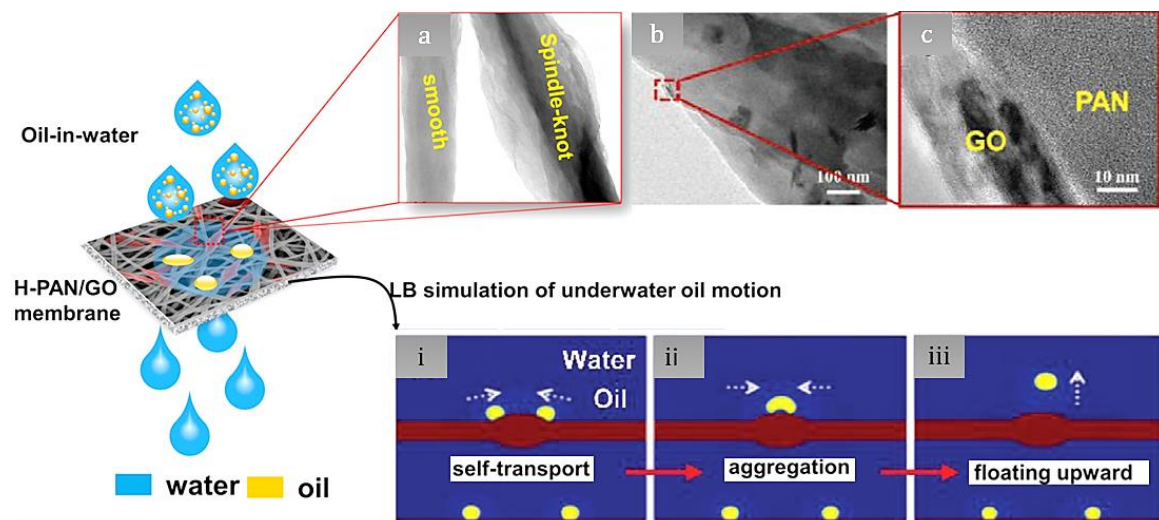
**(a)** Schematic of the coaxial electrospinning **(b)** SEM images of the electrospun spindle-knotted fibers containing PS fibers and PMMA spindle-knots, **(c)** fog collection experiment on the prepared electrospun fiber.

In the following, some studies explaining the progress of electrospun nanofiber membranes for the purification of emulsified oily wastewater are reported. *Zhang et al.* [147] prepared a bio-inspired superhydrophobic/superoleophilic membrane via electrospinning technology, in which silicon dioxide ( $\text{SiO}_2$ ) nanoparticles imitated the hydrophobic bio-wax and polycaprolactone (PCL) porous microspheres imitated the surface nano-protrusions of a lotus leaf [32]. This membrane was able to separate various oil-water mixtures efficiently and showed excellent recyclability. In another study, *Zhang et al.* [148] fabricated green and durable electrospun stereo complex polylactide (sc-PLA) membranes via green gallic acid-modified titanium dioxide ( $\text{TiO}_2$ ) coating. The membrane exhibited multifunctional oil/water separation with high separation efficiency and self-cleaning performance. Remarkably, such works have been done mostly to directly control the



surface wettability of electrospun fibrous membranes via the surface roughness modification e.g. to obtain superwetable membranes with selective separation. In addition, they mainly focused on general electrospun membrane performance in separating oil/water mixtures containing large oil droplets. Additionally, they did not focus on the thoughtful design in terms of fiber morphology and the benefit of membranes with structured fibers, specifically fibers with beads-on-string structure, which could enhance the separation efficiency of oil-in-water emulsions that contain very fine oil droplets.

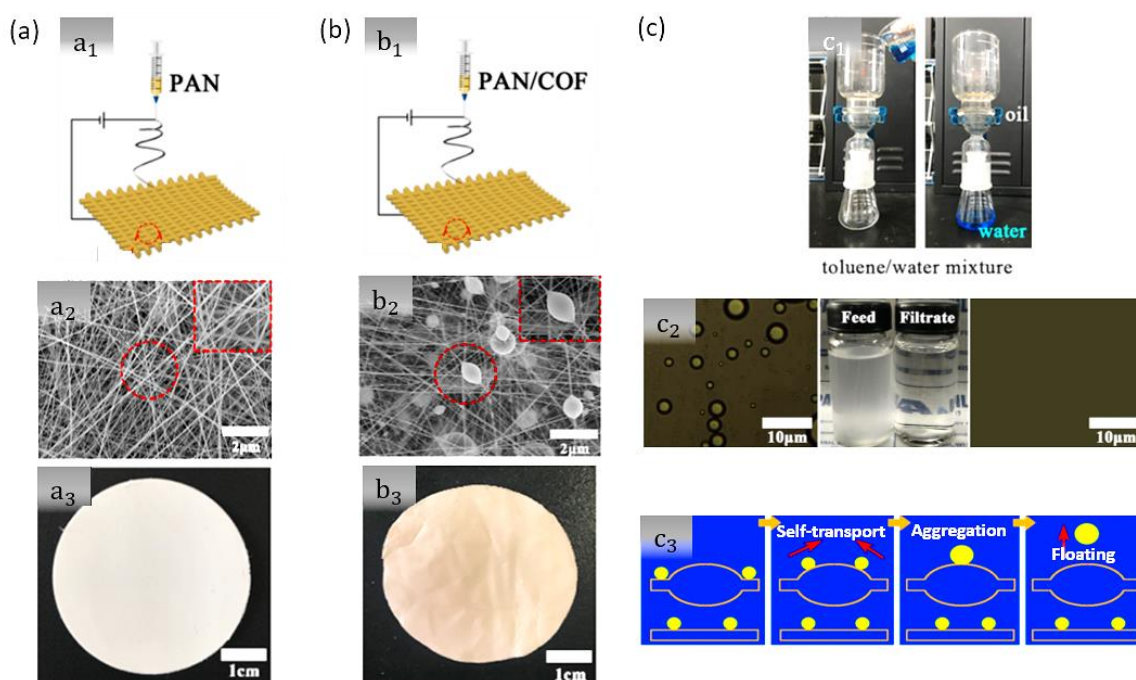
With this in mind, inspired by the directional water collection on spindle-knotted spider silk in nature, *Zhang et al.* [149] fabricated hydrolyzed polyacrylonitrile/graphene oxide (H-PAN/GO) nanofibrous membrane containing the structured fibers (Fig. 2.30). The membrane was composed of spider silk-like nanofibers by a combination of electrospinning of PAN/GO mixed solution and hydrolytic treatment with superhydrophilic and underwater oleophobic properties. The strong interfacial interactions of PAN and GO enabled the arrangement of polymer chains into ellipsoids, resulting in spindle-shaped structures on PAN/GO nanofibers (Fig. 2.30 (a-c)). Furthermore, as shown in successive images in Fig. 2.30 (i-iii), they demonstrated the mechanism of self-transport of oil along spindle-knotted fiber underwater by the Lattice Boltzmann method (LBM). Benefiting from the integrated features of spindle-shaped microstructures and selective wettability, the tiny oil droplets could move directionally towards the central position of the spindle-knot, aggregate into a large one, and float up. They believed that the H-PAN/GO fibrous membrane offers a novel insight into the fabrication of next-generation membranes for separating oil-water emulsions. [8,149]



**Fig. 2.30** Hydrolyzed polyacrylonitrile/graphene oxide (H-PAN/GO) nanofibrous electrospun membrane with oil/water separation [149];

(a) The microstructure of hybrid nanofibers, (b-c) spindle-knot structure at high magnification, (i-iii) successive images, showing the mechanism of the directional collection of oil droplets.

In another attempt, *Zhang et al.* [150] have developed another type of bioinspired electrospun nano-fibrous composite consisting of spindle-knotted fibers and capable of separating oil/water mixtures and emulsions. For this, they first electrospun the pristine PAN membrane as shown in Fig. 2.31 (a<sub>1</sub>). Fig. 2.31 (a<sub>2</sub>) and (a<sub>3</sub>) show the SEM and the optical images of the PAN membrane. From the SEM image, they observed that the pure PAN membrane had a smooth surface made of uniform cylindrical fibers. Next, they blended PAN with an additive made of COF-2,5-dihydroxyterephthalaldehyde (Dha) 1,3,5-Tris(4-aminophenyl)benzene (Tab) and electrospun COF-DhaTab/PAN nano-fibrous composite (Fig. 2.31 (b)). As shown in Fig. 2.31 (b<sub>2</sub>), they observed that the obtained composite membrane possessed the spindle-knotted fibers in an arbitrary state. As the optical images in Fig. 2.31 (a<sub>3</sub>) and (b<sub>3</sub>) show, they observed that the color of the membrane made of pure PAN was white, while the color of the COF-DhaTab/PAN composite membrane was in a light orange shade.



**Fig. 2.31 Electrospun PAN and COF-DhaTab/PAN nanofibrous membranes for oil/water separation [150];**

**(a)** Schematic of the electrospun pure PAN membrane preparation (a<sub>1</sub>), SEM image showing the uniform cylindrical fibers (a<sub>2</sub>), an optical image showing the white color of the membrane (a<sub>3</sub>), **(b)** schematic of the electrospun COF-DhaTab/PAN membrane preparation (b<sub>1</sub>), SEM image showing the spindle-knotted fibers (b<sub>2</sub>), an optical image showing the light orange color of the membrane (b<sub>3</sub>), **(c)** filtration device driven by gravity (c<sub>1</sub>), optical microscope images showing the oil droplet distribution in the feed and filtrate (toluene/water mixture) (c<sub>2</sub>), schematic representation of the mechanism of oil droplets accumulation and detachment from the spindle-knotted fibers (c<sub>3</sub>).

Furthermore, to evaluate the performance of the prepared composite membrane, they carried out an oil-in-water emulsion separation using a filtration device driven by gravity

as shown in Fig. 2.31 (c<sub>1</sub>). It was observed that the nanofibrous composite was able to separate the various kind of oil/water mixtures. Fig. 2.31 (c<sub>2</sub>) shows the sample optical microscope images of the toluene/water emulsion before (feed) and after (filtrate) filtration. The oil droplets could be detected in the feed, while no oil droplets were observed in the filtrate. They attributed this performance to the presence of spindle-knotted fibers, which exert directional movement on the captured oil droplets and therefore accelerate the aggregation and detachment (Fig. 2.31 (c<sub>3</sub>)).

## 2.8 Summary of the state-of-the-art

As described in chapter 1, the oil-in-water emulsion separation has received increasing attention in recent decades due to the ongoing adverse effects of oily wastewater on the environment and living beings. Among the conventional separation techniques, the filtration by nonwoven coalescer filter media turned out to be efficient for separating emulsified oil droplets and therefore was explained in detail in section 2.1. Besides the advantages of using them, it can often be observed that after a certain period of operation, the performance of the filter medium, a centerpiece of the filtration process, decreases and sooner or later the filter medium has to be rinsed, washed, or replaced. There are several reasons for this, a major one being mechanical blockage when the micro oil droplets in a dispersed phase overwhelm the pores of the filter medium due to the time-consuming stationary collection and coalescence. This occurrence is commonly referred to as fouling of filter media, which is detrimental to the function, and therefore a solution must be found to add value to them by preventing this side effect.

Prior to focusing on the efforts leading to finding the potential solution to this deficiency, section 2.2 introduced and defined the basic concepts of the main fundamental models that formed the basis of this study.

It turned out that the purposeful directional movement of droplets on the fibers has attracted great interest in the recent decade and may provide optimum solutions for increasing the performance of the nonwoven filter material in terms of accelerating coalescence and preventing pore-clogging. In this regard, nature has proposed new ideas for the development of functional surfaces, in particular the development of biomimetic fibers with superior surface functions that exert a directed movement on droplets. To illustrate this phenomenon, section 2.4 introduced the concepts of living systems present in nature, which are known to be capable to control the directional motion of liquid droplets on their surface by exploiting the gradients in surface wettability and geometry. Among the considered biological models, this study particularly focused on the directional water collection behavior of capture silk of cribellate spider with spindle-knotted structure (section 2.4.1). This effect was also seen on the conical spines of cactus plants, which represent a simplified model of spindle-knot structures and follow similar mechanisms of water collection. The

analysis of capture silk of cribellate spiders revealed a dynamic interaction between highly puffed elastic nanofibers and periodic spindle-knots with water droplets. To further elucidate the mechanism behind the directional water collection behavior by the wet-rebuilt spindle-knotted structured threads, a root cause analysis was performed in section 2.5. It was found that due to the Laplace pressure gradient generated by the structural and chemical gradients generated by the inhomogeneous surface energy and roughness, the water droplets move to the low-curvature and more wettable area along the spindle-knotted capture silk. It also turned out that to realize the directional droplet movement of droplets on spindle-knotted or conical models, the driving forces should surmount the resisting forces such as hysteresis force to accomplish the movement from one position to another position.

Based on the discovered fascinating structure-property relationships, considerable research efforts have been devoted to developing various methods and techniques to construct artificial materials with hierarchical features resembling these nature models. Indeed, all discoveries of intriguing structure-function relationships not only promoted the investigation of the theoretical bases of biomimetic surfaces but also provided important guidelines and design principles to mimic these natural structures and functionalities. To further explore the state-of-the-art, the pioneering and latest studies on bio-inspired spindle-knotted and conical solid models were reviewed in section 2.6. For a better systematic study on how the surfaces exert directional movement on droplets in different environments, either gaseous or liquid media, their application has been reviewed separately, which brought many ideas for this study. What the different studies had in common is their agreement in the causal analysis of dynamic liquid-moving process on/in bioinspired fibrous systems by implementing gradients in surface wettability and geometry or external stimuli.

Some research investigated systems that are responsive to stimuli from the surrounding environments. The majority of research resorted, however, to wettability and structural gradients due to the ease of operation and the lack of application of external forces or energy. Furthermore, despite extensive advances in the creation of wettability gradient using chemical heterogeneity and functionalization, migration of organic molecules was found to lead to chemical gradients degradation over long-term operation. Thus, the directional droplet transport purely by structural topography, which produces the substantial primary driving force known as the Laplace force, offered a compelling strategy to address this problem.

To overcome the inadequacies of manufacturing processes, introduced in section 2.6, which are limited to the production of short fibers, the cutting-edge studies were reviewed in section 2.7 on the large-scale fabrication of spindle-knotted fibers, realized by the electrospinning method. It was seen that the performance of the developed electrospun

membranes incorporating spindle-knotted fibers with regard to liquid-liquid separation has been evaluated mostly through experimental work in a pumpless simple filtration device (driven by gravity) and not against real flow conditions.

Overall, the aim of this review was to compile the so far studied works in this field to give a better understanding of the current state of the bio-inspired materials with structured fibers and surfaces with application in liquid-liquid separation. Despite the mentioned highlights above, there are some open points that have not yet been explored. The aforementioned studies have mainly paid attention to the droplet directional movement for the solid-air-water three phase system, studies of directionally-controlled transport of liquid in a second liquid phase are, however, scarce. Furthermore, even considering the limited published works, in none of them an in-depth and systematic analysis has been performed to reveal the mechanism of how the directional movement of droplets in another liquid medium occurs. Indeed, inference from the considered literature illustrates that to this date the investigated studies regarding the directional movement of droplets on surfaces are mostly research works containing experimental and visual efforts integrated with very superficial and transient theoretical studies. In most studies, at best, the theoretical consideration was based on the general form of the acting forces, listed in Tab. 2.2. In fact, the interpretation of the experimental results regarding the directional movement of droplets along the developed solid models was mostly done via an investigation that considers these forces individually, and not via a comprehensive model that brings together the acting forces. Furthermore, apart from limited efforts dealing with numerical solutions of the Laplace force, none of the reported work presented the corresponding solutions for other forces.

**Tab. 2.2 Acting forces/energies on the droplet moving along the structured surfaces (the forces generated by an external actuation with an external energy supply have been neglected);**

	Force	Formula	references
Driving	Laplace force	$\Delta P = - \int_{r_1}^{r_2} \frac{2\gamma}{(r+R)^2} \sin \alpha dz$	[22,32,37,57,84,86,91,94,99,115]
	Surface energy released in coalescence	$\Delta E = \gamma_{lv}\Delta A_{lv} + \gamma_{sl}\Delta A_{sl} + \gamma_{sv}\Delta A_{sv}$	[94]
	Chemical force	$F_C = \int_{L_i}^{L_k} \gamma (\cos \theta_A - \cos \theta_B) dl$	[22,32,37,84,91,94,99,110,111]
Resisting	Hysteresis force	$F_h = \int_{L_i}^{L_k} \gamma (\cos \theta_A - \cos \theta_R) dl$	[37,46,62,78,84,114]
	Viscous friction	$F_v = r \gamma^{1/3} (\mu_o l v)^{2/3}$	[57,63]
	Drag force	$F_D = \frac{1}{2} \rho v^2 C_D A$	[46]



### 3. Objective, hypothesis and approach

Based on the state-of-the-art described in section 2.1, conventional nonwoven filter membranes with liquid-liquid (oil-in-water emulsion) filtration applications are mostly membranes with fibers having uniform cross-sections. Nonwoven filter materials have been found to suffer from clogging due to the time-consuming coalescence/detachment of the dispersed phase (emulsified oil droplets), which hinders the restart of droplet collection and therefore reduces efficiency over time. Therefore, finding a way to accelerate the collection, coalescence, and detachment of the dispersed phase from the fibers on the downstream side could address this deficiency. The review of the literature reveals that some biological species in arid regions efficiently collect water from fog and exploit unique structural arrangements and microstructures on or within their surfaces to purposefully transport the collected droplets to the desired sites for consumption or storage. This behavior in nature has served as inspiration for developing materials/membranes with structures that can collect droplets and impart directional movement to them, thus taking advantage of rapid directional collection/coalescence along the structure. Among the numerous attempts to develop new bio-inspired materials with special structures effective in droplets separation/filtration application, only a few have resorted to the development of the membranes with spindle-knotted structured fibers. It also turned out that these studies initially focused on different possibilities/methods of fabrication and also on applications that take benefit of the movement of liquid droplets on filaments or surfaces surrounded by air. Therefore, despite the ongoing and extensive studies investigating the movement of liquid droplets on spindle-knotted filaments surrounded by air, research on the movement of liquid (oil) droplets on spindle-knotted filaments immersed in another liquid (water) is very limited. Although directional droplet transport in liquid-liquid applications has been realized in some reported studies, they mostly resorted to an external actuation with a power source, which severely limits its practical application. Therefore, a method to achieve directional fluid transport without external stimuli (needing an external energy supply) would be appreciated. Furthermore, the majority of the existing studies in a liquid-liquid environment deal primarily with experimental efforts, while the mechanisms of the directional movement of droplets on filaments remained undiscovered or were examined very cursory in the context of a theoretical model. As a consequence of this lack, we were motivated to develop a quantitative model based on first principles of physics that describes the underlying mechanism to predict values of the model-defining parameters that allow a straightforward construction of efficient oil-water separators.

### 3.1 Objectives of the thesis

The goal of this work is to find and model a bio-inspired methodology to give the conventional nonwoven coalescer filter media consisting of the uniform fibers added value for efficient use in liquid-liquid (oil/water) filtration. The main goal is the development of filter media comprising spider silk-like fibers with periodic spindle-knotted structures to exert a directional movement on tiny oil droplets along the fibers towards the spindle-knot sites, resulting in much bigger oil droplets that ascend much faster and thus improve the oil/water separation. To achieve this goal, the directional movement of underwater oil droplets on a spindle-knot structure needs to be modeled, leading to the prediction of the values of the model-defining parameters that allow a straightforward fabrication of efficient nonwoven membrane comprising spindle-knotted fibers. The following primary objectives realize the principle goal of this study:

- (1) Development of a theoretical model describing the mechanisms governing directional movement of droplets on spindle-knotted solids immersed in another liquid
- (2) Validation of the theoretical model through corresponding underwater experiments and numerical calculations
- (3) Fabrication of a spindle-knotted single fiber and membrane with spindle-knotted structured fibers using the corresponding fabrication methods
- (4) Development of a new measurement method to analyze and predict the wettability properties of spindle-knotted fibers (through dynamic contact angle measurements)
- (5) Development of a lab-scale pump-driven filtration test bench to evaluate the functionality and separation efficiency of spindle-knotted fibers with respect to collection/directional movement of emulsified oil droplets.

### 3.2 Research hypothesis

To implement these objectives, five working hypotheses are set up:

- (1) The water collection behavior of spider capture silk with spindle-knot structure in air suggests that spindle-knotted structured fibers can collect emulsified oil droplets in water and exert a directional movement on collected oil droplets along the fibers from the thinner (joints) to the thicker positions (spindle-knots) (chapter 5)
- (2) A good theoretical model can predict the effect of contributing/participating forces/parameters in the directional movement of oil droplets along the spindle-knotted fibers immersed in water (chapter 6).



- (3) The wettability properties of spindle-knot structured fibers with respect to dynamic contact angles can be predicted and estimated by the corresponding measurements on flat surfaces of the same material (chapter 7).
- (4) A filter medium with spindle-knot structured fibers can be fabricated in a facile electrospinning machine by optimizing the polymer solution concentration as one of the decisive factors for beads formation under specific operating parameters (chapter 5).
- (5) An electrospun filter medium with spindle-knot structured fibers can efficiently accelerate the collection of the emulsified oil droplets in a designed pump-driven filtration system, thereby improving the separation efficiency (chapter 8).

### 3.3 Methodological approach

This dissertation is divided into several sections, which focus on biological studies, the definition of a theoretical model, the design and fabrication of the bioinspired structured models, experimental set-ups, and procedures for evaluation.

Following the principle goal of the thesis, a comprehensive investigation was first carried out to determine the essential properties of the biological model (capture silk of cribellate spiders) considered in this work (section 2.4.1). The examined properties were; the morphology: wet-rebuilt spindle-knotted structure in a humid environment, the wettability: hydrophilic, and the functionality: an efficient collection of the micro-sized water droplets in the air. Moreover, an attempt was made to analyze the mechanisms of directional movement of water droplets along fibers from joints (thinner position) towards spindle-knots (thicker position), and to gain ideas to extend all knowledge from the water-air-solid to the oil-water-solid system (section 2.5).

As revealed by the literature review, the directional movement of liquid droplets along spindle-knot structured fibers immersed in another liquid is less understood and requires a systematic study to develop theory and experimental data to validate models. Indeed, a good theoretical model that can also reduce the number of experimental trials is required to predict the droplet movement behavior and to provide information which can be used to design an efficient membrane with structured fibers and application in liquid-liquid filtration. Thereby, a model is needed, which deciphers system parameters (micro/macro-structural geometry of fibers as well as the liquid properties) and forces exerting a directional movement on the droplets. In this work, as described in chapter 6, a specific model was developed and fitted to experiments that were conducted to study the directional movement of oil droplets on spindle-knotted fibers (immersed in water).

The theoretical model is based on the forces acting on the moving droplets which are well known from the literature.

To be able to systematically validate the developed theoretical model by means of corresponding underwater experiments, the design and production of a reproducible spindle-knot solid model proved to be a substantial factor. A simplification was introduced here, assuming that a spindle-knot model can be assembled by joining two cones at their bases. Thereby, for the fabrication of the conical models with an accurate and definable geometrical parameter, we have resorted to the 3D-printing method, which was used for further investigation in the section on the validation of the theoretical model (6.4). By bringing together the results of the theoretical model (the result of the programming language; *Python* solution) and the corresponding experiments, the underlying mechanism of the directional movement of droplets in another liquid medium was thoroughly investigated and modeled. The resulting model predicted the dependence of the droplet motion on time and on “system defining” parameters, such as droplet size, viscosity, and dynamic contact angles formed between droplet and filament surface.

Despite the growing achievements of various fabrication methods and designs for spindle-knot structured fibers, the characterization through their wettability was found to be still a difficult challenge because no measurement method has been specified and reported, so far. Therefore, as will be described in chapter 7, a novel method for evaluating spindle-knotted structured fibers with regard to their wettability was developed and reported. Here, the corresponding approach and the theoretical model (representation of forces acting on the immersed spindle-knotted fiber in liquid: weight, buoyancy, and surface forces) were developed and exemplified by applying them to the structured polydimethylsiloxane (PDMS) fibers with spindle-knots. The conformity of the results of the proposed method for PDMS spindle-knotted structured fiber using the Wilhelmy method and the results for flat PDMS surfaces using the direct optical method confirmed the reliability of the proposed method.

In view of the technical transfer of the concepts investigated here to nonwoven coalescer filter medium, electrospun membranes with spindle-knotted fibers were developed with underwater oleophilicity property (described in section 5.3). Among the various membranes produced here, the performance of the most promising membrane was predicted via the developed theoretical model (section 8.2). In addition, the performance of the membranes was experimentally evaluated by carrying out corresponding oil-in-water separation experiments using a designed pump-driven filtration system (chapter 8).

Due to the difficulty of tracking the aggregation and the directional movement of the emulsified oil droplets along the very fine ( $< 2 \mu\text{m}$ ) fibers of the electrospun membrane, the spindle-knotted fibers were fabricated in a larger size using dip- and spray-coating methods (section 5.1 and 5.2). Hereby, the role of spindle-knotted fibers in promoting the directional movement of droplets along the fibers from the thinner part to the thicker part which led to the efficient generation of larger droplets was confirmed.

## 4. Materials and methods

In this chapter, all materials used for the fundamental investigations and the measurement methods for the characterization of the liquid as well as the solid models developed in this work are described. The corresponding computer programs for the numerical calculation of the developed theoretical models are also outlined below.

### 4.1 Used materials

#### 4.1.1 Liquids (Oil/water)

The physical properties of water (as continuous phase) and oil (as dispersed phase) used in this work are summarized in Tab. 4.1.

**Tab. 4.1 Physical properties of used liquids;**

Identification within this work and properties as well as the manufacturer's information.

	Water	WACKER® AK 10	WACKER® AK 100	N-dodecane	Tudalen 3036
Identifier	Water	Silicon 10	Silicon 100	N-dodecane	Tudalen 3036
Color	Colorless transparent	Colorless transparent	Colorless transparent	Colorless transparent	yellowish
Surface tension against air @ 25 °C [mN m <sup>-1</sup> ]	72	20	21	24	30
Interfacial tension against water @ 25 °C [mN m <sup>-1</sup> ]	N/A	52	51	50	42
Density @ 25 °C [kg m <sup>-3</sup> ]	998	930	970	748	857.3
Dynamic viscosity @ 25 °C [mPa s]	1	~10	96	1.3	36
Boiling point @ 760 mmHg [°C]	100	390	N/A	215	N/A
Flash point [°C]	N/A	180	> 275	71	203
Melting point [°C]	0	-65	N/A	-12	N/A
Solubility in water @ 25 °C [mg L <sup>-1</sup> ]	N/A	insoluble	insoluble	insoluble	insoluble
Supplier	N/A	Wacker Chemie AG	Wacker Chemie AG	Th. Geyer GmbH	H&R Group

The water used in this work was fully desalinated. From the oils listed in Tab. 4.1, the silicon 10 and silicon 100 were used purely in the experiments carried out to validate the established theoretical model in chapter 6. Tudalen 3036 was used for the filtration experiment in chapter 8, where the experiments with oil-in-water emulsion had to be performed. For a better underwater visibility, the oil droplets were dyed red with Sudan III (Sigma-Aldrich, Germany), which is a common dye to stain nonpolar substances such as oils, fats, waxes, and various hydrocarbon products [151].

### Oil-in-water emulsion preparation

To carry out the filtration experiments, a stable oil-in-water emulsion (oil droplet size distribution  $< 2 \mu\text{m}$ ) had to be prepared. For this, the red-colored oil (0.05 wt% Sudan III-in-oil) and water were weighted in an appropriate amount to give a 0.1 wt% oil-in-water concentration. The mixture was then initially stirred with a mechanical stirrer (Ultra turrax-T25, IKA Werke GmbH & Co. KG) at 20,000 rpm and for half an hour. For generating the smaller oil droplets as well as the elimination of air bubbles from the emulsion, an Ultrasonic device (UP200S, Hielscher Ultrasound Technology GmbH) was applied for 10 minutes at an amplitude of 90 % and the pulse-pause ratio of 0.85.

#### 4.1.2 Polymeric and coating materials

The polymeric and coating materials used in this work are listed in Tab. 4.2.

**Tab. 4.2 Physical properties of used polymeric and coating materials;**

Identification within this work and properties as well as the manufacturer's information.

	SYLGARD® 184 Silicon Elastomer (PDMS)	PVDF	VerocyanV (RGD 845)	Tegotop® 210
Classification	Two-component Polymer	Polymer	Polymer	Two-component suspension
Physical state	Liquid	Solid pellets	Rigid solid	White turbid liquid
Solvents	N-hexane/N-dodecane	DMF/Aceton	-	-
Formula	$(\text{C}_2\text{H}_6\text{OSi})_n$	$-(\text{C}_2\text{H}_2\text{F}_2)_n-$	-	-
IUPAC name	Poly(dimethylsiloxane)	Poly(1,1-difluoroethylene)	-	-
Specific gravity [g cm <sup>-3</sup> ]	1.03	1.75-1.80	1.17-1.18	-
Dynamic viscosity [mPa s]	3500	-	-	-
Boiling point [°C]	-	-	-	-
Glass transition temperature [°C]	-	-40	52-54	-
Melting temperature [°C]	-	170	-	-
Water Absorption	-	$< 0.040 \%$	$< 1.1 - 1.5 \%$	-
Underwater wettability	Oleophilic	Oleophilic	Oleophobic	Oleophilic
Supplier	Sigma-Aldrich	Arkema	Alphacam GmbH	Evonik Nutrition & Care

PVDF is a hydrophobic, chemically and thermally very stable thermoplastic polymer with opaque and semi-crystalline properties. In this work, it was used to fabricate spindle-knotted single fibers and electrospun membranes in sections 5.1 and 5.3, respectively. To be used in this work, it had to be dissolved at the desired wt% concentration in the appropriate solvents as introduced in Tab. 4.2.

A SYLGARD<sup>®</sup> 184 silicone is a two-component PDMS elastomer. To prepare the PDMS elastomer, the base component was placed in a glass beaker and a curing agent component was added in a ratio of 10:1 (weight: weight) at room temperature. The mixture was then stirred vigorously by hand and kept in a refrigerator to prevent further cross-linking reactions. To prepare the PDMS coating solution in further concentrations, n-dodecane was added to the silicone mixture to dilute it to the defined wt%. [152–154] To achieve the spindle-knotted structured nonwovens in section 5.2, the diluted PDMS was applied. In chapter 7, the pure PDMS was used to prepare the spindle-knotted single fibers as well as flat surface samples used for the validation of the developed measurement method.

VerocyanV (RGD 845) is a PolyJet photopolymer with outstanding dimensional stability and high transparency, simulating thermoplastics such as PMMA [68]. It was the based polymer material that was used in the 3D-printing machine to print the conical models with defined geometry in section 5.4.

Tegotop<sup>®</sup> 210 is a white turbid liquid that forms superhydrophobic nanoagglomerates with particle size below 450 nm. It consists of 5%–10% Silicon dioxide (SiO<sub>2</sub>) and 80%–100% Decamethylcyclopentasiloxane (C<sub>10</sub>H<sub>30</sub>O<sub>5</sub>Si<sub>5</sub>) [68]. Tegotop<sup>®</sup> 210 was used to modify the wettability of the 3D-printed conical models described in section 5.4.1.

## 4.2 Test methods

Within the scope of this work, various test methods are used that provide information about the properties of the liquids, oil-in-water emulsion, fibers, and nonwoven textile materials in their original and coated condition.

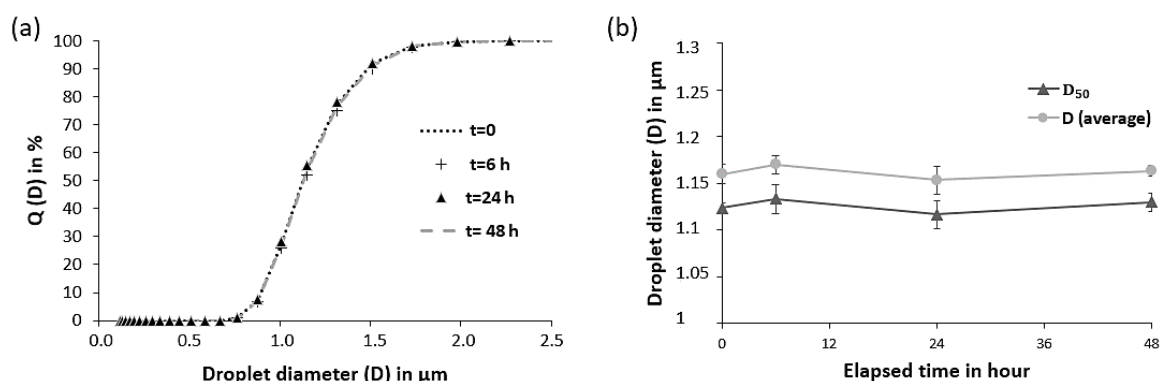
### 4.2.1 Particle size distribution

In order to be able to carry out a complete characterization of the collective of particles or droplets, their proportion with a certain property in the total amount must be known. A kind of representation of characteristic distribution is the cumulative distribution curve ( $Q(x_i)$ ) that for a certain dispersity quantity ( $x$ ) indicates which amount of a particle collective is less than or equal to the  $x_i$ : [155]

$$Q(x) = \frac{\text{Number of particles with } x \leq x_i}{\text{Total number of particles}} \quad (4.1)$$

For the cumulative distribution curve, the largest and smallest particle diameters  $x_{min}$  and  $x_{max}$  must be known to characterize the size range in which the particles are located. Then the standardization conditions follow from the conditions  $Q(x_{min}) = 0$  and  $Q(x_{max}) = 1$ . [155]

In this work, to check the emulsion stability, the oil droplet size distribution was measured based on the laser light scattering principle (according to DIN/ISO 13320) with a Particle Size Distribution Analyzer (LA-300, HORIBA, Japan). For this, an oil (Tudalen 3036)-in-water emulsion was prepared by mixing oil with water in concentration and procedure as described in section 4.1.1. The measurement results in the sequence of defined time-lapse (at room temperature) showed that 50% quantile of the size of the dispersed oil droplets ( $D_{50}$ ) remained  $\sim 1.1 \mu\text{m}$  within 2 days, confirming its stability.



**Fig. 4.1** Stability check of 0.1 wt% oil (Tudalen 3036)-in-water emulsion via droplet size distribution curves;

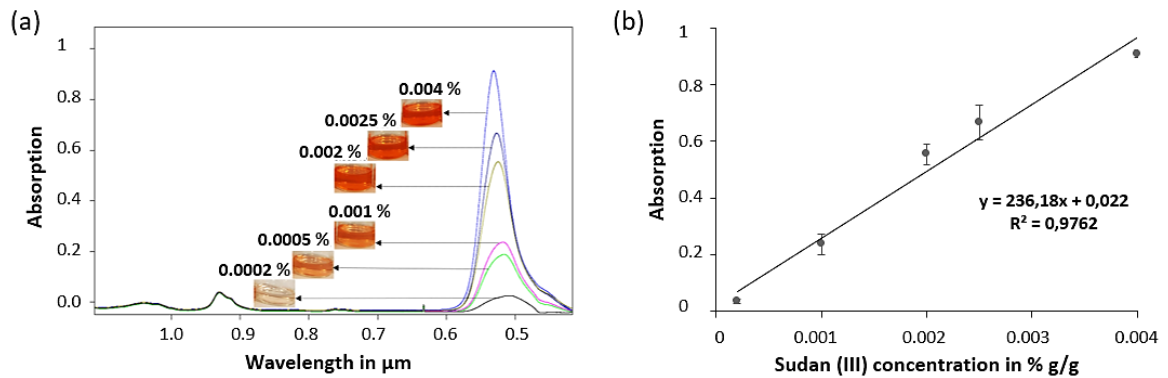
(a) Oil droplets cumulative number distribution curves after different time frames, (b) change in size of dispersed oil droplets within 2 days (diameter of 50% quantile of dispersed oil droplets:  $D_{50}$ , the average diameter of all dispersed oil droplets:  $D_{average}$ ).

#### 4.2.2 UV-Vis Spectroscopy

In this work, the spectroscopy analytical technique, based on the measurement of the amount of light absorbed by a sample at a given wavelength, was used to measure the concentration of the oil in the emulsion. For this, UV-Vis spectroscopy (VERTEX 80, Bruker, USA) was used to record the absorption spectra of Sudan III (the dye used in this work) at a given wavelength of about 520 nm [151].

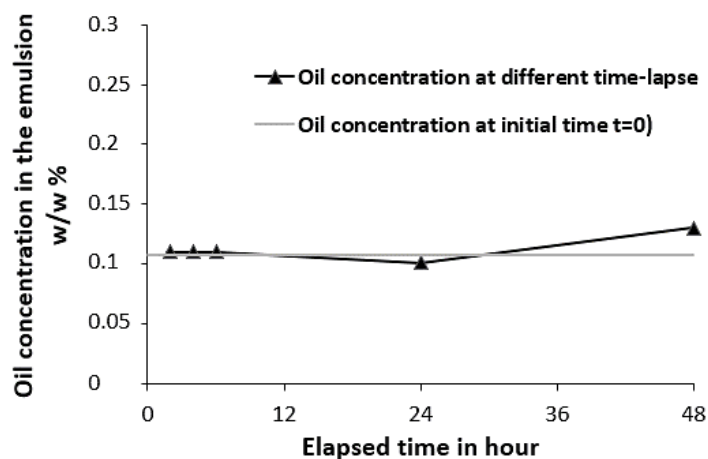
Here, the concentration of the used oil in the emulsion (Tudalen 3036) was determined by measuring the concentration of the dye in it (Sudan III). To measure the oil concentration in the emulsion, the dispersed oil (Tudalen 3036) dyed with Sudan III was first extracted with n-dodecane. For better phase separation, the solution was acidified with hydrochloric acid (HCl) to reach  $\text{pH} \sim 1$ . After complete extraction, the soluble oil was then dried in n-dodecane with sodium sulfate ( $\text{Na}_2\text{SO}_4$ ) and an infrared spectrum of the solution was taken. Since n-dodecane was used as the selected solvent for extraction, a calibration curve had to be created showing the relation between the absorption peak at 520 nm and the concentration of Sudan (III) dye in n-dodecane (Fig. 4.2 (b)). For this, the various n-dodecane solutions were prepared with the defined dye concentration and the infrared spectra of the solutions were created using the mentioned spectrometer (Fig. 4.2 (a)). The

concentration of oil in the emulsion was then determined using the created calibration curve in Fig. 4.2 (b).



**Fig. 4.2 Spectroscopy analytical technique to determine the oil concentration;**  
**(a)** Absorption spectra of Sudan (III) dye in n-dodecane, **(b)** calibration curve showing the maximum absorption at 520 nm as a function of Sudan (III) concentration in N-dodecane.

This method was used for two reasons, (i) to check the stability of the emulsion by recording the concentration of the emulsion within a defined time-lapse (ii) to measure the oil concentration before and after filtration (results in chapter 8 (section 8.3)). Fig. 4.3 shows the emulsion stability check with regard to concentration. The gray curve represents the initial oil concentration of the prepared emulsion (as described in section 4.1.1) and the black curve represents the recorded concentration within 2 days. The results at each time-lapse is the average of three times measurement and it can be seen that the concentration is almost constant for at least 24 hours.

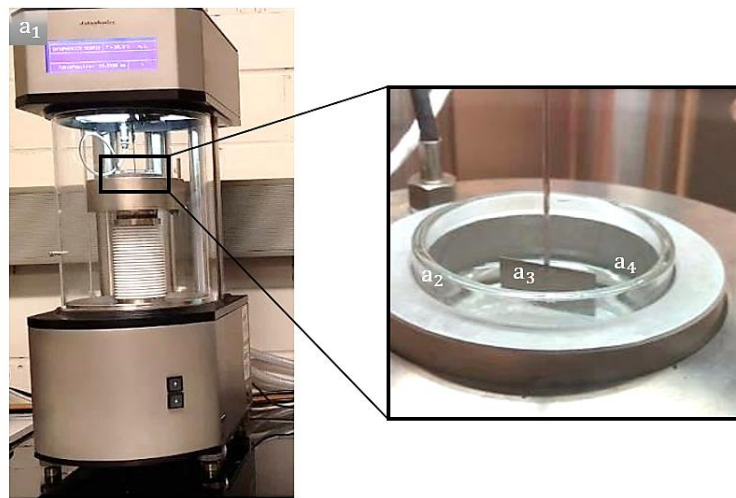


**Fig. 4.3 Stability check of 0.1 wt% oil (Tudalen 3036)-in-water emulsion via oil concentration measurement.**

#### 4.2.3 Surface and interfacial tension measurement

The literature review showed that the surface tension at an air-liquid (section 2.6.1) and the interfacial tension at a liquid-liquid interface (section 2.6.2) play vital roles in the

participating forces exerting directional movement on the droplets along the developed bio-inspired materials. Therefore, they had to be measured applying the corresponding measurement method. In this work, as shown in Fig. 4.4, the force tensiometry with Tensiometer instrument (DCAT11, Dataphysics Instruments GmbH, Germany) and Wilhelmy plate method [156] (according to DIN 53914) was used to measure the surface/interfacial tensions. In this method, the Wilhelmy plate (Fig. 4.4 (a<sub>3</sub>)) is a thin, generally rectangular plate with a few centimeters in length and height. The plate is made of iridium-platinum material and can be optimally wetted due to its very high surface-free energy.



**Fig. 4.4** The force tensiometry with tensiometer instrument.

For the measurement, the Wilhelmy plate was thoroughly cleaned and attached to a microbalance section of the tensiometer (Fig. 4.4 (a<sub>1</sub>)). The test liquid (Fig. 4.4 (a<sub>4</sub>)) was poured into the special crystallizing dish (Fig. 4.4 (a<sub>2</sub>)) belonged to the tensiometer and then situated on the movable stage. The measurements were carried out at room temperature (20 °C) and for a test duration of 10 s. The stage of the liquid was moved up until some millimeters below the Wilhelmy plate. By starting the measurement: The Wilhelmy plate was moved downward to immerse in the liquid and to the position which was defined as an immersion depth. Afterward, it was moved upward to emerge from the liquid to the defined starting position. Thereby, the force on the plate due to wetting was measured and used to calculate the surface tension of the test liquid using the Wilhelmy equation [51]

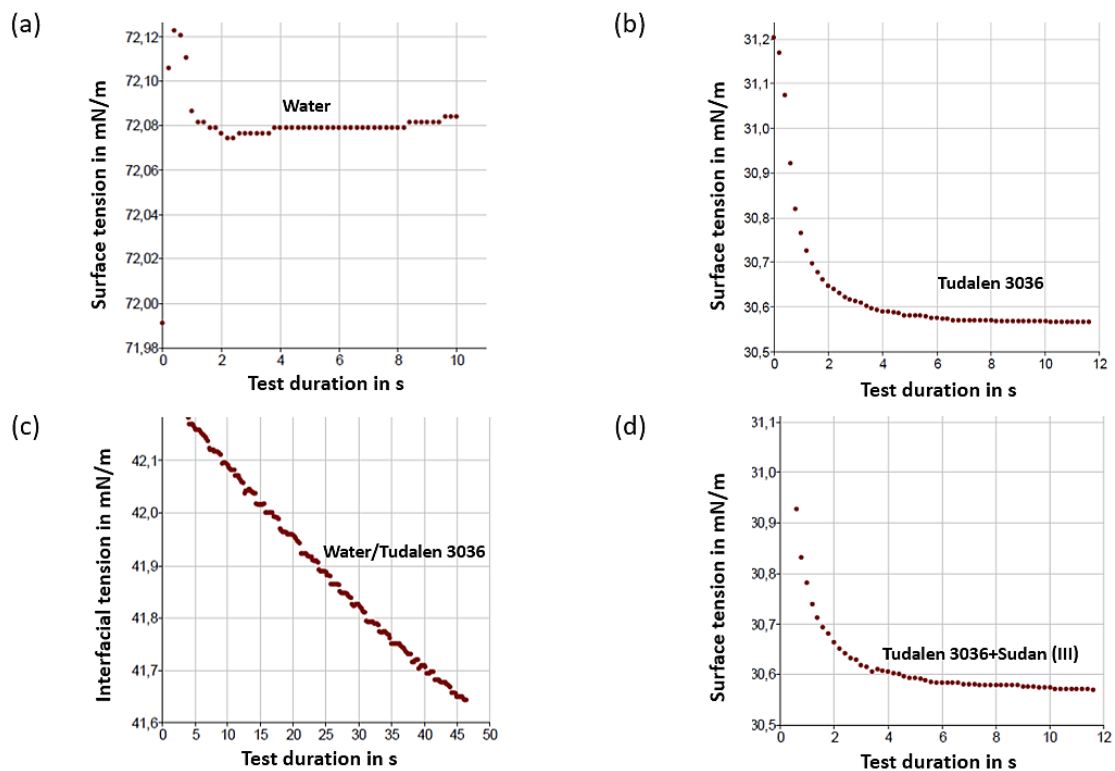
$$\gamma = \frac{F}{L \cos \theta} \quad (4.2)$$



where  $\gamma$  is the surface tension,  $F$  is the wetting force,  $L$  is the wetted length (rectangular perimeter for the Wilhelmy plate), and  $\theta$  is the contact angle between the liquid phase and the plate.

The interfacial tension between two immiscible liquids can be determined analogously to the surface tension measurement using the Wilhelmy plate method. To do this, here, the water is first poured into the glass vessel as the high-density liquid and the oil is poured over it as the low-density liquid. The plate itself is then located inside the upper liquid (oil) and the interfacial tension is determined when the Wilhelmy plate is at the interface between the two liquids. [157]

Fig. 4.5 shows the diagrams directly produced by the tensiometer device. Fig. 4.5 (a), (b), and (c) demonstrate the measurement of surface tension for water and Tudalen 3036 and interfacial tension measurement between them, respectively. To find the effect of the dye on the surface tension of the oils, the measurement was also carried out for dyed oil (Tudalen 3036 and Sudan (III)) and that was seen that the surface tension remained constant (comparing Fig. 4.5 (b) and (d)).



**Fig. 4.5** Diagrams of the surface/interfacial tension measurement using the Wilhelmy plate method;

(a) Surface tension measurement of water, (b) surface tension measurement of Tudalen 3036, (c) interfacial tension measurement between water and Tudalen 3036, (d) surface tension measurement of Tudalen 3036+Sudan (III).

The measurement results of the surface/interfacial tension for the liquids used in this work are given in Tab. 4.1. Here, three measurements were taken for each liquid.

### 4.2.4 Static and dynamic contact angle measurement on flat solid surfaces

One well-known method to characterize the wettability of the solid surfaces is the direct optical contact angle measuring through static and dynamic contact angle measurement (according to DIN 55660-2) between the liquid and the surface of the material. In this study, it was carried out using the sessile drop method and ellipse-fitting. Measurements were performed at at least three different positions on the same sample to confirm the homogeneity of the surface.

The wettability of the PDMS flat surfaces in chapter 7 were determined using a Drop Shape Analyzer DSA10 (Krüss, Germany). For this, a deionized water droplet of known volume 3-5  $\mu\text{L}$  was generated at the tip of the needle and then was gently brought into the surface to be placed at the desired position. The static contact angle was measured when the drop was standing on the surface and the three-phase boundary was not moving. For measuring the dynamic contact angle, a water droplet of known volume (5  $\mu\text{L}$ ) was firstly placed on the surface. While the needle was still at the drop, its volume was started to expand with a dosing rate of 10  $\mu\text{L min}^{-1}$ . A steady-state value of the contact angle at the growing state was defined as the advancing contact angle. Subsequently, the receding contact angle was measured when the three-phase boundary was moving by reducing the drop volume at the same rate.

The underwater contact angles of the oil droplets, either static or dynamic, on the prepared 3D-printed conical models (chapter 6), the flat surfaces of the same material (chapter 5), and on the electrospun membranes (chapters 5 and 8) were measured using an OCA200 contact angle measurement system (Dataphysics Instruments GmbH, Germany). For this, the oil droplets with volumes of 1.5-2  $\mu\text{L}$  were generated underwater and placed onto the surfaces and the measurements were carried out as explained when Drop Shape Analyzer DSA10 was used.

### 4.2.5 Dynamic contact angle measurement for a single fiber with a uniform circular cross-section (Axisymmetric fiber of constant cross-section)

To measure the dynamic contact angle of a solid body (advancing and receding contact angles), in the case of a single fiber with a uniform circular cross-section, the procedure is similar to what was explained when the Wilhelmy plate method was used. Here, the assumption is that the Wilhelmy plate is replaced by the single fiber. For this, the defined length of the tested fiber was cut and fixed on a special sample holder in order to be set into

the tensiometer instrument. Then, what was explained in section 4.2.3, was implemented for the suspended single fiber. Subsequently, the Wilhelmy equation must be modified to equation (4.3) based on the geometrical parameter of a single fiber with a uniform circular cross-section:

$$\gamma = \frac{F}{\pi D \cos \theta} \quad (4.3)$$

where  $\gamma$  is the surface tension,  $F$  is the wetting force,  $D$  is the diameter of fiber ( $L = \pi D$  is the wetted perimeter), and  $\theta$  is the contact angle between the liquid phase and the fiber. Fig. 4.6 shows the sample diagram obtained from the tensiometer using a uniform circular polyethyleneterephthalat (PET) single fiber with a diameter and a length of 55  $\mu\text{m}$  and 2 cm, respectively. The results shown in Fig. 4.6 have been obtained from three successive measurement cycles of dipping a fiber into the liquid (water) producing the solid graphs in the lower part of the diagram (corresponding to the advancing contact angle), and dragging the fiber out of the liquid, resulting in the triangles dots in the upper part of the diagram (corresponding to the receding contact angle). The abscissa and the ordinate axes of the diagram show the position of the fiber (immersion depth) in mm and recorded apparent mass by the tensiometer microbalance in g, respectively. The procedure explained in this section was mainly used in the development of chapter 7.

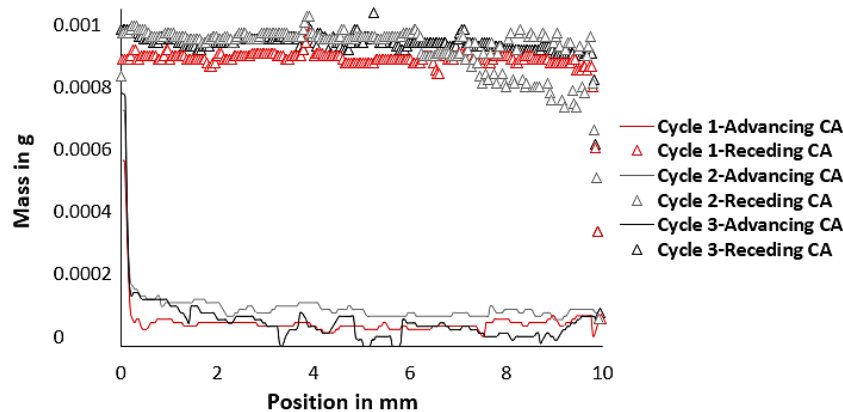


Fig. 4.6 Dynamic contact angle measurement for a uniform circular PET fiber.

#### 4.2.6 Morphology and geometry analysis

The surface morphology of natural spider silk and the studied solid models in this work were imaged and analyzed using a Scanning Electron Microscope (SEM) instrument (Hitachi TM1000, United States). The surface morphology of the electrospun PVDF membrane was examined by Field Emission Scanning Electron Microscopy (FESEM) (XL-ESEM FEG Scanning Electron Microscope FEI COMPANY). SEM images of the conical models coated with nanoparticles (Tegotop<sup>®</sup> 210) were imaged using FESEM

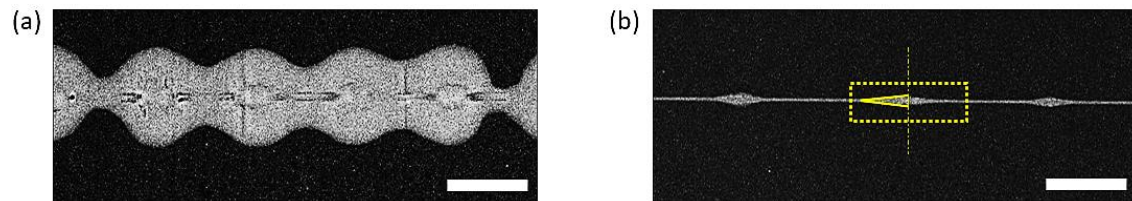
(Zeiss Auriga, Germany). For measurement, the samples were mounted on the corresponding stubs using carbon tape and when needed were sputter-coated to avoid sample charging.

#### 4.2.7 Numerical computations

For numerical evaluation of the developed mathematical models in chapters 6 and 7 the software *Maple* (Maplesoft, Waterloo, Canada) and *Python* (programming language) were used, respectively.

## 5. Material development

Fig. 5.1 (a) and (b) show the SEM images of dry and wet capture-silk of a cribellate spider. For the design and production of the solid model with varying cross-sections, either the spindle-knot structure or the conical model, we found inspiration from the periodic spindle-knotted structure of cribellate spider's capture silk in a humid environment.



**Fig. 5.1 Biological model, capture silk of a cribellate spider [68];**

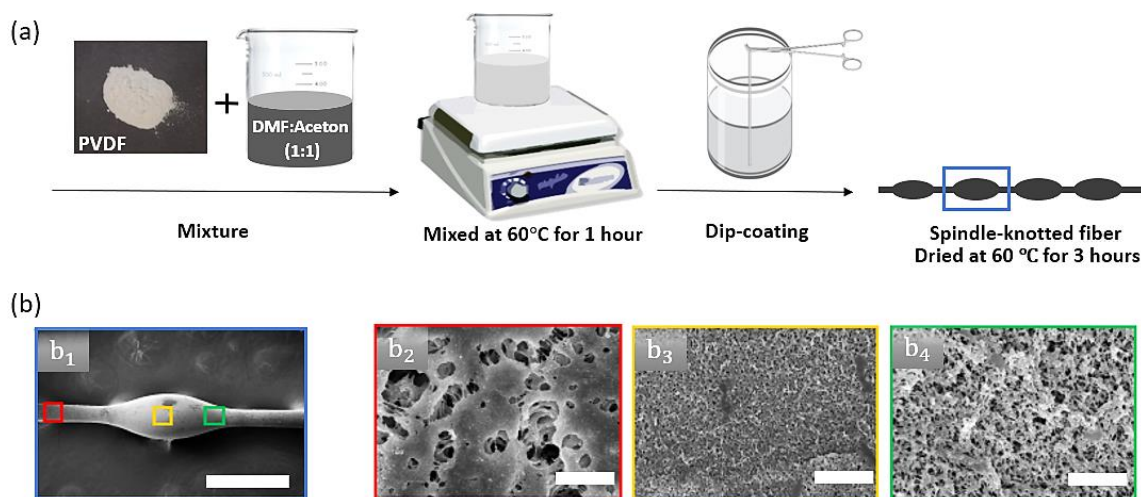
**(a)** SEM image of the capture silk in a dry environment, **(b)** SEM image of the capture silk in a humid environment. Scale bar: (a) and (b) 50  $\mu\text{m}$ .

In the following, the fabrication methods used in this work for the spindle-knot and the conical models as well as their characterization in terms of morphology and wettability are described. In addition, the functionality in terms of exerting directional movement on underwater oil droplets similar to what has been observed for the water collection behavior of the spider capture silk will be investigated to verify the hypothesis number (1) given in section 3.2.

### 5.1 Single fiber with spindle-knot structure

As can be seen from literature studies, the electrospinning method was the state-of-the-science for the fabrication of the membranes consisting of spindle-knotted fibers. It was also known that the individual fibers produced using this process are very fine (in the nanometer range). To verify the first hypothesis presented in section 3.2, it is practically impossible to carry out experiments to visually detect and analyze the behavior of the underwater oil droplets on such fine fibers. Thereby, the artificial spindle-knotted fibers with a micron-level spindle-knot structure had to be fabricated to evaluate the functionality in terms of directional movement and collection, which result in efficient coalescence of oil droplets at the spindle-knot positions. To prepare a micron-sized spindle-knot model, many researchers used the dip-coating method (solution-immersion process), which involved immersing a single fiber in a polymeric solution. According to 2.2.5, it has been found that when a perfectly uniform coating is applied to the surface of a fiber, it spontaneously disintegrates into small globules that adhere to the fiber at regular intervals. Here, the artificial single fibers with a micron-sized spindle-knotted structure were prepared by one-step dip-coating method and using different single base-fibers. For this,

among the various tested single fibers with cylindrical cross-section, either metallic or polymeric, a copper wire (diameter of 50  $\mu\text{m}$ ) and PET fibers (diameter of 10 and 20  $\mu\text{m}$  referred to as PET 10 and PET 20, respectively) were used. For the dip-coating procedure, the defined amount of PVDF powder was dissolved in a mixed solution of acetone and DMF (V:V=1:1) to achieve the concentrations of 2.5, 7.5, and 10 wt%. These concentrations were used in this study as they are the most privileged concentration used in various research studies to date. The solution was then stirred at 60 °C for 1 hour to obtain a uniform precursor solution. The fibers were vertically immersed into a 7.5 wt% PVDF solution for a short time and drawn out slowly from the solution container. As described in section 2.2.5, due to the Plateau-Rayleigh instability effect, in which the surface tension intends to reach the lowest energy, the PVDF solution on the cylindrical fibers was automatically broken into small droplets and formed the symmetrical oval shape; spindle-knot structure. Next, the fiber was dried at 60 °C for 3 hours. Fig. 5.2 (a) schematically shows the described process.

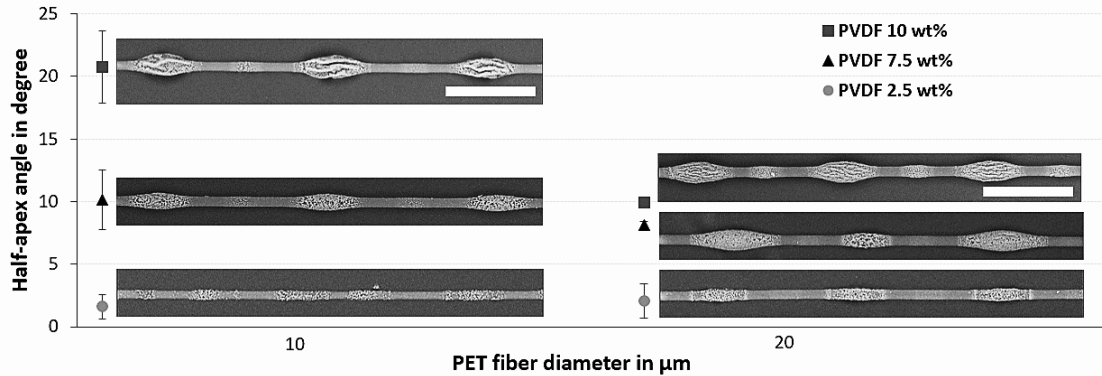


**Fig. 5.2 Dip-coating procedure for fabrication spindle knotted single fiber [158];**

**(a)** Schematic of the one-step dip-coating procedure, **(b)** SEM images showing the morphology of copper wire with PVDF spindle-knotted structure. Scale bar: 200 and 2  $\mu\text{m}$  for single spindle-knot (b1) and zoomed imaged (b2- b4), respectively.

The SEM images in Fig. 5.2 (b<sub>1</sub>) demonstrate one single spindle-knot structure, using the copper wire as fiber-base and PVDF 7.5 wt% as a polymeric solution. The zoomed SEM images in Fig. 5.2 (b<sub>2</sub>- b<sub>4</sub>) show differences in surface morphology at different positions. The observed cracks in the surface morphology of the red area (b<sub>2</sub>), the so-called joint position, could be due to elongations caused by the Rayleigh instability. The yellow (b<sub>3</sub>) and green areas (b<sub>4</sub>), referred to as spindle-knot position, exhibit a porous micro-structure in the surface morphology. It is known that a gradient in the roughness of the structure promotes the directional movement of droplets from the regions of less roughness (joints) to the regions of more roughness (spindle-knot site).

Fig. 5.3 demonstrates the SEM images of various spindle-knotted fibers using the PET base-fibers with different diameters, dip-coated in different PVDF solutions of varying concentrations. They are geometrically analyzed based on the dominant spindle-knots geometry through half-apex angle determination, which shows the geometry gradient and is a key factor for exerting the directional movement on droplets.



**Fig. 5.3 Spindle-knotted PET single fibers (PET 10 and PET 20) prepared by a dip-coating method using PVDF coating solution of various concentration;**  
Scale bar: 100 and 200 μm for PET fiber with diameter of 10 and 20 μm, respectively.

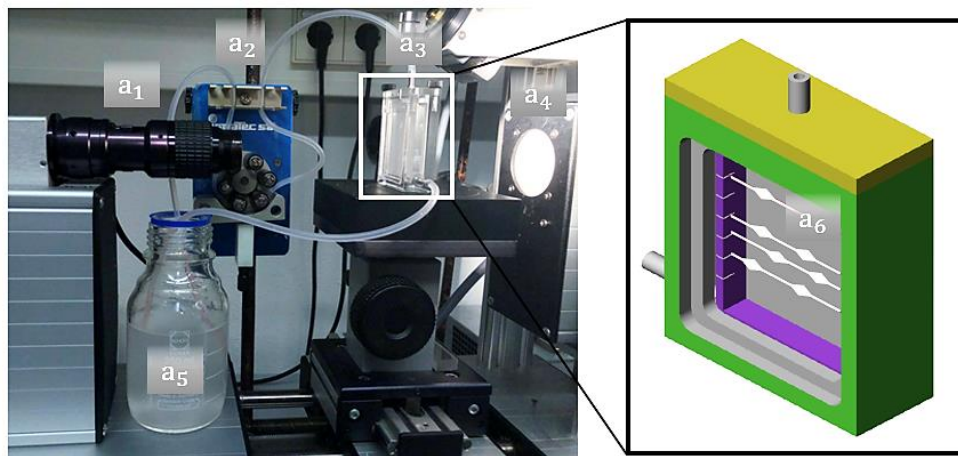
It can be seen that when using the low PVDF concentration (2.5 wt%), the structure of the spindle-knots is very flat with half-apex angles of  $1.6^{\circ} \pm 1^{\circ}$  and  $2.1^{\circ} \pm 1.4^{\circ}$  for PET 10 and PET 20, respectively. Increasing the concentration of PVDF to 7.5 wt%, the spindle-knots are bigger. The SEM images of PET 20 dip-coated in PVDF 7.5 wt% and 10 wt% show that the spindle-knots of different sizes are generated alternately. When the PET 10 is dip-coated in the mentioned concentration, spindle-knots of almost homogeneous size are formed. Using the PVDF 7.5 wt% resulted in half-apex angles for  $10.1^{\circ} \pm 2.4^{\circ}$  and  $8.1^{\circ} \pm 3^{\circ}$  for PET 10 and PET 20 (considering only the bigger spindles), respectively. Using the higher concentration of PVDF (10 wt%), spindle-knots of varying sizes were formed. Considering only the bigger-sized spindles as the main spindles, the size of spindle-knots increased to  $20.8^{\circ} \pm 2.9^{\circ}$  and  $10^{\circ} \pm 0.4^{\circ}$  for PET 10 and PET 20, respectively. The SEM images concerning the PVDF 10 wt% show shrinkage and wrinkles in the structure of spindle-knots using both PET 10 and PET 20, which is undesirable. Based on the size of the spindle-knots and the visual structure analysis over the SEM images, using the PET 10 fiber dip-coated in PVDF solution with a concentration of 7.5 wt% offers a more analogous solid model to the considered biological model owing to the half-apex angle of about  $9.5^{\circ}$  (see section 2.4).

The PET 10 and copper wire spindle-knotted fibers (using PVDF 7.5 wt%) were tested and visually monitored for directional collection of emulsified oil droplets in the setup developed in the next section.



### 5.1.1 Functionality in collection/separation of emulsified oil droplets

To verify the functionality of the spindle-knotted fibers with regard to the purposeful directional collection, movement, and coalescence of oil droplets at the spindle-knot positions, a test setup working in a continuous process was designed and the corresponding plexiglass cell was constructed. Fig. 5.5 shows the setup consisting of a camera ( $a_1$ ), a peristaltic micro-pump ( $a_2$ ), a plexiglass cell ( $a_3$ ), a light source ( $a_4$ ), and an oil-in-water emulsion container ( $a_5$ ).

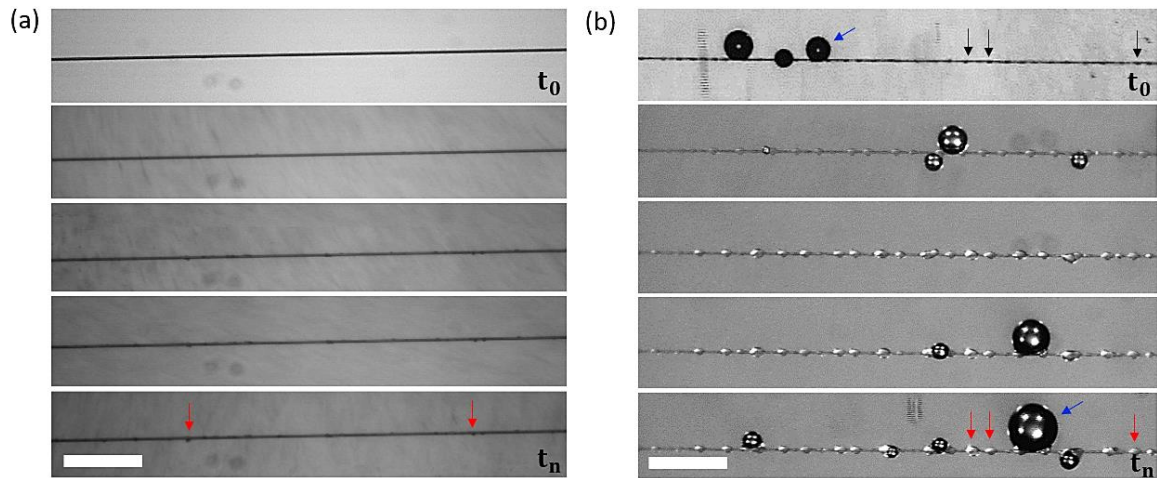


**Fig. 5.4** The experimental setup for tracking the oil droplet's directional collection behavior along the spindle-knotted fibers.

To investigate the role of the spindle-knots in the oil aggregation process, the spindle-knotted fibers were fixed to the center of the plexiglass cell ( $a_6$ ). The fibers were first immersed in water and then the prepared oil-in-water emulsion (described in section 4.1.1) was injected into the plexiglass cell via a pump at a defined velocity of  $1.66 \text{ cm s}^{-1}$  and encountered the fibers through one cross-flow process. The video documenting the collection of oil droplets on the fibers was recorded by an integrated camera of the contact angle measurement system. Fig. 5.5 (a) and (b) show the sequenced images of the pristine (uncoated) and spindle-knotted PET 10 fiber (using PVDF 7.5 wt%), respectively. In Fig. 5.5 (b), some spindle-knots on the structure of coated PET 10 have been pointed with black arrows. For the experiment, both fibers were installed in the setup and  $t_0 = 0$  shows the initial time when only water entered the plexiglass cell. It can be seen that after a while ( $t_n = 300 \text{ s}$ ), the oil droplets, pointed with red arrows in Fig. 5.5 (b), were efficiently collected at the spindle-knot sites of spindle-knotted fiber. While no significant oil collection on the original (uncoated) PET 10 fiber could be observed. Here some very small oil droplets collected on the uncoated fiber are also indicated by red arrows. The darker spheres pointed with blue arrows are accumulated air bubbles, which existed already in the cell or maybe were trapped air packets that filled the porous structure of the hydrophobic



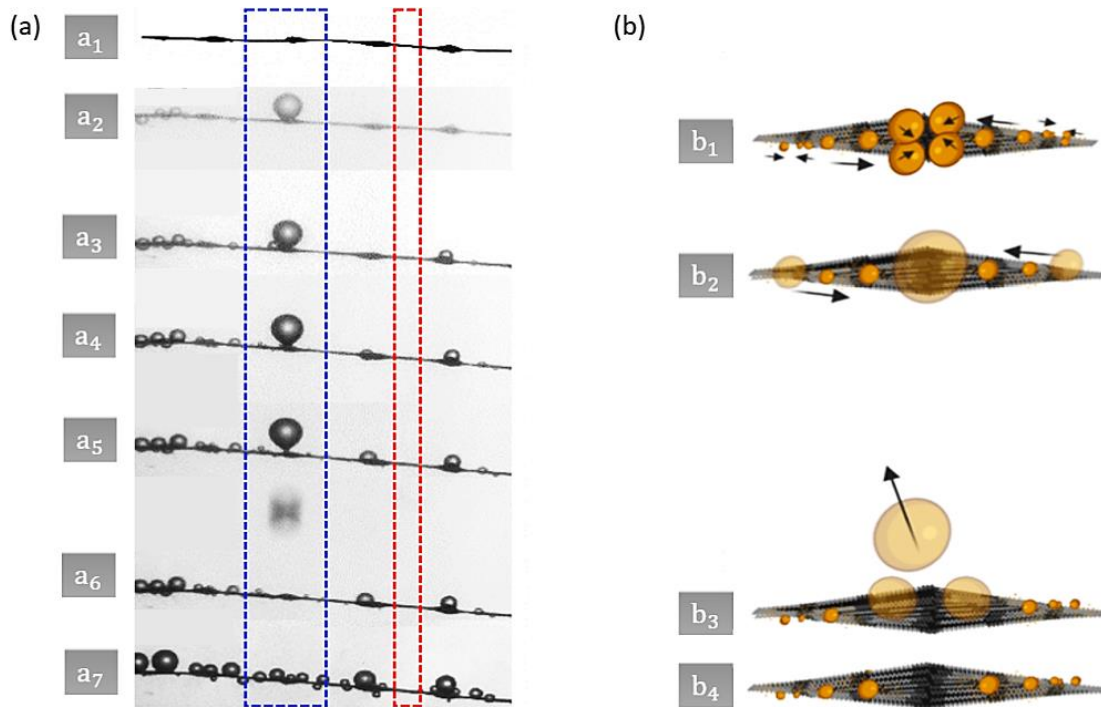
PVDF spindle-knots when placed underwater. These trapped air packets are replaced by oil droplets, once the emulsion enters and the oil collection on the surface begins.



**Fig. 5.5 Oil-in-water collection behavior on PET 10 single fiber with/without spindle-knotted structure;**  
**(a)** The successive snapshots of uncoated PET 10, **(b)** the successive snapshots of spindle-knotted PET 10 fiber (using PVDF 7.5 wt% as the coating solution). Scale bar: (a) and (b) 250  $\mu\text{m}$ .

To qualitatively observe and describe the aggregation (collection) process, the spindle-knotted copper wire with a larger spindle-knot size was installed in the designed setup shown in Fig. 5.4. Due to the limited zoom factor and light source of the previous camera, here, the camera of another contact angle measuring system was used. In Fig. 5.6 (a), the blue and red-marked areas show the spindle-knot and joint sites, respectively. In joint sites, no enlarged oil droplets can be observed, however, the majority of coalesced droplets can be seen in spindle-knot sites. Hence, the coalescence and collection of oil droplets occur mainly at the spindle-knot positions and not in the regions between two adjacent spindle-knots. It indicates the directional movement of the droplets from the joints (thinner part) to the spindle-knot positions (thicker part) and confirms the role of the spindle-knot structure in promoting the accumulation.

Fig. 5.6 (b) schematically illustrates the entire process, which can be divided into four stages: (i) oil droplets collection ( $b_1$ ) (ii) directional movement of coalesced droplets towards the center of the spindle-knots ( $b_2$ ) (iii) detachment of the coalesced droplets from the spindle-knots under buoyancy ( $b_3$ ) (iv) accumulation of the tiny oil droplets on the oil-free surface ( $b_4$ ). In summary, the tiny oil droplets initially deposited randomly on the spindle-knotted fibers. As deposition continues, oil droplets move toward the center of the spindle-knots, refreshing the original deposition sites for the newly arriving oil droplets. As soon as the newborn surface forms, the next cycle of "oil droplet deposition-droplet directional movement-oil collection" begins. [158]

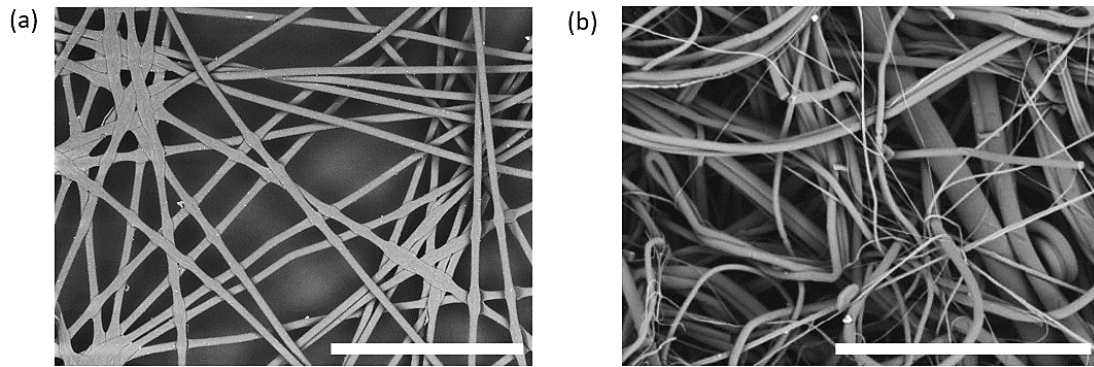


**Fig. 5.6 Oil in water collection behavior on the copper wire with spindle-knotted structure [158];**

**(a)** The successive snapshots of spindle-knotted copper wire (using PVDF 7.5 wt% as the coating solution), **(b)** a schematic showing the entire process of the directional oil collection cycle.

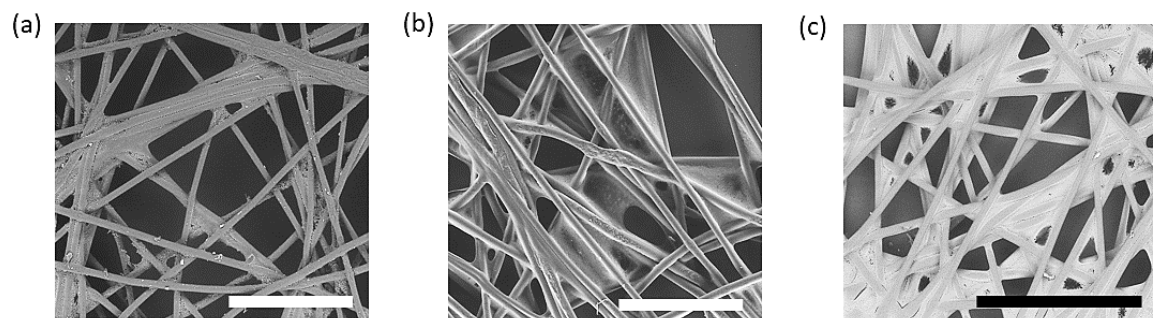
## 5.2 Spunbond/meltblown nonwoven textile with spindle-knotted fibers

As a further part of the work and prior to resorting to the electrospinning method, attempts were made to impart the periodic spindle-knotted structure to the nonwovens incorporating almost uniform fibers (with a circular cross-section). Here, among the various coating trials with the different nonwovens, the nonwoven samples that gave the most satisfactory spindle-knotted structure were PET spunbond and polybutylene terephthalate (PBT) meltblown shown in Fig. 5.7.



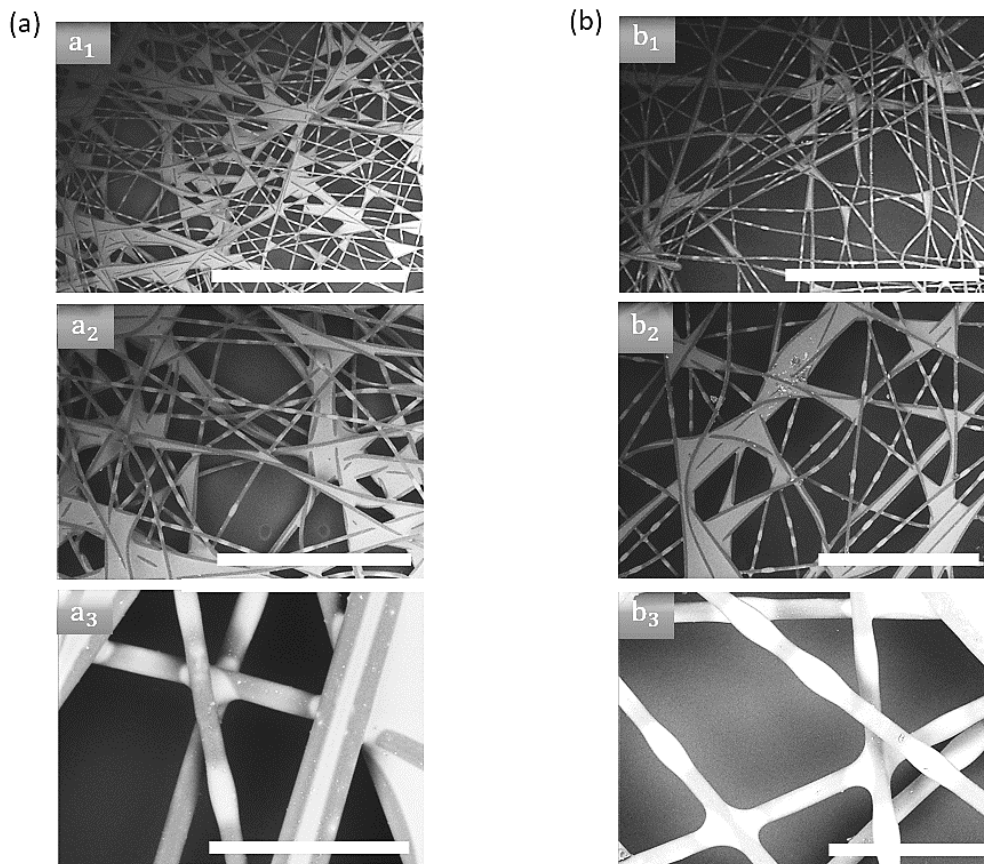
**Fig. 5.7 Nonwovens with almost uniform fibers having a cylindrical cross-section;** (a) SEM image of the PET spunbond (fiber size: 20 to 30  $\mu\text{m}$ ), (b) SEM image of the PBT meltblown (fiber size: 1 to 20  $\mu\text{m}$ ). Scale bar: (a) 500  $\mu\text{m}$ , (b) 200  $\mu\text{m}$ .

As shown in Fig. 5.8, here the experience was made that PVDF is not a suitable coating material for the considered nonwovens, because the attempt with different PVDF concentrations of 1.5, 2.5, and 7.5 wt% did not lead to the spindle-knotted structured fibers.



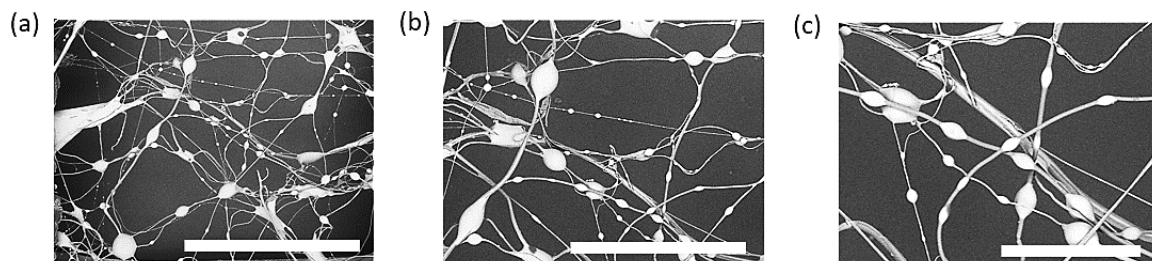
**Fig. 5.8 PET spunbond, dip-coated in PVDF solution of different concentrations;** (a) SEM image of PET spunbond dip-coated in PVDF 1.5 wt%, (b) PVDF 2.5 wt%, (c) PVDF 7.5 wt%. Scale bar: (a-c): 500  $\mu\text{m}$ .

As an alternative coating material, a further attempt was made to coat the spunbond nonwovens with PDMS. To do this, a specified amount of two-component PDMS elastomer was dissolved in the n-dodecane solvent to prepare polymer solutions with different concentrations of 15 and 30 wt%. Compared to the PVDF polymer solution, a higher drying temperature was required when PDMS was used as the coating material. Therefore, the samples needed to be dried at 100  $^{\circ}\text{C}$  for at least 2 hours after dip-coating. Fig. 5.9 (a) and (b) show the SEM images of prepared spindle-knotted fibers using PDMS solution with concentrations of 15 and 30 wt%, respectively. As the images show, using both the low and high concentrations resulted in some parts on the nonwoven being overly coated and filled with PDMS material, preventing the fibers of these parts from reaching the desired spindle-knotted structure.



**Fig. 5.9 PET spunbond, dip-coated in PDMS solution of different concentrations;**  
**(a)** SEM image of PET spunbond dip-coated in PDMS 30 wt%, **(b)** PDMS 15 wt%. Scale bar: (a<sub>1</sub>) and (b<sub>1</sub>) 2 mm, (a<sub>2</sub>) and (b<sub>2</sub>) 1 mm, (a<sub>3</sub>) and (b<sub>3</sub>) 200 μm.

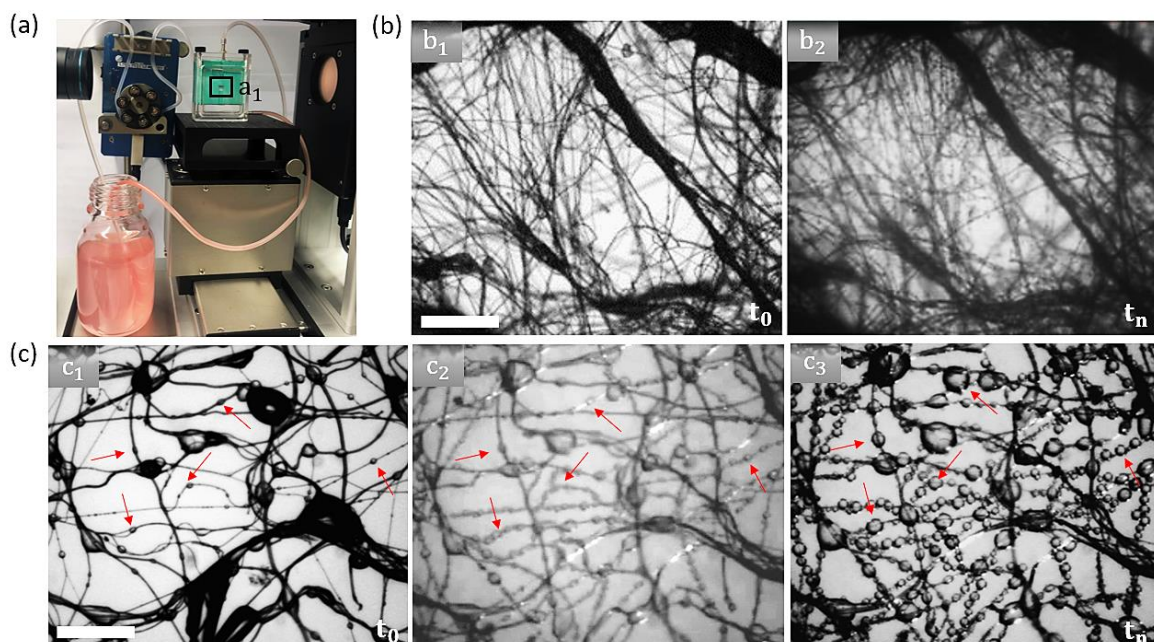
Since the fibers of the spunbonded nonwoven are almost fixed in their locations and are not flexible, hence, the fibrous PBT meltblown nonwoven was used in a further experiment in order to scatter the fibers and separate them from one another. Fig. 5.10 shows the resulted spindle-knotted fibers of the PBT meltblown nonwoven with partially separated fibers. Here, the best spindle-knotted structure was obtained using PDMS 20 wt% and the spray-coating method, in which the polymer solution was sprayed manually onto the surface and then dried at 100 °C for 2 hours.



**Fig. 5.10 PBT meltblown, spray-coated with PDMS;**  
**(a-c)** SEM image of PBT meltblown, spray-coated with PDMS 20 wt%. Scale bar: (a) 1 mm, (b) 500 μm, (c) 200 μm.



To verify the accumulation and directional movement of oil droplets on the prepared PBT spindle-knotted fibers, a test setup shown in Fig. 5.4 was used. A further modification was made for the inner part of the plexiglass cell so that the membrane can be fixed in the middle and a cross-flow can be directed through a shown window ( $0.5 \times 0.5 \text{ cm}^2$ ) in Fig. 5.11 (a<sub>1</sub>). Fig. 5.11 (b<sub>1</sub>) and (c<sub>1</sub>) show the images of the pristine (mostly with uniform cylindrical fibers) and spindle-knotted PBT meltblown fibers (PDMS coating) at the initial time ( $t_0 = 0$ ) when only water is in the cell. After a while ( $t_n = 600 \text{ s}$ ), as shown in Fig. 5.11 (c<sub>2</sub>-c<sub>3</sub>), a large number of spherical oil droplets accumulated on the surface of PBT meltblown fibers coated by PDMS can be seen. Some positions marked in red highlight some spindle-knots, which indicates that these are the positions where droplets are directed towards them and therefore produce bigger droplets. As a control of the role of spindle-knots in generating large droplets, the same experimental condition was repeated using the pristine PBT meltblown fibers with no coating (no structure). As shown in Fig. 5.11 (b<sub>2</sub>), after  $t_n$  elapsed, despite the partial accumulation of the oil droplets, no large droplets as seen on spindle-knotted structured fibers were observed, confirming the benefit of spindle-knot structure in large droplet generation.



**Fig. 5.11 Oil-in-water collection behavior on PBT meltblown fibers with/without spindle-knot structure;**

**(a)** The experimental setup with modified plexiglass cell, **(b)** PBT meltblown fibers without PDMS coating in water (b<sub>1</sub>) and in oil-in-water emulsion (b<sub>2</sub>), **(c)** spindle-knotted PBT meltblown fibers (PDMS 20 wt%) in water (c<sub>1</sub>) and in oil-in-water emulsion (c<sub>2</sub>-c<sub>3</sub>). Scale bar: (b<sub>1</sub>) and (c<sub>1</sub>) 500  $\mu\text{m}$ .

As previously mentioned, the design and production of the fiber network turned out to be a substantial and decisive factor on the way to efficient separators. It is known that fiber

networks achieve larger-scale droplet collection under the same condition. The aim of this work is therefore the development of a membrane/filter medium made of spindle-knotted fibers. Nevertheless, the fabrication methods described here, either dip- or spray-coating used for single fibers and nonwovens, are not controllable and do not apply to large-scale fabrication. Therefore, the focus is on the electrospinning fabrication method, which was introduced as the most promising manufacturing process that can produce the network of spindle-knotted fibers. Among the two types of polymer coatings mentioned in this section; PVDF and PDMS; it was found that the latter cannot be used in an electrospinning machine to produce nanofiber membranes, therefore, the PVDF was our polymer of choice for use in the next section.

### 5.3 Electrospun nonwoven textile with spindle-knotted fibers

Here, the PVDF membranes were prepared using an electrospinning machine shown in Fig. 5.12. The machine consists of a high-voltage power supply, a metallic rotating roller ( $a_1$ ), and a spraying device ( $a_2$ ) with a capillary needle having an inner and outer diameter of 0.6 mm and 0.8 mm, respectively.

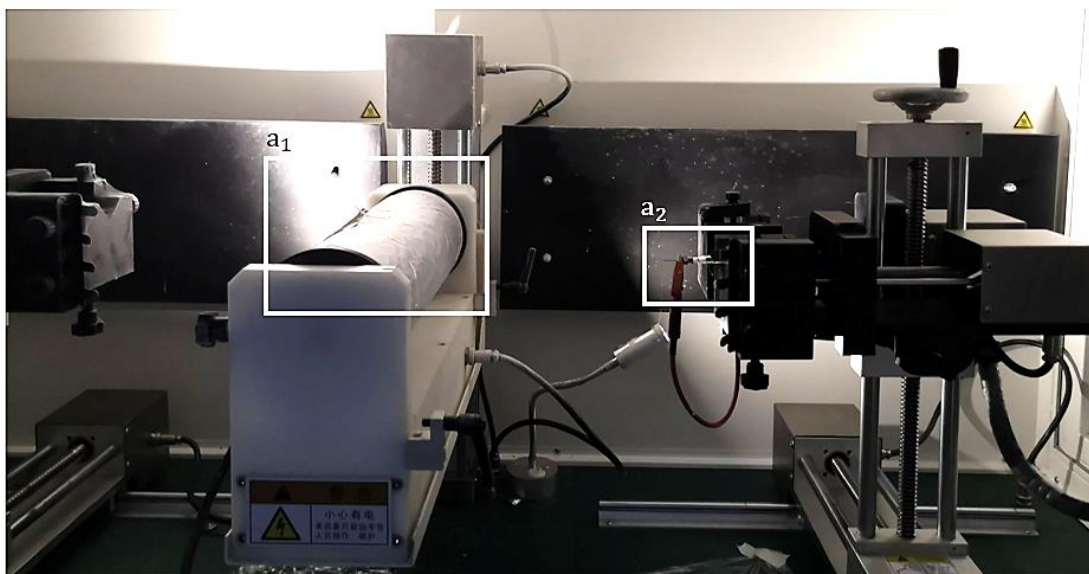


Fig. 5.12 Electrospinning machine at Key Laboratory of Bionic Engineering, Jilin University.

The precursor solution was made by dissolving the sufficiently dried PVDF powder in a mixed solution of acetone and DMF (V:V=1:1) at the desired concentration. The mixture was then stirred at 60 °C for 1 hour to obtain a uniform precursor solution and was then loaded into a 5 mL syringe.

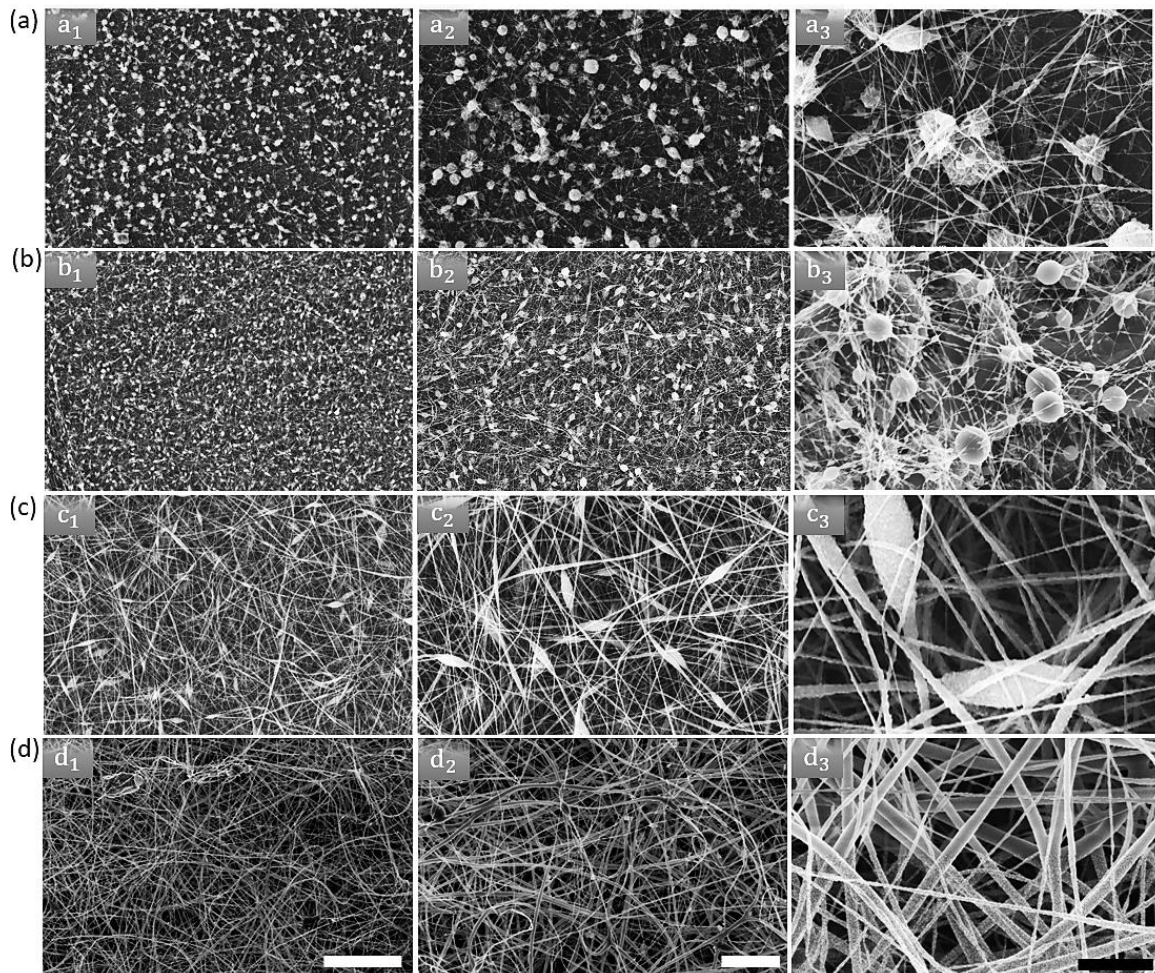
As the main decisive operational parameters were introduced in section 2.7, here a voltage of 15 kV was applied to the needle tip to provide a stable and sufficient electric field

intensity and the feed rate of the solution was kept at  $1 \text{ mL h}^{-1}$ . The distance between the cathode and anode that is from the needle tip to the surface of the collector was 18 cm, and the generated fibers were collected on the metal rotating roll with a rotation rate of 80 rpm. Temperature and the relative humidity were kept at  $25 \text{ }^\circ\text{C} \pm 5 \text{ }^\circ\text{C}$  and  $10\% \pm 5\%$ , respectively, throughout the experiment. The electrospinning process continued for 4 hours. The prepared PVDF membranes were washed with alcohol and dried at  $60 \text{ }^\circ\text{C}$  for 30 minutes in order to be completely solvent-free. [158]

From the literature study in 2.7, it emerged that either smooth and bead-free or bead-shaped (spindle-knotted) fibers can be obtained by the appropriate selection of polymer concentration in the corresponding solution. Therefore, in this study, among the various influencing parameters on the morphology of electrospun fibers, the individual influence of the polymer concentration on the surface morphologies of the electrospun fibers was investigated to verify hypothesis number (4) stated in section 3.2.

Fig. 5.13 (a-d) are FESEM images showing the morphology of as-prepared membrane made of PVDF in acetone and DMF (V:V=1:1) with concentrations of 2.5, 5, 7.5, and 10 wt%, respectively. Generally, from the FESEM images can be seen that surface morphologies of the membranes obtained from different solution concentration were quite different. Based on the used concentration, the electrospun fibers are without bead (fibers-only structure) or with heteromorphic, spherical, or spindle-shaped beads. From Fig. 5.13 (a<sub>1</sub>-a<sub>3</sub>) it can be seen that the membrane made of PVDF with a concentration of 2.5 wt% is composed of broken short nanofilaments and many large protruding particles with arbitrary shape distributed on their surface. By increasing the PVDF concentration to 5 wt%, many microspheres (quasi-spherically shaped) were sparsely decorated on the surface or along the single fibers, which maybe came from the electro spraying effect due to the low viscosity of the solution (Fig. 5.13 (b<sub>1</sub>-b<sub>3</sub>)). Interestingly, when the concentration of the polymer increased to 7.5 wt%, the spherical particles become elongated in the axis of the conjunctive nanofilaments, resulting in the spindle-knot structures (beads-on-string) which are evenly distributed along the fibers (Fig. 5.13 (c<sub>1</sub>-c<sub>3</sub>)). Fig. 5.13 (d<sub>1</sub>-d<sub>3</sub>) show the surface morphology of PVDF membrane with further increasing the polymer concentration up to 10 wt%. The spindle-knot structures on the surface are significantly reduced, and fibers of almost cylindrical cross-sections were formed (only a very few spindle-knot structures appear sporadically at various positions of the samples). The appearance of the conjunctive nanofilaments in the higher concentration of the polymers can be attributed to enhanced polymer chain interactions at higher polymer concentration [4]. Comparing the FESEM images, it can be concluded that the roughness of the electrospun fibers gradually decreased and became more uniform with the further increase in the concentration of the polymer, which resulted from the decrease in the number of beads (either random or spindle-shaped) and the formation of continuous fibers. Based on the FESEM image analysis as well as the

geometry of the natural spindle-knot model (ascribed to spindle-knotted capture silk of cribellate spider), the PVDF membrane with the concentration of 7.5 wt% is assumed to be the most promising solid-model fabricated in this study. [158]



**Fig. 5.13 Electrospun membranes prepared using PVDF solution with different concentrations [158];**

**(a)** FESEM images of electrospun membrane made of PVDF 2.5 wt%, **(b)** PVDF 5 wt%, **(c)** PVDF 7.5 wt%, **(d)** 10 wt%. Scale bar: (a<sub>1</sub>-d<sub>1</sub>) 50  $\mu$ m, (a<sub>2</sub>-d<sub>2</sub>) 20  $\mu$ m, (a<sub>3</sub>-d<sub>3</sub>) 5  $\mu$ m.

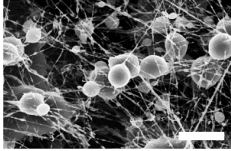
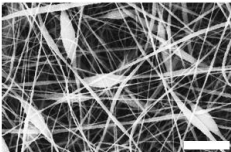
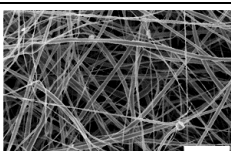
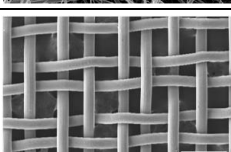
In addition, the satisfactory mechanical properties, which are of great importance for practical industrial applications, had to be taken into account. In fact, without the use of support base material, the stability of the membrane produced was very vulnerable to high flow applications, causing the membrane to tear and lose its separating function. Here, due to evaluating the prepared electrospun membrane in a filtration system (section 8.1), the membranes had to be mechanically robust enough to withstand the driving pressure. As a first attempt to select the base material, the electrospun membrane was fabricated and collected on the polymeric base material (PET spunbonded), but the adhesion of the nanofibers to it was very poor and they peeled off easily. Instead, the good, mechanically robust electrospun membranes could be successfully fabricated on the stainless-steel



meshes. Tab. 5.1 demonstrates the properties of various electrospun nanofibrous membranes that have been successfully fabricated.

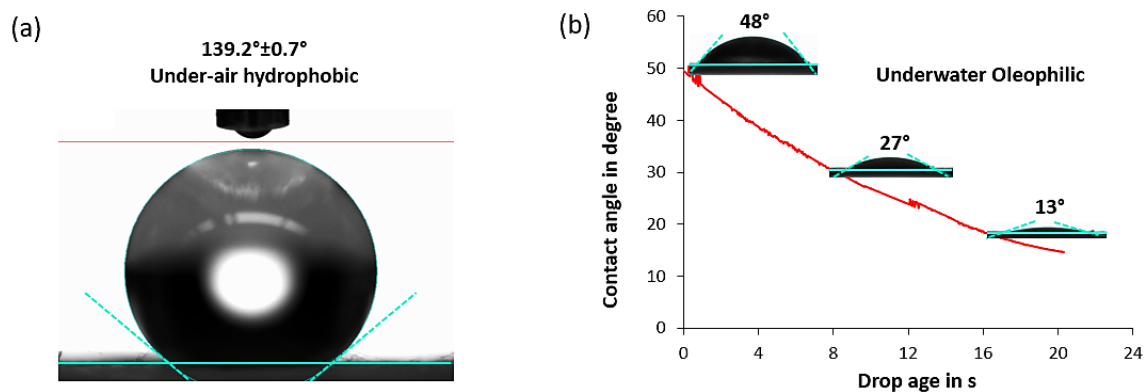
**Tab. 5.1 Specification of electrospun PVDF membranes;**

Scale bar: 5, 10, and 10  $\mu\text{m}$  for PVDF 5, 7.5, and 10 wt%, respectively. 200  $\mu\text{m}$  for stainless-steel.

Membrane type	SEM image	Fiber diameter [nm]	Thickness [ $\mu\text{m}$ ]	Weight [ $\text{g}/\text{m}^2$ ]	Air permeability @200Pa @5cm <sup>2</sup> [ $\text{L}/\text{m}^2/\text{s}$ ]
PVDF 5 %		<250	ultrathin	ultralight	847±12
PVDF 7.5 %		<500	20±5	4.5±0.1	104±21
PVDF 10 %		<750	30±5	4.75±0.8	89±19
Stainless-steel mesh (base)		50 $\mu\text{m}$	70±0	125±0.5	3815±20

### 5.3.1 Wettability of the prepared electrospun membranes

A high selective wettability for oil and water is a crucial material factor for oil/water separation. As explained in section 2.5, the hydrophilic wettability property of the capture silk of cribellate spider plays a key role in the collection and directional movement of tiny water droplets along the fibers. Analogously, here the underwater oleophilic membranes have to be fabricated to impart a similar effect on the tiny oil droplets. Thus, the wettability of the electrospun PVDF membranes has to be examined to prove that they have the desired wettability.



**Fig. 5.14 Wettability analysis of electrospun PVDF membrane;**

**(a)** A water droplet positioned on the electrospun membrane made of PVDF 7.5 wt% showing the under-air hydrophobic wettability with a static contact angle of  $139.2^{\circ} \pm 0.7^{\circ}$ , **(b)** an oil droplet positioned on the electrospun membrane made of PVDF 7.5 wt% showing the underwater oleophilic wettability. The diagram shows the change of static contact angle as a function of drop age.

As shown in Fig. 5.14 (a), the obtained membranes exhibited hydrophobic behavior in the air with a static water contact angle of  $139^{\circ}$ . The results in Fig. 5.14 (b) imply that the positioned oil droplet (Tudalen 3036) on the electrospun membrane changes its contact angle drastically from  $48^{\circ}$  to  $13^{\circ}$  within 20 seconds, which is attributed to the high underwater oleophilicity of the membrane. Remarkably, the results of wettability were almost the same for membranes made of different concentrations of PVDF.

## 5.4 Additive manufacturing (3D-printing) process

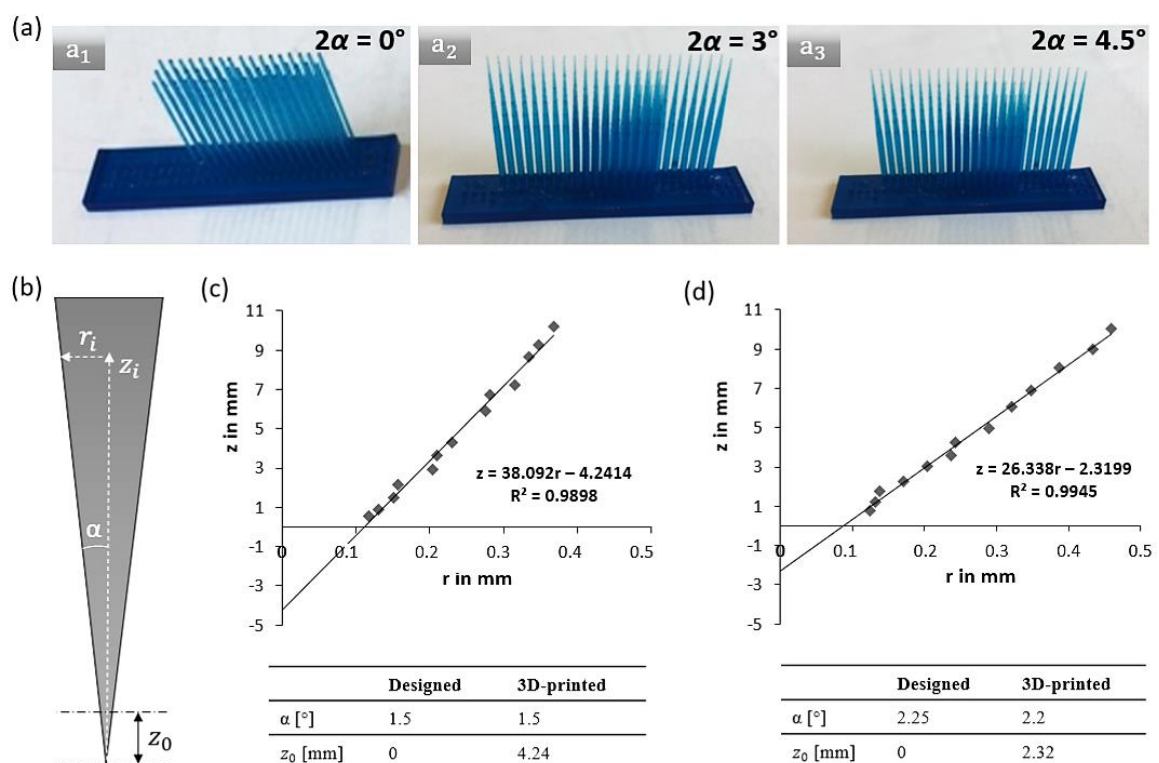
In section 2.6, that was mentioned that various attempts have been made to study the directional movement of droplets inspired by spindle-knotted spider silk as well as conical spines of cacti, which have functionally equivalent (analogous) structures [22]. Although the droplet collection and directional motion behavior on the spindle-knotted fibers could be easily seen and qualitatively analyzed (sections 2.6, 5.1, and 5.2), the results could not be examined quantitatively because the constructed spindle-knotted models were neither regular nor controlled. As the two mentioned biological models follow similar mechanisms for their water collection, here an assumption could be taken that a spindle-knot structure can be assembled by connecting two cones at their bases. Therefore, resorting to a reliable method for fabricating the conical model will lead to the systematic fabrication of solid models for further investigation and theoretical modeling (chapter 6).

In section 2.6.1, depending on the used material, the various existing methods for fabricating the conical solid models were introduced. It has been found that the methods of elongation of glass capillary tube, replica molding, chemical or electrochemical erosion/electroetching of metal wire, etc are plagued by a lack of reproducibility, flexibility, and accuracy. Alternatively, additive manufacturing technology represents a new direction

of fabricating customized parts and bioinspired structures with complex architectures and is widely used in science, industry, and daily usage [98].

In this study, the first step of fabrication of the conical models (filament) was allocated to elongating glass capillary tubes by heating and quickly drawing them, however, the models produced were very random and uncontrollable. To circumvent the mentioned shortcomings and to follow the state-of-the-science, we also resorted to additive manufacturing technology that offers a way to produce reliable and reproducible 3D-printed conical models.

Accordingly, the polymeric cone models were prepared to an accuracy of about 0.1 mm using an Object30 Prime machine (Stratasys, Ltd., Eden Prairie, Minnesota). To check the production feasibility of the model, the first models were created from Veroclear<sup>®</sup>, a standard material used in additive manufacturing technology. To increase the visibility of the models for underwater experiments, in further sample fabrication VerocyanV (RGD 845) was used, with blue-colored Veroclear<sup>®</sup> as the base material. Fig. 5.15 (a) show the 3D-printed conical models with different apex angle ( $2\alpha$ ) of  $0^\circ$ ,  $3^\circ$ , and  $4.5^\circ$ . As shown in Fig. 5.15 (b-d), the fabricated conical models were then dimensionally checked with regard to their apex angle, which was a determining parameter during the fabrication process. [68]

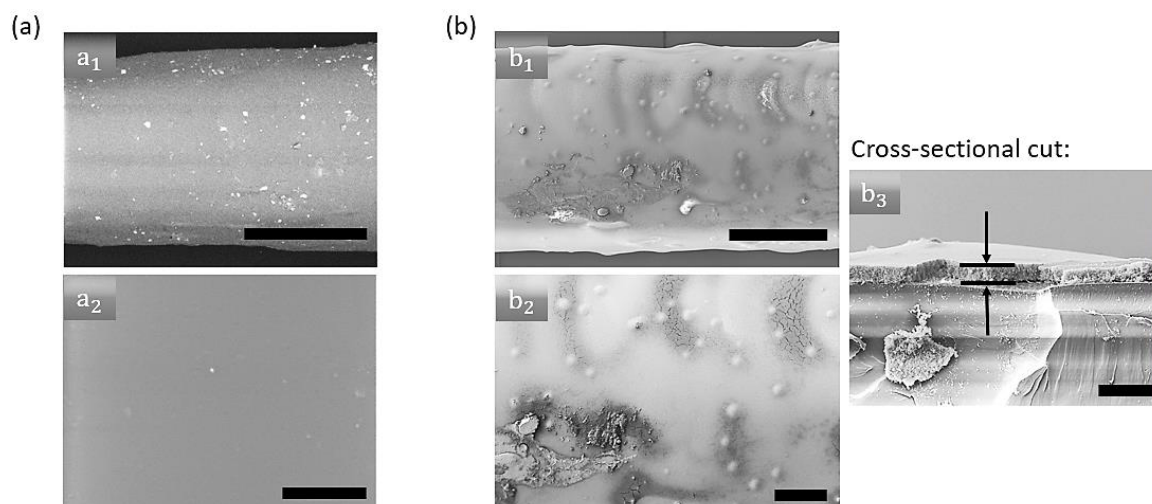


**Fig. 5.15 3D-printed conical models fabricated with Object30 Prime machine [68];**

(a) The 3D-printed conical models with different apex angles, fabricated in Alphacam GmbH, (b) a schematic showing the geometrical parameters of the cone, (c-d) dimensional check of the fabricated 3D-printed conical model.

### 5.4.1 Wettability of the fabricated conical models

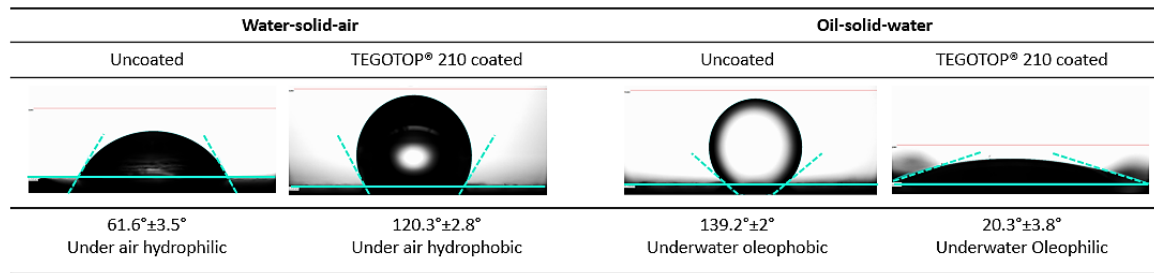
Due to the inability of the used 3D printer to create the desired rough surfaces in situ, the surfaces have to be roughened and modified with appropriate low surface energy substances or nanoparticles that impart the lower oil contact angles (underwater). To do this, the fabricated 3D-printed conical models in the previous section were post-processed (hydrophobized) to modify their wettability with a rough, oleophilic nanostructure using Tegotop<sup>®</sup> 210 (section 4.1.2). For this, using a pipette, 2–3 droplets were manually poured onto each individual conical model to completely wet the surface. The coated models were then dried at room temperature for at least 24 hours and the solution solidified into a thin film. Fig. 5.16 (a) and (b) show the SEM images of the uncoated and coated 3D-printed conical models, respectively. The SEM image of the cross-sectional cut of the coated conical model in Fig. 5.16 (b<sub>3</sub>) shows that the Tegotop<sup>®</sup> 210 coating formed a relatively uniform film on the conical models with a thickness of about 4.3  $\mu\text{m}$ . [68]



**Fig. 5.16 3D-printed conical model in coated and uncoated condition [68];**

**(a)** SEM images of uncoated conical model, **(b)** SEM images of coated conical model with Tegotop<sup>®</sup> 210. Scale bar: (a<sub>1</sub>) 500  $\mu\text{m}$ , (a<sub>2</sub>, b<sub>3</sub>) 10  $\mu\text{m}$ , (b<sub>1</sub>) 300  $\mu\text{m}$ , (b<sub>2</sub>) 100  $\mu\text{m}$ .

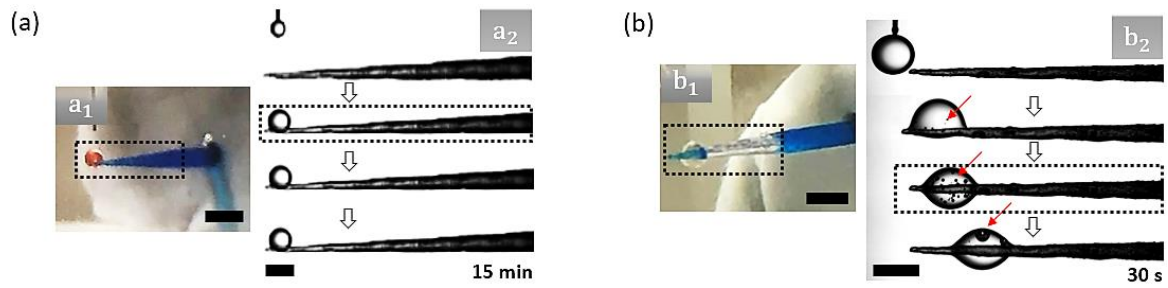
To analyze the VerocyanV (RGD 845) (polymer material used in the 3D-printing machine) with regard to wettability as described in 4.2.4, the flat musters made of it were printed. The results in Fig. 5.17 indicate that the uncoated VerocyanV (RGD 845) surfaces were under-air hydrophilic and underwater oleophobic. In contrast, by introducing nanoparticle coating (Tegotop<sup>®</sup> 210) to the surface, the wettability of the samples changed to under-air hydrophobic and underwater oleophilic. Therefore, wettability alteration using Tegotop<sup>®</sup> 210 resulted in a dramatic decrease in underwater oil contact angle from 139.2° to 20.3°, which is in the oleophilic range. [68]



**Fig. 5.17 Wettability analysis of uncoated/coated flat musters of VerocyanV (RGD 845) [68].**

As explained in section 2.2.2, generally speaking, droplets on fibers adopt one of two shape regimes: they are either shaped like a clamshell or like a barrel. Clamshell-shaped oil droplets develop on oleophobic fibers because the oil droplet tries to minimize the contact area with the fiber. Droplets on oleophilic fibers, in contrast, try to maximize the contact area by entwining the fiber, adopting hereby a barrel-like shape. Fig. 5.18 (a<sub>1</sub>) and (b<sub>1</sub>) illustrate these two shape regimes on the uncoated and Tegotop® 210 coated cone models. In Fig. 5.18 (a<sub>2</sub>), an oil droplet of silicon 10 with a diameter of 1 mm that was placed at the tip of an uncoated conical model (immersed in water) formed a clamshell-shaped regime and remained motionless. While, as illustrated by the image sequences in Fig. 5.18 (b<sub>2</sub>), the positioned oil droplet on the Tegotop® 210 coated cone started to transform from clamshell to barrel shape at the moment it came into contact with the coated surface. Once the barrel-shaped regime was established, the oil droplet spontaneously began to move from the tip towards the base of the cone. As shown in Fig. 5.18 (b<sub>1</sub>), due to high hydrophobicity as well as underwater air retention property, the Tegotop® 210 coated cone displayed a silvery shine underwater, while the uncoated surface did not (Fig. 5.18 (a<sub>1</sub>)). In particular, this feature was observed clearly when the moving oil droplet began to collect microscopic air pockets trapped beneath water droplets placed on the surface of the cone. In Fig. 5.18 (b<sub>2</sub>) the captured air bubbles inside the moving oil droplet are indicated by red arrows. [68]

As already mentioned in 2.2.1, the air pockets can be created when a rough hydrophobic surface is immersed in water [33]. In this study, this behavior arises from the enhanced oleophilicity caused by the nanoparticles increasing the surface roughness. It can be realized that the first oil droplet generated on the coated cone is initially in the Cassie state. However, due to the directional movement on the cone in which the air bubbles are gathered, the Cassie state is transformed to the Wenzel state for the next generated droplets on the model. [68]



**Fig. 5.18** Directional movement behavior of underwater oil droplet on uncoated/Tegotop® 210 coated conical models [68];

**(a)** A clamshell oil droplet (underwater) on an uncoated conical model with no directional movement, **(b)** a barrel-shaped oil droplet (underwater) on a Tegotop® 210 coated conical model with directional movement from the tip to the base. Scale bar: 2 mm.

In other words, the nanostructure is filled with oil as soon as the coated conical surface comes in contact with the first oil droplets. Thereafter, the pre-wetting condition is met for the next droplets positioned on the surface, resulting in the newly generated droplets being in the Wenzel state on the pre-wetted cone. [32,68]

## 6. Mathematical modeling of self-driven directional movement of underwater oil droplets

It is important to keep in mind that the directional motion of water droplets on the biological surfaces in nature does not warrant the same behavior for oil droplets moving on a similar biomimetic surface immersed in water. Therefore, modeling the behaviors and interactions considering the new presented conditions is an integral part of understanding and designing structured fibers in this study that impart directional motion to droplets in another liquid medium. This has to be realized through the comprehensive development of one theoretical model, which reveals the structural influence of micro and macro geometry of fiber surface as well as discloses the liquid droplet's behavior along them. As described in section 2.6.2, research dealing with the movement of a liquid on solid structures immersed in another liquid deals primarily with experimental efforts, in which the mechanisms governing the directional movement of droplets on solid surfaces are mostly investigated very cursory. Indeed, they have solely investigated the key parameters and at the best formulated or modeled them in the frame of individual acting forces listed in Tab. 2.2, through which the outcomes of the experimental observations could be interpreted qualitatively. As a consequence of the lack of a comprehensive theoretical model, which presents the effect of all acting forces together, it is difficult or even impossible to predict the values of model-defining parameters that allow a straightforward construction of efficient oil-water separators (oil separation in/from flowing aqueous media). Therefore, this deficiency has motivated us to investigate the underwater self-movement of barrel-shaped oil droplets on conical structures and to develop a comprehensive model based on first principles of physics to verify hypothesis number (2) stated in section 3.2. [68]

### 6.1 Simplification for solid model geometry and oil droplet shape regime

Based on literature studies in section 2.5, a spindle-knot structure can be regarded as composed of two opposite circular and conical objects, which are assembled by joining two cones at their base. [32]

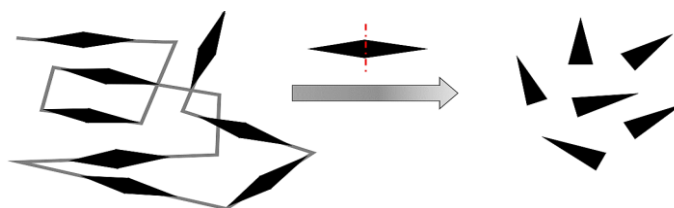


Fig. 6.1 The relationship between spindle-knot and conical model



In this study, the theoretical model for barrel-shaped oil droplets, which have an axially symmetrical spherical shape, will be developed. As explained in section 2.2.2, to have the mentioned shape regime on the considered solid model, the two main conditions must be met: creating a suitable wettability property on the solid model (underwater oleophilic) and maintaining a suitable ratio for liquid droplet and solid model radius ( $r < R$ ). Considering the described simplifications, the theoretical model is developed for a barrel-shaped oil droplet attached to a conical model with half-apex angle  $\alpha$  shown in Fig. 6.2.  $\theta_r$  and  $\theta_a$  denote the receding and advancing contact angle, respectively.  $d$  denotes the averaged thickness of the droplet and  $L$  is the length of the droplet parallel to the cone surface.  $r_r$  and  $r_a$  are the radii of the cone at the related contact lines. [68]

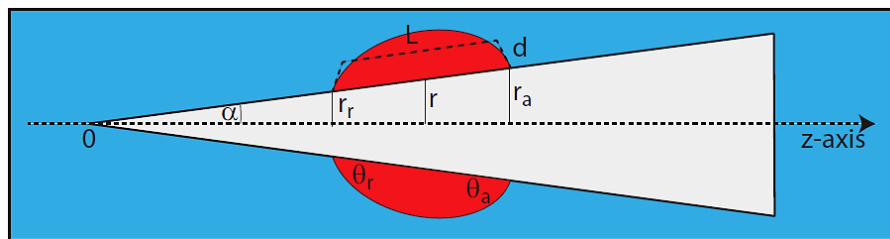


Fig. 6.2 A barrel-shaped oil droplet on a conical model with half-apex angle  $\alpha$  [68].

In the following, we start to analyze the fundamental principles of a local directed transport of oil droplets in water on chemically and topographically structured conical models.

## 6.2 Forces acting on the droplet

The findings in chapter 2 and the formulas listed in Tab. 2.2 provided us with a solid theoretical basis to further analyze the behavior of underwater oil droplet movements along the cone model through the main acting forces. The following subsections present the extended form of the acting forces and their adjustment according to the conditions considered in this study.

### 6.2.1 Laplace force

The main driving force moving the oil droplet towards the thicker end (i.e. the base) of the cone is due to the Laplace pressure gradient within the droplet, caused by the conical model geometry:

$$F_d \approx -\Omega \frac{dP}{dz} \quad (6.1)$$



$\Omega$  denotes the droplet volume and the z-axis is oriented to coincide with the symmetry axis of the cone (Fig. 6.2). An approximate expression of equation (6.1) for the case of a quasi-spherical barrel-shaped droplet reads [57,60,61,63,68]

$$F_d = \frac{2\gamma\Omega \tan \alpha}{(r + R)^2} \quad (6.2)$$

where  $\alpha$  denotes the half-apex angle of the cone (Fig. 6.2),  $r$  is the radius of the cone that varies with  $z$  according to  $r = z \tan \alpha$ , and  $\gamma := \gamma_w - \gamma_o$  is the surface tension of the water-oil interface (the subscripts  $w$  and  $o$  denote “water” and “oil”, respectively). The radius-like quantity  $R$  is defined via the volume  $\Omega$  of the oil droplet by the relation [68]

$$R = \sqrt{\frac{3\Omega}{4\pi}} \quad (6.3)$$

### 6.2.2 Hysteresis force

Coating the cone with nano-particles of which Tegotop<sup>®</sup> 210 consists (section 5.4) causes the pinning of both the advancing and the receding contact line (where oil and water meet with the cone surface), giving rise to the hysteresis force [68]

$$\begin{aligned} F_h &= -2\pi\gamma [r_r (\cos \theta_r - \cos \theta) + r_a (\cos \theta - \cos \theta_a)] \\ &= -2\pi\gamma \left[ r (\cos \theta_r - \cos \theta_a) \right. \\ &\quad \left. + \frac{L}{2} \sin \alpha (2 \cos \theta - \cos \theta_r - \cos \theta_a) \right] \end{aligned} \quad (6.4)$$

$r_r = r - (L/2) \sin \alpha$  and  $r_a = r + (L/2) \sin \alpha$  are the radii of the contact circles,  $\theta_r$  and  $\theta_a$  are the receding and the advancing contact angles between the oil droplet and the fiber, respectively,  $\theta = (\theta_a + \theta_r)/2$  is the mean value of both, and  $L$  denotes the length of the drop (Fig. 6.2). The rationale behind equation (6.4) is that the factor proportional to the difference  $(\cos \theta_r - \cos \theta)$  represents the pinning forces which the receding contact line has to overcome, and that  $(\cos \theta - \cos \theta_a)$  is similarly related to the advancing contact line; that is, both force terms act in a decelerating way on the droplet [159].

The measurements in this study showed that both the advancing and the receding contact angle decrease by about  $15^\circ - 25^\circ$  between the starting point and the endpoint of the droplet movement. To include this variation in equation (6.4) it is assumed for simplicity that the contact angles depend linearly on the droplet velocity  $v$  [160], according to

$$\theta_r = m_r v + b_r \quad (6.5)$$

$$\theta_a = m_a v + b_a \quad (6.6)$$

with  $m_r = \Delta\theta_r/v_0$  and  $b_r = \theta_{r,k} - m_r v_k$ .  $\Delta\theta_r$  denotes the range of  $\theta_r$ , while  $\theta_{r,k}$  and  $v_k$  are known values of  $\theta_r$  and  $v$ , respectively, measured at the point  $k$  of the droplet's trajectory.

Upon insertion of  $m_r$  and  $b_r$  (and similar expressions for  $\theta_a$ ), equations (6.5) and (6.6) transform to

$$\theta_r = \theta_{r,k} + \frac{\Delta\theta_r}{v_0} (v - v_k) \quad (6.7)$$

$$\theta_a = \theta_{a,k} + \frac{\Delta\theta_a}{v_0} (v - v_k) \quad (6.8)$$

The droplet velocity  $v_k$  related to the contact angles  $\theta_{r,k}$  and  $\theta_{a,k}$  can be calculated from the measurements via the fraction

$$v_k = \frac{z_{k+1} - z_{k-1}}{t_{k+1} - t_{k-1}} \quad (6.9)$$

### 6.2.3 Friction force (internal dissipation)

The movement of the droplet along the cone generates an energy-consuming spatial reorganization of the oil molecules within the droplet. The energy dissipated in this process contributes to its deceleration. For a quasi-spherical droplet, this type of friction force ( $F_v$ ) can be described as [57,63]

$$F_v = -r^3 \sqrt{\gamma(\mu_o l v)^2} \quad (6.10)$$

where  $\mu_o$  and  $v$  are the dynamic viscosity and the absolute value of the velocity of the oil droplet, respectively. Here,  $l$  is an approximately constant factor in equation (6.10) and the value  $l \approx 5$  has been adopted because during experiments the surface of the cone was covered with a thin oil layer [127]. [68]

### 6.2.4 Drag force

In this study, drag forces hindering the motion of the droplet come in two varieties: (i) the friction between the oil droplet and the surrounding water ( $F_{fluid-drop}$ ), and (ii) the friction

between the oil droplet and the surface of the cone ( $F_{drop-fiber}$ ). Both drag forces depend on the droplet velocity  $v$  (it is assumed that the water body does not move with respect to the cone) and are expressed in equations (6.11) and (6.12), respectively. [68]

$$F_{fluid-drop} = -\frac{1}{2} \rho_{fluid} v_{drop}^2 C_{fluid-drop} A_{drop} \quad (6.11)$$

$$F_{drop-fiber} = -\frac{1}{2} \rho_{drop} v_{drop}^2 C_{drop-fiber} A_{fiber} \quad (6.12)$$

We use for the sum of the friction forces the expression

$$F_f = -\frac{1}{2} v^2 (\rho_w C_{wo} A_{wo} + \rho_o C_{fo} A_{fo}) \quad (6.13)$$

where,  $\rho_w$  and  $\rho_o$  are the densities of water and oil, respectively.  $A_{wo}$  and  $A_{fo}$  denote the areas where water and oil and the cone surface and oil are in contact.  $C_{wo}$  and  $C_{fo}$  are the drag coefficients related to the two cases.

The droplet velocities obtained from the experimental data yield values of roughly  $Re \approx 1$ . This suggests applying the expression [66,161]

$$c_i = \frac{24}{Re_i} (1 + 0.14 Re_i^{0.7}) \quad (i = wo, fo) \quad (6.14)$$

for the drag coefficients with the corresponding Reynolds numbers

$$Re_{wo} = \frac{\rho_w v L_{wo}}{\mu} \quad (6.15)$$

$$Re_{fo} = \frac{\rho_o v L_{fo}}{\mu_o} \quad (6.16)$$

Here,  $L_{wo}$  and  $L_{fo}$  denote typical lengths that characterize the contact areas of water and oil droplet and the cone and the oil droplet, respectively. For an oil droplet (viscosity  $\mu_o$ ) moving through a bulk of water (viscosity  $\mu_w$ ) the viscosity of both liquids should be considered. This is achieved by redefining the (dynamic) viscosity as [66,162]

$$\mu = \mu_w \left( \frac{1 + \frac{2\mu_w}{3\mu_o}}{1 + \frac{\mu_w}{\mu_o}} \right) \quad (6.17)$$

Using equation (6.14) to (6.17) in equation (6.13) produced

$$F_f = -12v \left( \frac{\mu A_{wo}}{L_{wo}} + \frac{\mu_o A_{fo}}{L_{fo}} \right) - 1.68 v^{1.7} \left( \frac{\mu^{0.3} \rho_w^{0.7} A_{wo}}{L_{wo}^{0.3}} + \frac{\mu_o^{0.3} \rho_o^{0.7} A_{fo}}{L_{fo}^{0.3}} \right) \quad (6.18)$$

In order to evaluate equation (6.18), more detailed expressions for the quantities  $L_{wo}$ ,  $L_{fo}$ ,  $A_{wo}$  and  $A_{fo}$  are required.  $L_{wo}$  and  $L_{fo}$ , introduced by the Reynolds numbers equation (6.15) and (6.16), imply a certain ambiguity regarding the choice of a typical length. Since it is assumed that friction (and not body drag) is the essential drag component, the length (taken parallel to the flow) of the water-oil contact area  $A_{wo}$  and of the cone-oil contact area  $A_{fo}$  were taken as the reference lengths.

In principle, it is possible to calculate  $A_{wo}$ ,  $A_{fo}$ ,  $L_{wo}$  and  $L_{fo}$  from the shape of the droplet, which depends in turn on the droplet volume, the model geometry and the contact angle and its hysteresis. In reality, however, one is confronted with complicated and extremely lengthy mathematical relations. Therefore, resorting to a crude simplification, which is to some extent justified by the barrel-like shape of the droplet: the droplet was modeled as a collar of averaged thickness  $d$ , assuming that  $d$  is small compared to the cone radius  $r$  at the position of the droplet (Fig. 6.2).

These assumptions imply immediately  $L_{wo} = L_{fo} =: L$  and  $A_{wo} = A_{fo} =: A$ . The geometry of truncated cones (Fig. 6.2) supplies the relation

$$A = 2\pi rL \quad (6.19)$$

Insertion of equation (6.19) into equation (6.18) with the approximations  $L_{wo} = L_{fo} =: L$  and  $A_{wo} = A_{fo} =: A$  results in

$$F_f = -24\pi r(\mu + \mu_o)v - 3.36\pi rL^{0.7}(\mu^{0.3}\rho_w^{0.7} + \mu_o^{0.3}\rho_o^{0.7})v^{1.7} \quad (6.20)$$

### 6.2.5 Gravity force

As far as the equation of motion is concerned, gravity is negligible if it is much smaller than the surface forces. This is the case if the Bond-Number [36,63]

$$Bo = \frac{(\rho_w - \rho_o)gR^2}{\gamma} \quad (6.21)$$

is smaller than about one. The condition  $Bo \ll 1$  transforms to

$$R \ll \lambda_c \quad (6.22)$$

where

$$\lambda_c = \sqrt{\frac{\gamma}{(\rho_w - \rho_o)g}} \quad (6.23)$$

denotes the capillary length [63]. The densities of the silicon oils used in the experiments were  $\rho_o = 930 \text{ kg m}^{-3}$  and  $\rho_o = 970 \text{ kg m}^{-3}$  for silicon 10 and silicon 100, respectively. By inserting these values together with  $\rho_w = 998 \text{ kg m}^{-3}$  for the density of water into the right-hand side of the equation (6.22), one obtains the conditions  $R \ll 8.8 \text{ mm}$  for  $\rho_o = 930 \text{ kg m}^{-3}$  and  $R \ll 13 \text{ mm}$  for  $\rho_o = 970 \text{ kg m}^{-3}$ , where  $R$  is the radii of oil droplets that are unaffected by gravitation. In this study, the generated droplets fulfilled these conditions and also attained a highly axially symmetric shape with respect to the cone axis to which they adhered. [68]

### 6.3 Theoretical model: equation of motion

Identifying the  $z$ -axis with the symmetry axis of the cone and choosing the tip of the cone as its origin, the local cone radius  $r$  can be expressed as (Fig. 6.2)

$$r = z \tan \alpha \quad (6.24)$$

The equation of motion connects the droplets acceleration in the  $z$ -direction with the  $z$ -components of the forces discussed above. Due to the axial symmetry of cone and droplet, these are obtained by multiplying the forces with the factor  $\cos \alpha$ , yielding

$$\frac{dMv}{dt} = \rho_o \Omega \frac{d^2z}{dt^2} = F_{d,z} + F_{h,z} + F_{v,z} + F_{f,z} \quad (6.25)$$

Where  $M$ ,  $v$ ,  $\rho_o$ , and  $\Omega$  denote the mass, velocity, density, and the volume of the oil droplet, respectively. Inserting expressions equation (6.2), (6.4), (6.10), and (6.20) into equation (6.25), a comprehensive expression results that describes the movement of an oil droplet on a cone that is immersed in water:

$$\begin{aligned}
\rho_o \Omega \frac{d^2 z}{dt^2} = & \frac{2\gamma \Omega \sin \alpha}{(z \tan \alpha + R)^2} - z \sin \alpha \sqrt[3]{\gamma (\mu_o l)^2} \left(\frac{dz}{dt}\right)^{2/3} \\
& - k_1 \left[ 24\pi z \sin \alpha (\mu + \mu_o) \left(\frac{dz}{dt}\right) \right. \\
& \left. + 3.36\pi z \sin \alpha L^{0.7} (\mu^{0.3} \rho_w^{0.7} + \mu_o^{0.3} \rho_o^{0.7}) \left(\frac{dz}{dt}\right)^{1.7} \right] \quad (6.26) \\
& - 2\pi\gamma \left[ \left(z - \frac{L}{2} \cos \alpha\right) (\cos \theta_r - \cos \theta) \right. \\
& \left. + \left(z + \frac{L}{2} \cos \alpha\right) (\cos \theta - \cos \theta_a) \right] \sin \alpha
\end{aligned}$$

with

$$\theta_r = k_2 [\theta_{r,k} - v_k] + \frac{\Delta \theta_r}{v_0} \left(\frac{dz}{dt}\right) \quad (6.27)$$

$$\theta_a = k_2 [\theta_{a,k} - v_k] + \frac{\Delta \theta_a}{v_0} \left(\frac{dz}{dt}\right) \quad (6.28)$$

This is a nonlinear ordinary differential equation of second order for the function  $z(t)$ ; a definite solution requires that the initial position  $z|_{t=0}$  and the initial velocity  $dz/dt|_{t=0}$  of the oil droplet are prescribed. Unfortunately, closed solutions cannot be obtained. The constants  $k_1$  and  $k_2$  in equation (6.26) are fitting parameters that slightly generalize the forces  $F_h$  and  $F_f$  and they are used to bring solutions of equation (6.26) into agreement with experimental data. For  $k_1 = k_2 = 1$  equation (6.4), (6.7), (6.8), and (6.20) are recovered.

For meaningful values of the parameters the first term on the right-hand side of the equation (6.26) (representing  $F_d$ ) is invariably positive, that is, it accelerates the droplet, whereas the other terms (related to  $F_v$ ,  $F_f$ , and  $F_h$ ) are necessarily negative, they decelerate the droplet.

If a droplet is placed at  $z \approx 0$ , that is, close to the tip of the cone, due to the  $z$ -dependence of the other forces the first term on the right-hand side (the accelerating force  $F_d$ ) dominates and the droplet is pushed to higher  $z$ -values. If  $z$  is increased,  $F_d$  decreases (but remains positive) while the other terms attain increasingly negative values that compensate more and more for  $F_d$ . If the cone is long enough, there exists consequently a point  $z_f$ , where the acceleration and deceleration forces are balanced and the droplet stops.

At  $z_f$ , the droplet's velocity and acceleration vanish. Setting  $dz/dt = 0$  and  $d^2z/dt^2 = 0$ , the right-hand side of the equation (6.26) becomes an algebraic third order equation in  $z$  from which exact but lengthy solutions for  $z_f$  can be calculated. An approximate solution for  $z_f$  is obtained by setting  $dz/dt = 0$  and  $d^2z/dt^2 = 0$  in equation (6.26), expanding the result up to the linear term in  $z$ , and solving for  $z$ . This yield

$$z_f \approx \frac{\cos \alpha}{2} \left[ \frac{8R + 3L \cos \alpha (\cos \theta_a + \cos \theta_r) - 6L \cos \left( \frac{\theta_a + \theta_r}{2} \right)}{8 \sin \alpha + 3(\cos \theta_r - \cos \theta_a)} \right] \quad (6.29)$$

with equations (6.27) and (6.28) simplifying to

$$\theta_r = k_2 \theta_{r,k} - \Delta \theta_r \frac{v_k}{v_0} \quad (6.30)$$

$$\theta_a = k_2 \theta_{a,k} - \Delta \theta_a \frac{v_k}{v_0} \quad (6.31)$$

as a consequence of setting  $dz/dt = 0$ . If the equilibrium contact angle  $\theta = (\theta_a + \theta_r)/2$  and the hysteresis (half) angle  $\chi = (\theta_a - \theta_r)/2$  are introduced, equation (6.29) simplifies further to

$$z_f = \frac{\cos \alpha}{2} \left[ \frac{4R - 3L \cos \theta (1 - \cos \alpha \cos \chi)}{4 \sin \alpha + 3 \sin \theta \sin \chi} \right] \quad (6.32)$$

Although equation (6.32) is an approximate expression, experimental results suggest that it describes the droplet behavior qualitatively correctly.

- i. Droplet radius  $R = \sqrt[3]{3\Omega/4\pi}$  and droplet length  $L$  (Fig. 6.2) indicate the volume of the droplet and they appear only in the numerator of  $z_f$  (equation (6.32)). Thus, bigger droplets stop farther away from the tip of the model than smaller droplets. In case a droplet that has already reached its final position  $z_f$  is hit by and united with another droplet, the newly formed droplet (whose radius exceeds necessarily the radii of its constituents) will either restart and move away from the tip of the cone toward an adjusted value of  $z_f$ , or it detaches from the cone because the buoyancy force of the newly formed droplet exceeds the surface forces that bind the droplet to the cone surface.
- ii. If the half-apex angle  $\alpha$  of a cone is increased, the final positions  $z_f$  of traveling droplets move towards the tip of the cone. This is because  $\sin \alpha$  increases and  $\cos \alpha$  decreases with  $\alpha$  in equation (6.32), implying that  $z_f$  decreases with increasing  $\alpha$ .
- iii. For a given hysteresis (half) angle  $\chi$ , oleophilic cone surfaces (characterized by small values of  $\theta < \pi/2$ ) produce higher values of  $z_f$  than oleophobic surfaces (characterized by  $\pi/2 < \theta < \pi$ ).
- iv. For a given contact angle  $\theta$ , low hysteresis (half) angles  $\chi$  yield higher values of  $z_f$  than high hysteresis angles.

Notice that the droplet's approach to its terminal position  $z_f$  is asymptotic, that is, it requires an infinite amount of time. [68]

## 6.4 Validation of the theoretical model

### 6.4.1 Solution of the equation of motion

In this section, numerical solutions of equation (6.26) calculated with the programming language *Python* will be compared with path-time graphs obtained from the corresponding experiments. To investigate if equation (6.26) (together with appropriate initial values for position and velocity) predicts path-time graphs  $z(t)$  correctly, the dynamic behavior of oil droplets released on the conical models (immersed in water) was recorded. The videos and the images were taken using a high-performance camera with a USB 3.0 interface and a 10-fold zoom lens of the contact angle measurement system (OCA200, Dataphysics, Germany). Since the size and the viscosity of the oil droplet play vital roles in the unfolding droplet dynamics, therefore the tests were run for three different droplet diameters and two different oil viscosities. [68]

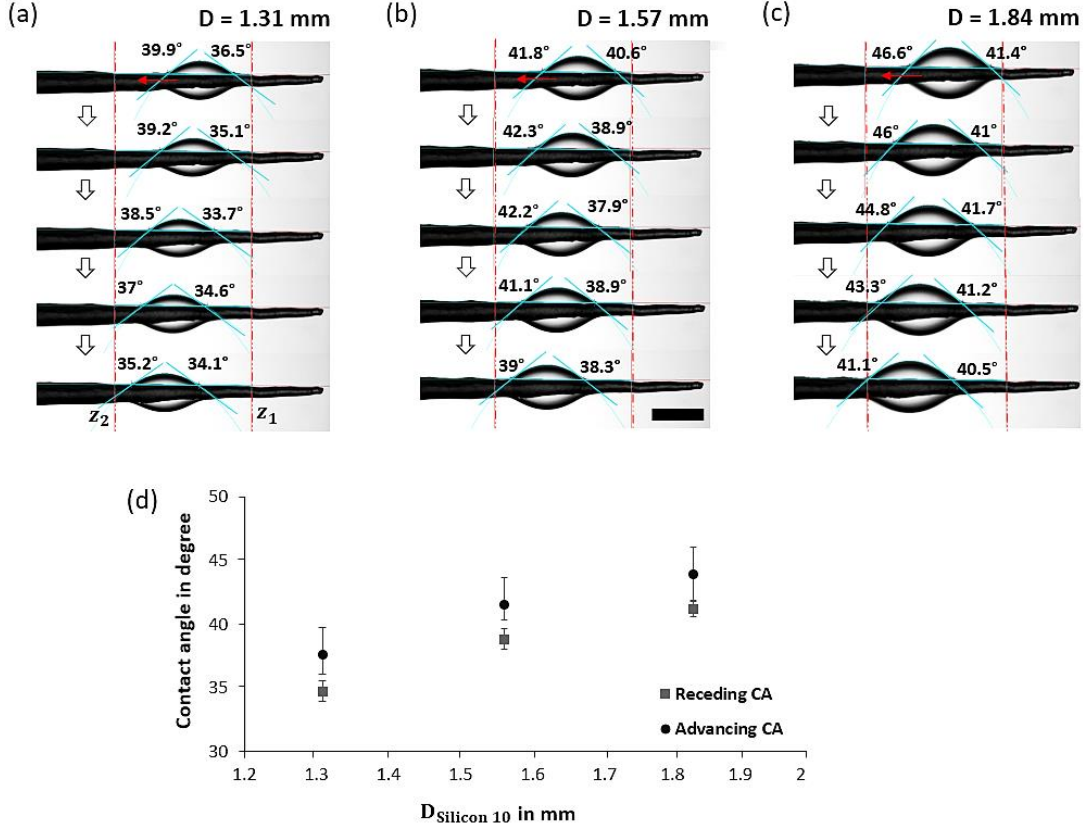
### 6.4.2 Input data

In equation (6.26), the size of an oil droplet is characterized by its volume  $\Omega$  and by its length  $L$  (as indicated in Fig. 6.2). In the figures that display experimental results, however, size is described by the (fictitious) radius  $R$ , defined via equation (6.3), or the diameter  $D = 2R = \sqrt[3]{6\Omega/\pi}$ . The size of the oil droplets used in the experiments (with diameters in the millimeter range) was dictated (a) by the dimensions of the fabricated conical models and (b) by the requirements to maintain a quasi-spherical barrel-shaped regime along the cone (that is,  $r < R$  was to be guaranteed as the droplets moved from the tip to the base of the cone). In the experiments, it appeared that the droplet length  $L$  is approximately constant, i.e. it depends only weakly on the droplet's position on the cone. Path-time graphs were recorded at altogether six test runs for the droplet diameter/length pairs  $(D, L) = (1.31 \text{ mm}, 2.41 \text{ mm}), (1.57 \text{ mm}, 2.68 \text{ mm})$  and  $(1.84 \text{ mm}, 2.90 \text{ mm})$ , combined with oils of two different viscosities, namely  $\mu_o = 9.3 \text{ mPa s}$  (silicon 10) and  $\mu_o = 96 \text{ mPa s}$  (silicon 100). In all six test runs the same cone with a half-apex angle  $\alpha = 1.5^\circ$  and coated with Tegotop<sup>®</sup> 210 was used.

The contact angles were measured during the movement of the droplets. It was observed that they depend on droplet size (see Fig. 6.3 (d) for silicon 10 droplets) and — only weakly — on the  $z$ -position of the droplet (see Fig. 6.3 (a-c) for silicon 10 droplets). The latter dependency is not very pronounced; this suggests to approximate the real values by averages for the advancing and receding contact angles in equation (6.26). For silicon 10 oil these values amounted to:  $(\theta_r, \theta_a) = (34.7^\circ, 37.6^\circ)$  for a droplet with  $D = 1.31 \text{ mm}$ ,



$(\theta_r, \theta_a) = (38.8^\circ, 41.5^\circ)$  for  $D = 1.57$  mm, and  $(\theta_r, \theta_a) = (41.2^\circ, 43.9^\circ)$  for  $D = 1.84$  mm. For silicon 100 oil we obtained nearly identical values:  $(\theta_r, \theta_a) = (34.1^\circ, 37.6^\circ)$  for a droplet with  $D = 1.31$  mm,  $(\theta_r, \theta_a) = (38.1^\circ, 40.9^\circ)$  for  $D = 1.57$  mm, and  $(\theta_r, \theta_a) = (41.2^\circ, 43.9^\circ)$  for  $D = 1.84$  mm. For the parameter  $l$  in equation (6.10) we chose, following an argument of *Lorenceanu et al.* [57], the value  $l = 5$ . [68]



**Fig. 6.3 Advancing and receding contact angle of underwater barrel-shaped oil droplet moving along a cone [68];**

**(a-c)** Advancing and receding contact angles measured for silicon 10 droplets of three different diameters  $D$  moving from right to left on a cone with a half-apex angle of  $1.5^\circ$ , **(d)** mean values and standard deviations of the receding and advancing contact angles shown in (a-c). Scale bar: 2 mm.

### 6.4.3 Initial values

In order to obtain definite solutions of equation (6.26), the initial position  $z_0 = z|_{t=0}$  and the initial velocity  $v_0 = dz/dt|_{t=0}$  of the oil droplet have to be prescribed. When the oil droplets were applied to the tip of the cone (using a fine needle with an outer diameter of 0.21 mm), they underwent a short phase of consolidation until they had assumed the barrel-like shape that is a precondition for the applicability of equation (6.26). Accordingly, the first position where this was achieved was chosen as the initial position  $z_0$ . Similarly, the initial velocity  $v_0$  was obtained by dividing the distance between  $z_0$  and the next but

one measured droplet position divided by the related time span. This procedure resulted in the following initial value pairs:

- **Silicon 10 droplets**  $(z_0, v_0) = (6.64 \text{ mm}, 3.93 \text{ mm s}^{-1}), (6.64 \text{ mm}, 5.65 \text{ mm s}^{-1}),$  and  $(6.64 \text{ mm}, 7.22 \text{ mm s}^{-1})$  for droplets with diameters  $D = 1.31 \text{ mm}, D = 1.57 \text{ mm},$  and  $D = 1.84 \text{ mm},$  respectively.
- **Silicon 100 droplets**  $(z_0, v_0) = (6.64 \text{ mm}, 0.58 \text{ mm s}^{-1}), (6.64 \text{ mm}, 0.85 \text{ mm s}^{-1}),$  and  $(6.64 \text{ mm}, 0.99 \text{ mm s}^{-1})$  for droplets with diameters  $D = 1.31 \text{ mm}, D = 1.57 \text{ mm},$  and  $D = 1.84 \text{ mm},$  respectively.

equation (6.26) was numerically solved for these initial values and the parameter combinations already discussed, employing time steps  $\Delta t \approx 3 \text{ ms}.$  [68]

#### 6.4.4 Comparison of predictions and experimental results

Subfigures (a) of Fig. 6.4 and Fig. 6.5 show experimentally obtained (time, position)-data points (red, black, and blue triangles) and the related solutions  $z(t)$  of equation (6.26) (solid curves) for several combinations of droplet size and droplet viscosity and the parameters discussed above.

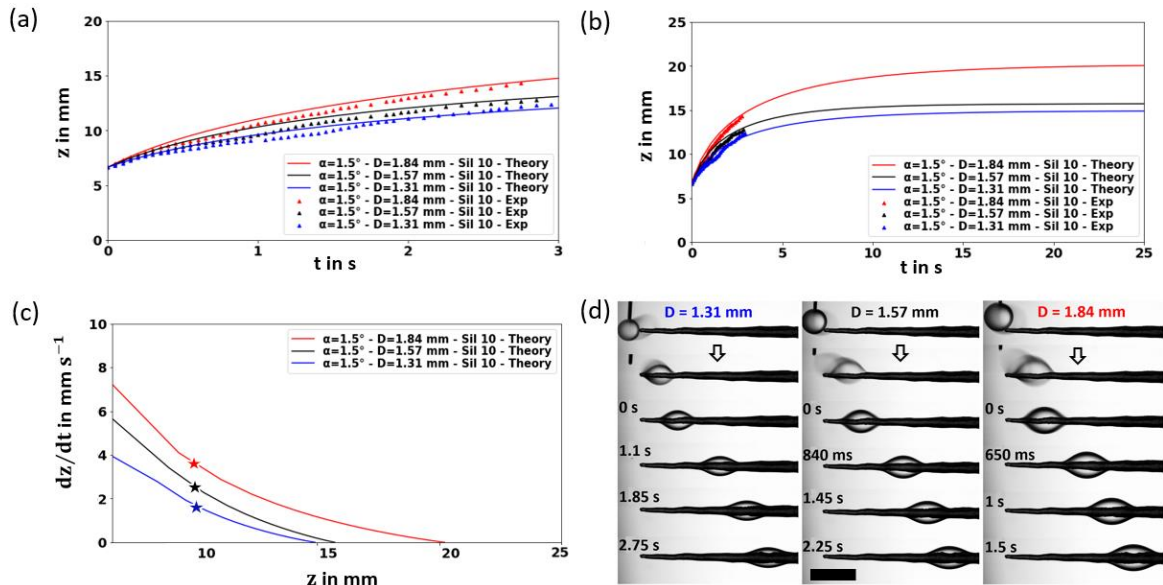
As mentioned before, the fitting parameters  $k_1$  and  $k_2$  have been introduced in equation (6.26) to compensate for deviations between the theoretical considerations that lead to equation (6.26) and reality. The theoretical curves shown in of Fig. 6.4 and Fig. 6.5 were obtained by adjusting them to the following values:

- **Silicon 10 droplets**  $(k_1, k_2) = (2, 0.9), (k_1, k_2) = (3, 1.25),$  and  $(k_1, k_2) = (3.8, 1),$  for droplets with diameters  $D = 1.31 \text{ mm}, D = 1.57 \text{ mm},$  and  $D = 1.84 \text{ mm},$  respectively.
- **Silicon 100 droplets**  $(k_1, k_2) = (2.5, 1.1), (k_1, k_2) = (2.8, 1.3),$  and  $(k_1, k_2) = (3.8, 1.3),$  for droplets with diameters  $D = 1.31 \text{ mm}, D = 1.57 \text{ mm},$  and  $D = 1.84 \text{ mm},$  respectively.

Subfigures (b) of Fig. 6.4 and Fig. 6.5 show the course of the theoretical curves beyond the experimentally obtained (time, position)-data points and subfigures (c) depict the corresponding (velocity, position)-diagrams. Notable properties of these diagrams are: [68]

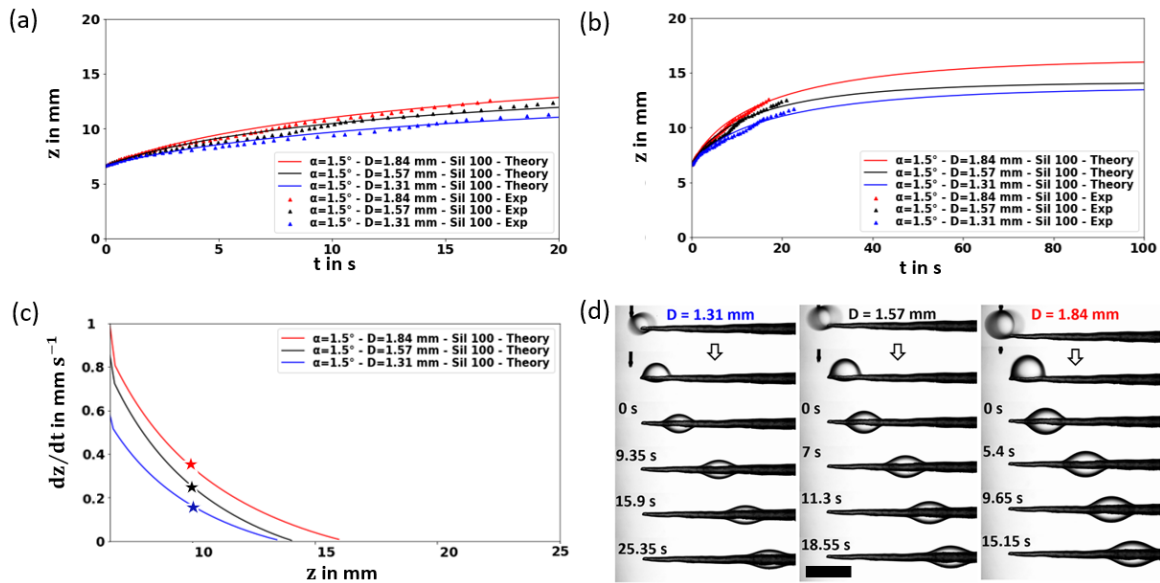
- Larger droplets move with higher velocities than smaller droplets of the same viscosity, according to subfigures (c).
- As predicted by equation (6.32), the position  $z_f$  where the droplet motion terminates increases with droplet size (in subfigures (c),  $z_f$  is indicated by the intersection of the velocity-distance curves with the  $z$ -axis).

- Comparison of Fig. 6.4 (b) and Fig. 6.5 (b) suggests that the distances  $z_f - z_0$  covered by the droplets are dependent on the viscosity of the oil: droplets with lower viscosity (but the same diameter) traverse slightly longer distances. The influence of viscosity on the time spans that the droplets need to cover the distance  $z_f - z_0$  is much more pronounced: they differ by about an order of magnitude, because the more viscous droplets move much slower, as is evident by comparing Fig. 6.4 (c) and Fig. 6.5 (c).



**Fig. 6.4 Results of experiments and theoretical model for an underwater barrel-shaped oil droplet moving along a cone [68];**

(a) Experimentally obtained (time, position)-data points (red, black, and blue triangles) and the related solutions  $z(t)$  of equation (6.26) (solid curves) for several combinations of size and viscosity of a Silicon 10 droplet. Other parameter values are as given in the section on input data. (b) theoretical curves calculated from equation (6.26) beyond the experimentally obtained (time, position)-data points, (c) (velocity, position)-diagrams derived from the curves shown in (b), (d) optical images of the dynamic behavior of oil droplets of different sizes (underwater) on the prepared conical model. Scale bar: 2 mm.

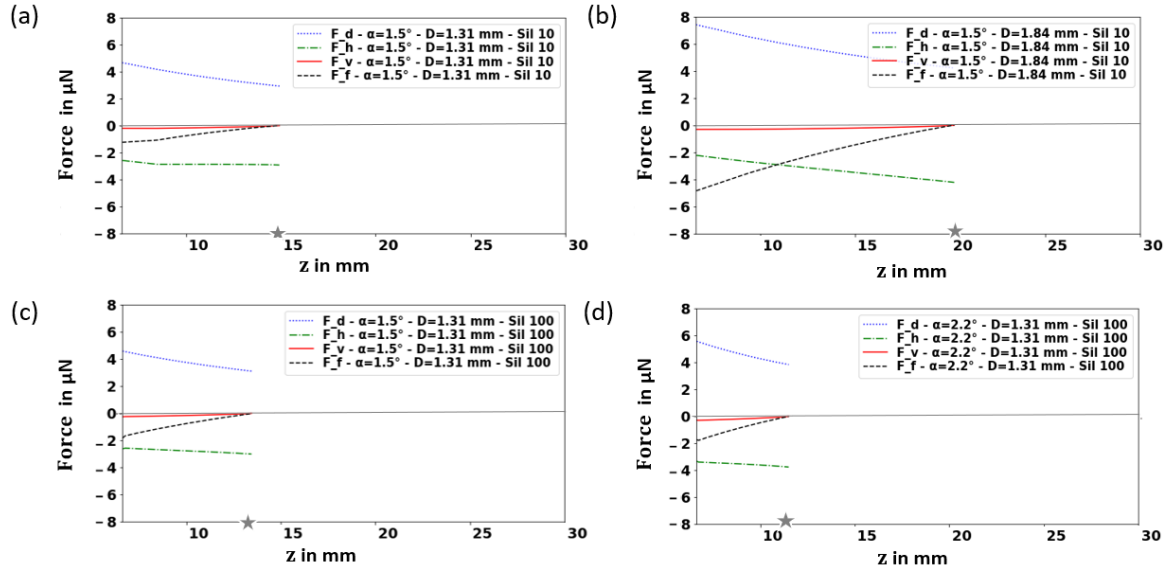


**Fig. 6.5 Results of experiments and theoretical model for an underwater barrel-shaped oil droplet moving along a cone [68];**

**(a)** Experimentally obtained (time, position)-data points (red, black, and blue triangles) and the related solutions  $z(t)$  of equation (6.26) (solid curves) for several combinations of size and viscosity of a Silicon 100 droplet. Other parameter values are as given in the section on input data. **(b)** theoretical curves calculated from equation (6.26) beyond the experimentally obtained (time, position)-data points, **(c)** (velocity, position)-diagrams derived from the curves shown in (b), **(d)** optical images of the dynamic behavior of oil droplets of different sizes (underwater) on the prepared conical model. Scale bar: 2 mm.

### 6.4.5 Forces, revisited

It is instructive to insert the solutions of equation (6.26) into equations equation (6.2), (6.4), (6.10), and (6.20) for the forces acting on the oil droplet. Fig. 6.6 shows  $F_d$ ,  $F_h$ ,  $F_v$ , and  $F_f$  as functions of the  $z$ -axis for the different cases. Curve segments above the  $z$ -axis represent forces that push the droplet towards the base of the cone whereas segments below the  $z$ -axis are related to forces that retard it. [68]



**Fig. 6.6** Driving and resisting forces acting on an underwater barrel-shaped oil droplet moving along a cone [68];

(a-d) Influence of droplet size, viscosity and the half-apex angle of the cone on the forces acting on the droplet. Parameter values are as given in the section on input data.

- Size:** Fig. 6.6 (a) and (b) represent two oil droplets of different size ((a):  $D = 1.31$  mm, (b):  $D = 1.84$  mm) but of the same viscosity (silicon 10) moving along the same cone (with half-apex angle  $\alpha = 1.5^\circ$ ). Obviously, the bigger droplet experienced a stronger (accelerating) Laplace force  $F_d$  (blue, dotted line) and a stronger (decelerating) friction force  $F_f$  (gray, dashed line). This corroborates expression in (6.2), which states  $F_d \propto \Omega$  and expression in (6.20), according to which  $F_f$  increases with droplet length (indicated by  $L$ ) and droplet velocity  $v$ . The latter increases also with droplet size (indicated by  $D$ ), according to Fig. 6.4 (c). The hysteresis force  $F_h$  (green dash-dotted line) is slightly more pronounced for the bigger droplet, as is to be expected from expression in (6.4) of which one term is proportional to  $L$ . The viscous friction force  $F_v$  (red solid line) is in both cases much smaller than the other forces. The movement of the droplet stops in both cases at the final position  $z_f$  (equation (6.32), indicated by gray stars in Fig. 6.6), where the forces are balanced and the droplet cannot move any further. Notice that  $F_v$  and  $F_f$  become zero (they are proportional to the droplet velocity) whereas neither  $F_d$  nor  $F_h$  are zero but balance one another. The value of  $z_f$  is somewhat higher for the bigger droplet which is to be expected from equation (6.32).
- Viscosity:** Comparison of Fig. 6.6 (a) and (c) shows that an increase of the viscosity of the oil droplet by a factor of about 10 ((a): silicon 10,  $\mu_0 = 9.3$  mPa s, (b): silicon 100,  $\mu_0 = 96$  mPa s) affects the forces  $F_d$ ,  $F_h$ ,  $F_v$ , and  $F_f$  only marginally. This is because (i)  $F_d$  and  $F_h$  depend neither on  $\mu_0$  (the viscosity of the oil) nor on  $\mu$

(defined by expression in (6.17)), (ii) the absolute value of  $F_v$  is — for the input parameters used here — very small, compared with the other forces, and, (iii) the viscosity of water  $\mu_w$  is one order of magnitude smaller than the viscosity of silicon 10, which implies, together with the structure of equation (6.17),  $\mu \approx \mu_w$ .

- **Cone geometry:** The influence of the half-apex angle  $\alpha$  on the forces acting on the droplet is documented by Fig. 6.6 (c) and (d) that differ only by the value of  $\alpha$  ((c):  $\alpha = 1.5^\circ$ , (d):  $\alpha = 2.2^\circ$ ). Since all forces are proportional to  $\sin \alpha$  (according to equation (6.26)) it is to be expected that the ratio of corresponding forces in subfigures (d) and (c) amounts to about  $\sin 2.2^\circ / \sin 1.5^\circ \approx 1.5$ . This is obviously the case.

## 6.5 Conclusion of modeling of self-driven directional movement of underwater oil droplets

In chapter 6 a comprehensive model of the separation of oil and water was developed, which is based on the effect that liquid droplets move on cone-shaped structures driven by capillary forces. For this, the forces acting on the droplets were derived from first principles of physics. Additionally, the relevant existing models and forces introduced in Tab. 2.2 in section 2.8 were extended to a barrel-shaped oil droplet surrounded by water that moves along suitably shaped filaments as fabricated in section 5.4. By bringing together the results of the theoretical model and the corresponding experiments, the underlying mechanism of the directional movement of droplets in another liquid medium was thoroughly investigated and modeled. The resulting model predicts the dependence of the droplet motion on time and on “system defining” parameters, such as droplet size, viscosity, dynamic contact angles formed between droplet and filament surface, and geometry gradient on the filament defined by half-apex angle. [68] Application of the results could predict and facilitate the design of either conical or spindle-knotted fibers that lead to efficient oil/water separation by generating the large and fast ascending oil droplets that can be easily collected from the liquid surface (chapter 8).

## 7. A novel method for measuring dynamic contact angles of fibers with spindle-knots

As can be understood from the literature study, the determination of the dynamic contact angle is of significant interest for the characterization of the wettability of technical fibers and textiles in diverse fields of science and technology. Indeed, it provides information about the contact angle hysteresis, defined as the difference between advancing and receding contact angle, and also the adhesion. It turned out that there exist traditional methods for dynamic contact angle measurements of flat surfaces and of fibers with a uniform cross-sectional shape along the fiber. Since the focus of this study is on the structured fibers, despite the growing achievements of various fabrication methods and designs for spindle-knotted structured fibers, characterization by their wettability still proves to be a major challenge, and no measurement method has been specified and reported, until now. Therefore, as part of this study, a novel method for evaluating spindle-knotted structured fibers with regard to their wettability by measuring the dynamic contact angle was developed, by which the hypothesis number (3) given in section 3.2 was verified. [51]

### 7.1 Basic idea

The basic idea is in the spirit of the Wilhelmy plate method previously described in 4.2.3 and 4.2.5. To measure the contact angle between an object and a liquid, the object is lowered into (or withdrawn from) the liquid and the increase (or decrease) in weight is noted. This change in weight can be attributed to the surface force between liquid and object and the contact angle can be calculated from an equation describing the situation. [59]

### 7.2 Axisymmetric fiber of constant cross-section

Fig. 7.1 illustrates the principle of force tensiometry according to the slightly modified Wilhelmy method. A circular fiber of uniform cross-section (radius  $r = 27.5 \mu\text{m}$ , length  $\ell = 2 \text{ cm}$ ) made of PET was clamped to a force sensor that could be moved up and down. The forces resulting from the immersion in the liquid (deionized water) were recorded together with the position of the fiber and depicted as red and blue dots in Fig. 7.1 (c). The results shown in Fig. 7.1 (c) have been obtained from three successive measurement cycles of dipping a fiber into the liquid producing the blue dots in the lower part of the graph (corresponding to the advancing contact angle), and dragging the fiber out of the liquid, resulting in the red dots in the upper part of the graph (corresponding to the receding contact angle). The measured forces shown in Fig. 7.1 (c) are the sum of three force components in equation (7.1): the weight of the fiber under air ( $F_w$ ), the buoyant force acting on the part

of the fiber that is immersed into the liquid ( $F_b$ ), and the vertical component of the force resulting from the surface tension of the liquid ( $F_t$ ),

$$F(u) = F_w + F_b + F_t = \pi \rho g r^2 \ell - \pi \rho_w g r^2 u + 2\pi r \gamma \cos \theta \quad (7.1)$$

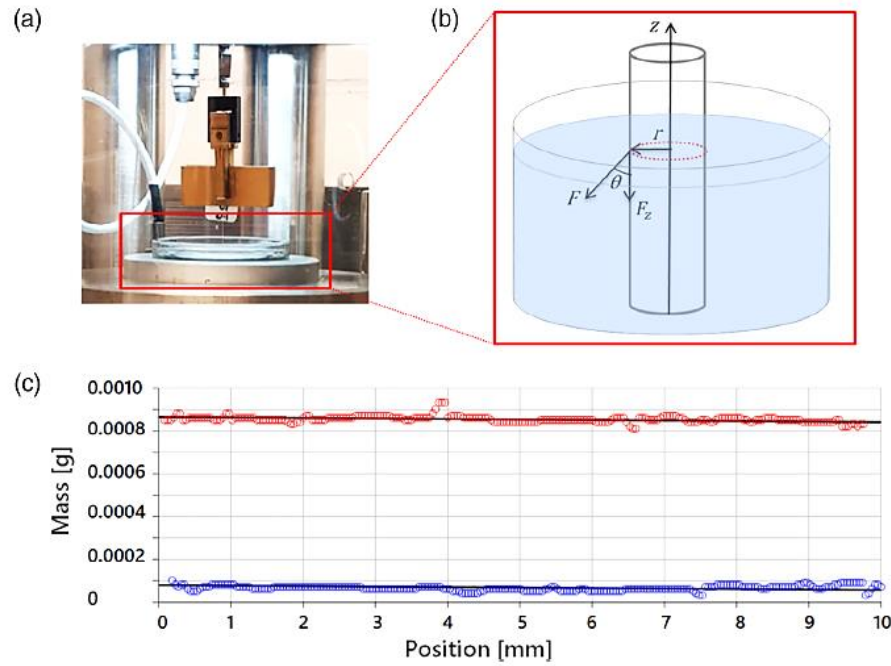
$u$  denotes the immersion depth (designated “position” in Fig. 7.1 (c)).  $\rho_w = 1000 \text{ kg m}^{-3}$  and  $\rho = 1380 \text{ kg m}^{-3}$  are the densities of water and of the PET fiber, respectively,  $g = 9.81 \text{ m s}^{-2}$  is the gravitational acceleration, and  $\gamma$  is the surface tension of the liquid ( $\gamma_w = 72 \text{ mN m}^{-1}$ , as shown in Fig. 4.5).

In order to obtain the contact angle  $\theta$  from the data displayed in Fig. 7.1 (c), we apply the least-squares method. For this, we form the expression

$$\begin{aligned} S(\theta) &:= \sum_{\mu=1}^N [F(u_\mu) - F_\mu]^2 \\ &= \sum_{\mu=1}^N [\pi g r^2 (\rho \ell - \rho_w u_\mu) + 2\pi r \gamma \cos \theta - F_\mu]^2 \end{aligned} \quad (7.2)$$

where the  $(u_\mu, F_\mu)$  are the  $N$  data pairs of one of the measurement cycles. Notice that — apart from the angle  $\theta$  — all quantities on the right-hand side of equation (7.2) are known. To determine  $\theta$  one has to locate the minimum of  $S(\theta)$ , that is, to solve  $dS(\theta)/d\theta = 0$  for  $\theta$ . In view of the fact that typical measurement cycles produce several hundred  $(u_\mu, F_\mu)$ -pairs, therefore, it is reasonable to do this by a numerical calculation. Application of this procedure to one of the measurement cycles shown in Fig. 7.1 (c) yields  $89^\circ$  and  $50^\circ$  for the advancing and receding contact angles, respectively. These values are consistent with the results obtained directly from the tensiometer instrument as well as with values found in the literature for uniform PET fibers with circular cross-section. [163]



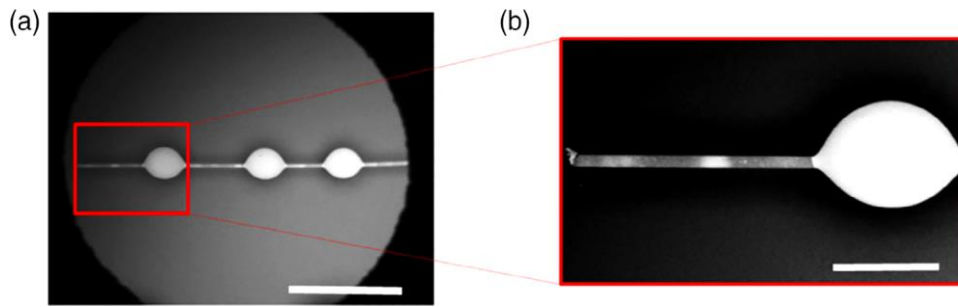


**Fig. 7.1** Dynamic contact angle measurement by the Wilhelmy method, applied to single fiber with a uniform cross-section [51];

(a) A uniform circular PET single fiber of radius  $27.5 \mu\text{m}$  suspended from the tensiometer instrument via a clamp, (b) schematic image of a fiber dipped into the test liquid (water):  $F$  indicates the wetting force exerted on the fiber,  $\theta$  is the contact angle between the liquid phase and the fiber,  $F_z = F \cos \theta$  is the  $z$ -component of  $F$ ,  $r$  is the radius of the fiber, and  $z$  is the direction of movement. The red dotted circle indicates the contact line between liquid, air, and fiber, (c) The abscissa axis of the diagram shows the immersion depth  $u$  (denoted “position” in the diagram) of the fiber into the liquid. The ordinate axis shows the apparent mass  $F/g$  (denoted “mass” in the diagram) recorded by the tensiometer microbalance where  $g$  is the gravitational acceleration. Units of  $F/g$  are g (grams),  $u$  is given in mm. Red and blue dots represent data points ( $u_\mu, F_\mu/g$ ) obtained by tensiometer measurements and the black lines result from the theoretical approach (equation (7.2)). [51]

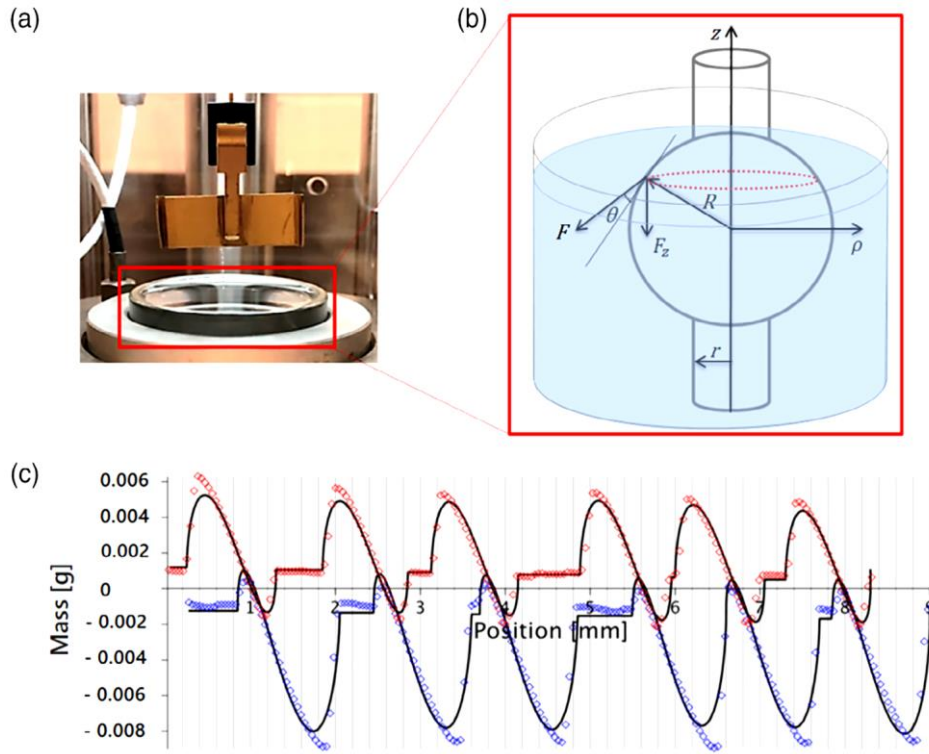
### 7.3 Axisymmetric fiber of varying cross-section

To generalize the approach outlined in the preceding section to axisymmetric fibers of varying cross-section, the spindle-knotted fiber has to be manufactured (as described in 5.1) and used in the tensiometry measurement. For this, a PET original fiber with a circular cross-section and a diameter of  $55 \mu\text{m}$  was degreased by washing out with acetone. Then it was dip-coated in PDMS with a defined weight ratio (10:1 = PDMS: [crosslinking agent]) and drawn out horizontally. This resulted in the formation of a circular film of the polymer solution on the fiber which broke apart into drops, cause by the Plateau-Rayleigh instability. Finally, the fibers then were put in an oven at  $100 \text{ }^\circ\text{C}$  and dried for 1 h. Fig. 7.2 shows SEM images of the prepared spindle-knotted fiber. The central strand consists of a circular PET fiber with a radius  $r = 27.5 \mu\text{m}$ , partially covered by a very thin layer of PDMS. The quasi-spherical knots attached to the central fiber consist also of PDMS.



**Fig. 7.2** SEM image of a PDMS spindle-knotted structured fiber consisting of a cylindrical PET fiber with a radius of  $27.5 \mu\text{m}$ , dip-coating method [51]; Scale bar: (a) 2 mm, (b)  $500 \mu\text{m}$ .

The measurement procedure of the dynamic contact angle of this fiber is similar as for the uniform and circular PET single fiber described in the preceding section: The fiber was clamped to the force sensor of the tensiometer instrument and then lowered into the water, down to a depth of 10 mm below the water surface. The blue dots in Fig. 7.3 (c) represent the [position/tensiometer] readings obtained during this process; they correspond to the advancing contact angle. At a depth of 10 mm the movement was reversed and the fiber retracted to the starting position, resulting in the red dots in Fig. 7.3 (c) which correspond to the receding contact angle. Onto a fiber with non-uniform structure act the same three forces as onto the uniformly structured fiber discussed in the preceding section (see equation (7.1)). However, the more complex shape of the fiber and the fact that it consists of two materials with different densities leads to more complex expressions for the force components. ( $\rho_{PET} = 1380 \text{ kg m}^{-3}$ ,  $\rho_{PDMS} = 965 \text{ kg m}^{-3}$ ).



**Fig. 7.3 Dynamic contact angle measurement by the Wilhelmy method, applied to single fiber with a non-uniform cross-section [51];**

(a) PDMS spindle-knotted structured fiber suspended from the tensiometer instrument via a clamp, (b) schematic image of a spindle-knot (radius of  $R$ ) dipped into the test liquid (water),  $F$  indicates the wetting force exerted on the fiber,  $F_z$  is the  $z$ -component of  $F$ , and  $z$  is the direction of movement. The red dotted circle indicates the contact line between liquid, air, and fiber, (c) The abscissa axis of the diagram shows the immersion depth  $u$  (denoted “position” in the diagram) of the fiber into the liquid. The ordinate axis shows the apparent mass  $F/g$  (denoted “mass” in the diagram) recorded by the tensiometer microbalance where  $g$  is the gravitational acceleration. Units of  $F/g$  are g (grams),  $u$  is given in mm. Red and blue dots represent data points ( $u_\mu, F_\mu/g$ ) obtained by tensiometer measurements and the black lines result from the theoretical approach (equations (7.19) and (7.20)). [51]

The segmented structure of the fiber (Fig. 7.2 (a)) suggests to envisage the fiber to be built up of  $i = 1, \dots, n$  units, as shown in Fig. 7.4 (a). Each unit consists of a quasi-spherical knot of radius  $R_i$  attached to a fiber segment of length  $L_i$  and uniform radius  $r$  (Fig. 7.4 (b)). Employing axially symmetric coordinates  $(\rho, z)$  fixed at the center of the sphere, as in Fig. 7.4 (b), the shape of each unit can be described as

$$\rho(z) = \begin{cases} r & \text{if } -\left(L_i + \sqrt{R_i^2 - r^2}\right) < z < -\sqrt{R_i^2 - r^2} \\ \sqrt{R_i^2 - z^2} & \text{if } -\sqrt{R_i^2 - r^2} < z < \sqrt{R_i^2 - r^2} \end{cases} \quad (7.3)$$

Now, we derive explicit expressions for the force components, in analogy to expression (7.2). The weight of the fiber under air is the sum of the weight contributions of the central PET-fiber and of the PDMS-sphere, that is,

$$F_w = g(\rho_{PET}V_{PET} + \rho_{PDMS}V_{PDMS}) \quad (7.4)$$

(For simplicity, we ignore the very thin layer of PDMS covering the PET strand connecting the knots.) In the  $i$ -th structural unit (defined by its radius  $R_i$  and its length  $L_i$ ), the volume contributions of PET and PDMS amount to:

$$V_{PET} = \pi r^2 \left( L_i + 2\sqrt{R_i^2 - r^2} \right) \quad (7.5)$$

and

$$V_{PDMS} = 4\frac{\pi}{3}r^2(R_i^2 - r^2)^{3/2} \quad (7.6)$$

The weight of the whole fiber (under air) is therefore:

$$F_w = g \sum_{i=1}^n \left[ \rho_{PET}\pi r^2 \left( L_i + 2\sqrt{R_i^2 - r^2} \right) + \rho_{PDMS}4\frac{\pi}{3}(R_i^2 - r^2)^{3/2} \right] \quad (7.7)$$

To obtain the buoyant force  $F_b(z_\ell) = -\rho_w g V(z_\ell)$  acting on the fiber one has to calculate the volume of the immersed part of the fiber. If the fiber intersects the liquid surface at the  $k$ -th unit, the immersed volume consists of two contributions:

1. The completely immersed units ( $i=1, \dots, (k-1)$ ) thrust aside the volume:

$$V_{k-1} = \sum_{i=1}^{k-1} \left[ \pi r^2 \left( L_i + 2\sqrt{R_i^2 - r^2} \right) + 4\frac{\pi}{3}(R_i^2 - r^2)^{3/2} \right] \quad (7.8)$$

2. The  $k$ -th unit is only partially immersed. It displaces the liquid volume:

$$V_k(z_\ell) = \frac{\pi}{3} \begin{cases} 3r^2 \left( z_\ell + L_k + \sqrt{R_k^2 - r^2} \right) & \text{if } I \\ 3r^2 L_k + \sqrt{R_k^2 - r^2} (2R_k^2 + r^2) + 3R_k^2 z_\ell - z_\ell^3 & \text{if } II \end{cases} \quad (7.9j)$$

where (I) is  $-(L_k + \sqrt{R_k^2 - r^2}) < z < -\sqrt{R_k^2 - r^2}$  and (II) is  $-\sqrt{R_k^2 - r^2} < z < \sqrt{R_k^2 - r^2}$ .

$z_\ell$  denotes the liquid level in terms of the “local” coordinates (as defined in equation ((7.3)), that is, their origin is the center of the  $k$ -sphere.

Using equations (7.8) and (7.9), the buoyant force reads:

$$F_b(z_\ell) = -\rho_w g [V_{k-1} + V_k(z_\ell)] \quad (7.10)$$

The vertical component of the force resulting from the surface tension of the liquid can be obtained from geometrical relationships (see Fig. 7.3 (b) and Fig. 7.4):

$$F_t(z_\ell) = \begin{cases} 2\pi r \gamma \cos \theta & \text{if } I \\ -2\pi \gamma \sqrt{R_k^2 - z_\ell^2} \sin \left[ \theta - \arccos \left( \frac{z_\ell}{R_k} \right) \right] & \text{if } II \end{cases} \quad (7.11)$$

where (I) and (II) are the conditions as in equation (7.9) and  $\theta$  denotes the contact angle that is formed between PDMS and the liquid.

The measurement equipment (tensiometer) produces output in the form of  $N$  data pairs ( $u_\mu, F_\mu$ ) where  $u_\mu$  denotes the immersion depth of the fiber and  $F_\mu$  is the force measured at  $u_\mu$  (to avoid confusion we designate subscripts related to data points by Greek letters  $\mu, \nu$  and subscripts related to structural units by Latin letters  $i, k$ ). Equations (7.10) and (7.11) are, however, formulated in terms of the local liquid level  $z_\ell$ . Before these results can be applied, they must therefore be reformulated in terms of  $u$ . For this, the relation between immersion depth  $u$  and local liquid level  $z_\ell$  has to be obtained. If the contact line between liquid and fiber (denoted by  $z_\ell$  in local coordinates) is within the  $k$ -th unit, Fig. 7.4 (a) suggests the following relation between  $z_\ell$  and  $u$ :

$$u = z_\ell + L_k + \sqrt{R_k^2 - r^2} + \sum_{i=1}^{k-1} L_i + 2\sqrt{R_i^2 - r^2} = z_\ell + v_k - \sqrt{R_k^2 - r^2} \quad (7.12)$$

or, if solved for  $z_\ell$ ,

$$z_\ell = u - \left( v_k - \sqrt{R_k^2 - r^2} \right) \quad (7.13)$$

with

$$v_k := \sum_{i=1}^k L_i + 2\sqrt{R_i^2 - r^2} \quad (7.14)$$

We calculate  $\theta$  by the least-squares method, in analogy with the case of the uniform fiber. To this end, we combine in a first step the model results of equations (7.7), (7.10), (7.11), and (7.13), forming the expression

$$F(u) = F_w + F_b(u) + F_t(u, \theta) \quad (7.15)$$

and then the sum

$$S(\theta) := \sum_{\mu=1}^N [F(u_\mu) - F_\mu]^2 \quad (7.16)$$

As above, the  $(u_\mu, F_\mu)$  denote the  $N$  input data pairs (diamond symbols in Fig. 7.3 (c)). The value of  $\theta$  follows by minimizing  $S(\theta)$ , that is, by solving the expression:

$$\frac{dS(\theta)}{d\theta} = 0 \quad (7.17)$$

for  $\theta$ . In practice, however, substantial discrepancies arise between measured mass/position-curves and those calculated via equations (7.15) – (7.17). The reason is that the shape of the most spindle-knots deviates considerably from a perfect sphere. A simple remedy for this defect is to introduce the constants  $a$ ,  $b$ , and  $c$  to rewrite equation (7.15) as

$$F(u) = aF_w + bF_b(u) + cF_t(u, \theta) \quad (7.18)$$

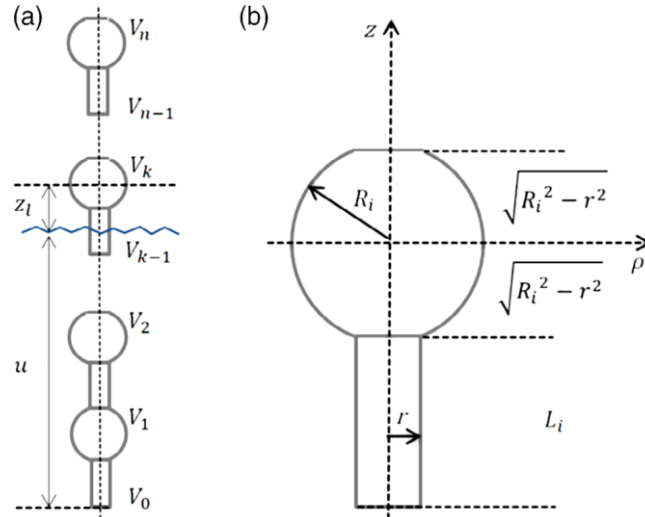
and then to minimize the expression

$$S(\theta, a, b, c) := \sum_{\mu=1}^N [F(u_\mu) - F_\mu]^2 \quad (7.19)$$

By solving expressions

$$\frac{dS(\theta, a, b, c)}{d\theta} = 0, \frac{dS(\theta, a, b, c)}{da} = 0, \frac{dS(\theta, a, b, c)}{db} = 0, \frac{dS(\theta, a, b, c)}{dc} = 0 \quad (7.20)$$

for  $\theta$ ,  $a$ ,  $b$ , and  $c$ .



**Fig. 7.4 Schematic of spindle-knotted structured fiber [51];**  
**(a)  $i = 1, \dots, n$  units, (b) single unit.**

## 7.4 Validation of the model

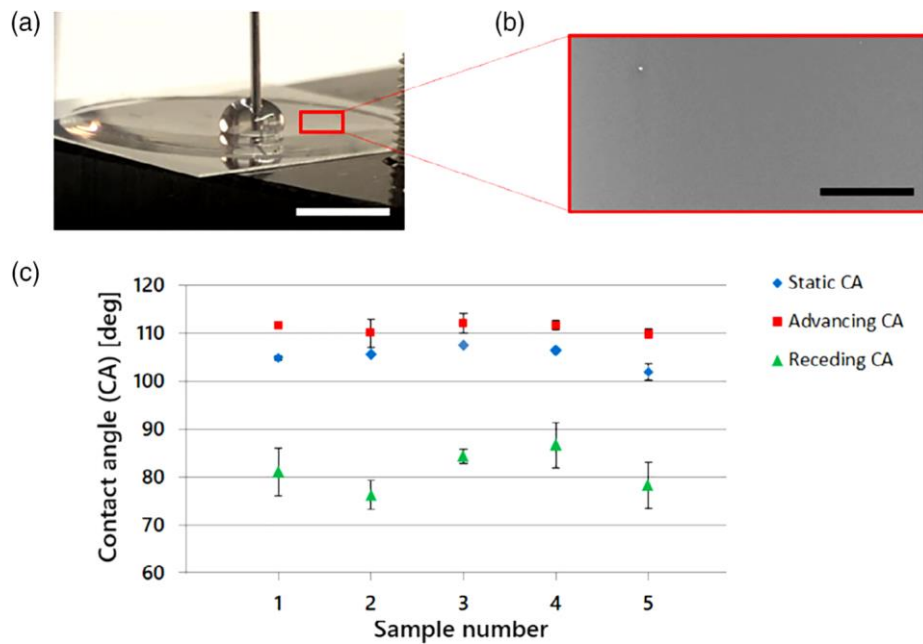
Fig. 7.3 (c) shows for a complete measurement cycle both the [position/tensiometer] readings (red and blue dots) that serve as input data for equations (7.18) – (7.20) and the curves calculated from these equations (black, solid lines).

As already noted, the exact shape of the spindle-knots (or, rather, their deviation from a perfect sphere) affects the value of the contact angle obtained by this method considerably. A procedure that mitigates this systematic error by including the different forces acting on the fiber in the optimization scheme has been presented in equations (7.18) – (7.20).

Random errors due to inaccuracies of force or position readings, for instance, seem to be small in comparison. Moreover, they can be reduced by increasing the number of measurement cycles, as shown in Fig. 7.3 (c). Comparing four such cycles, no significant deviation was detected between the cycles. Indeed, the overlap between the four curves consisting of blues dots (representing the advancing contact angle) and between the four curves of red dots (representing receding the contact angle) was very good. Accordingly, the values

$$\theta_{advancing} = 123^\circ, \theta_{receding} = 73^\circ, \quad (7.21)$$

calculated via equations (7.18) – (7.20) from the cycle shown in Fig. 7.3 (c) were very similar to the results from the other cycles, corroborating that the method produces self-consistent results.



**Fig. 7.5** Static and dynamic contact angle measurement by the direct optical method, applied to PDMS flat surface [51];

(a) Drop of water, positioned on PDMS flat surface, (b) SEM image of PDMS flat surface, (c) static and dynamic contact angle measurement results of water-in-air for five PDMS flat surface samples. The mean values including the standard deviations are; static contact angle:  $105^{\circ} \pm 2^{\circ}$ , advancing contact angle  $111^{\circ} \pm 1^{\circ}$ , receding contact angle  $80^{\circ} \pm 5^{\circ}$ . Scale bar: (a) 7 mm, (b) 50  $\mu\text{m}$ .

In order to test if the results calculated from equations (7.18) – (7.20) coincide with results from established measurement methods, we compared the dynamic contact angles in (7.21) related to PDMS spindle-knotted fibers with corresponding results obtained for flat PDMS surfaces that were obtained by the direct optical method (Fig. 7.5). For the contact angle measurement with direct optical method, the homogeneous and bubble-free PDMS film was needed. For this, PDMS (10:1; PDMS: [crosslinking agent], by weight) was poured into a microscope glass slide plate (2\*2 cm<sup>2</sup>) and cured at 100 °C for 2 hours in an oven. The measurements were then carried out by placing a water drop of defined volume on a prepared microscope glass slide that has been coated with a flat PDMS surface (Fig. 7.5 (a)). The results of five measurements with the Drop Shape Analyzer are shown in Fig. 7.5 (c) (the detailed method is explained in 4.2.4). A comparison of these results, which can be assumed to represent realistic values, with (7.21) reveals that the discrepancy between the two methods amounts to about 11% for the advancing contact angle and to about 9% for the receding contact angle. [51]



## 7.5 Conclusion of a novel method for measuring dynamic contact angles of fibers with spindle-knots

In chapter 7, a new method for measuring the dynamic contact angle of an axisymmetric, but otherwise arbitrarily shaped solid object was presented. The method consists of the following steps:

- (1) The forces acting on the object (weight, buoyancy, and surface forces) are calculated as a function of the immersion depth, assuming that the symmetry axis of the object is oriented normally with respect to the liquid surface.
- (2) While lowering the object into the liquid, a tensiometer is used to measure the total force acting on it as a function of the immersion depth.
- (3) At any immersion depth, the forces calculated in Step 1 and the forces measured in Step 2 ought to coincide. This equality can be exploited to obtain the desired contact angle. To obtain reliable results, despite the fact that the mathematical description of a real object is usually not accurate, it is reasonable to calculate the contact angle via an optimization procedure (such as the least squares method) which comprises tensiometer readings from a multitude of immersion depths.

The approach was exemplified by applying it to structured PDMS fibers with spindle-knots that were immersed in water. The conformity of the results of the proposed method for PDMS spindle-knotted structured fiber and the results for flat PDMS surfaces using the direct optical method confirmed the reliability of the proposed method. The generalization of the proposed method to other liquids and to fibers that consist of other materials and are differently shaped (but still axisymmetrically) is straightforward. The method developed in this work could therefore be useful in the wettability analysis of a wide range of structured fibers, when the structured fiber is not available as a flat surface. What is more, a comparison of dynamic contact angle results of PDMS spindle-knotted fiber with PDMS flat surface reveals that the discrepancy between the two methods amounts to about 11% for the advancing contact angle and about 9% for the receding contact angle. It can therefore be assumed that if there are difficulties in measuring the dynamic contact angle of structured fibers, the measured values on the flat surface of the same material can approximately be used. This outcome will support in the development of chapter 8 of this study to estimate the dynamic contact angle of developed electrospun spindle-knotted fibers in section 5.3.

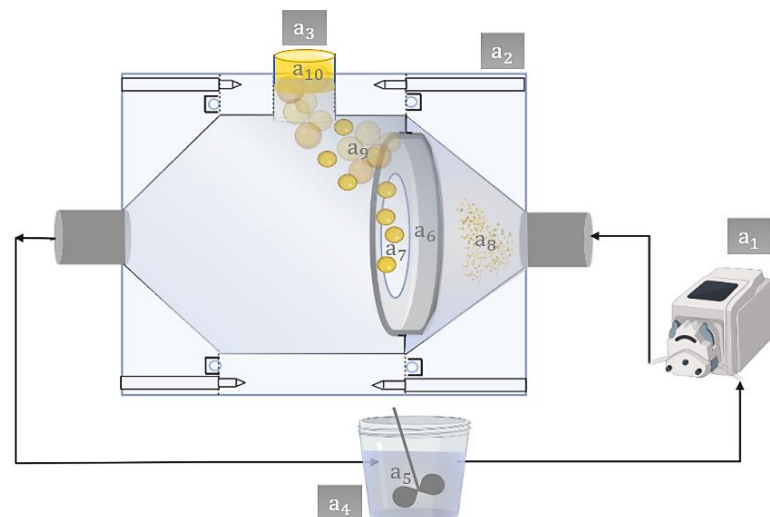


## 8. Evaluation of the electrospun PVDF membrane with regard to oil-in-water collection/separation

After the development of the electrospun PVDF membranes with spindle-knotted structured fibers (described in section 5.3), they have to be evaluated with regard to their oil-in-water emulsion separation efficiency to verify hypothesis number (5) stated in section 3.2.

### 8.1 Development of a filtration setup

To carry out the filtration experiments, a pump-driven filtration system that works in a continuous process had to be designed and constructed. Fig. 8.1 shows the designed test bench including a peristaltic pump (IS116CA33, AxFLOW GmbH, Germany) (a<sub>1</sub>), an appropriate filter housing (a<sub>2</sub>, consisting of three components: inlet, middle, and outlet parts), a chamber for collecting the separated oil droplets (a<sub>3</sub>), an oil-in-water emulsion container (a<sub>4</sub>), a high-speed mixer (Ultra turrax-T25, IKA Werke GmbH & Co. KG) (a<sub>5</sub>), and a membrane holder (a<sub>6</sub>). The PVDF electrospun filter media with spindle-knotted structured fibers (a<sub>7</sub>) was placed vertically into the filter housing at the corresponding position so that the flow direction was perpendicular to the plane of that. Fig. 8.1 (a<sub>8</sub>) shows the entered emulsified oil droplets, which after passing through the filter medium are captured and coalesced into larger ones (a<sub>9</sub>), which will then ascend faster to form an oil film (a<sub>10</sub>) and can be collected in the oil collection chamber.



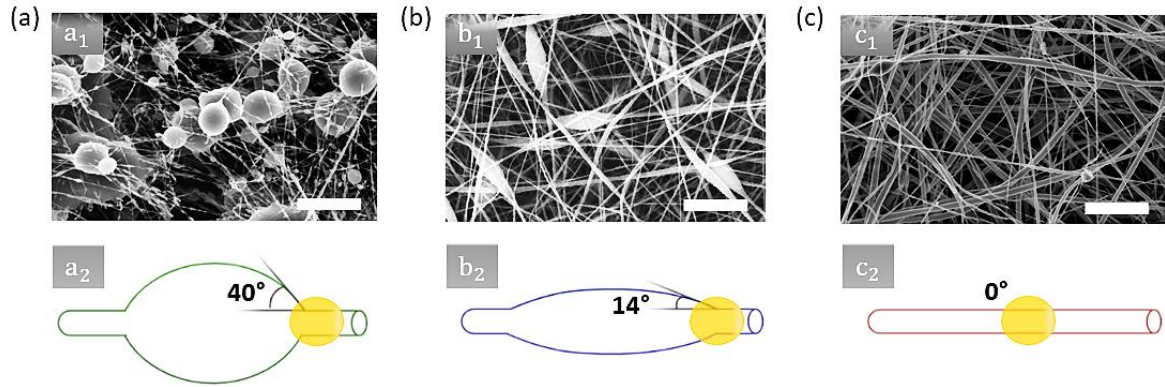
**Fig. 8.1** Scheme of the constructed pump-driven filtration setup.

As already explained, the main function of the coalescer medium (the oil-in-water emulsion separation application) is to create as large droplets as possible on the downstream side to

assure that the droplets ascend quickly, driven by their strong buoyancy force and are not re-entrained in the fluid flow. Briefly, the coalescence process using a coalescer filter medium with spindle-knotted fibers works as follows: the oil-in-water emulsion passes through the electrospun filter media, the micron-sized oil droplets are caught on the fibers and moved directionally along the spindle-knotted fibers towards the equilibrium positions (the spindle-knots). There, they rapidly coalesce to larger droplets that can be drained out on the downstream surface of the medium.

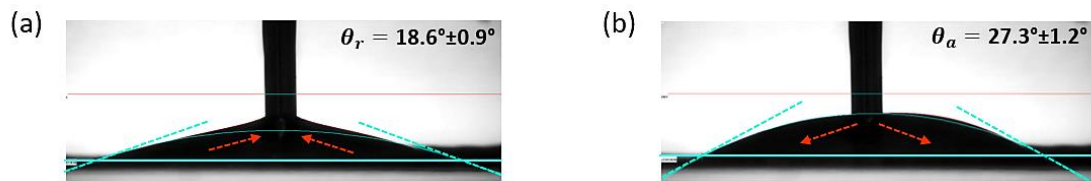
## 8.2 Predicting the functionality of the electrospun spindle-knotted fibers with the theoretical model

To apply equation (6.26) to the proposed theoretical model for electrospun spindle-knotted fibers, information about the geometry ( $\alpha$ ) as well as the wettability properties of the spindle-knotted fibers ( $\theta_r, \theta_a$ ) is required. As shown in Fig. 8.2 (a<sub>1</sub>- c<sub>2</sub>), to clarify the value of  $\alpha$ , the electrospun membranes made of different PVDF concentrations in section 5.3 were imaged and geometrically analyzed to identify the predominant spindle-knot models that developed in the different PVDF concentrations. The membrane made from 2.5 wt% PVDF was excluded from the oil-in-water emulsion separation experiments because they were made from very arbitrarily shaped short and broken fibers and their geometry could not be clearly defined. Fig. 8.2 (a<sub>1</sub>) shows that for the PVDF membrane made of the concentration of 5 wt%, a large number of protrusion droplets has an almost spherical shape with a half-apex angle of  $\alpha \approx 40^\circ$ . The predominant half-apex angle of the spindle-knot structures in the membrane with 7.5 wt% in Fig. 8.2 (b<sub>1</sub>) turned out to be  $\alpha \approx 14^\circ$ , which indicated a flatter structure compared to the spindle-knots presented in 5 wt%. For the membrane of a higher concentration, i.e. 10 wt%, almost no spindle-knot structure was observed, implying  $\alpha \approx 0^\circ$  and meaning that the fabricated fibers had an almost uniform cylindrical cross-section (Fig. 8.2 (c<sub>1</sub>)).



**Fig. 8.2 SEM image and schematic of the predominant spindle-knot structure of electrospun membranes prepared with PVDF solutions of different concentrations [158]; (a) 5 wt% PVDF (b) 7.5 wt% PVDF (c) 10 wt% PVDF. An orange sphere shows a quasi-spherical oil droplet (barrel-shaped) attached to each spindle-knot model. Scale bar: (a<sub>1</sub>) 5  $\mu\text{m}$ , (b<sub>1</sub>) and (c<sub>1</sub>) 10  $\mu\text{m}$ .**

As mentioned, the next need is to have information about the dynamic contact angle of the moving oil droplet along the spindle-knotted fibers. Due to the difficulty or impracticability of measuring the receding and advancing contact angle of an oil droplet along the electrospun micro- or nano-sized spindle-knotted fibers directly, the value of  $\theta_r$  and  $\theta_a$  had to be estimated by carrying out measurements on the quasi-flat surface of the electrospun membrane. This approximation could be made according to the third hypothesis defined in section 3.2 and its realization based on the results of chapter 7. Fig. 8.3 shows the measurement of dynamic contact angles of oil droplets (Tudalen 3036) on electrospun membranes with spindle-knotted fibers. The results are  $18.6^\circ$  and  $27.3^\circ$  for receding and advancing contact angles, respectively.

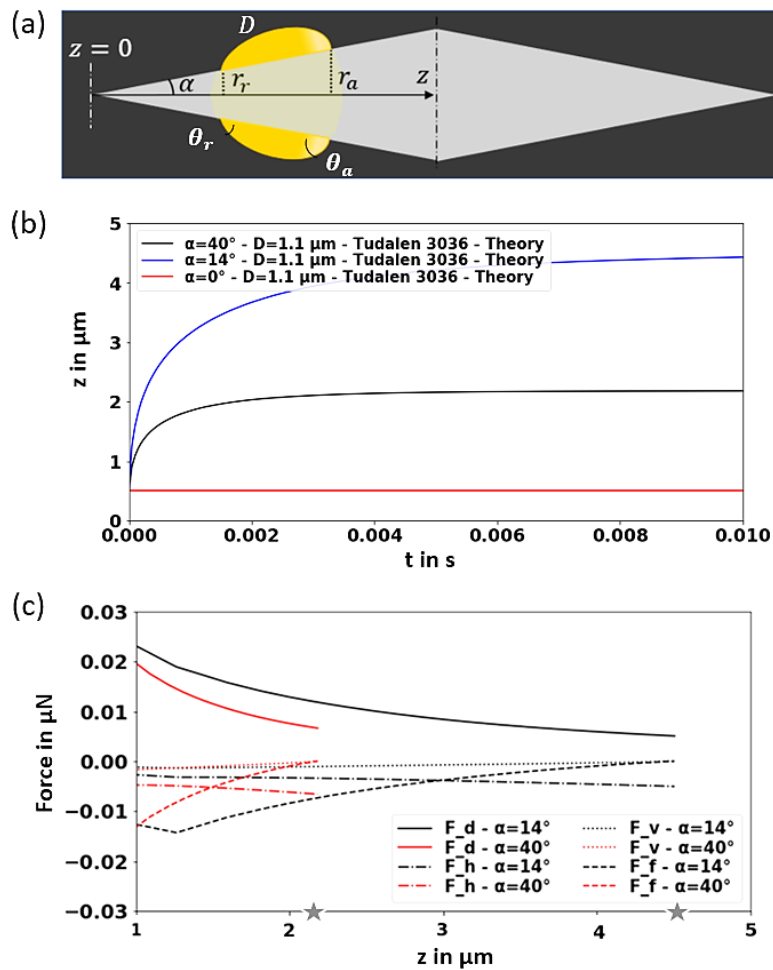


**Fig. 8.3 Dynamic contact angle measurement on the electrospun membrane with spindle-knotted fibers;**  
**(a) Receding contact angle measurement, (b) advancing contact angle measurement.**

Using the measured values for  $\alpha$ ,  $\theta_r$ ,  $\theta_a$ , and defined parameters as given in the scheme and caption of Fig. 8.4 (a), the plots (b) and (c) show the numerical solution of equation (6.26) for a moving barrel-shaped oil droplet ( $D_{50} \approx 1.1 \mu\text{m}$ , see section 4.2.1) along various spindle-knotted electrospun fibers with varied half-apex angle.

Fig. 8.4 (b) illustrates that for the fibers without a spindle-knot structure, no directional motion is exerted on the oil droplet, so the droplet remained motionless (solid red line). Therefore, oil droplets on electrospun fibers with an almost uniform cylindrical cross-

section, prepared by 10 wt%, which are mainly fibers without geometry gradient, do not move along the fibers. In contrast, on the blue and black curves in Fig. 8.4 (b) that correspond to electrospun fibers with spindle-knotted structures with half-apex angles of  $\alpha \approx 14^\circ$  and  $40^\circ$ , respectively, oil droplets do show directional movement along the fibers. Comparing the blue and black curves, it turned out that droplets moving on the flatter spindle-knots ( $\alpha \approx 14^\circ$ ), which are mainly presented in the membrane made of 7.5 wt%, stop farther away from the initial position ( $z_f \approx 4.5 \mu\text{m}$ ) compared to spherical spindle-knots ( $z_f \approx 2.2 \mu\text{m}$ ).



**Fig. 8.4 Numerical solution of the theoretical model in equation (6.26) for electrospun spindle-knotted fibers;**

(a) A quasi-spherical (barrel-shaped) oil droplet attached to a spindle-knot model, (b) path-time diagram derived from the numerical solution of equation (6.26) for a moving oil droplet with a diameter of  $\sim 1.1 \mu\text{m}$  (Tudalen 3036,  $\mu_o = 36 \text{ mPa s}$ ,  $\gamma_o = 30 \text{ mN s}^{-1}$ ) along different spindle-knot models with various  $\alpha$ , (c) different forces acting on the oil droplet moving along a spindle-knot model with half-apex angles of  $14^\circ$  and  $40^\circ$ . The initial values of droplet position and velocity were  $0.5 \mu\text{m}$  and  $14.5 \text{ mm s}^{-1}$ , respectively.  $k_1 = 2$  and  $k_2 = 0.9$  have been used.

Analogous to section 6.4.5, Fig. 8.4 (c) plots the forces acting on the oil droplet as a function of the  $z$ -coordinate along the spindle-knotted fibers of varying half-apex angles of  $14^\circ$  and  $40^\circ$ . For both cases, there is a final position  $z_f$  (indicated by a gray star on the  $z$ -axis), where the forces are balanced and the droplet cannot move any further. All in all, it is obvious from the plots in Fig. 8.4 (b) and (c) that an increase in  $\alpha$  slows down the directional movement of the droplets from the joints to the center of the spindle-knots and thus shortens the final position. Therefore, the fibers with the flatter spindle-knots ( $\alpha \approx 14^\circ$ ) are more advantageous in promoting the directional movement of the droplets from thinner to thicker parts. This ultimately leads to the efficient generation of large droplets that do ascend and can be separated faster.

### 8.3 Evaluation of electrospun PVDF membrane with regard to oil-in-water separation efficiency

This section shows the experimental results and evaluation of electrospun membranes made of 5, 7.5, and 10 wt% PVDF with regard to oil-in-water emulsion separation using the pump-driven filtration system described in 8.1. The experiment was carried out at a room temperature of  $23^\circ\text{C}$ . To carry out the corresponding experiments, an oil-in-water emulsion was prepared with a concentration of 0.1 wt% red-colored Tudalen 3036 according to the procedure described in section 4.1.1. The prepared emulsion particularly contained oil droplets with a diameter smaller than  $2.5\ \mu\text{m}$  ( $D_{50} \approx 1.1\ \mu\text{m}$ ) (Fig. 4.1 (a) in section 4.2.1).

A membrane holder of the filter housing was designed so that the electrospun filter media can be evaluated in a frame of a round flat sheet sample with a diameter of 5.6 cm, giving an actual surface area of  $24.6\ \text{cm}^2$ . The membrane with the defined area was cut and placed in its corresponding position in the housing. After assembling the components of the filter housing, to ensure stability and homogenization as well as to evacuate any air from the housing (to assure the complete filling), the water was first circulated for about 5 minutes before the emulsion was introduced to the housing. For this, the peristaltic pump was turned on to inject the water into the housing and to reach the desired volumetric flow rate of  $126\ \text{L h}^{-1}$ . With this, the volumetric flux ( $Q_{flux}$ ) of the oil-in-water emulsion permeating through the electrospun membrane amounted to  $1.42\ \text{mL s}^{-1}\ \text{cm}^{-2}$ , based on the relation [158]

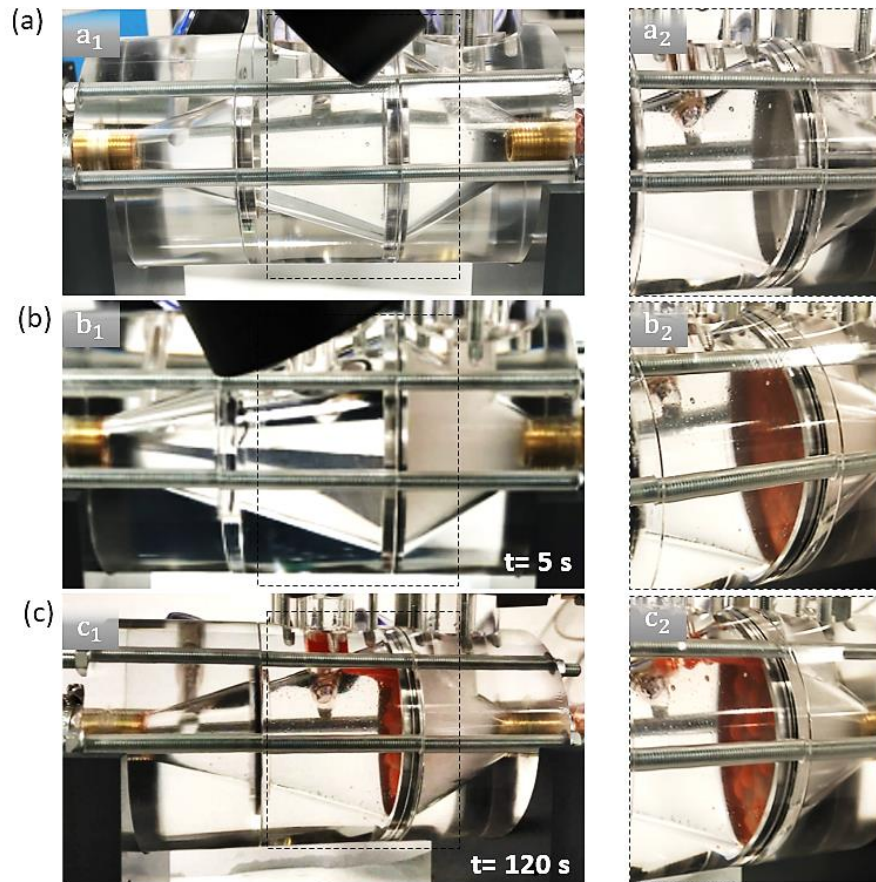
$$Q_{flux} = \frac{V/t}{A} \quad (8.1)$$

where  $V/t$  is the volumetric flow rate in  $\text{mL s}^{-1}$  that is circulated via the filter housing (here:  $35\ \text{mL s}^{-1}$ ) and  $A$  in  $\text{cm}^2$  is the area of the filter media (here:  $24.6\ \text{cm}^2$ ).

After reaching a stable condition, the emulsion began to enter the filtration housing. The defined test time of 10 minutes was then measured from the beginning of the emulsion run-in.

According to Fig. 8.5, the performance of the electrospun PVDF membrane (7.5 wt% PVDF) can be explained qualitatively based on the sequenced images within 120 s. Fig. 8.5 (a<sub>1</sub>) shows a homogeneous state of a filter housing filled with water and before the emulsion started to enter. Fig. 8.5 (a<sub>2</sub>) shows more clearly the downstream side of the membrane (gray color of the stainless-steel mesh). Fig. 8.5 (b<sub>1</sub>) shows the initial moment of entry of a milky oil-in-water emulsion into the housing with a cross-flow. In Fig. 8.5 (b<sub>1</sub>) it was observed that the membrane on the downstream side turned red after 5 s, confirming the instantaneous capture of the oil droplets (colored in red) by fibers. As observed in the experimental work evaluating the functionality of a single spindle-knotted fiber described in section 5.1.1, the tiny oil droplets in the emulsion easily adhered to the oleophilic fiber and were propelled towards the center of the spindle-knots. Then, the oil droplets that had been directed to the spindle-knots gradually converged and formed large droplets at the center of the spindle-knots. Analogously, it is assumed here that the oil droplets begin to coalesce and move directionally from joints to spindle-knots, known as the equilibrium positions. Once a sufficient number of droplets have concentrated and coalesced at such an equilibrium position, the buoyancy force of the newly formed droplet exceeds the surface forces binding the droplet to the filament, and the droplet starts to detach and ascend to the surface on the downstream side (Fig. 8.5 (c)). Fig. 8.5 (c<sub>2</sub>) shows the surface of the electrospun membrane on the downstream side after 120 s. The large red-colored oil droplets confirm the coalescence process, which efficiently produced large droplets that are easy to be removed. After sufficiently large droplets were formed, the buoyancy effect dislodged them from the membrane surface, hence the large droplets rose to the collecting chamber.



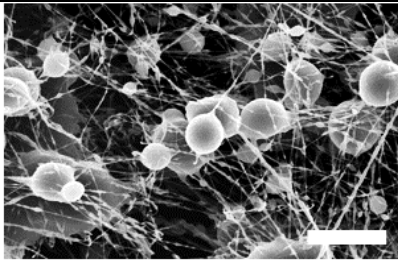
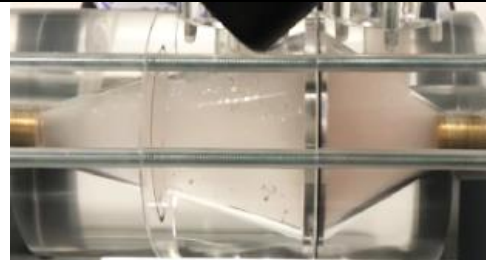
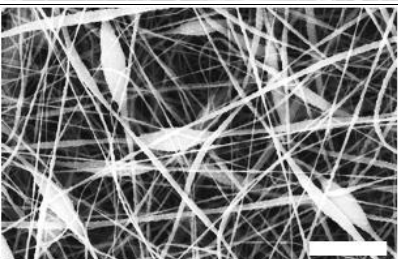

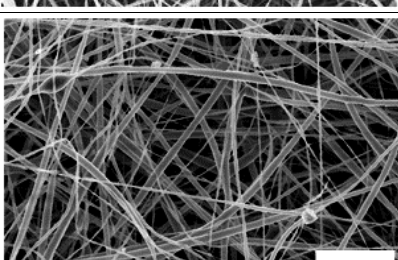
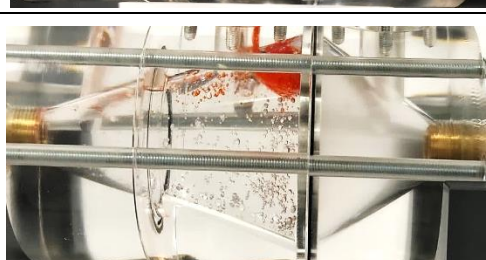


**Fig. 8.5 Emulsified oil-in-water separation performance of electrospun membrane (prepared by PVDF 7.5 wt%) in the filtration system; (a-c) Sequenced images at 0, 5, and 120 s.**

The same test procedure was carried out under the same conditions for at least three times for the electrospun membranes made of PVDF 5, 7.5, 10 wt% of varying spindle-knotted structured fibers and with properties introduced in Tab. 5.1.

Tab. 8.1 shows the comparable functionality of the membranes after 10 minutes. The membrane made with 5 wt% PVDF exhibited undesirable functionality as the membrane failed to capture and separate significant oil droplets on the downstream side. The similar turbidity of the emulsion on either side of the membrane, upstream and downstream, confirms its poor ability to do so. The reason for this poor performance can be attributed to the very small thickness of the membrane and its high air permeability as indicated in Tab. 5.1. Considering the images of filter housing using PVDF 7.5 and 10 wt%, the better functionality compared to PVDF 5 wt% is obvious. The greater amount of oil collected on the downstream side as well as the almost transparent liquid on the upstream side of the housing when using PVDF 7.5 wt%, after 10 minutes of operation, confirms the better performance compared to PVDF 10 wt%.

**Tab. 8.1 Oil-in-water separation performance (after 10 min) of electrospun membranes prepared by PVDF 5, 7.5, 10 wt%;**Scale bar: 5, 10, 10  $\mu\text{m}$  for PVDF 5, 7.5, 10 wt%, respectively.

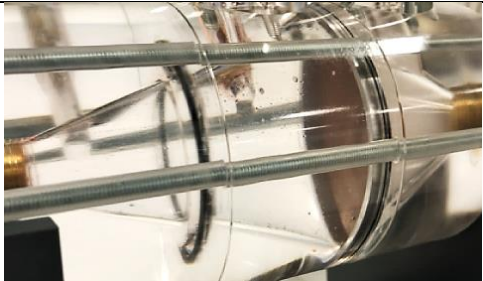
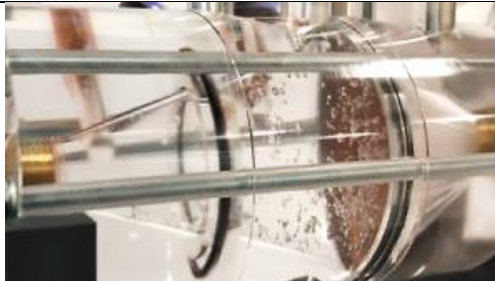
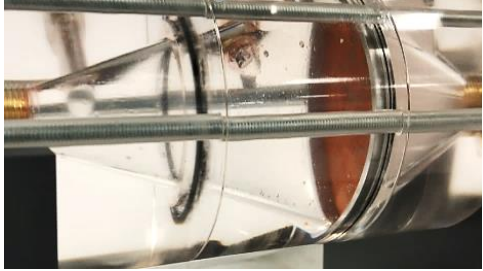



Membrane	SEM image	t=10 min
PVDF 5 wt%		
PVDF 7.5 wt%		
PVDF 10 wt%		

Comparing the images in Tab. 8.1 regarding the functionality of membranes with varying fiber structures prompted us to disregard PVDF 5 wt% for further consideration and instead to carry out further investigations on the functionality of PVDF 7.5 and 10 wt% qualitatively (visually) and quantitatively. To elucidate the difference in functionality based on visual analysis, the selected sequenced images within 10 minutes are shown in Tab. 8.2. The images made 1 s after emulsion entry show that the gray surface of both membranes has started to turn red, showing that the trapping of oil droplets occurs in the initial moments for both types, PVDF 7.5 and 10 wt%. After 10 s the amount of accumulated oil droplets is larger because the surface has completely turned red. Comparing images after 30 s illustrate that in the case of using PVDF 7.5 wt%, the initial detachment of the oil droplets had already taken place and an oil layer appeared, which floated to a chamber for collecting the separated oil droplets. This confirms that the coalescence of the droplets on the membrane with spindle-knotted fibers has been accelerated compared to the membrane having uniform cylindrical fibers (PVDF 10 wt%). Comparing the collected amounts of oil on the downstream side of membranes by observing the images taken after 75 and 95 s shows the different rates in separation more evident, confirming that the separation has been accelerated when using PVDF 7.5 wt%. After 95 s, however, the accumulation of oil

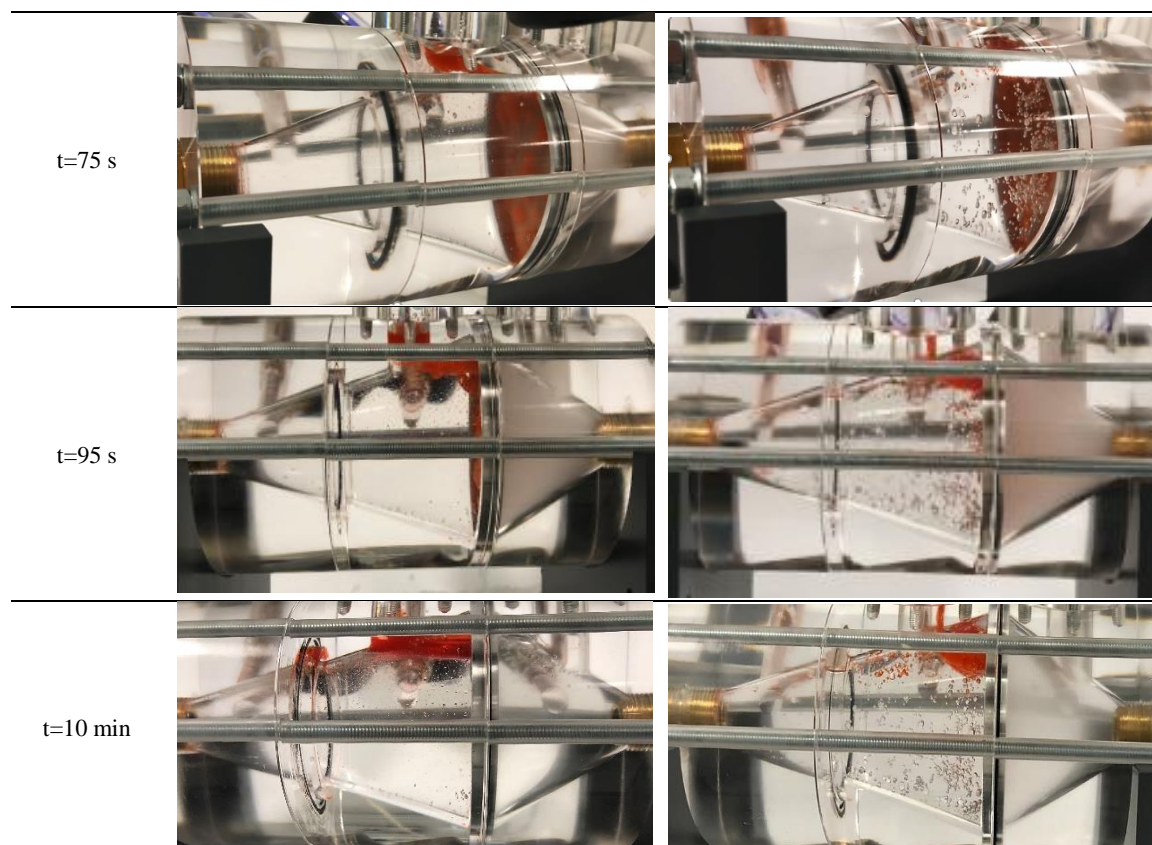
droplets on the downstream side of the PVDF 7.5 wt% membrane is evident, but the emulsion is still turbid on the upstream side, showing that there are still significant oil droplets in the fluid. After 10 minutes, which was considered the test time of the filtration process, the better functionality of the PVDF 7.5 wt% compared to 10 wt% could be visually confirmed; (i) a larger amount of oil collected on the downstream side, (ii) the more transparent liquid on the upstream side of the membrane.

To sum up, although the accumulation, coalescence, detachment, and collection of oil droplets also occurred using PVDF 10 wt%, comparing the images in each time frame, it can be seen that these stages are accelerated using PVDF 7.5 wt%. Although the thickness and the air permeability are almost the same for both membranes and slightly better for PVDF 10 wt%, the functionality of PVDF 7.5 wt% more efficient, which can be attributed to the conjunctive nanofilaments with a spindle-knotted structure.

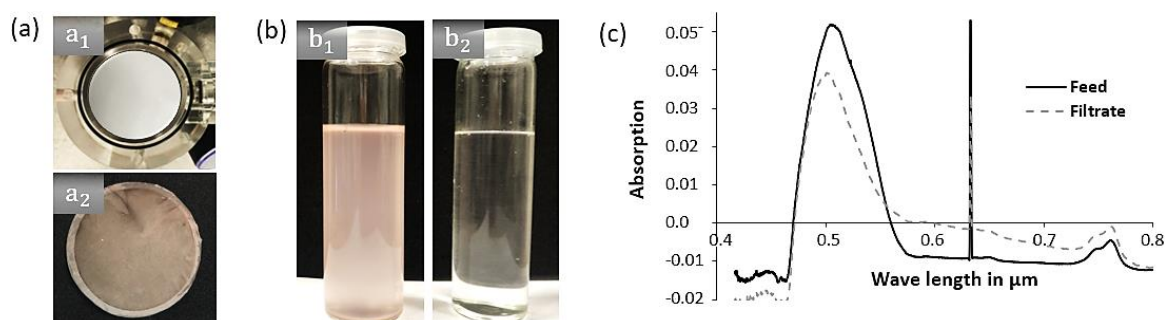
**Tab. 8.2 Oil-in-water separation performance (sequenced images in different time frames) of electrospun membranes prepared by PVDF 7.5 and 10 wt%;**

Membrane	PVDF 7.5 %	PVDF 10 %
t=1 s		
t=10 s		
t=30 s		





In Fig. 8.6 (a<sub>1</sub>) and (a<sub>2</sub>), the upstream side of the electrospun membrane made of PVDF 7.5 wt% is shown before and after the filtration test. As can be seen, the color of the membrane has changed from white to red, which is due to the red-colored oil. Fig. 8.6 (b<sub>1</sub>) and (b<sub>2</sub>) show the emulsion before (denoted as feed) and after (denoted as filtrate) the filtration process. Comparing the images, the emulsion was transformed from milky pink to a clear and transparent solution, indicating significant separability and implying that the emulsified oil droplets were effectively removed.



**Fig. 8.6** Electrospun membrane, emulsion, and UV-Vis spectrum before and after filtration test;

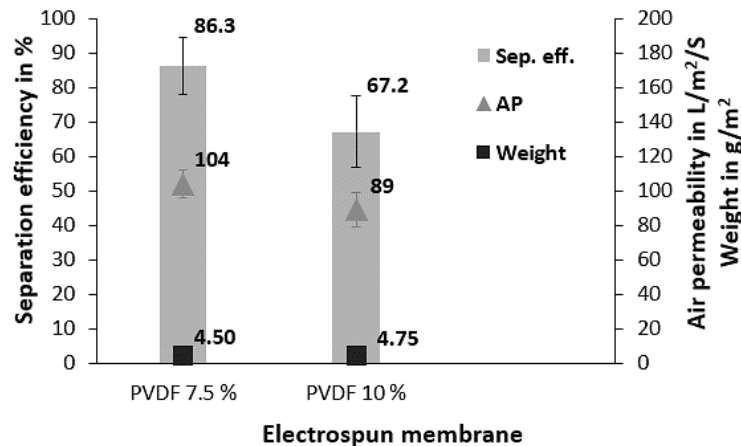
**(a)** Images of underwater oleophilic electrospun PVDF membrane (PVDF 7.5 wt%) before (a<sub>1</sub>) and after (a<sub>2</sub>) the filtration, **(b)** images of the feed (red-colored oil-in-water emulsion) (b<sub>1</sub>) and the filtrate (b<sub>2</sub>), **(c)** UV-Vis spectra of oil-in-water emulsion before and after filtration.

After the visual assessment of the functionality of the oil collection process of the considered electrospun membranes with and without spindle-knotted fibers, it was necessary to evaluate them quantitatively. Here, the separation efficiency in percent was considered as an evaluation indicator (measure). It was calculated according to [158]

$$W = \frac{c_{o,in} - c_{o,out}}{c_{o,in}} \cdot 100\% \quad (8.2)$$

where,  $c_{o,in}$  is an initial oil concentration in the emulsion before the filtration (feed), and  $c_{o,out}$  is the oil concentration in the filtrate after the filtration.

Fig. 8.6 (c) shows the sample result of UV-Vis spectroscopy (VERTEX 80, Bruker) that was carried out to measure the oil concentration before and after the filtration with the electrospun membrane made of PVDF 7.5 wt%. As shown, the absorption peak of the Sudan III dye at 510 nm, which represents the oil concentration, is lower for the filtrate (gray dashed-line) than for the feed (black solid line), confirming the performance of the membranes. Applying the results of spectroscopy and the method described in section 4.2.2, the concentration of oil before and after the filtration was measured. Eventually, exploiting the calculated concentrations with equation (8.2), the diagram in Fig. 8.7 reports the separation efficiency of electrospun membrane made of PVDF 7.5 and 10 wt% after 10 minutes of filtration test.



**Fig. 8.7** Oil-in-water separation efficiency of electrospun membranes prepared by PVDF 7.5 and 10 wt%. The error bars show the standard deviation.

As can be seen, the membranes made from PVDF 7.5 and 10 wt% have an average separation efficiency (results of at least three measurements) of about 86.6% and 67.2%, respectively. Through the embedded manometer in the filtration housing, a pressure difference of ~500 mbar was measured between the upstream and downstream sides for both membranes. Looking again at the weight and air permeability values as shown in the diagram in Fig. 8.7, the superior functionality for PVDF 7.5 wt% is evident due to the

spindle-knotted structured fibers. The explanation for the weaker functionality of the electrospun membrane made of 10 wt% (that is without the spindle-knotted structured fiber) is that more time is required for the oil to reach the threshold volume of the buoyancy force. In contrast, for PVDF 7.5 wt%, the spindle-knotted structured fibers having the half-apex angle value of  $\alpha \approx 14^\circ$  (similar to the considered biological model with  $\alpha \approx 10^\circ$ ) accelerate the achievement of the threshold volume for oil droplets. Consequently, this confirms the predictions of the theoretical model shown in Fig. 8.4 (superior functionality for PVDF 7.5 wt%) as well as the stated hypothesis number (5) in section 3.2.

## 9. Summary and future scope

### 9.1 Summary

It is well known that the customary filtration/separation technology of oil-in-water emulsions using conventional nonwoven coalescer filter media containing uniform fibers, is affected with performance bottlenecks. Therefore, this study aimed to improve this technology by endowing it with a good and timely compromise and trade-off between the capture and release of coalesced oil droplets. The solution was a new design of the coalescing filter medium with regard to its fiber structure. A key inspiration for this work is biological structures in nature and their fascinating structure-function relationships that allowed to realize the directional collection of water droplets. The most useful biological models were found among animals that exploit the directional collection of water droplets. Considering the research works developed so far, the in-depth study on the relevant biological model in this study, the capture silk of cribellate spiders, revealed the dynamic interaction between the highly puffed elastic nanofibers and the periodic spindle-knots with water droplets. Furthermore, a root cause analysis was performed to discover which structural elements cause the directional movement of droplets along the capture silk from joints towards the center of spindle-knots. The hereby gained findings extended the basic knowledge on new bionic materials with geometric gradients for the efficient separation of an oil-in-water emulsion.

The mathematical models that were developed and applied in this study were positively evaluated by experiments.

Various bioinspired oil extracting structured models were fabricated applying dip- and spray-coating, electrospinning, and 3D-printing methods, which supported the development of further investigations. The basic units of the oil extracting network structure, the cone-shaped filaments, were reliably and with constant quality manufactured by 3D-printing of polymers. They were post-treated using a suspension of nano-particles, generating a thin coating film with an oleophilic nanostructure. The centerpiece of the oil droplets filtration process, filter media with spindle-knotted fibers, that extract the oil component from oil/water emulsions efficiently was developed using the electrospinning method. It was found that only under proper operational conditions (temperature, humidity, flow rate, electric field) and a proper concentration of the polymeric solution, the spindle-knotted fibers with a proper geometrical gradient can be obtained. Without further post-processing, the developed membrane showed oleophilic wettability under water. The advantages of the electrospinning method to produce nanofiber membranes for the separation of oil-in-water emulsions mainly included the following two aspects: i) it is a simple process that allows the production of spindle-knotted structured fibers, endowing

the directed collection of oil droplets ii) it offers the possibility to produce membranes with the right pore size, a high porosity, a good pore connectivity, and low thickness.

The underlying dynamical mechanisms of directed motion of droplets on a surface with geometric gradients in another fluid medium was modeled and solved numerically. The derived formulas were validated by carrying out corresponding underwater experiments. The developed comprehensive theoretical model predicted how the motion of barrel-shaped droplets on the cone-shaped basic units of the filament network depends on time, the properties of the filaments (length, half-apex angle, and contact angles), and the properties of the oil droplets (size, viscosity, and density). These results supported further development and analysis of electrospun membranes.

A new method was developed that permitted the measurement of the dynamic contact angles of structured fibers with an axisymmetric but otherwise arbitrarily shaped solid, in particular spindle-knotted structured fibers used in our work. The reliability of the method was validated and verified by comparing the results obtained for polydimethylsiloxane (PDMS) spindle-knots with the results obtained for flat surfaces of the same material. The outcomes of this chapter opened up the possibility to evaluate the wettability of spindle-knotted structured fibers against various test liquids when the coated material is not available as a flat surface. What is more, if there are difficulties in measuring the dynamic contact angle of structured fibers, the measured values on the flat surface of the same material can be used as an approximate value. The latter was a particularly favorable result and allowed to approximately evaluate the wettability of electrospun spindle-knotted fibers. In fact, the dynamic contact angles of oil droplets on electrospun spindle-knotted fibers have been estimated by corresponding measurements on the prepared membrane.

The pump-driven test setup with the corresponding filtration housing was designed and constructed to evaluate the performance of the electrospun membranes with regard to oil/water separation. The developed numerical model allowed the prediction of the effect of the geometric gradients of the fibers of the filter medium, which contributes to effective oil-in-water separation. Thereby, the performance of the most promising electrospun filter media with appropriate spindle-knotted fibers was predicted via the developed theoretical model. The model allowed the calculation of the time-dependent movement of droplets as a function of system-relevant parameters and the wetting and viscoelastic properties of the two fluids. The separation efficiency was then quantified applying the developed filtration system. Using electrospun membranes with suitable spindle-knotted fibers, a rapid coalescence of the fine oil droplets on the filter media was observed, which promoted the oil to rise rapidly towards the surface for subsequent mechanical separation from the water.

All in all, we have developed a nonwoven coalescer filter medium that can stimulate droplet movement through structural topography. These outcomes distinguish this work from other



research studies that have been developed to date. Application of the results of the present work can facilitate oil/water separation, resulting in big, fast ascending oil droplets that can easily be collected from the liquid surface. Indeed, if the goals and conditions of an oil/water filtration system are specified (for instance the volume of contaminated water that has to be purified in a given amount of time, the spatial distribution of oil droplets in the emulsion, or the requested grade of water purification) the presented model can be used to develop an optimized spatial filament structure that meets the specification.

## 9.2 Future scope

This section assesses possible future development trends of electrospun membranes with spindle-knotted fibers.

Despite the knowledge of the factors that affect the formation of spindle-knots in the electrospinning method (for instance varying the concentration of polymer solution) to the best of our knowledge, no systematic modeling and fundamental research have been developed so far to theoretically study, predict, and describe the mechanism of spindle-knotted fiber formation. Therefore, as applications of the membrane with spindle-knotted fibers increase, specifically in liquid-liquid filtration applications, it is essential to precisely control the morphology and number of spindle-knotted fibers to achieve specific criteria. Research on electrospun membrane with spindle-knotted fibers for oily wastewater treatment is, however, still in its infancy and in-depth research and development still have a long way to go. Among the problems that need to be addressed in the future, are the following:

First, in terms of scale and structure complexity, the control of micro/nanoscale structures is very difficult and the precise biomimetic fabrication of both the geometry and the wetting properties (composition, roughness) remains an open challenge. For example, it was understood that the roughness gradient from the joints to the spindle-knots in the natural biological model enhances the directional collection and movement of droplets. Therefore, the further in-depth experimental works exerting such roughness gradients will help to improve the performances of electrospun spindle-knotted fibers and further expand their application prospects for oily wastewater treatment.

Second, the laboratory scale electrospinning machine used in this study is limited to produce a limited surface area of the membrane and thus is difficult to be industrialized. As the research work on the large-scale production of the electrospun membrane with spindle-knotted fibers continuously deepens, therefore, in future work, it needs to be well thought out in terms of scalability to be mass-produced.

It is advisable to also consider real filtration with regard to durability under extreme conditions such as the use of surfactants, service life, membrane replacement, pressure differences, and potential energy savings, which are crucial for practical products.

The theoretical model that was developed in this study can be applied not only in the development of filter media for the treatment of oily wastewater, but also to other functional surfaces in applications dealing with droplet transport phenomena including water collection systems, drug delivery, and microfluidic devices working with one or more fluids. To this end, the model has to be further extended to cover the different cases of droplets in terms of shape regime and composition, as well as different cases of the solid model in terms of composition and geometric shape. In this regard, in-depth studies, efforts, and a clear direction for future bio-inspired materials development are necessary.

## References

1. Gupta, R.K., Dunderdale, G.J., England, M.W., and Hozumi, A., “Oil/water separation techniques: a review of recent progresses and future directions,” *J. Mater. Chem. A* 5(31):16025–16058, 2017, doi:10.1039/C7TA02070H.
2. Bhushan, B., “Bioinspired oil–water separation approaches for oil spill clean-up and water purification,” *Phil. Trans. R. Soc. A.* 377(2150):20190120, 2019, doi:10.1098/rsta.2019.0120.
3. Kocherginsky, N.M., Tan, C.L., and Lu, W.F., “Demulsification of water-in-oil emulsions via filtration through a hydrophilic polymer membrane,” *Journal of Membrane Science* 220(1–2):117–128, 2003, doi:10.1016/S0376-7388(03)00223-0.
4. Ge, J., Zong, D., Jin, Q., Yu, J., and Ding, B., “Biomimetic and Superwetable Nanofibrous Skins for Highly Efficient Separation of Oil-in-Water Emulsions,” *Adv. Funct. Mater.* 28(10):1705051, 2018, doi:10.1002/adfm.201705051.
5. Tummons, E., Han, Q., Tanudjaja, H.J., Hejase, C.A., Chew, J.W., and Tarabara, V.V., “Membrane fouling by emulsified oil: A review,” *Separation and Purification Technology* 248:116919, 2020, doi:10.1016/j.seppur.2020.116919.
6. An, L., Bai, C., Bai, Y., Zhang, B., Yu, Y., and Hu, Y., “Superhydrophobicity of polyvinylidene fluoride induced by integrating liquid-exfoliated hexagonal boron nitride nanosheets,” *High Performance Polymers* 32(1):73–82, 2020, doi:10.1177/0954008319851173.
7. Li, S., Huang, J., Chen, Z., Chen, G., and Lai, Y., “A review on special wettability textiles: theoretical models, fabrication technologies and multifunctional applications,” *J. Mater. Chem. A* 5(1):31–55, 2017, doi:10.1039/C6TA07984A.
8. Zhang, J., Liu, L., Si, Y., Yu, J., and Ding, B., “Electrospun Nanofibrous Membranes: An Effective Arsenal for the Purification of Emulsified Oily Wastewater,” *Adv. Funct. Mater.* 30(25):2002192, 2020, doi:10.1002/adfm.202002192.
9. Zhan, B., Liu, Y., Li, S., Kaya, C., Stegmaier, T., Aliabadi, M., Han, Z., and Ren, L., “Fabrication of superwetting Cu@Cu<sub>2</sub>O cubic film for oil/water emulsion separation and photocatalytic degradation,” *Applied Surface Science* 496:143580, 2019, doi:10.1016/j.apsusc.2019.143580.
10. Zhan, B., Liu, Y., Zhou, W.-T., Li, S.-Y., Chen, Z.-B., Stegmaier, T., Aliabadi, M., Han, Z.-W., and Ren, L.-Q., “Multifunctional 3D GO/g-C<sub>3</sub>N<sub>4</sub>/TiO<sub>2</sub> foam for oil-water separation and dye adsorption,” *Applied Surface Science* 541:148638, 2021, doi:10.1016/j.apsusc.2020.148638.
11. Wilke, S., “Wassereinsatz des verarbeitenden Gewerbes,” Text, Umweltbundesamt, <https://www.umweltbundesamt.de/daten/umwelt-wirtschaft/industrie/wassereinsatz-des-verarbeitenden-gewerbes>, 2013.

12. Eyvaz, M., Arslan, S., Gürbulak, E., and Yüksel, E., "Textile Materials in Liquid Filtration Practices: Current Status and Perspectives in Water and Wastewater Treatment," in: Kumar, B. and Thakur, S., eds., *Textiles for Advanced Applications*, InTech, ISBN 978-953-51-3500-5, 2017, doi:10.5772/intechopen.69462.
13. Karabulut, D.F., "Melt-Blown Fibres vs Electrospun Nanofibres as Filtration Media," <https://www.semanticscholar.org/paper/Melt-Blown-Fibres-vs-Electrospun-Nanofibres-as-Karabulut/babf83496e23e816824213d87478af34ffa74997>, 2020.
14. Zhang, K., Liu, F., Williams, A.J., Qu, X., Feng, J.J., and Chen, C.-H., "Self-Propelled Droplet Removal from Hydrophobic Fiber-Based Coalescers," *Phys. Rev. Lett.* 115(7):074502, 2015, doi:10.1103/PhysRevLett.115.074502.
15. Krasinski, A., "A Numerical Model of Droplets Coalescence and Drainage in Fibrous Structures," *Chemical Engineering Transactions* 32:1495–1500, 2013, doi:10.3303/CET1332250.
16. Mao, N., "10 - Nonwoven fabric filters," in: Kellie, G., ed., *Advances in Technical Nonwovens*, Woodhead Publishing, ISBN 978-0-08-100575-0: 273–310, 2016, doi:10.1016/B978-0-08-100575-0.00010-3.
17. Fang, J., "Study of Liquid Drop Migration on Fibers and Mats due to Liquid Flow in a Thin Slit Geometry," University of Akron, 2015.
18. Gregor, E., "Primer on Nonwoven Fabric Filtration Media," 159, 2009.
19. Andan, S., "Modeling of Drainage in Coalescence Filtration," University of Akron, 2010.
20. Nonwoven Fabrics Market Global Forecast to 2025 | MarketsandMarkets, <https://www.marketsandmarkets.com/Market-Reports/non-woven-fabrics-market-101727296.html>, Jun. 2022.
21. Dawar, S., Li, H., Dobson, J., and Chase, G.G., "Drag Correlation of Drop Motion on Fibers," *Drying Technology* 24(10):1283–1288, 2006, doi:10.1080/07373930600838082.
22. Li, M., Lu, T., and Xu, F., "Soft Fibrous Structures in Nature as Liquid Catcher," *Acta Mech. Solida Sin.* 32(5):580–590, 2019, doi:10.1007/s10338-019-00102-w.
23. Li, X., Yang, Y., Liu, L., Chen, Y., Chu, M., Sun, H., Shan, W., and Chen, Y., "3D-Printed Cactus-Inspired Spine Structures for Highly Efficient Water Collection," *Adv. Mater. Interfaces* 7(3):1901752, 2020, doi:10.1002/admi.201901752.
24. Chen, Y., Wang, L., Xue, Y., Zheng, Y., and Jiang, L., "Bioinspired spindle-knotted fibers with a strong water-collecting ability from a humid environment," *Soft Matter* 8(45):11450, 2012, doi:10.1039/c2sm26880a.
25. Yan, Y., Zhang, Q., Li, Y., Guo, Z., Tian, D., Zhang, X., and Jiang, L., "The highly efficient collection of underwater oil droplets on an anisotropic porous cone surface via an electric field," *J. Mater. Chem. A* 8(17):8605–8611, 2020, doi:10.1039/D0TA02055A.

26. Kong, T., Luo, G., Zhao, Y., and Liu, Z., “Bioinspired Superwettability Micro/Nanoarchitectures: Fabrications and Applications,” *Adv. Funct. Mater.* 29(11):1808012, 2019, doi:10.1002/adfm.201808012.
27. Getting Back to Basics: What is Depth Filtration?, <https://www.fileder.co.uk/blog/getting-back-to-basics-what-is-depth-filtration/>, Jun. 2022.
28. Charvet, A., Gonthier, Y., Bernis, A., and Gonze, E., “Filtration of liquid aerosols with a horizontal fibrous filter,” *Chemical Engineering Research and Design* 86(6):569–576, 2008, doi:10.1016/j.cherd.2007.11.008.
29. Kulkarni, P., Patel, S., and Chase, G., “Mixed hydrophilic/hydrophobic fiber media for water-in-oil coalescence,” *Separation and Purification Technology - SEP PURIF TECHNOL* 85, 2011, doi:10.1016/j.seppur.2011.10.004.
30. Tuteja, A., Choi, W., Mabry, J.M., McKinley, G.H., and Cohen, R.E., “Robust omniphobic surfaces,” *Proc. Natl. Acad. Sci. U.S.A.* 105(47):18200–18205, 2008, doi:10.1073/pnas.0804872105.
31. Jung, Y.C. and Bhushan, B., “Wetting Behavior of Water and Oil Droplets in Three-Phase Interfaces for Hydrophobicity/philicity and Oleophobicity/philicity,” *Langmuir* 25(24):14165–14173, 2009, doi:10.1021/la901906h.
32. Wan, K., Gou, X., and Guo, Z., “Bio-inspired Fog Harvesting Materials: Basic Research and Bionic Potential Applications,” *J Bionic Eng* 18(3):501–533, 2021, doi:10.1007/s42235-021-0040-0.
33. Hancock, M.J., Sekeroglu, K., and Demirel, M.C., “Bioinspired Directional Surfaces for Adhesion, Wetting, and Transport,” *Adv. Funct. Mater.* 22(11):2223–2234, 2012, doi:10.1002/adfm.201103017.
34. Zhang, W., “Wetting Behavior of Liquid Aerosols on Spider Webs and Creation of Liquid Aerosol Barriers,” North Carolina State University, 2015.
35. Konrad, W. and Roth-Nebelsick, A., “Sorting of droplets by migration on structured surfaces,” *Beilstein J. Nanotechnol.* 2:215–221, 2011, doi:10.3762/bjnano.2.25.
36. Berry, J.D., Neeson, M.J., Dagastine, R.R., Chan, D.Y.C., and Tabor, R.F., “Measurement of surface and interfacial tension using pendant drop tensiometry,” *Journal of Colloid and Interface Science* 454:226–237, 2015, doi:10.1016/j.jcis.2015.05.012.
37. Zheng, Y., Bai, H., Huang, Z., Tian, X., Nie, F.-Q., Zhao, Y., Zhai, J., and Jiang, L., “Directional water collection on wetted spider silk,” *Nature* 463(7281):640–643, 2010, doi:10.1038/nature08729.
38. Jiang, L., Zhao, Y., and Zhai, J., “A Lotus-Leaf-like Superhydrophobic Surface: A Porous Microsphere/Nanofiber Composite Film Prepared by Electrohydrodynamics,” *Angew. Chem. Int. Ed.* 43(33):4338–4341, 2004, doi:10.1002/anie.200460333.

39. Yang, S., Yin, K., Chu, D., He, J., and Duan, J.-A., “Femtosecond laser structuring of Janus foam: Water spontaneous antigavity unidirectional penetration and pumping,” *Appl. Phys. Lett.* 113(20):203701, 2018, doi:10.1063/1.5061723.
40. Yin, K., Du, H., Dong, X., Wang, C., Duan, J.-A., and He, J., “A simple way to achieve bioinspired hybrid wettability surface with micro/nanopatterns for efficient fog collection,” *Nanoscale* 9(38):14620–14626, 2017, doi:10.1039/C7NR05683D.
41. Contact Angle | Measurements | Biolin Scientific, <https://www.biolinscientific.com/measurements/contact-angle>, Jun. 2022.
42. Yu, Z., Zhang, H., Huang, J., Li, S., Zhang, S., Cheng, Y., Mao, J., Dong, X., Gao, S., Wang, S., Chen, Z., Jiang, Y., and Lai, Y., “Namib desert beetle inspired special patterned fabric with programmable and gradient wettability for efficient fog harvesting,” *Journal of Materials Science & Technology* 61:85–92, 2021, doi:10.1016/j.jmst.2020.05.054.
43. Dai, H., Gao, C., Sun, J., Li, C., Li, N., Wu, L., Dong, Z., and Jiang, L., “Controllable High-Speed Electrostatic Manipulation of Water Droplets on a Superhydrophobic Surface,” *Adv Mater* 31(43):e1905449, 2019, doi:10.1002/adma.201905449.
44. Qiu, S., Fuentes, C.A., Zhang, D., Van Vuure, A.W., and Seveno, D., “Wettability of a Single Carbon Fiber,” *Langmuir* 32(38):9697–9705, 2016, doi:10.1021/acs.langmuir.6b02072.
45. Van de Velde, K. and Kiekens, P., “Wettability and surface analysis of glass fibres.,” *INDIAN JOURNAL OF FIBRE & TEXTILE RESEARCH* 25(1):8–13, 2000.
46. Wu, J., Yin, K., Li, M., Wu, Z., Xiao, S., Wang, H., Duan, J.-A., and He, J., “Under-oil self-driven and directional transport of water on a femtosecond laser-processed superhydrophilic geometry-gradient structure,” *Nanoscale* 12(6):4077–4084, 2020, doi:10.1039/C9NR09902F.
47. Ghasemlou, M., Daver, F., Ivanova, E.P., and Adhikari, B., “Bio-inspired sustainable and durable superhydrophobic materials: from nature to market,” *J. Mater. Chem. A* 7(28):16643–16670, 2019, doi:10.1039/C9TA05185F.
48. Zheng, Y., “Bioinspired Design of Materials Surfaces,” Elsevier, ISBN 978-0-12-814844-0, 2019.
49. Dynamic contact angle, <https://www.kruss-scientific.com/en/how-glossary/dynamic-contact-angle>, Jun. 2022.
50. DataPhysics Instruments, <https://www.dataphysics-instruments.com/>, Jun. 2022.
51. Aliabadi, M., Konrad, W., Stegmaier, T., Arnim, V., Kaya, C., Liu, Y., Zhan, B., Wang, G., and Gresser, G., “A novel method for measuring dynamic contact angles of fibers with spindle-knots,” *J Appl Polym Sci* 138(28), 2021, doi:10.1002/app.50673.

52. Mchale, G., Newton, M.I., and Carroll, B.J., “The Shape and Stability of Small Liquid Drops on Fibers,” *Oil & Gas Science and Technology - Rev. IFP* 56(1):47–54, 2001, doi:10.2516/ogst:2001006.
53. Mullins, Benjamin James, “Study of Capture, Fibre Wetting and Flow Processes in Wet Filtration and Liquid Aerosol Filtration,” 2004, doi:10.25904/1912/992.
54. Ju, J., Xiao, K., Yao, X., Bai, H., and Jiang, L., “Bioinspired Conical Copper Wire with Gradient Wettability for Continuous and Efficient Fog Collection,” *Adv. Mater.* 25(41):5937–5942, 2013, doi:10.1002/adma.201301876.
55. McHale, G. and Newton, M.I., “Global geometry and the equilibrium shapes of liquid drops on fibers,” *Colloids and Surfaces A: Physicochemical and Engineering Aspects* 206(1):79–86, 2002, doi:10.1016/S0927-7757(02)00081-X.
56. Chou, T.-H., Hong, S.-J., Liang, Y.-E., Tsao, H.-K., and Sheng, Y.-J., “Equilibrium phase diagram of drop-on-fiber: coexistent states and gravity effect,” *Langmuir* 27(7):3685–3692, 2011, doi:10.1021/la2000969.
57. Lorenceau, L. and Qur, D., “Drops on a conical wire,” *J. Fluid Mech.* 510:29–45, 2004, doi:10.1017/S0022112004009152.
58. Luo, C. and Wang, X., “Conditions for Barrel and Clam-Shell Liquid Drops to Move on Bio-inspired Conical Wires,” *Sci Rep* 7(1):9717, 2017, doi:10.1038/s41598-017-10036-3.
59. Adamson, A. W. and Gast, A. P., “Physical Chemistry of Surfaces,” A WILEY-INTERSCIENCE PUBLICATION, New York, ISBN 978-0-471-14873-9, 1997.
60. Carroll, B.J., “The accurate measurement of contact angle, phase contact areas, drop volume, and Laplace excess pressure in drop-on-fiber systems,” *Journal of Colloid and Interface Science* 57(3):488–495, 1976, doi:10.1016/0021-9797(76)90227-7.
61. Carroll, B.J., “Equilibrium conformations of liquid drops on thin cylinders under forces of capillarity. A theory for the roll-up process,” *Langmuir* 2(2):248–250, 1986, doi:10.1021/la00068a024.
62. Liu, C., Sun, J., Li, J., Xiang, C., Che, L., Wang, Z., and Zhou, X., “Long-range spontaneous droplet self-propulsion on wettability gradient surfaces,” *Sci Rep* 7(1):7552, 2017, doi:10.1038/s41598-017-07867-5.
63. Li, E.Q. and Thoroddsen, S.T., “The fastest drop climbing on a wet conical fibre,” *Physics of Fluids* 25(5):052105, 2013, doi:10.1063/1.4805068.
64. Gurera, D. and Bhushan, B., “Optimization of bioinspired conical surfaces for water collection from fog,” *Journal of Colloid and Interface Science* 551:26–38, 2019, doi:10.1016/j.jcis.2019.05.015.
65. Lorenceau, L. and Qur, D., “Drops on a conical wire,” *J. Fluid Mech.* 510:29–45, 2004, doi:10.1017/S0022112004009152.

66. Kelbaliyev, G.I., “Drag coefficients of variously shaped solid particles, drops, and bubbles,” *Theor Found Chem Eng* 45(3):248–266, 2011, doi:10.1134/S0040579511020084.
67. Vajpeyi, A., “Stokes’ and Newton’s Viscous Drag,” [https://physics-archive.wooster.edu/JrIS/Files/Web\\_Article\\_Vajpeyi.pdf](https://physics-archive.wooster.edu/JrIS/Files/Web_Article_Vajpeyi.pdf), 2017.
68. Aliabadi, M., Konrad, W., Stegmaier, T., Liu, Y., Zhan, B., Wang, G., Kaya, C., and Gresser, G., “Modeling of self-driven directional movement of underwater oil droplets on bio-inspired nano-coated 3D-printed conical models,” *Separation and Purification Technology* 305:122405, 2023, doi:10.1016/j.seppur.2022.122405.
69. Bagheri, G. and Bonadonna, C., “On the drag of freely falling non-spherical particles,” *Powder Technology* 301:526–544, 2016, doi:10.1016/j.powtec.2016.06.015.
70. McCabe, W. L., Smith, J. C., and Harriott, P., “Unit Operations of Chemical Engineering,” McGraw-Hill, Inc., New Delhi, ISBN 0-07-112738-0, 1993.
71. Levich, V.G. and Levich, V., “Physicochemical Hydrodynamics,” Prentice-Hall, 1962.
72. Clift, R., Grace, J.R., and Weber, M.E., “Bubbles, drops, and particles,” Academic Press, New York, ISBN 978-0-12-176950-5, 1978.
73. Quéré, D., “FLUID COATING ON A FIBER,” 1999, doi:10.1146/ANNUREV.FLUID.31.1.347.
74. Haefner, S., Benzaquen, M., Bäumchen, O., Salez, T., Peters, R., McGraw, J.D., Jacobs, K., Raphaël, E., and Dalnoki-Veress, K., “Influence of slip on the Plateau–Rayleigh instability on a fibre,” *Nat Commun* 6(1):7409, 2015, doi:10.1038/ncomms8409.
75. Mullins, B., Mead-Hunter, R., and King, A., “Simulating Plateau-Rayleigh instability and liquid reentrainment in a flow field using a VOF method,” *Proceedings of the 18th Australasian Fluid Mechanics Conference*, Australasian Fluid Mechanics Society, ISBN 978-0-646-58373-0, 2012.
76. Sharifikolouei, E., Najmi, Z., Cochis, A., Scalia, A.C., Aliabadi, M., Perero, S., and Rimondini, L., “Generation of cytocompatible superhydrophobic Zr–Cu–Ag metallic glass coatings with antifouling properties for medical textiles,” *Materials Today Bio* 12:100148, 2021, doi:10.1016/j.mtbio.2021.100148.
77. Yiu, P., Diyatmika, W., Bönninghoff, N., Lu, Y.-C., Lai, B.-Z., and Chu, J.P., “Thin film metallic glasses: Properties, applications and future,” *Journal of Applied Physics* 127(3):030901, 2020, doi:10.1063/1.5122884.
78. Li, K., Ju, J., Xue, Z., Ma, J., Feng, L., Gao, S., and Jiang, L., “Structured cone arrays for continuous and effective collection of micron-sized oil droplets from water,” *Nat Commun* 4(1):2276, 2013, doi:10.1038/ncomms3276.



79. Dirany, M., Dies, L., Restagno, F., Léger, L., Poulard, C., and Miquelard-Garnier, G., “Chemical modification of PDMS surface without impacting the viscoelasticity: Model systems for a better understanding of elastomer/elastomer adhesion and friction,” *Colloids and Surfaces A: Physicochemical and Engineering Aspects* 468:174–183, 2015, doi:10.1016/j.colsurfa.2014.12.036.
80. Stegmaier, T., Arnim, V. von, Linke, M., Milwich, M., Sarsour, J., Scherrieble, A., Schneider, P., and Planck, H., “Bionic developments based on textile materials for technical applications,” ISBN 978-1-84569-247-6: 193–211, 2008, doi:10.1533/9781845695088.2.193.
81. Mares, M.A. and Oklahoma Museum of Natural History (Norman, Okla.), “Encyclopedia of deserts,” University of Oklahoma Press, Norman, ISBN 978-0-585-19478-3, 1999.
82. Wang, Y., Ma, K., and Xin, J.H., “Stimuli-Responsive Bioinspired Materials for Controllable Liquid Manipulation: Principles, Fabrication, and Applications,” *Adv. Funct. Mater.* 28(6):1705128, 2018, doi:10.1002/adfm.201705128.
83. Venkatesan, H., Chen, J., Liu, H., Liu, W., and Hu, J., “A Spider-Capture-Silk-Like Fiber with Extremely High-Volume Directional Water Collection,” *Adv. Funct. Mater.* 30(30):2002437, 2020, doi:10.1002/adfm.202002437.
84. Ju, J., Zheng, Y., and Jiang, L., “Bioinspired One-Dimensional Materials for Directional Liquid Transport,” *Acc. Chem. Res.* 47(8):2342–2352, 2014, doi:10.1021/ar5000693.
85. Bai, H., Sun, R., Ju, J., Yao, X., Zheng, Y., and Jiang, L., “Large-Scale Fabrication of Bioinspired Fibers for Directional Water Collection,” *Small* 7(24):3429–3433, 2011, doi:10.1002/sml.201101408.
86. Knapczyk-Korczak, J. and Stachewicz, U., “Biomimicking spider webs for effective fog water harvesting with electrospun polymer fibers,” *Nanoscale* 13(38):16034–16051, 2021, doi:10.1039/D1NR05111C.
87. Parker, A.R. and Lawrence, C.R., “Water capture by a desert beetle,” *Nature* 414(6859):33–34, 2001, doi:10.1038/35102108.
88. Roth-Nebelsick, A., Ebner, M., Miranda, T., Gottschalk, V., Voigt, D., Gorb, S., Stegmaier, T., Sarsour, J., Linke, M., and Konrad, W., “Leaf surface structures enable the endemic Namib desert grass *Stipagrostis sabulicola* to irrigate itself with fog water,” *J R Soc Interface* 9(73):1965–1974, 2012, doi:10.1098/rsif.2011.0847.
89. Beetles & *Stipagrostis sabulicola* – Water harvesting in arid area | spatial experiments, <https://spatialexperiments.wordpress.com/2016/02/06/beetles-stipagrostis-sabulicola-water-harvesting-in-arid-area/>, Jul. 2022.
90. Ju, J., Bai, H., Zheng, Y., Zhao, T., Fang, R., and Jiang, L., “A multi-structural and multi-functional integrated fog collection system in cactus,” *Nat Commun* 3(1):1247, 2012, doi:10.1038/ncomms2253.

91. Zhang, M. and Zheng, Y., “Bioinspired Structure Materials to Control Water-collecting Properties,” *Materials Today: Proceedings* 3(2):696–702, 2016, doi:10.1016/j.matpr.2016.01.115.
92. Hamilton, W.J. and Seely, M.K., “Fog basking by the Namib Desert beetle, *Onymacris unguicularis*,” *Nature* 262(5566):284–285, 1976, doi:10.1038/262284a0.
93. Chen, Y., Wang, L., Xue, Y., Jiang, L., and Zheng, Y., “Bioinspired tilt-angle fabricated structure gradient fibers: micro-drops fast transport in a long-distance,” *Sci Rep* 3(1):2927, 2013, doi:10.1038/srep02927.
94. Song, Y., Liu, Y., Jiang, H., Li, S., Kaya, C., Stegmaier, T., Han, Z., and Ren, L., “Bioinspired Fabrication of one dimensional graphene fiber with collection of droplets application,” *Sci Rep* 7(1):12056, 2017, doi:10.1038/s41598-017-12238-1.
95. Zhou, H., Wang, H., Niu, H., and Lin, T., “Superphobicity/philicity Janus Fabrics with Switchable, Spontaneous, Directional Transport Ability to Water and Oil Fluids,” *Sci Rep* 3(1):2964, 2013, doi:10.1038/srep02964.
96. Dong, H., Wang, N., Wang, L., Bai, H., Wu, J., Zheng, Y., Zhao, Y., and Jiang, L., “Bioinspired Electrospun Knotted Microfibers for Fog Harvesting,” *ChemPhysChem* 13(5):1153–1156, 2012, doi:10.1002/cphc.201100957.
97. Ebner, M., Miranda, T., and Roth-Nebelsick, A., “Efficient fog harvesting by *Stipagrostis sabulicola* (Namib dune bushman grass),” *Journal of Arid Environments* 75(6):524–531, 2011, doi:10.1016/j.jaridenv.2011.01.004.
98. Li, X., Yang, Y., Liu, L., Chen, Y., Chu, M., Sun, H., Shan, W., and Chen, Y., “3D-Printed Cactus-Inspired Spine Structures for Highly Efficient Water Collection,” *Adv. Mater. Interfaces* 7(3):1901752, 2020, doi:10.1002/admi.201901752.
99. Liu, J., Cao, M., Li, L., Xu, X., Zheng, J., Yao, W., and Hou, X., “Bioinspired interfacial design for gravity-independent fluid transport control,” *Giant* 10:100100, 2022, doi:10.1016/j.giant.2022.100100.
100. Zhou, H., Zhang, M., Li, C., Gao, C., and Zheng, Y., “Excellent Fog-Droplets Collector via Integrative Janus Membrane and Conical Spine with Micro/Nanostructures,” *Small* 14(27):1801335, 2018, doi:10.1002/smll.201801335.
101. Regassa, Y., Lemu, H.G., Sirabizuh, B., and Rahimeto, S., “Studies on the Geometrical Design of Spider Webs for Reinforced Composite Structures,” *J. Compos. Sci.* 5(2):57, 2021, doi:10.3390/jcs5020057.
102. Eisoldt, L., Smith, A., and Scheibel, T., “Decoding the secrets of spider silk,” *Materials Today* 14(3):80–86, 2011, doi:10.1016/S1369-7021(11)70057-8.
103. Joel, A.-C., Baumgartner, W., and Bräunig, P., “Cribellate Spinnen und die Produktion ihrer Fangfäden,” Dissertation, RWTH Aachen University, 2016, 2016.
104. Foelix, R., “Biology of Spiders,” Third Edition, Oxford University Press, Oxford, New York, ISBN 978-0-19-973482-5, 2011.

105. Sahni, V., Blackledge, T.A., and Dhinojwala, A., “A Review on Spider Silk Adhesion,” *The Journal of Adhesion* 87(6):595–614, 2011, doi:10.1080/00218464.2011.583588.
106. Joel, A.-C. and Baumgartner, W., “Nanofibre production in spiders without electric charge,” *Journal of Experimental Biology* jeb.157594, 2017, doi:10.1242/jeb.157594.
107. Gu, Y., Yu, L., Mou, J., Wu, D., Zhou, P., and Xu, M., “Mechanical properties and application analysis of spider silk bionic material,” *E-Polymers* 20(1):443–457, 2020, doi:10.1515/epoly-2020-0049.
108. Mallis, R.E. and Miller, K.B., “Natural history and courtship behavior in *Tengella perfuga* Dahl, 1901 (Araneae: Zoropsidae),” *The Journal of Arachnology* 45(2):166, 2017, doi:10.1636/15-004.1.
109. De Volder, M. and Hart, A.J., “Engineering Hierarchical Nanostructures by Elastocapillary Self-Assembly,” *Angew. Chem. Int. Ed.* 52(9):2412–2425, 2013, doi:10.1002/anie.201205944.
110. Chaudhury, M.K. and Whitesides, G.M., “How to Make Water Run Uphill,” *Science* 256(5063):1539–1541, 1992, doi:10.1126/science.256.5063.1539.
111. Daniel, S., Chaudhury, M.K., and Chen, J.C., “Fast drop movements resulting from the phase change on a gradient surface,” *Science* 291(5504):633–636, 2001, doi:10.1126/science.291.5504.633.
112. Yang, J.-T., Yang, Z.-H., Chen, C.-Y., and Yao, D.-J., “Conversion of Surface Energy and Manipulation of a Single Droplet across Micropatterned Surfaces,” *Langmuir* 24(17):9889–9897, 2008, doi:10.1021/la8004695.
113. Fang, G., Li, W., Wang, X., and Qiao, G., “Droplet Motion on Designed Microtextured Superhydrophobic Surfaces with Tunable Wettability,” *Langmuir* 24(20):11651–11660, 2008, doi:10.1021/la802033q.
114. Bai, H., Tian, X., Zheng, Y., Ju, J., Zhao, Y., and Jiang, L., “Direction Controlled Driving of Tiny Water Drops on Bioinspired Artificial Spider Silks,” *Adv. Mater.* 22(48):5521–5525, 2010, doi:10.1002/adma.201003169.
115. Mahmood, A., Chen, L., Chen, S., Chen, C., Yu, Y., Weng, D., and Wang, J., “Nature-inspired design of conical array for continuous and efficient fog collection application,” *Colloid and Interface Science Communications* 37:100283, 2020, doi:10.1016/j.colcom.2020.100283.
116. Michielsen, S., Zhang, J., Du, J., and Lee, H.J., “Gibbs Free Energy of Liquid Drops on Conical Fibers,” *Langmuir* 27(19):11867–11872, 2011, doi:10.1021/la202952e.
117. Deng, S., Shang, W., Feng, S., Zhu, S., Xing, Y., Li, D., Hou, Y., and Zheng, Y., “Controlled droplet transport to target on a high adhesion surface with multi-gradients,” *Sci Rep* 7(1):45687, 2017, doi:10.1038/srep45687.

118. Li, Y., Cui, Z., Li, G., Bai, H., Dai, R., Zhou, Y., Jiao, Y., Song, Y., Yang, Y., Liu, S., and Cao, M., “Directional and Adaptive Oil Self-Transport on a Multi-Bioinspired Grooved Conical Spine,” *Adv Funct Materials* 2201035, 2022, doi:10.1002/adfm.202201035.
119. Sarsour, J., Stegmaier, T., and Gresser, G., “3D Textile Structures for Harvesting Water from Fog: Overview and Perspectives: Recent Developments and Future Trends,” ISBN 978-1-119-42676-9: 325–343, 2017, doi:10.1002/9781119426790.ch9.
120. Lv, C., Chen, C., Yin, Y., and Zheng, Q., Surface Curvature-Induced Directional Movement of Water Droplets, 2010, doi:10.48550/arXiv.1011.3689.
121. Bhushan, B., “Bioinspired water collection methods to supplement water supply,” *Phil. Trans. R. Soc. A.* 377(2150):20190119, 2019, doi:10.1098/rsta.2019.0119.
122. Gurera, D. and Bhushan, B., “Bioinspired conical design for efficient water collection from fog,” *Phil. Trans. R. Soc. A.* 377(2150):20190125, 2019, doi:10.1098/rsta.2019.0125.
123. Schriener, C.T. and Bhushan, B., “Water droplet dynamics on bioinspired conical surfaces,” *Phil. Trans. R. Soc. A.* 377(2150):20190118, 2019, doi:10.1098/rsta.2019.0118.
124. Fisher, L.R., Gamble, R.A., and Middlehurst, J., “The Kelvin equation and the capillary condensation of water,” *Nature* 290(5807):575–576, 1981, doi:10.1038/290575a0.
125. Hoffman, R.L., “A study of the advancing interface. I. Interface shape in liquid—gas systems,” *Journal of Colloid and Interface Science* 50(2):228–241, 1975, doi:10.1016/0021-9797(75)90225-8.
126. Tanner, L.H., “The spreading of silicone oil drops on horizontal surfaces,” *J. Phys. D: Appl. Phys.* 12(9):1473–1484, 1979, doi:10.1088/0022-3727/12/9/009.
127. Bico, J. and Quéré, D., “Falling Slugs,” *Journal of Colloid and Interface Science* 243(1):262–264, 2001, doi:10.1006/jcis.2001.7891.
128. Chen, Y., Li, D., Wang, T., and Zheng, Y., “Orientation-Induced Effects of Water Harvesting on Humps-on-Strings of Bioinspired Fibers,” *Sci Rep* 6(1):19978, 2016, doi:10.1038/srep19978.
129. Song, C., Du, R., and Zheng, Y., “Wet-Induced Fabrication of Heterogeneous Hump-on-String Fibers,” *Materials* 8(7):4249–4257, 2015, doi:10.3390/ma8074249.
130. Bai, H., Ju, J., Zheng, Y., and Jiang, L., “Functional Fibers with Unique Wettability Inspired by Spider Silks,” *Advanced Materials* 24(20):2786–2791, 2012, doi:10.1002/adma.201200289.
131. Hou, Y., Chen, Y., Xue, Y., Wang, L., Zheng, Y., and Jiang, L., “Stronger water hanging ability and higher water collection efficiency of bioinspired fiber with

- multi-gradient and multi-scale spindle knots,” *Soft Matter* 8(44):11236–11239, 2012, doi:10.1039/C2SM26421H.
132. Breslauer, D.N., Muller, S.J., and Lee, L.P., “Generation of Monodisperse Silk Microspheres Prepared with Microfluidics,” *Biomacromolecules* 11(3):643–647, 2010, doi:10.1021/bm901209u.
133. Tian, X., Chen, Y., Zheng, Y., Bai, H., and Jiang, L., “Controlling Water Capture of Bioinspired Fibers with Hump Structures,” *Adv. Mater.* 23(46):5486–5491, 2011, doi:10.1002/adma.201103111.
134. Wang, S., Feng, S., Hou, Y., and Zheng, Y., “Controlling of Water Collection Ability by an Elasticity-Regulated Bioinspired Fiber,” *Macromolecular Rapid Communications* 36(5):459–464, 2015, doi:10.1002/marc.201400695.
135. Chen, W. and Guo, Z., “Hierarchical fibers for water collection inspired by spider silk,” *Nanoscale* 11(33):15448–15463, 2019, doi:10.1039/C9NR04065J.
136. Chen, Y. and Zheng, Y., “Bioinspired micro-/nanostructure fibers with a water collecting property,” *Nanoscale* 6(14):7703–7714, 2014, doi:10.1039/C4NR02064B.
137. Zhao, H. and Chi, H., “Electrospun Bead-on-String Fibers: Useless or Something of Value?,” in: Lin, T., ed., *Novel Aspects of Nanofibers*, InTech, ISBN 978-1-78923-074-1, 2018, doi:10.5772/intechopen.74661.
138. Hufenus, R., Yan, Y., Dauner, M., and Kikutani, T., “Melt-Spun Fibers for Textile Applications,” *Materials* 13(19):4298, 2020, doi:10.3390/ma13194298.
139. Hoffmann, A. and Kuehne, A.J.C., “High Throughput Centrifugal Electrospinning of Polyacrylonitrile Nanofibers for Carbon Fiber Nonwovens,” *Polymers (Basel)* 13(8):1313, 2021, doi:10.3390/polym13081313.
140. Ying, T., Su, J., Jiang, Y., Ke, Q., and Xu, H., “A pre-wetting induced superhydrophilic/superlipophilic micro-patterned electrospun membrane with self-cleaning property for on-demand emulsified oily wastewater separation,” *J Hazard Mater* 384:121475, 2020, doi:10.1016/j.jhazmat.2019.121475.
141. Ma, W., Zhang, M., Li, Y., Kang, M., Huang, C., and Fu, G., “Flexible, durable and magnetic nanofibrous membrane with pH-switchable wettability for efficient on-demand oil/water separation,” *Environ. Sci.: Nano* 6(12):3699–3711, 2019, doi:10.1039/C9EN01023H.
142. Azimi, B., Maleki, H., Zavagna, L., De la Ossa, J.G., Linari, S., Lazzeri, A., and Danti, S., “Bio-Based Electrospun Fibers for Wound Healing,” *JFB* 11(3):67, 2020, doi:10.3390/jfb11030067.
143. Zuo, W., Zhu, M., Yang, W., Yu, H., Chen, Y., and Zhang, Y., “Experimental study on relationship between jet instability and formation of beaded fibers during electrospinning,” *Polymer Engineering & Science* 45(5):704–709, 2005, doi:10.1002/pen.20304.

144. Fong, H., Chun, I., and Reneker, D.H., "Beaded nanofibers formed during electrospinning," *Polymer* 40(16):4585–4592, 1999, doi:10.1016/S0032-3861(99)00068-3.
145. Buchko, C.J., Chen, L.C., Shen, Y., and Martin, D.C., "Processing and microstructural characterization of porous biocompatible protein polymer thin films," *Polymer* 40(26):7397–7407, 1999, doi:10.1016/S0032-3861(98)00866-0.
146. Zhang, C., Yuan, X., Wu, L., Han, Y., and Sheng, J., "Study on morphology of electrospun poly(vinyl alcohol) mats," *European Polymer Journal* 41(3):423–432, 2005, doi:10.1016/j.eurpolymj.2004.10.027.
147. Zhang, X., Zhao, J., Ma, L., Shi, X., and Li, L., "Biomimetic preparation of a polycaprolactone membrane with a hierarchical structure as a highly efficient oil–water separator," *J. Mater. Chem. A* 7(42):24532–24542, 2019, doi:10.1039/C9TA08660A.
148. Zhang, Z.-M., Gan, Z.-Q., Bao, R.-Y., Ke, K., Liu, Z.-Y., Yang, M.-B., and Yang, W., "Green and robust superhydrophilic electrospun stereocomplex polylactide membranes: Multifunctional oil/water separation and self-cleaning," *Journal of Membrane Science* 593:117420, 2020, doi:10.1016/j.memsci.2019.117420.
149. Zhang, J., Pan, X., Xue, Q., He, D., Zhu, L., and Guo, Q., "Antifouling hydrolyzed polyacrylonitrile/graphene oxide membrane with spindle-knotted structure for highly effective separation of oil-water emulsion," *Journal of Membrane Science* 532:38–46, 2017, doi:10.1016/j.memsci.2017.03.004.
150. Zhang, Z., Han, N., Tan, L., Qian, Y., Zhang, H., Wang, M., Li, W., Cui, Z., and Zhang, X., "Bioinspired Superwetable Covalent Organic Framework Nanofibrous Composite Membrane with a Spindle-Knotted Structure for Highly Efficient Oil/Water Emulsion Separation," *Langmuir* 35(50):16545–16554, 2019, doi:10.1021/acs.langmuir.9b02661.
151. Zakerhamidi, M.S., Ahmadian, S.M.S., and Kian, R., "The specific and nonspecific solvatochromic behavior of Sudan dyes in different solvents," *Can. J. Chem.* 93(6):639–647, 2015, doi:10.1139/cjc-2014-0489.
152. Zhao, B., Peng, N., Liang, C., Yong, W., and Chung, T.-S., "Hollow Fiber Membrane Dehumidification Device for Air Conditioning System," *Membranes* 5(4):722–738, 2015, doi:10.3390/membranes5040722.
153. Lee, J.N., Park, C., and Whitesides, G.M., "Solvent Compatibility of Poly(dimethylsiloxane)-Based Microfluidic Devices," *Anal. Chem.* 75(23):6544–6554, 2003, doi:10.1021/ac0346712.
154. Koschwanetz, J.H., Carlson, R.H., and Meldrum, D.R., "Thin PDMS Films Using Long Spin Times or Tert-Butyl Alcohol as a Solvent," *PLoS ONE* 4(2):e4572, 2009, doi:10.1371/journal.pone.0004572.
155. Stieß, M., "Mechanische Verfahrenstechnik - Partikeltechnologie 1," Springer-Verlag, ISBN 978-3-540-32552-9, 2008.

156. Wilhelmy, L., “Ueber die Abhängigkeit der Capillaritäts-Constanten des Alkohols von Substanz und Gestalt des benetzten festen Körpers,” *Annalen Der Physik* 195(6):177–217, 1863, doi:10.1002/andp.18631950602.
157. Wilhelmy plate method - DataPhysics Instruments, <https://www.dataphysics-instruments.com/knowledge/understanding-interfaces/wilhelmy-plate-method/>, Jun. 2022.
158. Zhan, B., Aliabadi, M., Wang, G., Chen, Z.-B., Zhou, W.-T., Stegmaier, T., Konrad, W., Gresser, G., Kaya, C., Liu, Y., Han, Z., and Ren, L., “Underwater Oleophobic Electrospun Membrane with Spindle-Knotted Structured Fibers for Oil-in-Water Emulsion Separation,” *Langmuir* 39(6):2301–2311, 2023, doi:10.1021/acs.langmuir.2c02943.
159. Butt, H.-J., Liu, J., Koynov, K., Straub, B., Hinduja, C., Roismann, I., Berger, R., Li, X., Vollmer, D., Steffen, W., and Kappl, M., “Contact angle hysteresis,” *Current Opinion in Colloid & Interface Science* 59:101574, 2022, doi:10.1016/j.cocis.2022.101574.
160. Shikhmurzaev, Y.D., “Moving contact lines and dynamic contact angles: a ‘litmus test’ for mathematical models, accomplishments and new challenges,” *Eur. Phys. J. Spec. Top.* 229(10):1945–1977, 2020, doi:10.1140/epjst/e2020-900236-8.
161. Tresvik, K.L., “Experimental and numerical investigation of oil-water dispersions - Eksperimentell og numerisk analyse av olje-vann dispersjoner,” *123*, 2016.
162. Barry, D.A. and Parlange, J.-Y., “Universal expression for the drag on a fluid sphere,” *PLoS ONE* 13(4):e0194907, 2018, doi:10.1371/journal.pone.0194907.
163. Smith, R.E., “Surface Energy Data for PET: Poly(ethylene terephthalate), CAS # 25038-59-9,” 3.





## List of formulas

(2.1)	Buoyancy force .....	7
(2.2)	Young's model .....	11
(2.3)	Wenzel's model .....	12
(2.4)	Cassies's model .....	12
(2.5)	Change in the area of the curved surface .....	14
(2.6)	Work done by surface tension in creating the change in area .....	14
(2.7)	Balance of pressure difference and the work done by surface tension .....	14
(2.8)	Equation of Laplace pressure .....	15
(2.9)	Equation of capillary length .....	15
(2.10)	Equation of Laplace pressure for a droplet sitting on a constant curvature surface .....	15
(2.11)	Laplace pressure gradient along a conical fiber .....	16
(2.12)	Equation of the Laplace pressure for a droplet sitting on a conical fiber .....	16
(2.13)	Reynolds number .....	16
(2.14)	Stokes' law .....	17
(2.15)	Newton's law .....	17
(2.16)	Lord Rayleigh drag force equation .....	17
(2.17)	Expression for the drag coefficient .....	18
(2.18)	Expression for the drag coefficient as a function of the reynolds number .....	18
(2.19)	Equation of drag coefficient for Stockes flow .....	18
(2.20)	Equation of drag coefficient for large Reynolds number .....	18
(2.21)	Force generated by a surface energy gradient .....	27
(2.22)	Equation of Laplace pressure gradient on a spindle-knot model .....	28
(2.23)	Gibbs free energy .....	30
(2.24)	Expression of Laplace force on a hydrophilic cone .....	30
(2.25)	Expression of Laplace force on a hydrophobic cone .....	30
(2.26)	Expression of chemical force on a cone with wettability gradient .....	31
(2.27)	Laplace gradient on the 3D-printed cone .....	33
(2.28)	Expression for the liquid wedge angle .....	34
(2.29)	Expression for a local magnitude of the viscous friction .....	35
(2.30)	Viscous friction for the quasi-spherical droplet .....	35
(2.31)	Energy released during the coalescence process .....	37
(2.32)	Total force exerted on the water droplet moving along a spindle-knotted fiber ...	39

(2.33) Laplace force exerted on an oil droplet, moving on the conical model immersed in water.....	41
(2.34) Hysteresis force exerted on an oil droplet moving on the conical model immersed in water.....	41
(2.35) Mechanism of the underwater oil droplet motion on the porous gradient PS-coated cone array .....	43
(2.36) Force generated by the porous surface of the porous gradient PS-coated cone array .....	44
(2.37) Electro-capillary force, generated by the electric field on the porous surface of the porous gradient PS-coated cone array .....	44
(2.38) Mechansim of the underwater oil droplet motion on the nano-coated stainless-steel trapezoidal platform.....	44
(4.1) Cumulative distribution curve formula.....	63
(4.2) Wilhelmy equation .....	66
(4.3) Modified Wilhelmy equation for a single fiber with a uniform circular cross-section .....	69
(6.1) Laplace force within a moving droplet along a cone.....	90
(6.2) Laplace force within a moving barrel-shaped droplet along a cone.....	91
(6.3) Radius of a quasi-spherical barrel-shaped droplet.....	91
(6.4) Hysteresis force exerted on a moving barrel-shaped droplet along a cone.....	91
(6.5) Dependency of the receding contact angle on the droplet velocity .....	92
(6.6) Dependency of the advancing contact angle on the droplet velocity .....	92
(6.7) Expanded expression for the receding contact angle.....	92
(6.8) Expanded expression for the advancing contact angle .....	92
(6.9) The droplet velocity at the point k of the droplet’s trajectory.....	92
(6.10) Friction force within a moving barrel-shaped droplet along a cone.....	92
(6.11) Drag force between a moving droplet and a surrounding fluid.....	93
(6.12) Drag force between a moving droplet and a surface of a cone .....	93
(6.13) Overall drag force exerted on an underwater moving barrel-shaped oil droplet along a cone.....	93
(6.14) Drag coefficient .....	93
(6.15) Reynolds number for a moving oil droplet within water .....	93
(6.16) Reynolds number for a moving oil droplet along a cone solid model.....	93
(6.17) Viscosity expression for a moving oil droplet within water .....	93
(6.18) Overall drag force exerted on an underwater moving barrel-shaped oil droplet along a cone.....	94
(6.19) Area, where water and oil and a cone surface and oil are in contact.....	94

(6.20) Simplified expression for overall drag force exerted on an underwater moving barrel-shaped oil droplet along a cone .....	94
(6.21) Bond number .....	94
(6.22) Condition for neglecting gravity force .....	95
(6.23) Capillary length expression for a moving oil droplet within water .....	95
(6.24) Relation between radius and length of a cone via apex-angle.....	95
(6.25) Motion equation of an underwater moving barrel-shaped oil droplet along a cone .....	95
(6.26) Comprehensive motion equation of an underwater moving barrel-shaped oil droplet along a cone .....	96
(6.27) Expanded expression for the receding contact angle applied in the developed theoretical model.....	96
(6.28) Expanded expression for the advancing contact angle applied in the developed theoretical model.....	96
(6.29) An approximate expression for the final position of an underwater moving barrel-shaped oil droplet along a cone .....	97
(6.30) Simplified expression for the receding contact angle applied in the droplet final position formula.....	97
(6.31) Simplified expression for the advancing contact angle applied in the droplet final position formula.....	97
(6.32) Simplified approximate expression for the final position of an underwater moving barrel-shaped oil droplet along a cone .....	97
(7.1) Forces ( $F(u)$ ) acting on the circular fiber immersed in water in the tensiometer device .....	106
(7.2) Least-squares equation ( $S(\theta)$ ) for measuring contact angle for circular fiber in tensiometer device .....	106
(7.3) Description equation ( $\rho(z)$ ) of the shape of each spindle-knot unit.....	109
(7.4) Weight of PET-fiber and PDMS-spindle .....	110
(7.5) Volume of PET-fiber .....	110
(7.6) Volume of PDMS-spindle .....	110
(7.7) Weight of PET-fiber and PDMS-spindle .....	110
(7.8) Volume of completely immersed units in water.....	110
(7.9) Volume of $k$ -th unit partially immersed in water.....	110
(7.10) Buoyant force exerted on spindle-knotted fiber in tensiometer device .....	111
(7.11) Vertical component of force resulting from the surface tension in tensiometer device .....	111
(7.12) Relation between immersion depth ( $u$ ) and local liquid level.....	111
(7.13) Relation between immersion depth ( $u$ ) and local liquid level.....	111
(7.14) Definition of $k$ -th data point .....	111

(7.15) Forces ( $F(u)$ ) acting on the spindle-knotted fiber immersed in water in the tensiometer device .....	112
(7.16) Least-squares equation ( $S(\theta)$ ) for measuring contact angle of spindle-knotted fiber in tensiometer device .....	112
(7.17) Minimizing $S(\theta)$ equation .....	112
(7.18) Modified $F(u)$ equation .....	112
(7.19) Modified $S(\theta)$ equation .....	112
(7.20) Minimizing modified $S(\theta)$ equation.....	112
(7.21) Advancing and receding contact angles of PDMS-spindle measured by force tensiometry .....	113
(8.1) Volumetric flux .....	121
(8.2) Separation efficiency .....	127

## List of figures

Fig. 1.1	Water consumption in manufacturing industries in Germany in 2016 [11]. ....	1
Fig. 2.1	Typical materials used for oil/water separation [1].....	8
Fig. 2.2	Droplet capturing mechanism [13,19].....	9
Fig. 2.3	Functional schematic of nonwoven coalescing filter medium in oil-in-water separation. ....	10
Fig. 2.4	Wetting models of a droplet on solid surface [22].....	12
Fig. 2.5	The different configurations of a droplet on a fiber .....	13
Fig. 2.6	The condition for mechanical equilibrium for an arbitrarily curved surface [34]. ....	14
Fig. 2.7	Shape of a wetting drop on a cylindrical fiber [65].....	15
Fig. 2.8	Relation between drag coefficient ( $C_D$ ) and Reynolds number ( $Re$ ) [69]. ....	17
Fig. 2.9	Plateau-Rayleigh instability on a fiber [74].....	19
Fig. 2.10	Different spider silk and their specific purpose .....	22
Fig. 2.11	Structure of dry and wet-rebuilt spider silk [37].....	23
Fig. 2.12	Detailed directional water collection behavior along spindle-knotted capture silk [37].....	25
Fig. 2.13	Mechanism scheme showing the directional water collection on spindle-knot [37]. ....	26
Fig. 2.14	Microscopic observation of fog collection on cones [54] .....	31
Fig. 2.15	Fog collection tower inspired by beetle back, desert grass, and cactus spine	32
Fig. 2.16	Water collection on 3D-printed cactus-mimetic spine structure [98] .....	33
Fig. 2.17	A silicon oil on a conical glass fiber [63].....	34
Fig. 2.18	Fabrication techniques for creating the spindle-knotted fibers [84,85,91].....	36
Fig. 2.19	Bioinspired fibers with gradient spindle-knots, tilt-angle dip-coating method [93].....	37
Fig. 2.20	Bioinspired fibers with multi-level spindle-knots, twice dip-coating method [94].....	38
Fig. 2.21	In situ observation of moving tiny water droplets with controllable direction on synthetic spider silk [114].....	39
Fig. 2.22	An all silk-protein fiber (ASPF), dip-coating method [83] .....	40
Fig. 2.23	Structured conical models for continuous and effective collection of micron-sized oil droplets from water [78,84] .....	41
Fig. 2.24	Electric field-assisted collection of micron-sized oil droplets from water using the structured porous cone array [25].....	43
Fig. 2.25	Directional transport of under-oil water droplet on the trapezoidal platform surface [46] .....	45

Fig. 2.26	Schematic of an electrospinning system with different nozzle systems [86] ..	47
Fig. 2.27	Fibers with different morphological structures, obtained by electrospinning [8,142] .....	48
Fig. 2.28	Controlling the morphology of electrospun surfaces by varying the polymer concentration [30] .....	49
Fig. 2.29	Coaxial electrospinning method [84,91,96] .....	50
Fig. 2.30	Hydrolyzed polyacrylonitrile/graphene oxide (H-PAN/GO) nanofibrous electrospun membrane with oil/water separation [149] .....	51
Fig. 2.31	Electrospun PAN and COF-DhaTab/PAN nanofibrous membranes for oil/water separation [150].....	52
Fig. 4.1	Stability check of 0.1 wt% oil (Tudalen 3036)-in-water emulsion via droplet size distribution curves.....	64
Fig. 4.2	Spectroscopy analytical technique to determine the oil concentration .....	65
Fig. 4.3	Stability check of 0.1 wt% oil (Tudalen 3036)-in-water emulsion via oil concentration measurement .....	65
Fig. 4.4	The force tensiometry with tensiometer instrument.....	66
Fig. 4.5	Diagrams of the surface/interfacial tension measurement using the Wilhelmy plate method.....	67
Fig. 4.6	Dynamic contact angle measurement for a uniform circular PET fiber .....	69
Fig. 5.1	Biological model, capture silk of a cribellate spider [68] .....	71
Fig. 5.2	Dip-coating procedure for fabrication spindle knotted single fiber [158].....	72
Fig. 5.3	Spindle-knotted PET single fibers (PET 10 and PET 20) prepared by a dip-coating method using PVDF coating solution of various concentration.....	73
Fig. 5.4	The experimental setup for tracking the oil droplet's directional collection behavior along the spindle-knotted fibers. ....	74
Fig. 5.5	Oil-in-water collection behavior on PET 10 single fiber with/without spindle-knotted structure.....	75
Fig. 5.6	Oil in water collection behavior on the copper wire with spindle-knotted structure [158].....	76
Fig. 5.7	Nonwovens with almost uniform fibers having a cylindrical cross-section....	77
Fig. 5.8	PET spunbond, dip-cotaed in PVDF solution of different concentrations.....	77
Fig. 5.9	PET spunbond, dip-cotaed in PDMS solution of different concentrations .....	78
Fig. 5.10	PBT meltblown, spray-coated with PDMS .....	78
Fig. 5.11	Oil-in-water collection behavior on PBT meltblown fibers with/without spindle-knot structure.....	79
Fig. 5.12	Electrospinning machine at Key Laboratory of Bionic Engineering, Jilin University .....	80
Fig. 5.13	Electrospun membranes prepared using PVDF solution with different concentrations [158].....	82

Fig. 5.14	Wettability analysis of electrospun PVDF membrane .....	84
Fig. 5.15	3D-printed conical models fabricated with Object30 Prime machine [68] ....	85
Fig. 5.16	3D-printed conical model in coated and uncoated condition [68] .....	86
Fig. 5.17	Wettability analysis of uncoated/coated flat musters of VerocyanV (RGD 845) [68] .....	87
Fig. 5.18	Directional movement behavior of underwater oil droplet on uncoated/Tegotop <sup>®</sup> 210 coated conical models [68] .....	88
Fig. 6.1	The relationship between spindle-knot and conical model.....	89
Fig. 6.2	A barrel-shaped oil droplet on a conical model with half-apex angle $\alpha$ [68].	90
Fig. 6.3	Advancing and receding contact angle of underwater barrel-shaped oil droplet moving along a cone [68] .....	99
Fig. 6.4	Results of experiments and theoretical model for an underwater barrel-shaped oil droplet moving along a cone [68] .....	101
Fig. 6.5	Results of experiments and theoretical model for an underwater barrel-shaped oil droplet moving along a cone [68] .....	102
Fig. 6.6	Driving and resisting forces acting on an underwater barrel-shaped oil droplet moving along a cone [68] .....	103
Fig. 7.1	Dynamic contact angle measurement by the Wilhelmy method, applied to single fiber with a uniform cross-section [51] .....	107
Fig. 7.2	SEM image of a PDMS spindle-knotted structured fiber consisting of a cylindrical PET fiber with a radius of 27.5 $\mu\text{m}$ , dip-coating method [51] ...	108
Fig. 7.3	Dynamic contact angle measurement by the Wilhelmy method, applied to single fiber with a non-uniform cross-section [51] .....	109
Fig. 7.4	Schematic of spindle-knotted structured fiber [51].....	113
Fig. 7.5	Static and dynamic contact angle measurement by the direct optical method, applied to PDMS flat surface [51].....	114
Fig. 8.1	Scheme of the constructed pump-driven filtration setup.....	117
Fig. 8.2	SEM image and schematic of the predominant spindle-knot structure of electrospun membranes prepared with PVDF solutions of different concentrations [158] .....	119
Fig. 8.3	Dynamic contact angle measurement on the electrospun membrane with spindle-knotted fibers .....	119
Fig. 8.4	Numerical solution of the theoretical model in equation (6.26) for electrospun spindle-knotted fibers .....	120
Fig. 8.5	Emulsified oil-in-water separation performance of electrospun membrane (prepared by PVDF 7.5 wt%) in the filtration system.....	123
Fig. 8.6	Electrospun membrane, emulsion, and UV-Vis spectrum before and after filtration test.....	126
Fig. 8.7	Oil-in-water separation efficiency of electrospun membranes prepared by PVDF 7.5 and 10 wt% .....	127

Fig. 9.1	Results of experiments and theoretical model for an underwater barrel-shaped oil droplet moving along a cone [68] .....	XXXIX
Fig. 9.2	Results of experiments and theoretical model for an underwater barrel-shaped oil droplet moving along a cone [68] .....	XL
Fig. 9.3	Driving and resisting forces on the moving oil droplet (Silicon 100) with different sizes along a cone with half-apex angle of $2.2^\circ$ [68] .....	XLI
Fig. 9.4	Driving and resisting forces on the moving oil droplet (Silicon 100) of the same size along a cone with different half-apex angles [68].....	XLI
Fig. 9.5	Driving and resisting forces on the moving oil droplet (Silicon 100) with different sizes along a cone with half-apex angle of $1.5^\circ$ [68] .....	XLI
Fig. 9.6	Dynamic contact angle measurement by the Wilhelmy method, applied to single fiber with a non-uniform cross-section [51].....	XLII
Fig. 9.7	Dynamic contact angle measurement by the Wilhelmy method, applied to single fiber with a non-uniform cross-section [51].....	XLII
Fig. 9.8	An inlet part, where the fluid enters.....	XLIII
Fig. 9.9	A middle part, where the membrane is fixed.....	XLIV
Fig. 9.10	An outlet part, where the fluid exits.....	XLV
Fig. 9.11	A chamber for collecting the separated oil droplets.....	XLVI



---

## List of tables

Tab. 2.1	Biological models and selected dimensions describing the water collecting species.....	20
Tab. 2.2	Acting forces/energies on the droplet moving along the structured surfaces (the forces generated by an external actuation with an external energy supply have been neglected) .....	55
Tab. 4.1	Physical properties of used liquids.....	61
Tab. 4.2	Physical properties of used polymeric and coating materials.....	62
Tab. 5.1	Specification of electrospun PVDF membranes .....	83
Tab. 8.1	Oil-in-water separation performance (after 10 min) of electrospun membranes prepared by PVDF 5, 7.5, 10 wt% .....	124
Tab. 8.2	Oil-in-water separation performance (sequenced images in different time frames) of electrospun membranes prepared by PVDF 7.5 and 10 wt% .....	125



# Appendix

A: Results of experiments and theoretical model for various underwater barrel-shaped oil droplets moving along various cones (Chapter 6)

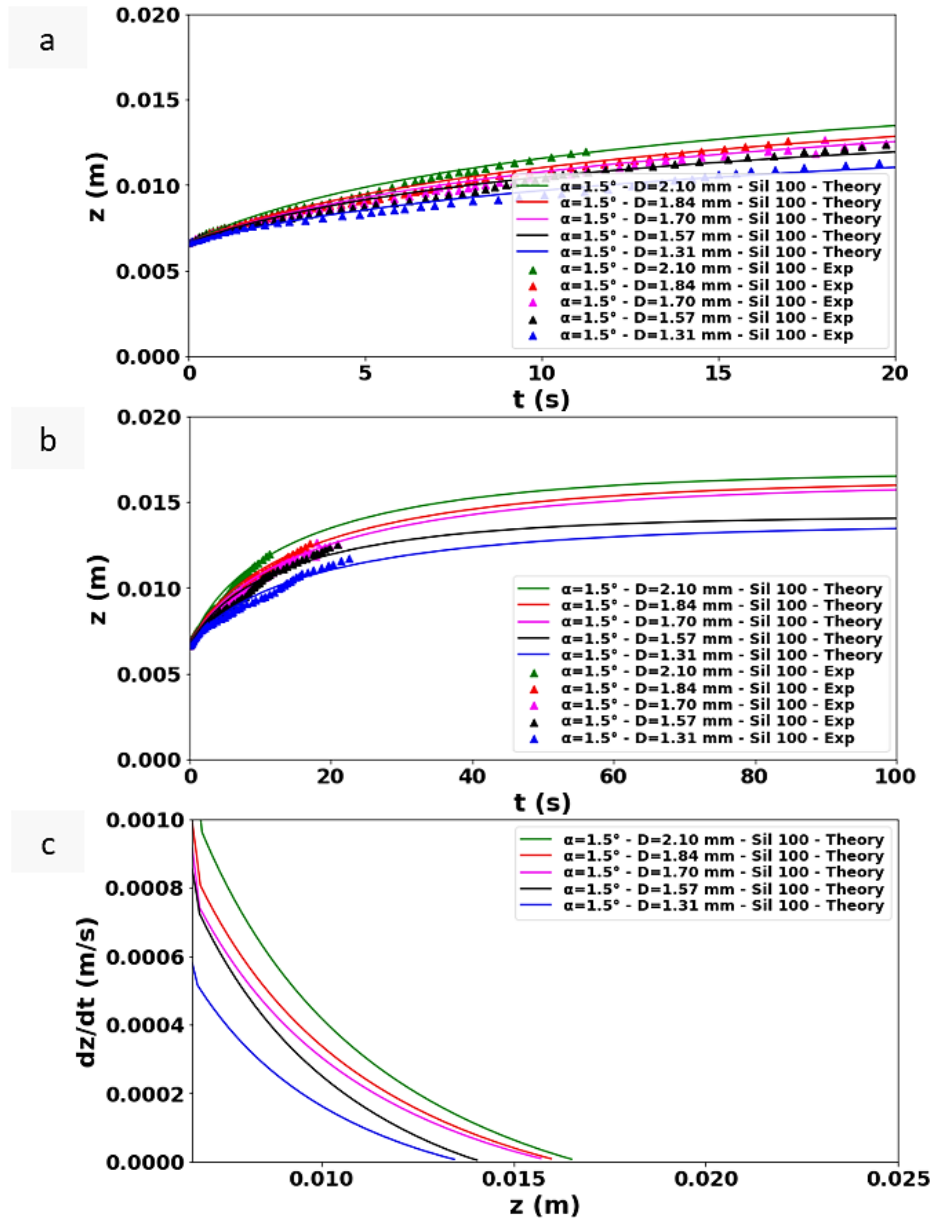
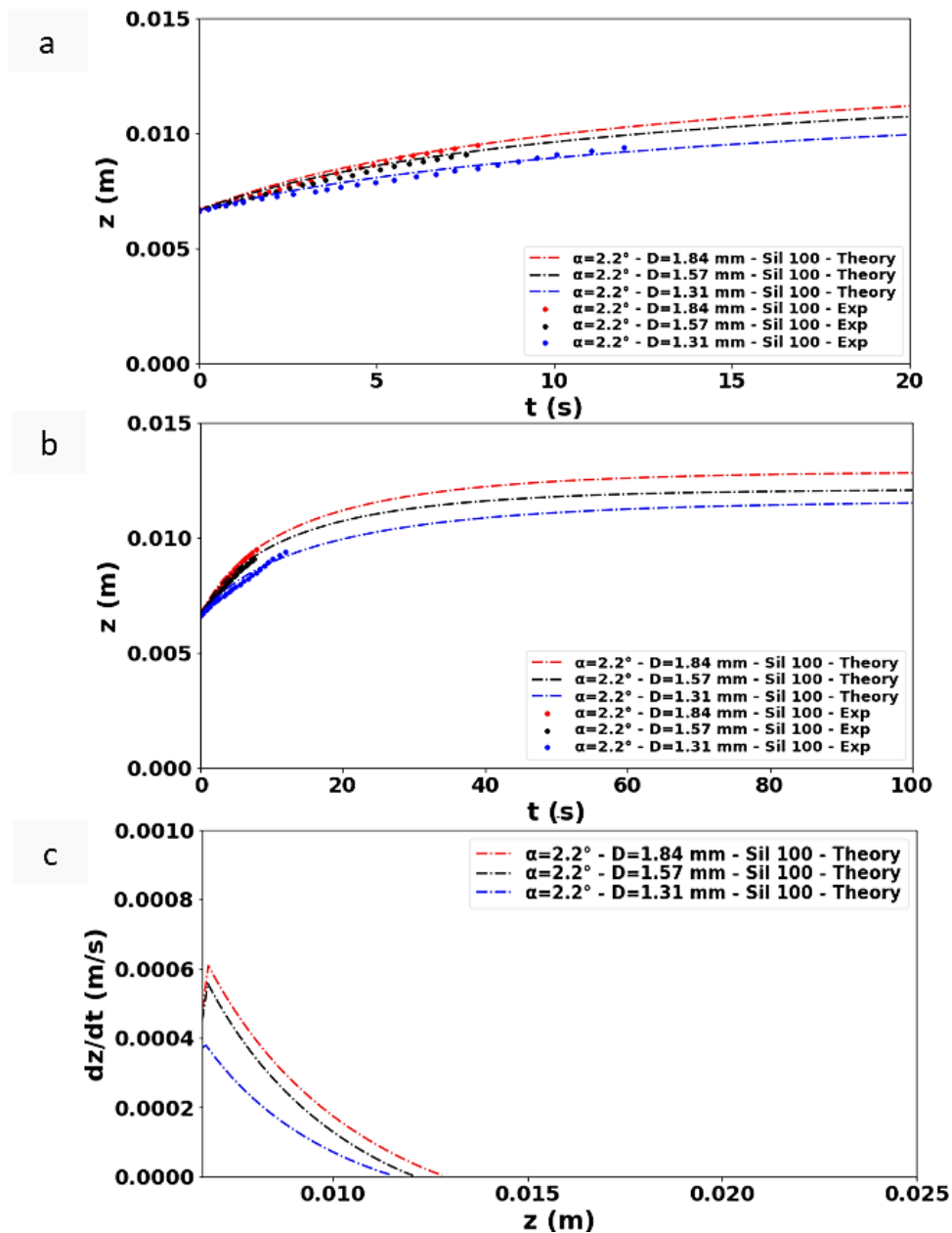


Fig. 9.1 Results of experiments and theoretical model for an underwater barrel-shaped oil droplet moving along a cone [68];

(a) Experimentally obtained (time, position)-data points (triangles) and the related solutions  $z(t)$  of equation (6.26) (solid curves) for several oil droplet size (Silicon 100) using a cone with half-apex angle of  $1.5^\circ$ . (b) theoretical curves calculated from equation (6.26) beyond the experimentally obtained (time, position)-data points, (c) (velocity, position)-diagrams derived from the curves shown in (b). The values of  $(k_1, k_2)$  are (2.5, 1.1), (2.8, 1.3), (3.8, 1.15), (3.8, 1.3), (3.8, 1.4) for droplets with diameters  $D = 1.31, 1.57, 1.70, 1.84, 2.10$  mm, respectively.



**Fig. 9.2** Results of experiments and theoretical model for an underwater barrel-shaped oil droplet moving along a cone [68];

**(a)** Experimentally obtained (time, position)-data points (triangles) and the related solutions  $z(t)$  of equation (6.26) (solid curves) for several oil droplet size (Silicon 100) using a cone with half-apex angle of  $2.2^\circ$ . **(b)** theoretical curves calculated from equation (6.26) beyond the experimentally obtained (time, position)-data points, **(c)** (velocity, position)-diagrams derived from the curves shown in (b). The values of  $(k_1, k_2)$  are (2.5, 1.1), (2.8, 1.3), (3.8, 1.4) for droplets with diameters  $D = 1.31, 1.57, 1.84$  mm, respectively.

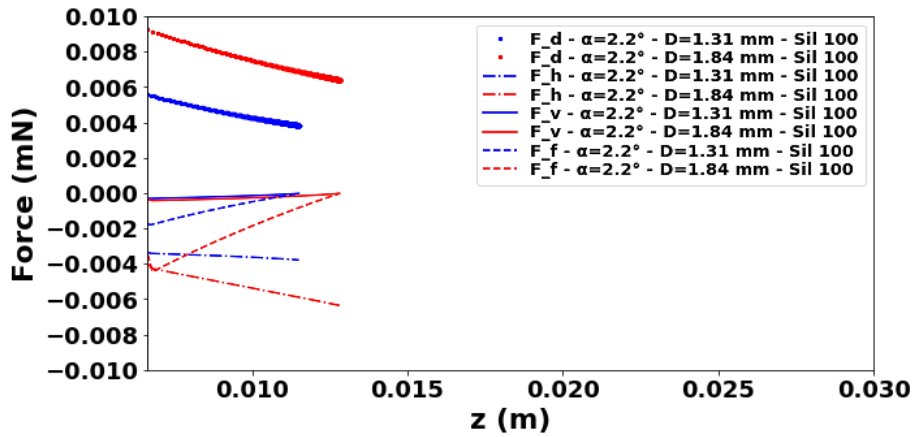


Fig. 9.3 Driving and resisting forces on the moving oil droplet (Silicon 100) with different sizes along a cone with half-apex angle of  $2.2^\circ$  [68].

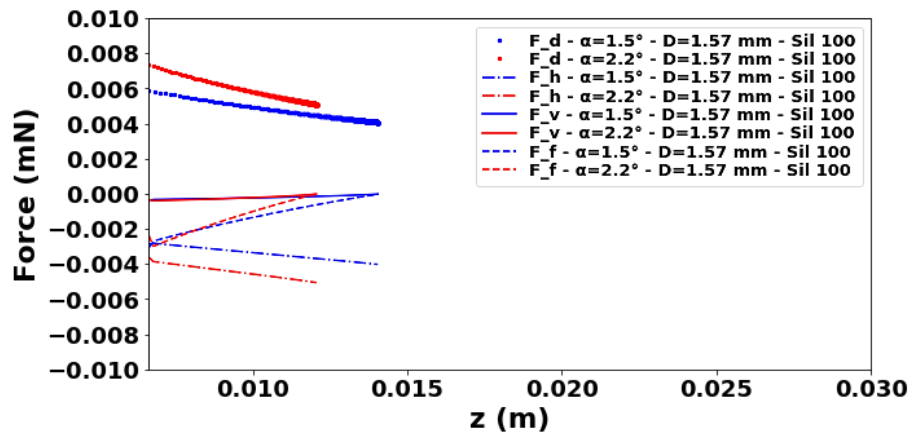


Fig. 9.4 Driving and resisting forces on the moving oil droplet (Silicon 100) of the same size along a cone with different half-apex angles [68].

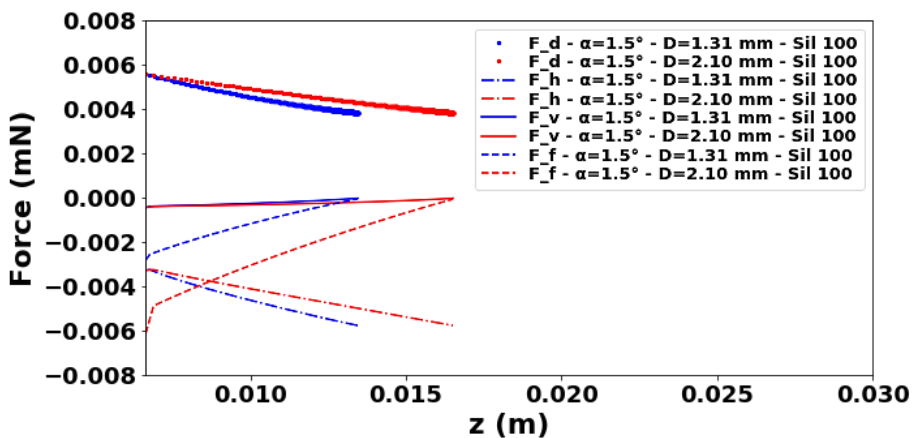
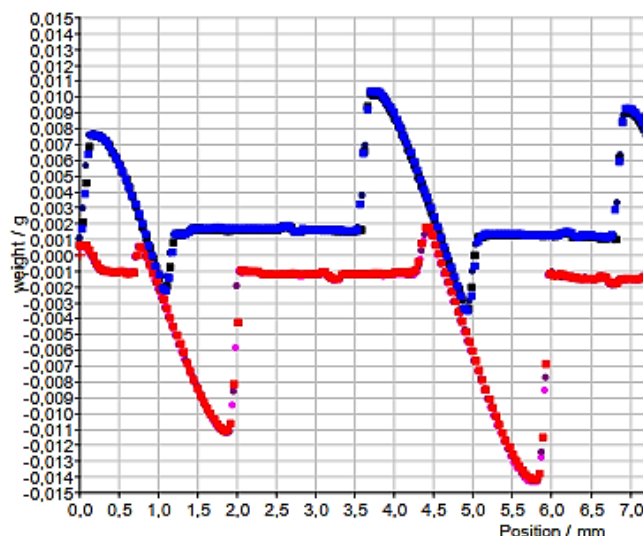


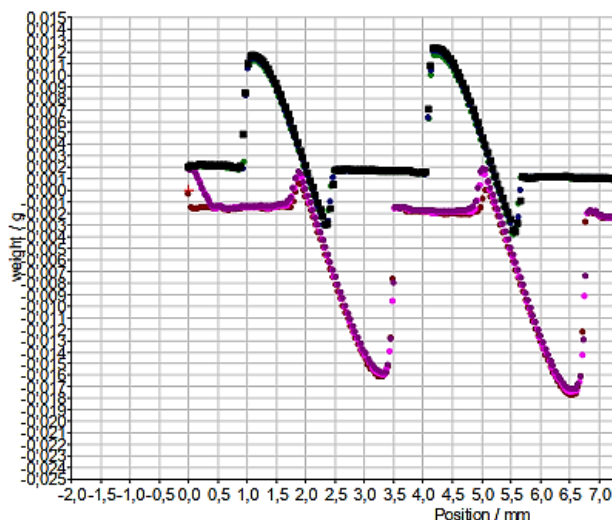
Fig. 9.5 Driving and resisting forces on the moving oil droplet (Silicon 100) with different sizes along a cone with half-apex angle of  $1.5^\circ$  [68].

B: Dynamic contact angle measurement by the Wilhelmy method, applied to single fiber with a non-uniform cross-section (Chapter 7)



**Fig. 9.6 Dynamic contact angle measurement by the Wilhelmy method, applied to single fiber with a non-uniform cross-section [51];**

An original diagram obtained from the tensiometer instrument applied to a PDMS spindle-knotted fiber using an original PET fiber with a diameter of 70  $\mu\text{m}$ . The abscissa axis of the diagram shows the immersion depth  $u$  (denoted "position" in the diagram) of the fiber into the liquid. The ordinate axis shows the apparent mass  $F/g$  (denoted "mass" in the diagram) recorded by the tensiometer microbalance where  $g$  is the gravitational acceleration. Units of  $F/g$  are g (grams),  $u$  is given in mm.



**Fig. 9.7 Dynamic contact angle measurement by the Wilhelmy method, applied to single fiber with a non-uniform cross-section [51];**

An original diagram obtained from the tensiometer instrument applied to a PDMS spindle-knotted fiber using an original PET fiber with a diameter of 90  $\mu\text{m}$ . The abscissa axis of the diagram shows the immersion depth  $u$  (denoted "position" in the diagram) of the fiber into the liquid. The ordinate axis shows the apparent mass  $F/g$  (denoted "mass" in the diagram) recorded by the tensiometer microbalance where  $g$  is the gravitational acceleration. Units of  $F/g$  are g (grams),  $u$  is given in mm.

C: 2D design of major components of the filter housing, produced by *SolidWorks* application. (Chapter 8)

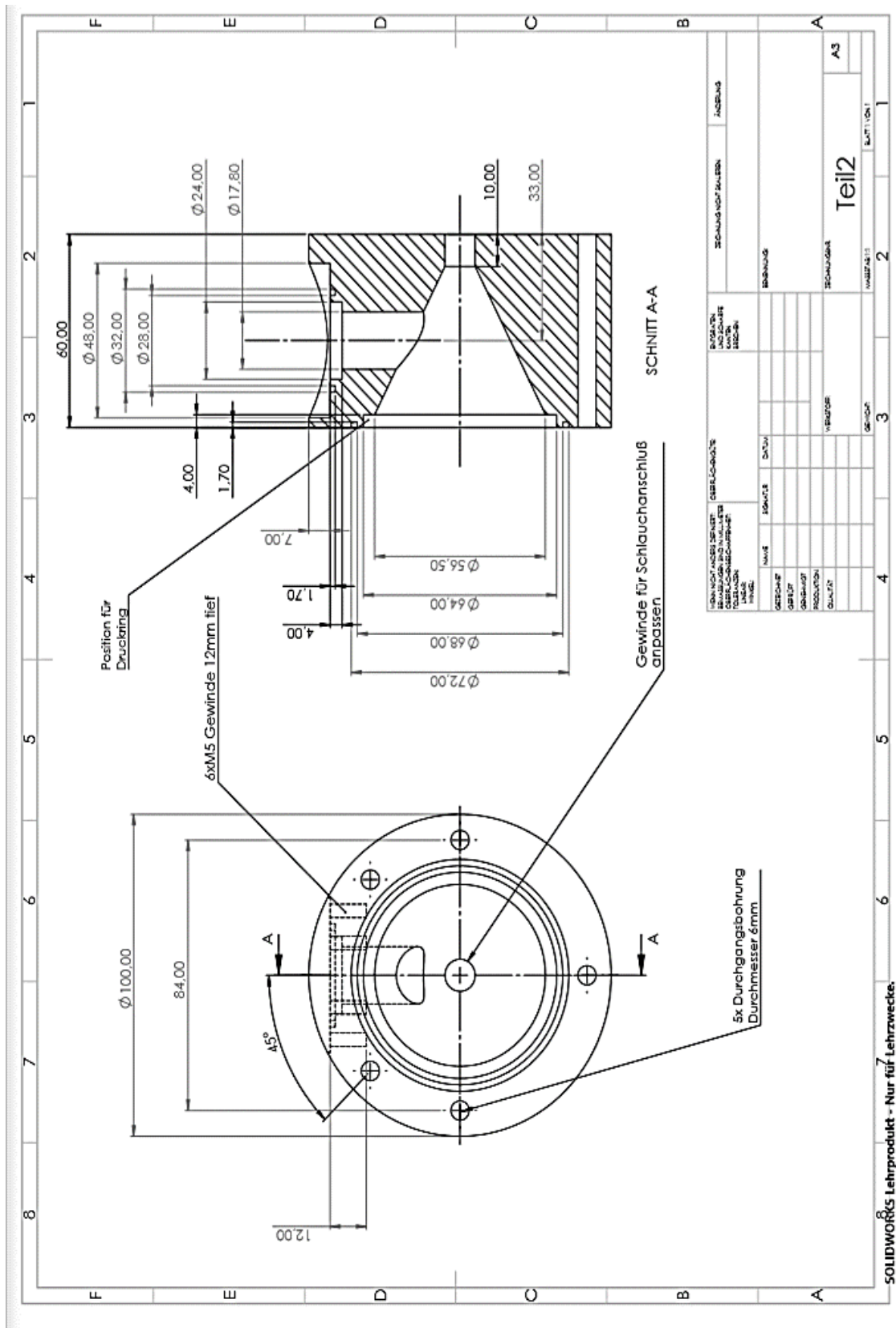


Fig. 9.8 An inlet part, where the fluid enters.

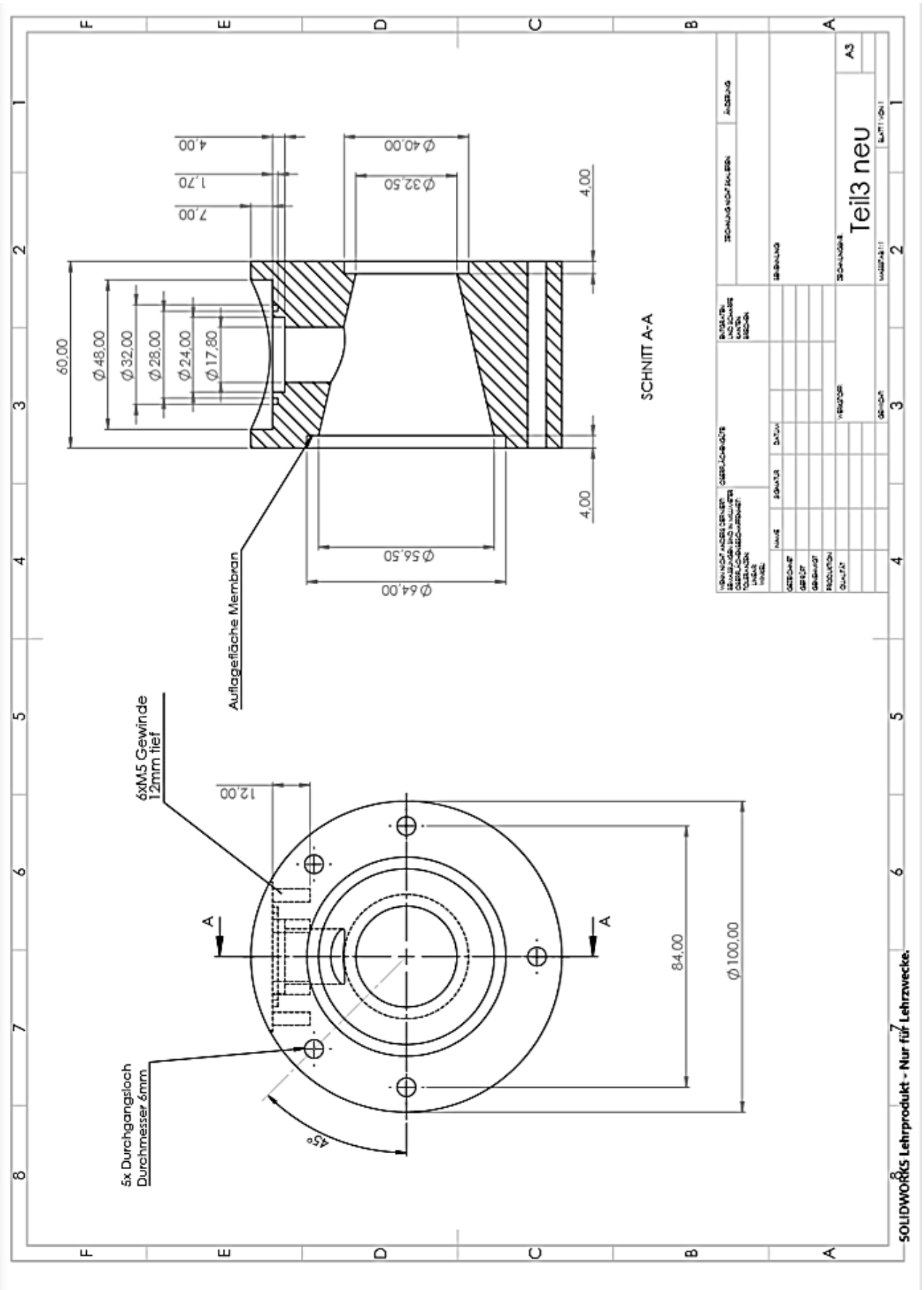


Fig. 9.9 A middle part, where the membrane is fixed.



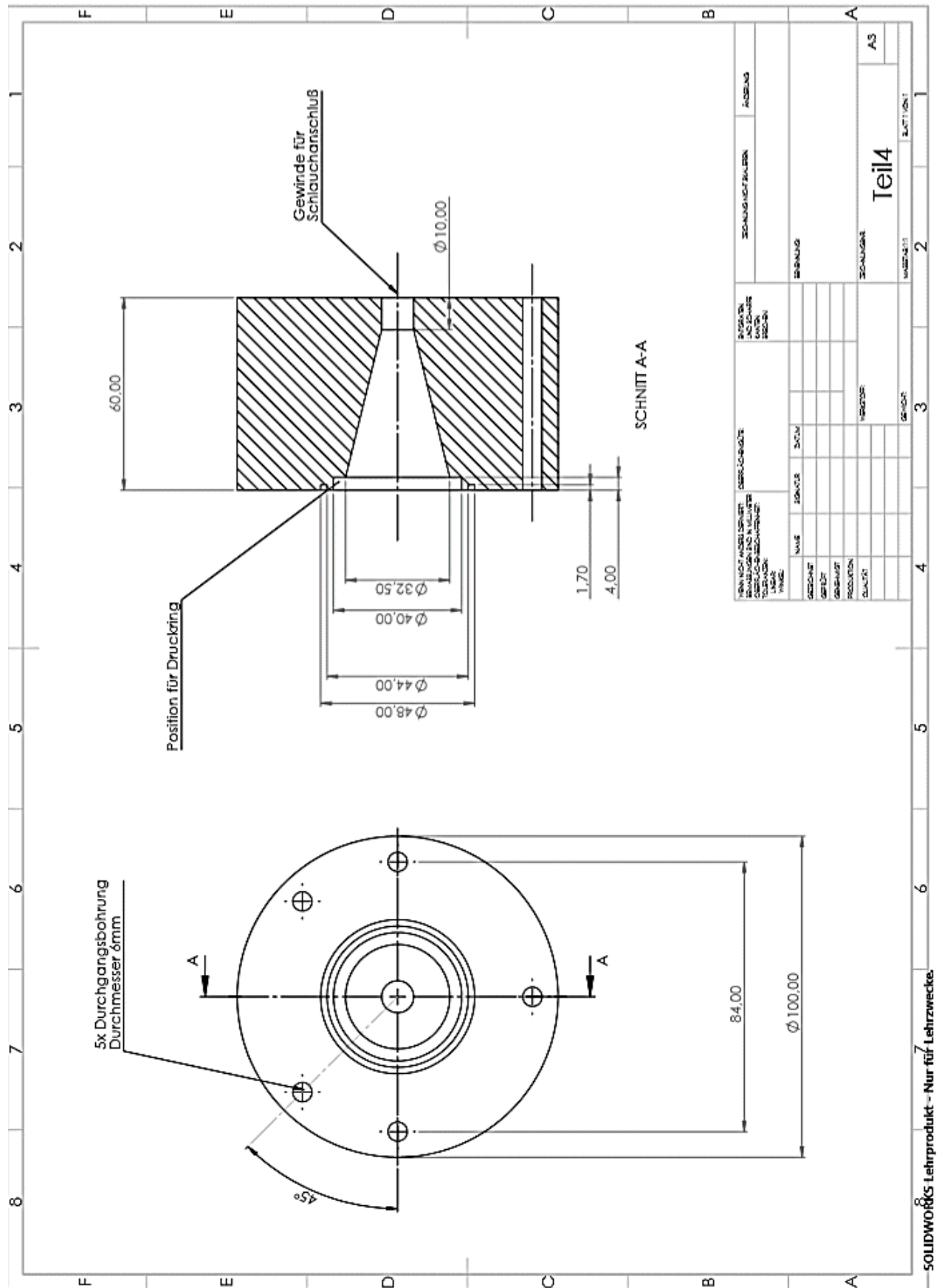


Fig. 9.10 An outlet part, where the fluid exits.



D: Codes for numerical solution of the developed theoretical model, produced in the programming language *Python*.

```

import numpy as np
import matplotlib.pyplot as plt
from scipy.integrate import odeint
from math import *
import pandas as pd
R31=0.655*10**(-3) #31=Droplet 3-silicon 10
R51=0.785*10**(-3) #51=Droplet 5-silicon 10
R71=0.92*10**(-3) #71=Droplet 7-silicon 10
o31=(4/3)*pi*(R31)**(3)
o51=(4/3)*pi*(R51)**(3)
o71=(4/3)*pi*(R71)**(3)
a31=(2*52*10**(-3)*sin(1.5*pi/180)*(o31)) #Coefficient in Laplace force
a51=(2*52*10**(-3)*sin(1.5*pi/180)*(o51))
a71=(2*52*10**(-3)*sin(1.5*pi/180)*(o71))
g31=(2*pi*52*10**(-3)*sin(1.5*pi/180)) # Coefficient in Hysteresis force
g51=(2*pi*52*10**(-3)*sin(1.5*pi/180))
g71=(2*pi*52*10**(-3)*sin(1.5*pi/180))
j31=((2.419*10**(-3)/2)*cos(1.5*pi/180)) #Coefficient in Hysteresis force
j51=((2.682*10**(-3)/2)*cos(1.5*pi/180))
j71=((2.901*10**(-3)/2)*cos(1.5*pi/180))
vk31=((9.78015-7.9164)/(1.4-0.35))*10**(-3) #Vk=V18=(z(k+10)-z(k-10))/(t(k+10)-t(k-10))
vk51=((10.6464-8.113275)/(1.4-0.35))*10**(-3) #Vk=V18
vk71=((10.974525-7.6014)/(1.15-0.15))*10**(-3) #Vk=V14
dth=25*pi/180
mr31=dth/0.003933
br31=(33*pi/180)-(mr31*vk31)
ba31=(37*pi/180)-(mr31*vk31)
bt31=(br31+ba31)/2
mr51=dth/0.005649
br51=(38.8*pi/180)-(mr51*vk51)
ba51=(41*pi/180)-(mr51*vk51)
bt51=(br51+ba51)/2
mr71=dth/0.007218
br71=(41.5*pi/180)-(mr71*vk71)
ba71=(44.2*pi/180)-(mr71*vk71)
bt71=(br71+ba71)/2

```

```

mu31=0.9*((1+((2*0.9)/(3*9.3)))/(1+((0.9)/(9.3))))*10**(-3) #Viscosity of mixture
c31=(24*pi*sin(1.5*pi/180)*((mu31)+(9.3*10**(-3)))) #Coefficient in Drag force
c51=(24*pi*sin(1.5*pi/180)*((mu31)+(9.3*10**(-3))))
c71=(24*pi*sin(1.5*pi/180)*((mu31)+(9.3*10**(-3))))
e31=(3.36*pi*sin(1.5*pi/180)*(2.419*10**(-3))**(0.7)*(((mu31)**(0.3)*(998)**(0.7))+((9.3*10**(-3))**(0.3)*(930)**(0.7)))) #Coefficient in Drag force
e51=(3.36*pi*sin(1.5*pi/180)*(2.682*10**(-3))**(0.7)*(((mu31)**(0.3)*(998)**(0.7))+((9.3*10**(-3))**(0.3)*(930)**(0.7))))
e71=(3.36*pi*sin(1.5*pi/180)*(2.901*10**(-3))**(0.7)*(((mu31)**(0.3)*(998)**(0.7))+((9.3*10**(-3))**(0.3)*(930)**(0.7))))
d31=(sin(1.5*pi/180)*(52*10**(-3))**(1/3)*(9.3*10**(-3)*5)**(2/3)) #Coefficient in Friction force
d51=(sin(1.5*pi/180)*(52*10**(-3))**(1/3)*(9.3*10**(-3)*5)**(2/3))
d71=(sin(1.5*pi/180)*(52*10**(-3))**(1/3)*(9.3*10**(-3)*5)**(2/3))
m31=930*(o31) #Coefficient in Inertia
m51=930*(o51)
m71=930*(o71)
#31
k1=2
k2=0.9
k3=1
#51
k4=3
k5=1.25
k6=1
#71
k7=3.8
k8=1
k9=1
def dy31_dt31(X,t):
    z,y = X
    dy31_dt31 = (1/m31)*((a31*(((tan(1.5*pi/180)*z)+R31)**(-2)))
        -(g31*((z-j31)*(cos((mr31*k3*y)+(br31*k2)))-(cos((mr31*k3*y)+(bt31*k2))))
        +((z+j31)*(cos((mr31*k3*y)+(bt31*k2)))-(cos((mr31*k3*y)+(ba31*k2))))))
        -(k1*c31*z*y)-(k1*e31*z*y**(1.7))
        -(d31*z*y**(2/3)))
    return [y,dy31_dt31]
def dy51_dt51(X,t):
    z,y = X
    dy51_dt51 = (1/m51)*((a51*(((tan(1.5*pi/180)*z)+R51)**(-2)))
        -(g51*((z-j51)*(cos((mr51*k6*y)+(br51*k5)))-(cos((mr51*k6*y)+(bt51*k5))))
        +((z+j51)*(cos((mr51*k6*y)+(bt51*k5)))-(cos((mr51*k6*y)+(ba51*k5))))))

```

```

-(k4*c51*z*y)-(k4*e51*z*y**(1.7))
-(d51*z*y**(2/3)))
return [y,dy51_dt51]
def dy71_dt71(X,t):
z,y = X
dy71_dt71 = (1/m71)*((a71*(((tan(1.5*pi/180)*z)+R71)**(-2)))
-(g71*((z-j71)*(cos((mr71*k9*y)+(br71*k8)))-(cos((mr71*k9*y)+(bt71*k8))))
+((z+j71)*(cos((mr71*k9*y)+(bt71*k8)))-(cos((mr71*k9*y)+(ba71*k8))))))
-(k7*c71*z*y)-(k7*e71*z*y**(1.7))
-(d71*z*y**(2/3)))
return [y,dy71_dt71]
t=np.linspace(0,50,100)
X031 = [0.006643,0.003933]
X051 = [0.006643,0.005649]
X071 = [0.006643,0.007218]
Z31 = odeint(dy31_dt31,X031,t)
Z51 = odeint(dy51_dt51,X051,t)
Z71 = odeint(dy71_dt71,X071,t)
data31= pd.read_excel('./data/silicon10-alpha 3-Drop3-01.03.2021-kopie.xlsx')
data51= pd.read_excel('./data/silicon10-alpha 3-Drop5-01.03.2021-kopie.xlsx')
data71= pd.read_excel('./data/silicon10-alpha 3-Drop7-01.03.2021-kopie.xlsx')
plt.rcParams['figure.figsize'] = 10,16.5
plt.rcParams['axes.grid'] = False
plt.rcParams['lines.markersize'] = 5
plt.rcParams['font.size'] = 18
plt.rcParams["font.weight"] = "bold"
plt.rcParams["axes.labelweight"] = "bold"
plt.subplot(311)
plt.plot(t, Z71[:,0], color='red',linestyle='-', label='α=1.5° - D=1.84 mm - Sil 10 - Theory')
plt.plot(t, Z51[:,0], color='black',linestyle='-', label='α=1.5° - D=1.57 mm - Sil 10 - Theory')
plt.plot(t, Z31[:,0], color='blue',linestyle='-', label='α=1.5° - D=1.31 mm - Sil 10 - Theory')
plt.scatter(x='t in s',marker='^',c='r',s=20, y='z in mm', data=data71, label='α=1.5° - D=1.84 mm - Sil 10 - Exp')
plt.scatter(x='t in s',marker='^',c='k',s=20, y='z in mm', data=data51, label='α=1.5° - D=1.57 mm - Sil 10 - Exp')
plt.scatter(x='t in s',marker='^',c='b',s=20, y='z in mm', data=data31, label='α=1.5° - D=1.31 mm - Sil 10 - Exp')
plt.xlabel("t (s)", fontsize='large')
plt.ylabel("z (m)", fontsize='large')
plt.legend(loc="lower right", ncol=1,prop={'size':15},labelspacing=0.1)
plt.ylim(0,0.02)

```

```
plt.xlim(0,3)
plt.locator_params(axis='y', nbins=5)
plt.locator_params(axis='x', nbins=5)
plt.subplot(312)
plt.plot(t, Z71[:,1], 'red',linestyle='-',label='α=1.5° - D=1.84 mm - Sil 10 - Theory')
plt.plot(t, Z51[:,1], 'black',linestyle='-', label='α=1.5° - D=1.57 mm - Sil 10 - Theory')
plt.plot(t, Z31[:,1], 'blue',linestyle='-',label='α=1.5° - D=1.31 mm - Sil 10 - Theory')
plt.xlabel("t (s)", fontsize='large')
plt.ylabel("dz/dt (m/s)", fontsize='large')
plt.legend(loc="best",ncol=1,prop={'size':15},labelspacing=0.1)
plt.ylim(0,0.01)
plt.xlim(0,25)
plt.subplot(313)
plt.plot(Z71[:,0], Z71[:,1], 'red',linestyle='-', label='α=1.5° - D=1.84 mm - Sil 10 - Theory')
plt.plot(Z51[:,0], Z51[:,1], 'black',linestyle='-', label='α=1.5° - D=1.57 mm - Sil 10 - Theory')
plt.plot(Z31[:,0], Z31[:,1], 'blue', linestyle='-',label='α=1.5° - D=1.31 mm - Sil 10 - Theory')
plt.xlabel("z (m)", fontsize='large')
plt.ylabel("dz/dt (m/s)", fontsize='large')
plt.legend(loc="best",ncol=1,prop={'size':15},labelspacing=0.1)
plt.ylim(0,0.01)
plt.xlim(0.006643,0.025)
plt.locator_params(axis='y', nbins=5)
plt.locator_params(axis='x', nbins=5)
plt.subplots_adjust(top=0.9, bottom=0.05, left=0.10, right=0.95, hspace=0.2, wspace=0.35)
plt.savefig('fODE_plots.png')
plt.show()
#Forces
import pdb
def f_d(Z31):
    z = Z31[:,0]
    y = Z31[:,1]
    return (a31*(((tan(1.5*pi/180)*z)+R31)**(-2))) #Laplace force
def f_h(Z31):
    z = Z31[:,0]
    y = Z31[:,1]
    return -(g31*((z-j31)*((np.cos((mr31*k3*y)+(br31*k2)))-(np.cos((mr31*k3*y)+(bt31*k2))))
            +((z+j31)*((np.cos((mr31*k3*y)+(bt31*k2)))-(np.cos((mr31*k3*y)+(ba31*k2)))))) #Hysteresis
force
def f_f(Z31):
    z = Z31[:,0]
```

```

y = Z31[:,1]
return -(k1*c31*z*y)-(k1*e31*z*y**(1.7)) #Drag force
def f_v(Z31):
z = Z31[:,0]
y = Z31[:,1]
return -(d31*z*y**(2/3)) #Friction force
Fd = f_d(Z31)*1000
Fh = f_h(Z31)*1000
Ff = f_f(Z31)*1000
Fv = f_v(Z31)*1000
## Plot results
plt.rcParams['figure.figsize'] = 10, 5
plt.rcParams['axes.grid'] = False
plt.rcParams['lines.markersize'] = 5
plt.rcParams['font.size'] = 18
plt.rcParams["font.weight"] = "bold"
plt.rcParams["axes.labelweight"] = "bold"
plt.plot(Z31[:,0], Fd, 'b:', label='F_d -  $\alpha=1.5^\circ$  - D=1.31 mm - Sil 10')
plt.plot(Z31[:,0], Fh, 'g-.', label='F_h -  $\alpha=1.5^\circ$  - D=1.31 mm - Sil 10')
plt.plot(Z31[:,0], Fv, 'r-', label='F_v -  $\alpha=1.5^\circ$  - D=1.31 mm - Sil 10')
plt.plot(Z31[:,0], Ff, 'k--', label='F_f -  $\alpha=1.5^\circ$  - D=1.31 mm - Sil 10')
plt.xlabel("z (m)", fontsize='large')
plt.ylabel("Force (mN)", fontsize='large')
plt.legend(loc="best",ncol=1,prop={'size':15},labelspacing=0.1)
plt.xlim(0.006643, 0.03)
plt.ylim(-0.008, 0.008)
plt.locator_params(axis='y', nbins=10)
plt.locator_params(axis='x', nbins=5)
plt.savefig(fForce_plots_together.png)
plt.show()

```